

biomass coreh₂o premier
→ REPORT FOR MISSION SELECTION

An Earth Explorer to observe atmospheric composition

SP-1324/3
May 2012

biomass coreh₂o premier
→ **REPORT FOR MISSION SELECTION**

An Earth Explorer to observe atmospheric composition

This report is based on contributions from the following members of the PREMIER Mission Advisory Group (MAG):

Brian Kerridge – MAG Chairman (Rutherford Appleton Laboratory, GB)
Michaela Hegglin (University of Toronto, CA)
Jack McConnell (York University, Ontario, CA)
Donal Murtagh (Chalmers University of Technology, SE)
Johannes Orphal (Karlsruhe Institute of Technology, DE)
Vincent-Henri Peuch (ECMWF, GB)
Martin Riese (Jülich Research Centre, DE)
Michiel van Weele (Royal Dutch Meteorological Institute, NL)

The scientific content of the report was compiled by Jörg Langen (Scientific Coordinator) with additional contributions, in particular, from Ugo Cortesi (CNR-IFAC, IT), Peter Preusse and Bärbel Vogel (both Jülich Research Centre, DE) and from ESA, Dirk Schüttemeyer.

The technical content of the report was compiled by Bernardo Carnicero Domínguez (Technical Coordinator) with contributions from Jérôme Caron, Christophe Caspar, Antonio Gabriele, Pedro Jurado, Ville Kangas, Stefan Kraft, Chung-Chi Lin, Herbert Nett and David Patterson (all from ESA), and Anders Emrich, Urban Frisk, Fredrik von Schéele (all from Omnisys, SE), based on inputs derived from the industrial Phase-A system and technical activities, and the Swedish nationally-funded STEAMR Programme.

Recommended citation: ESA (2012). Report for Mission Selection: PREMIER, ESA SP-1324/3 (3 volume series), European Space Agency, Noordwijk, The Netherlands.

Cover image: ESA/AOES Medialab

An ESA Communications Production

Publication	<i>Report for Mission Selection: PREMIER</i> (ESA SP-1324/3, May 2012)
Production Editor	K. Fletcher
Text Editing	H. Rider
Layout	D. Wishart
Publisher	ESA Communication Production Office ESTEC, PO Box 299, 2200 AG Noordwijk, The Netherlands Tel: +31 71 565 3408 Fax: +31 71 565 5433 www.esa.int
ISBN	978-92-9221-422-7 (3 volumes)
ISSN	0379-6566
Copyright	© 2012 European Space Agency

Contents

Executive Summary	3
1. Introduction	9
2. Background and Scientific Justification	13
2.1 Introduction	13
2.2 Why is the UTLS Important for Climate?.	14
2.2.1 Key Radiative Processes	14
2.2.2 Key Roles of Atmospheric Constituents in the UTLS	15
2.2.3 Key Dynamic Processes	18
2.3 Chemistry-climate Interactions	20
2.3.1 Sensitivity of Surface Climate to UTLS Variability and General Circulation	20
2.3.2 Trace-gas Exchange between Troposphere and Stratosphere	23
2.3.3 Impacts of Convection, Pyroconvection and Outflow on the UTLS	25
2.3.4 Processes Linking the UTLS to the Lower Troposphere	27
2.4 Improving Medium-range to Seasonal Meteorological Forecasts	29
2.5 The Unique Contribution of PREMIER	31
3 Research Objectives	35
4 Observational Requirements	41
4.1 Rationale for Global Height-resolved Observations from Space in 2019–23	41
4.2 Geophysical Level-2 Data Requirements.	41
4.2.1 Height-domain, Coverage, Spatio-temporal Sampling and Resolution.	41
4.2.2 Driving Geophysical Level-2 Data Requirements	42
4.2.3 Requirements for Ancillary Data	44
4.2.4 Additional Level-2 Products.	44
4.3 Geophysical Level-2 Data Requirements for Operational Applications	45
4.3.1 Generic Requirements Supporting GMES Atmosphere Service and NWP	45
4.3.2 Timeliness Requirement for Operational Applications	45
4.4 Requirement for Limb-emission Sounding and Tandem Flying with MetOp	46
4.4.1 Introduction	46
4.4.2 Atmospheric Limb Emission Sounding Heritage	47
4.4.3 Combining Advanced Infrared and Millimetre-wave Limb Sounders	48
4.4.4 Combination of PREMIER Limb-emission with MetOp/MetOp-SG Nadir Observations	50
4.4.5 Exploitation of Data from Other Concurrent Missions.	51
4.5. Level-1b Data Requirements	51
4.5.1 Level-1b Data Requirements for IRLS	51
4.5.2 Level-1b Data Requirements for STEAMR	53
5. System Concept	59
5.1 Introduction	59
5.2 Mission Architecture Overview	59
5.3 Mission Analysis	60

5.4	Space Segment.	62
5.4.1	Overview	62
5.4.2	Satellite Configuration.	63
5.4.3	Payload	66
5.4.4	Platform.	92
5.4.5	Budgets	103
5.5	Launcher.	104
5.6	Ground Segment and Data Processing	106
5.6.1	Overview	106
5.6.2	Ground Segment Elements	106
5.6.3	Flight Operation Segment	109
5.6.4	Payload Data Ground Segment.	111
5.6.5	Mission Data Processing	114
5.7	Operation and Utilisation Concept.	117
5.7.1	Overview	117
5.7.2	LEOP and Commissioning	117
5.7.3	Routine Operations/Calibrations	118
5.7.4	Contingency Operations	119
5.7.5	Disposal.	120
6	Scientific Data Processing and Validation Concept	123
6.1	Introduction	123
6.2	Atmospheric Composition Retrieval	123
6.2.1	Limb-Emission Sounding.	123
6.2.2	Nadir-sounding and Limb–Nadir Synergy.	129
6.3	Data Assimilation.	130
6.4	Validation Concept	131
6.4.1	Established Techniques for Limb-emission Sounders.	132
6.4.2	New Techniques for PREMIER	133
7	Performance Estimation	137
7.1	Background.	137
7.2	Level-1b Performance	137
7.2.1	Introduction	137
7.2.2	System Performance	137
7.2.3	IRLS	139
7.2.4	STEAMR.	145
7.2.5	Geo-location, LOS Stability and Inter-instrument Co-registration	150
7.2.6	End-to-end Simulator Description and Results	152
7.3	Individual Profile Retrievals	155
7.3.1	Introduction	155
7.3.2	Estimated Errors on Retrieved Profiles	155
7.3.3	Summary of Overall Compliance with Geophysical Data Requirements	161
7.4	Scientific Impact	162
7.4.1	Impact of UTLS Variability and General Circulation on Surface Climate (Objective A)	163
7.4.2	Stratosphere–Troposphere Trace-gas Exchange (Objective B)	167
7.4.3	Impacts of Convection, Pyroconvection and Outflow on the UTLS (Objective C)	171
7.4.4	Processes Linking the Composition of UTLS and Lower Troposphere (Objective D)	175

7.5	Value-Added Operational Applications	179
7.5.1	Introduction	179
7.5.2	Impact of MIPAS and IASI Data on the Analysis and Forecast of Tropospheric Ozone	179
7.5.3	Impact of PREMIER Data on Background Error Covariances	179
7.5.4	The Impact of PREMIER in Numerical Weather Prediction	180
7.5.5	The Impact of PREMIER in Detection of Volcanic Ash Plumes	181
7.6	Summary.	182
8	Mission Context	187
8.1	Introduction	187
8.2	PREMIER Scientific User Community and its Readiness	187
8.3	PREMIER in Global Context	188
8.4	Application Potential of PREMIER.	190
8.4.1	Global Height-resolved Monitoring of Atmospheric Composition and Links with Climate	190
8.4.2	Operational GMES Atmosphere Services	191
8.4.3	Operational Numerical Weather Prediction	193
9	Programmatics	197
9.1	Introduction	197
9.2	Scientific Maturity, Critical Areas and Risks	197
9.3	Technical Maturity, Critical Areas and Risks	198
9.3.1	Summary	198
9.3.2	Satellite and Platform	199
9.3.3	IRLS	199
9.3.4	STEAMR.	202
9.4	Development Approach and Schedule	205
9.4.1	Overall Design and Development Approach	205
9.4.2	Schedule	207
9.5	Conclusion	207
	References.	211
	Acronyms	221
	Chemical Species	224

→ EXECUTIVE SUMMARY

Executive Summary

The Earth Explorer PREMIER mission will be the first satellite mission to determine 3D fields of atmospheric trace gases and temperature at a resolution high enough to study chemical, dynamic and radiative processes in the upper troposphere and lower stratosphere, the UTLS. Climate is particularly sensitive to atmospheric composition in this region because this is where much infrared radiation escapes to space, where cirrus clouds trap outgoing terrestrial radiation, and where ozone is most effective as a greenhouse gas. In synergy with nadir-viewing operational weather satellites, such as MetOp, PREMIER will also contribute to improved estimates of pyrogenic, biogenic, anthropogenic and volcanic emissions that affect global and regional air quality.

State-of-the-art coupled chemistry-climate models provide the best means of predicting future changes in climate on decadal to century time scales. However, for processes occurring on spatial scales smaller than a model's grid size, the models rely on parameterisations of the physical and chemical processes. The current understanding of the interactions between climate change and atmospheric chemistry is subject to large uncertainties, often because of a lack of knowledge about processes at high spatial resolution. PREMIER will unveil the coupled chemistry and dynamics of the UTLS and provide improved parameterisations for climate-change modelling. The mission's four scientific objectives relate to the impacts of UTLS variability and general atmospheric circulation on Earth's surface climate, the exchange of trace gases between the troposphere and stratosphere, convection and pyroconvection and their impact on the composition of the UTLS, and processes that link the composition of the UTLS and the lower troposphere.

The Intergovernmental Panel on Climate Change has identified the interaction between air quality and climate as an area of high priority for future research. This resulted in the establishment of a major joint project on atmospheric chemistry and climate involving the World Climate Research Programme and the International Geosphere Biosphere Programme. PREMIER responds to needs identified in the project and also addresses four (out of five) scientific challenges relating to the atmosphere in ESA's Living Planet Programme.

The UTLS is a region that is difficult to measure from space. Instruments looking through the UTLS in the nadir direction do not have the vertical resolution to resolve details. Existing limb-viewing instruments have limitations in the upper troposphere where they often fail to see through clouds. PREMIER will provide new limb observations from innovative space sensors from which chemical composition and temperature profiles can be retrieved with unprecedented spatial detail and, at the same time, with global coverage. Such observations will be key in improving our understanding of atmospheric processes in the UTLS. The mission performs 3D observations of the atmosphere in the infrared (710–1650 cm^{-1}) and 2D observations in the mm-wave (320–360 GHz) spectral range, and links atmospheric and surface processes by combining the PREMIER limb and MetOp nadir observations. The PREMIER space segment consists of a single satellite carrying two instruments: the infrared limb sounder, IRLS, and the STEAMR mm-wave limb sounding radiometer provided in-kind by Sweden. The satellite will fly in the same orbit as Eumetsat's MetOp mission (or planned follow-on) to achieve the required co-registration between the PREMIER limb observations and the MetOp nadir observations. More precisely, PREMIER flies in loose formation with MetOp, some eight minutes ahead and, therefore, in a rearward limb-viewing configuration. The IRLS is an imaging Fourier-transform spectrometer that combines the functions of spectrometer and imager with a cloud discrimination

function. The IRLS operates in two mutually exclusive operational modes, namely the dynamics mode and the chemistry mode, with different spatial, spectral and radiometric performance. The dynamics mode focuses on observing atmospheric temperature and constituents at very fine spatial scales to study dynamic processes, while the chemistry mode provides observations of a wider range of trace gases at high spectral resolution to investigate the transport and chemical processes controlling their distributions. STEAMR is a mm-wave radiometer based on a tomographic multibeam limb-sounding concept. It observes 14 tangent altitudes simultaneously and provides vertical and horizontal well-resolved information on the distribution of key UTLS constituents such as water vapour, ozone and carbon monoxide, even in the presence of cirrus clouds. The instrument has heritage from the sub-mm wave radiometer on the Odin mission. The PREMIER satellite has a launch mass of ~1125 kg, versus a launcher nominal capability of 1240 kg, and a power generation capability at end of life of ~2.3 kW. The instantaneous instrument data rate of 19–29 Mbit/s requires, for the different communication architectures under consideration, an onboard mass memory of ~260–400 Gbit and a data downlink capacity of ~270 Mbit/s.

The baseline Vega launcher will inject the satellite into a phasing orbit from which PREMIER will manoeuvre into its nominal orbit, i.e. that of MetOp. PREMIER is also compatible with the Polar Satellite Launch Vehicle, as a backup. The ground segment uses the generic Earth Explorer ground segment infrastructure. This comprises the Flight Operation Segment and the Payload Data Ground Segment. The scientific data are downlinked via an X-band to a single high-latitude ground station in, for example, Svalbard (Norway) or to two stations in, for example, Kiruna (Sweden) and Inuvik (Canada) to meet the maximum five-hour data latency requirement.

No critical scientific issues were identified by the Earth Science Advisory Committee at the mission down-selection following Phase-0. During Phase-A, scientific studies and campaigns were performed to consolidate the requirements and establish mission performance on the basis of simulations and data from airborne precursor instruments. Also, the considerable scientific impact of the mission has been demonstrated in studies for each of the four mission objectives. A high data uptake by a wide international community can be expected. For the analysis of PREMIER data, the scientific community can build on retrieval techniques developed for previous limb-emission sounders on missions such as Envisat, Aura and Odin. Spaceborne data on stratospheric and tropospheric composition have been used extensively to improve and validate atmospheric models. The required improvements of data assimilation schemes and models to take full benefit of PREMIER data are part of ongoing developments in the scientific community, progressively integrating previously separated components towards the development of Earth system models. There is confidence in the availability of suitable models and assimilation tools when PREMIER would be launched. The risk associated with the availability of MetOp/MetOp-Second Generation data is considered low, owing to the continuity and reliability of the operational weather satellite system.

PREMIER is considered technically feasible, but some risks about the compatibility of the development with the target date of 2019 have been identified owing to the length of time needed for the development and manufacturing of the IRLS detectors.

The system design is well consolidated. However, at this stage of development, the small clearance within the Vega fairing is considered to be a risk for the mission. An optimisation of the payload size to increase the margin is in progress. The platform subsystems are largely based on flight-proven designs and are considered technologically mature with no major associated risks. Careful consideration, however, needs to be given to minimise microvibrations. The IRLS is considered a challenging, but feasible, instrument with few risk items identified. The large existing heritage (e.g.

IASI, MIPAS, GOSAT), the ongoing predevelopments and the large number of similarities both in common equipment and risk areas with the Meteosat Third Generation-infrared sounder increase confidence in the instrument feasibility. The STEAMR is a complex instrument with heritage from the sub-mm wave radiometer on the Swedish Odin mission. The development plan proposed within the Swedish national programme is based on early prototyping and testing. The instrument is considered feasible, but there may be a potential risk for the development depending on the space qualification approach of critical components, which is to be clearly defined in the development programme. The ground segment is not considered critical.

Assuming the expected successful outcome of ongoing and planned predevelopments, the maturity of critical technologies will reach the required level prior to the start of the implementation phase. Nevertheless, the two instruments are on the critical path. For the IRLS, the schedule is driven by the development of the detectors. For STEAMR, the space qualification of critical components is considered as a potential development risk. Based on these elements and assuming that a technology maturity elongation in Phase-B1 is not required, the launch would be feasible in early 2020.

→ INTRODUCTION

1. Introduction

The changing Earth system poses significant scientific challenges and opportunities for Earth observations from the vantage point of space. As part of its Earth Observation Envelope Programme, the European Space Agency's (ESA's) series of Earth Explorer missions offers new observational capabilities to explore and understand different aspects of the Earth system.

These missions are developed in response to priorities identified by the scientific community. They address and fulfil ESA's Living Planet Programme strategic objectives (SP-1304, 2006) and comprise a critical component of the global Earth observing system.

The fundamental principle of defining, developing and operating Earth Explorer missions in close cooperation with the scientific community provides an efficient tool to address pressing Earth-science questions as effectively as possible. Coupled with an ability to develop and embark novel sensing technologies, this gives the possibility to substantially advance the frontier of our scientific knowledge of the Earth system and the human impact on natural processes.

Since the science and research elements of the Living Planet Programme were established in the mid-1990s, this user-driven strategy has resulted in the selection of six Earth Explorer missions for implementation. Together, they cover a broad range of scientific topics. Importantly, the complementarity between the selected missions also offers new opportunities for exploiting mission synergies, thereby establishing a stimulus for the development of new applications of Earth observation data.

Earth Explorer missions are split into two categories: Core and Opportunity. Core Earth Explorers are larger missions addressing complex issues of scientific interest and which require substantial elements of new technology. By contrast, Opportunity missions are smaller and have more focused scientific goals that are normally achieved by novel uses of existing lower-risk technologies. Through a process of peer review and selection, both types are implemented in separate cycles to ensure a steady flow of missions to address key Earth-science questions.

The first cycle for Core missions resulted in the Gravity field and steady-state Ocean Circulation Explorer, GOCE, which was launched in March 2009, and the Atmospheric Dynamics Mission ADM-Aeolus, scheduled for launch in 2014. The second cycle, initiated in 2000, resulted in the Earth Clouds Aerosols and Radiation Explorer, EarthCARE, due for launch in 2015. The first cycle for Opportunity missions resulted in the ice mission CryoSat, which was rebuilt and launched in April 2010 following a launch failure in 2005, and the Soil Moisture and Ocean Salinity, SMOS, mission, also launched in 2009. The second cycle resulted in the magnetic field mission, Swarm, which is scheduled to be launched in 2012.

A third cycle of Earth Explorer Core missions was initiated by a Call for Ideas released in 2005. In May 2006, six of the candidate missions were selected for Assessment Study following a peer review of 24 proposed mission ideas. Upon completion of Pre-Feasibility Study (Phase-0), a User Consultation Meeting was held in January 2009 in Lisbon, Portugal, at which the six candidates were presented to the scientific community together with their accompanying Reports for Assessment (SP-1313, 2008).

In February 2009, three out of the six candidates were selected for Feasibility Study (Phase-A): Biomass, Cold Regions Hydrology high-resolution Observatory (CoReH₂O) and Process Exploration through Measurement of infrared and millimetre-wave Emitted Radiation (PREMIER).

- Biomass aims to observe global forest biomass for a better understanding of the carbon cycle.
- CoReH₂O aims to observe snow and ice for a better understanding of the water cycle.
- PREMIER aims to observe atmospheric composition for a better understanding of chemistry–climate interactions.

The Report for Mission Selection for each candidate captures the status of the respective mission concept at the end of Phase-A activities. The three reports are provided to the Earth observation research community prior to the User Consultation Meeting to be held in 2013 and subsequent selection of a single Earth Explorer 7 mission.

The three reports follow a common structure comprising this introductory first chapter and eight subsequent chapters as follows:

- Chapter 2 – identifies the background and scientific issues to be addressed by the mission, considering the contribution of past and present activities in the field. It provides the justification for the mission, set within the post-2018 timeframe, and includes a review of the current scientific understanding of the issue in question while identifying the potential ‘delta’ that the mission could provide.
- Chapter 3 – drawing on arguments presented in Chapter 1 and Chapter 2, this chapter summarises the specific research objectives of the mission.
- Chapter 4 – outlines the mission requirements, including required geophysical data products and observational parameters, the need for observations from space and aspects of timeliness and timing of the mission.
- Chapter 5 – provides an overview of the system elements, including the space and ground segments; and of the operations, calibration and data processing up to Level 1b.
- Chapter 6 – describes the advances in scientific algorithms and processing, validation and assimilation techniques which may be required to meet the data product requirements.
- Chapter 7 – makes a comparison of expected versus required performance and ability to fulfil the research/observational objectives based upon the documented system concept.
- Chapter 8 – documents the maturity of the scientific user community in respect to planned use of the anticipated scientific products, the global context in terms of complementary missions as well as the operational or applications potential of the data products.
- Chapter 9 – outlines a programme of implementation. It also addresses scientific and technical maturity, the development status of key technologies, risks, logistics and schedules.

This Report for Selection covers the PREMIER mission.

**→ BACKGROUND
AND SCIENTIFIC
JUSTIFICATION**

2. Background and Scientific Justification

2.1 Introduction

Climate change is one of the greatest challenges facing society this century. *The Changing Earth* (ESA, SP-1304, 2006) highlights several climate-change challenges for the scientific community, including better qualitative and quantitative understanding of the role the atmosphere plays in the climate system. The Intergovernmental Panel on Climate Change (IPCC) has identified the interactions between atmospheric composition and climate to be a key uncertainty in our understanding of climate change (Denman et al., 2007). In this context Earth-System Models (ESMs) are being built to investigate global environmental issues in an integrated manner. It is clear that atmospheric chemistry-climate interactions need to be incorporated into ESMs to gain an understanding of how changes in atmospheric composition, driven by natural and anthropogenic emissions, influence both the current and future climate.

Climate is particularly sensitive to changes in the chemical composition and temperature of the UTLS. This region lies at an altitude of about 6–25 km where the thermal contrast with the surface is largest and, therefore, Earth's thermal radiation can be trapped most effectively (Gettelman et al., 2011). Furthermore, interaction of the radiation field with water vapour, ozone, cirrus cloud and aerosol distributions in the UTLS leads to important, though poorly quantified, climate feedbacks. Couplings between radiative, dynamic, and chemical feedbacks in this region modulate the surface climate and atmospheric general circulation on daily to decadal and century timescales.

Figure 2.1 illustrates some processes that should be included in climate models. The tropopause is the boundary between the free troposphere (light blue) and the stratosphere (medium and dark blue). The light-blue arrow indicates wave-driven Brewer–Dobson circulation, which is the main transport pathway in the stratosphere. Tropospheric air enters the stratosphere predominantly in the Tropics and is transported poleward and downwards at high latitudes. In the extratropics, exchange between the lowermost stratosphere (medium blue) and the free troposphere is bidirectional. Nitrogen oxides (NO_x), carbon monoxide and organic compounds emitted from industry and biomass-burning into the planetary boundary layer (light green) can be transported quickly into the free troposphere through convection or long-range transport. Other sources of NO_x in the free troposphere are lightning

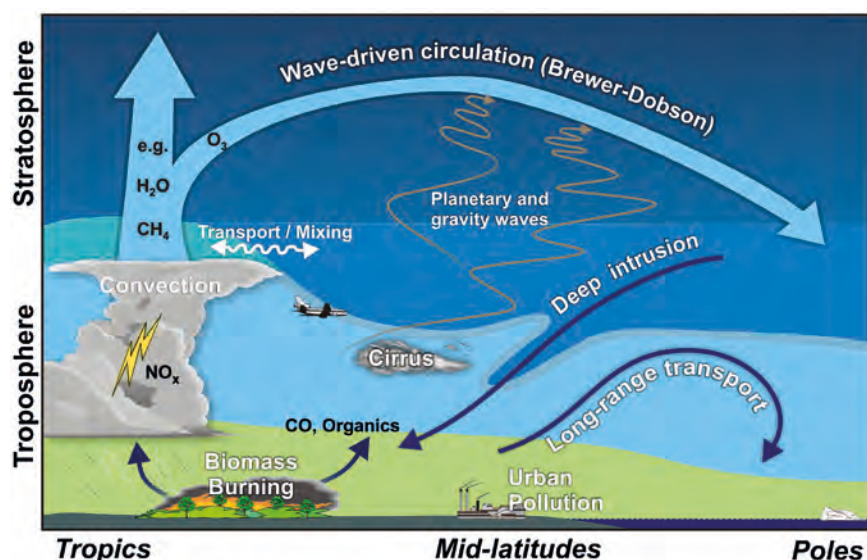


Figure 2.1. The global structure of the troposphere and lower stratosphere. (P. Preusse)

and aircraft emissions. These processes, which affect the distribution of important radiative gases, are known to occur on the mesoscale (<50–200 km), in narrow atmospheric layers (<1–3 km) and in short timescales (<1–5 days). Since climate models do not have sufficient high resolution, these processes must be parameterised. Multimodel comparisons have revealed significant disagreements that can often be traced to varying representation of processes in the UTLS (SPARC CCMVal, 2010), highlighting that the validation of models in the UTLS is hampered by a lack of suitable measurements. Clearly, a reduction of the uncertainties in model projections of climate change requires an improvement in our scientific understanding and representation of these processes, which in turn requires global observations in the UTLS with markedly improved spatial resolution.

This poses a formidable challenge because the physical and chemical properties of the UTLS are difficult to measure. *In situ* measurements from aircraft and balloons are of high resolution and high accuracy, but cannot provide sufficient spatial and temporal coverage to yield a representative picture of this highly variable atmospheric region. Nadir-viewing satellite instruments can provide adequate geographical coverage and horizontal resolution, but their vertical resolution is generally too coarse to capture relevant structures. While higher vertical-resolution data can be obtained from current limb-viewing satellite measurements, their horizontal sampling is insufficient. A new satellite mission dedicated to meeting this challenge is therefore essential.

In this chapter we describe the UTLS and the advances in understanding that will follow from this mission. Section 2.2 explains why the UTLS is a critical region in the climate system. Section 2.3 outlines relevant interactions between chemistry and climate, and the underlying processes that PREMIER will address. Section 2.4 outlines how medium- to long-range weather forecasts are expected to improve by using PREMIER measurements, and Section 2.5 summarises the unique scientific contribution that PREMIER will make.

2.2 Why is the UTLS Important for Climate?

Radiative, dynamic and chemical processes in the UTLS region are important to the climate system. Figure 2.1 illustrates the complexity of processes that occur in this region. It is a region where the concentrations of radiatively active gases such as ozone and water vapour exhibit steep vertical gradients and large spatial and temporal variability, where lateral exchange of air occurs between the tropical upper-troposphere (UT) and the extratropical lower-stratosphere (LS) and where dynamic interactions between the troposphere and the stratosphere take place. The UTLS is also influenced by the injection of surface emissions from convection or the upward transport in frontal systems, and is the region where commercial aircraft fly, injecting pollutants *in situ*, and also forming contrails, thereby, affecting the distribution of cirrus cloud.

This section provides some introductory information on key radiative processes in the atmosphere (Subsection 2.2.1) and how different constituents and their interplay with temperature determine the direct radiative forcing of climate (Subsection 2.2.2). It also highlights the importance of the atmospheric circulation as a driver of the climate system, since it affects the distribution of atmospheric trace gases and aerosols and dynamic couplings to the surface climate that result from interactions between atmospheric temperatures, winds and waves (Subsection 2.2.3).

2.2.1 Key Radiative Processes

Radiative forcing (in units of Wm^{-2}) is a measure of the influence a parameter has in altering the balance of incoming and outgoing energy in the Earth-

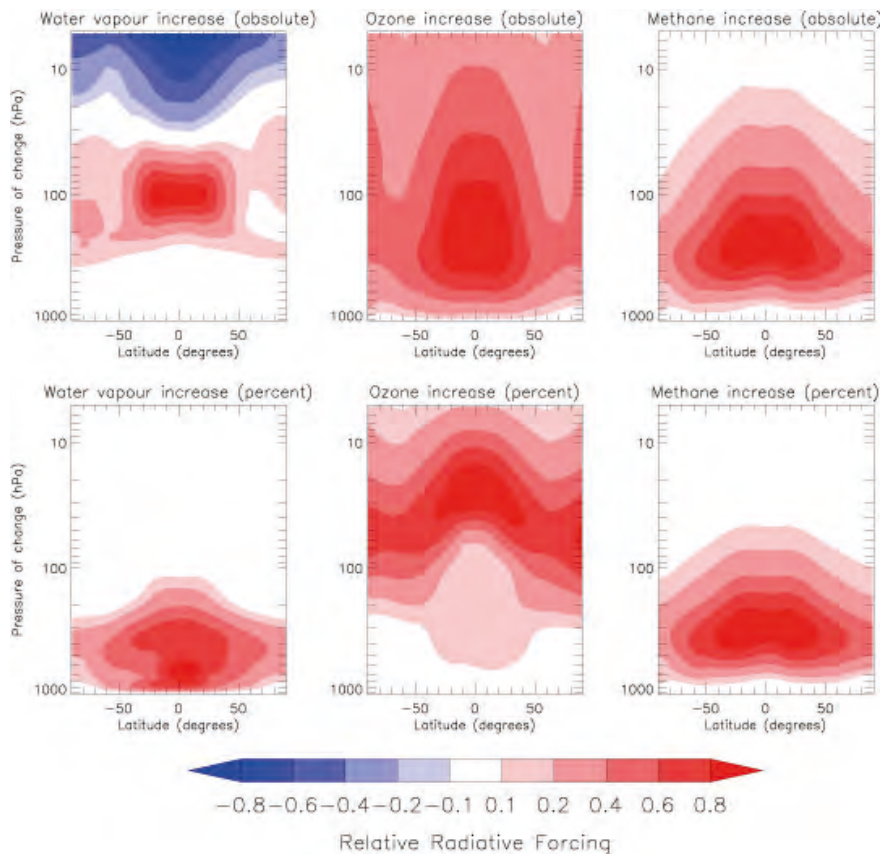


Figure 2.2. The sensitivity of surface-temperature on changes in the UTLS. The impact depends on the altitude and latitude where the water vapour (left), ozone (middle), or methane change (right) takes place. Shading shows relative surface impact, measured as a radiative forcing, from either a fixed mass increase applied at different altitudes (upper panels) or a fixed percentage increase applied at different altitudes (lower panels). Red shows where increases in the gas lead to maximum surface warming – this is typically in the UTLS region. Increases are applied to a 1 km-thick layer centred on the y-axis pressure. The figure follows methodology outlined in Forster and Shine (1997).

atmosphere system and is an index of the importance of the factor as potential climate-change mechanism (IPCC, 2007). Such factors include changing greenhouse gas concentrations, cloud cover or surface albedo. A positive radiative forcing causes a warming of Earth’s surface; a negative radiative forcing causes a cooling. The radiative properties of the UTLS region are determined by the distributions of greenhouse gases such as ozone (O_3) and water vapour (H_2O), both of which are highly variable, methane (CH_4) and nitrous oxide (N_2O), which are variable in the stratosphere, and those such as carbon dioxide (CO_2) which are more uniformly-mixed, along with cirrus clouds and aerosols. While radiatively-active constituents have a local effect on temperatures and hence winds, they also affect surface temperatures. Figure 2.2 shows the sensitivity of surface temperature to changes in atmospheric composition as a function of height and latitude. Owing to the very low temperatures found in the vicinity of the tropopause, the largest effects occur in the UTLS region. Thus, knowledge of the vertical distribution of radiatively-active constituents and of temperature is critical.

2.2.2 Key Roles of Atmospheric Constituents in the UTLS

2.2.2.1 Water vapour and ice

Water vapour is the dominant greenhouse gas in the atmosphere. Water vapour radiative feedback amplifies the radiative forcing of uniformly-mixed greenhouse gases by a factor of 2 (Randall et al., 2007). In the lower-troposphere, water vapour changes are largely driven by thermodynamic constraints. In the UT, our understanding of the processes that control humidity is poor, especially in the Tropics, reflecting the sparseness of high-quality measurements (e.g. Trenberth et al., 2007). In the two decades prior to about 2001, the observations of stratospheric water-vapour suggested that it had increased by ~20%, thus

resulting in a significant contribution to global surface-warming. Subsequently (2000–2006), stratospheric water vapour concentrations decreased by about 10% but are now increasing again (e.g. Hurst et al., 2011). The drop in the early 2000's may have resulted in a slowing down of the increase of global surface-temperature by ~25% compared to the effect of anthropogenic greenhouse gases alone (Solomon et al., 2010). These findings suggest that water vapour is an important modulator of decadal global surface climate change.

Understanding the competing processes that affect the vertical transport of water vapour in the UTLS relies on observations that can accurately capture spatial and temporal heterogeneity of the water vapour distribution. The vertical transport of water vapour to the UT and also into the LS can occur rapidly in convective updrafts and in large-scale frontal ascent, but also more slowly over large horizontal distances in the Tropics (Holton & Gettelman, 2001). It has been suggested that rapid ascent in the Asian monsoon may also play a significant role (e.g. Sherwood et al., 2010). Hence a variety of mechanisms at different spatial and temporal scales seem to contribute to water-vapour transport in the UTLS, with their relative importance still to be investigated. Owing to our incomplete understanding, current uncertainties in the water-vapour feedback are in the order of 20% (e.g. Randall et al., 2007).

Cirrus clouds play a significant role in determining Earth's energy balance. However, observations of their effects on outgoing longwave radiation do not agree with model predictions, especially in the Tropics (e.g. Clement & Soden, 2005). Also, the formation and microphysical properties of cirrus clouds are still poorly measured and understood. In addition, aviation contributes in an important manner to the generation of cirrus clouds via the production and spreading of condensation trails (e.g. Voigt et al., 2010). Some of these issues have been studied by recent aircraft campaigns (e.g. NASA-TC4, www.espo.nasa.gov/tc4/). However, satellite observations are urgently required to provide global-scale information.

2.2.2.2 Ozone

Ozone is also a very important greenhouse gas with large spatial and temporal variability in the UTLS. A given change in ozone concentrations produces the largest change in surface temperature when placed at the tropopause (Lacis et al., 1990; see also Fig. 2.2). As mentioned in Subsection 2.2.1, this is due to the very low temperatures found in the tropopause, and the strong contrast with Earth's surface temperatures. The magnitude of the radiative forcing from ozone is highly dependent on its spatial distribution within the UTLS, which is affected by transport and chemical processes, which in turn depend on climate.

Up to 60% of total column ozone resides in the LS, hence this region is important in determining how much ultraviolet radiation (UV) reaches the troposphere and Earth's surface. Anthropogenic emissions of chlorofluorocarbons (CFCs) have caused severe ozone depletion in this region, leading to the Antarctic ozone hole and increased levels of UV affecting human and ecosystem health. The effects of CFCs on ozone (and thus surface UV) are expected to decrease over this century as a result of the Montreal Protocol and its amendments, which banned the use of CFCs. However, recent model studies suggest that climate change, through changing thermal structure and transport patterns, will affect ozone distributions in the UTLS, and thereby surface UV distributions (Hegglin and Shepherd, 2009a).

Lower-stratospheric ozone distributions strongly affect tropospheric background levels of ozone, and hence influence surface air quality as shown from observational studies (e.g. Ordoñez et al., 2007). Chemistry-Transport Model (CTM) studies have, indeed, demonstrated that models with realistic ozone precursor emissions, but without realistic stratospheric ozone distributions, fail to reproduce background ozone levels in the troposphere

(Parrish et al., 2009) as well as UT ozone trends (WMO, 2011). Observing chemical and dynamic processes in the UTLS on a global scale is therefore key to improving these models and gaining confidence in their predictions of the tropospheric ozone budget. This is especially important since chemistry-climate models (CCMs) predict a climate-induced increase in stratosphere-to-troposphere transport of ozone, which could strongly affect tropospheric ozone chemistry.

2.2.2.3 Long-lived greenhouse gases

Global annual trends in long-lived greenhouse gases such as CO₂, CH₄, N₂O, CFCs and sulphur hexafluoride (SF₆) are adequately sampled for most applications using the existing ground-based networks that capture the global north-south gradients, even though the emissions of these greenhouse gases are spatially and temporally heterogeneous.

Methane is the most important carbon-based greenhouse gas apart from CO₂, and triggers important chemical feedback processes involving tropospheric O₃ and CO. Most of the tropospheric ozone climate forcing has been related to CH₄ emissions (Shindell et al., 2011) making them, together with NO_x, a dominant force for changes in the oxidising capacity of the troposphere. In spite of the methane lifetime of about 9 years, small inhomogeneities in its mixing ratio in the troposphere are detectable from space (Frankenberg et al., 2011) and are used in inversion schemes to infer surface emissions (Bergamaschi et al., 2009). In the LS, the mixing ratio of CH₄ decreases with increasing altitude as its lifetime is shorter than vertical mixing timescales. This results in CH₄ exhibiting significant spatiotemporal variability in the UTLS (Schuck et al., 2010). In addition, the oxidation of CH₄ to CO and H₂O contributes significantly to the stratospheric H₂O budget, indirectly influencing climate. Similar spatiotemporal behaviour in the UTLS is observed for N₂O (Kort et al., 2011).

CFCs act both as greenhouse gases and as ozone-depleting substances (ODSs). By reducing ODS emissions to protect the ozone layer, the Montreal Protocol has provided the added benefit of protecting the climate. The reduction in ODS emissions will have avoided an additional 30% equivalent CO₂ positive radiative forcing by 2020 (Velders et al., 2007). In the LS, CFC-11 and CFC-12 are passive tracers and have been used for diagnosing transport and mixing processes (e.g. Kuell et al., 2005). Similarly, SF₆ observations throughout the stratosphere have been found to be powerful for diagnosing the evolution of the Brewer–Dobson circulation (Stiller et al., 2008).

2.2.2.4 Short-lived gases and aerosols

Short-lived species with lifetimes of a few months or less, carry a lot of information on atmospheric processes relating to chemistry, convection, and emissions and, thus, indirectly climate. In the troposphere and lower stratosphere, O₃ is formed by sunlight-driven smog reactions involving precursor species (CO, volatile organic compounds (VOCs), and reactive nitrogen oxides, i.e. NO_x = NO + NO₂). Ozone itself also activates tropospheric chemistry as UV photolysis releases O(¹D), a very reactive form of atomic oxygen. O(¹D) can then react with H₂O to produce hydroxyl (OH), which has been called the tropospheric detergent since it reacts with many species including CH₄, CO and VOCs, often with CO₂ as an end product.

Biomass burning, anthropogenic and biogenic emissions are the major sources of NO_x, CO, and VOCs in the lower troposphere which can be lofted into the UTLS region by large-scale convection and pyroconvection (Subsection 2.3.3) and also by large-scale uplifting by the conveyor belt dynamic systems (Subsection 2.3.4). NO_x is also generated locally in the UT by lightning, and by direct input from commercial aircraft or transport from the

stratosphere. Heterogeneous reactions occur on aerosols and ice crystals (cirrus clouds) transforming NO_x into nitric acid (HNO_3). The chemical composition (e.g. tracer ratios such as NO_x/HNO_3) yields insight into the chemical aging and transport history of air masses in the UTLS, and also emission sources. Another example is hydrogen cyanide (HCN), which is a unique tracer for biomass burning. The combination of spatial information on HCN with satellite-imaging data that determines fire hot spots can yield important information on the dynamics, emissions and chemistry of fires and their impact on the global UTLS.

While an increase in NO_x in the stratosphere generally leads to a decrease in ozone, conversely in the troposphere an increase of NO_x generally leads to production of ozone depending on the NO_x/VOC ratio. In the past, the transition zone (or critical level) between these regimes appeared to be about 20 km. However, recent aircraft measurements indicate that the critical level may be as low as the tropopause determined by the observed seasonality in UTLS ozone and CO concentrations (Hegglin et al., 2006), and that the issue may be more complex with halogen chemistry and aerosols playing a role (Søvde et al., 2007). There is also growing evidence that, as a result of convective activity, very short-lived halogen species can reach the UTLS and make a significant contribution to the halogen budget, thereby impacting ozone in that region (e.g. Sturges, 2000).

In the LS, ozone can be destroyed by catalytic cycles involving reactive oxides of the hydrogen, chlorine, bromine and nitrogen ‘families’ (HO_x , ClO_x , and BrO_x as well as NO_x). The species, which react with ozone, can also be transformed to and from inactive reservoirs, which are longer-lived. The ozone distribution is therefore affected by these chemical transformations, which are themselves affected by prevailing temperatures and photolysing solar radiation. In the extreme cold of the polar vortex, for example, partitioning between active and inactive species can be affected strongly by heterogeneous reactions on polar stratospheric clouds (PSCs), giving rise to the springtime ozone hole. More generally, aerosols play an important role in atmospheric chemistry by acting as catalytic surfaces on which chemical reactions can occur and as condensation nuclei for cloud droplets and ice crystals. Aerosol sources in the UTLS are both direct, through pyroconvective uplifting or volcanic eruptions, and indirect through *in situ* formation of sulphate and nitrate aerosols from the conversion of sulphur dioxide (SO_2) and NO_x . Aerosols in the UTLS region scatter and absorb radiation, thereby affecting the heat budget, and can influence cirrus cloud formation and the water vapour budget.

2.2.3 Key Dynamic Processes

2.2.3.1 Atmospheric circulation

Atmospheric circulation together with chemical source and sink characteristics determines the distribution of atmospheric trace gases and aerosols. Knowledge of the various facets of UTLS transport processes is critical. The primary driver of atmospheric circulation is the thermal imbalance between the Tropics and polar regions. Heating in the Tropics results in convective instability with concomitant vertical transport in cloud towers, surrounded by gradual descent. The net effect is upward transport with descent in the subtropics forming the Hadley cell. At extratropical latitudes, the pole-to-equator temperature gradient results in the formation of high- and low-pressure weather systems (cyclones and anticyclones) that transport heat poleward. Vertical mixing of trace gases can occur on the timescale of days and hemispheric-scale zonal mixing over several weeks. In contrast to the troposphere, the stratosphere is dynamically stable in the vertical and transport acts on much slower timescales varying from months to years. Tropospheric air enters the stratosphere mostly in the Tropics, where it moves slowly upwards and polewards, before descending at

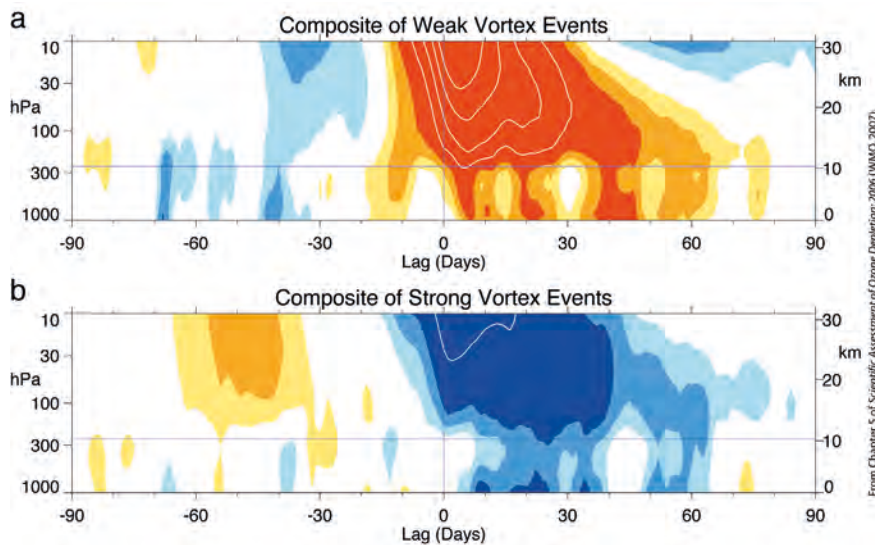


Figure 2.3. Weather from above? A weakening (red) or strengthening (blue) stratospheric vortex can alter circulation patterns down to the surface. See text for details. (WMO, 2007)

higher latitudes. This large-scale stratospheric circulation, which is driven by planetary and synoptic-scale Rossby waves, and smaller-scale gravity waves vertically propagating from the troposphere, is known as the Brewer–Dobson circulation. While the general features of the circulation in the UTLS are known, we still lack a quantitative understanding of variability in transport and its effect on trace-gas distributions.

2.2.3.2 Dynamic coupling to surface climate

While incoming solar radiation and near-surface processes (e.g. heat fluxes) largely control surface temperatures, surface winds are controlled by momentum fluxes, which are at a maximum in the UTLS. It is ultimately these surface winds, the prevailing westerlies, that control the weather experienced at mid-latitudes. Planetary and synoptic-scale Rossby waves, and also gravity waves (discussed in more detail in Section 2.3), determine the momentum fluxes in the UTLS that control the surface winds. A prominent example is given in Fig. 2.3, which shows stratosphere–troposphere coupling through ‘annular modes’ (a hemispheric-scale pattern of climate variability). Fluctuations in the strength of the stratospheric polar vortices are observed to couple downward to surface climate (Baldwin & Dunkerton, 1999). On average, anomalous vortex conditions tend to descend through the LS and are followed by corresponding circulation anomalies at Earth’s surface for about two months, which affect temperature and precipitation patterns over Europe. Figure 2.3 shows composites of the time-height development of the northern hemisphere annular mode (NAM) index for: (a) 22 weak vortex events; and (b) 35 strong vortex events in 1958–2006 (updated from Baldwin & Dunkerton, 2001). In the stratosphere, negative NAM values correspond to a weak polar vortex, while positive values correspond to a strong polar vortex. The white areas correspond to NAM index values between ± 0.25 . Higher values are in blue and lower are in red with a contour interval of 0.25; white contours start at ± 1.25 with an interval of 0.5. Large anomalies in the strength of the polar vortex at 10 hPa tend to descend to the lowermost stratosphere, where they last, on average, more than two months. After the stratospheric event, the tropospheric NAM anomaly is of the same sign as the stratospheric anomaly. A positive tropospheric NAM value corresponds, for example, to pressure values lower than normal over the pole and higher than normal at low latitudes. As a result, stronger westerlies occur over the Atlantic, leading to warm wet winters in northern Europe and dry winters in southern Europe.

This points to the possibility of improved seasonal or at least sub-seasonal weather forecasting. As climate changes, it is expected that the downward coupling would be modified by changes in both the tropospheric wave forcing of the stratosphere and changes to the stratosphere itself. Although the described phenomenon is robust in both observations and models, and involves changes in UTLS momentum fluxes, the precise mechanisms are not well understood.

2.3 Chemistry-climate Interactions

Chemistry-climate interactions encompass direct and indirect feedback processes between chemistry, radiation, and dynamics. Over the past decade, there has been increasing awareness of the importance of chemistry-climate interactions in ESMs. Within the stratosphere, the focus has been on the impact of CFC-induced ozone depletion and recovery on surface radiative forcing. However, in the most recent WMO Ozone Assessment (WMO, 2011), the connections between climate-induced changes in transport and temperatures and their effect on the ozone distribution have been recognised. In addition, the ozone hole has had an important effect in modifying surface climate through dynamic coupling. Within the troposphere, the most recent focus has been on how climate, through changes in UV, transport, and temperature, may affect chemical processes such as the generation of ozone. Changing temperatures will also impact the magnitude of biogenic emissions (e.g. isoprene), as their sources are often sensitive to temperature. Effects will also result from changing biomes, both in extent and location, through adaptation of the biosphere to new climate regimes.

The radiative, dynamic and chemical processes relevant for chemistry-climate interactions act on a variety of spatial and temporal scales. They include, for example, cooling and heating by greenhouse gases, interactions with cirrus clouds, and Rossby and gravity-wave processes (Subsection 2.3.1). They act through processes such as transport and mixing between the troposphere and the stratosphere (Subsection 2.3.2), convection, lightning, gas-phase or heterogeneous chemistry (Subsection 2.3.3). Finally, these transport pathways connect surface emissions and air pollution to the UT (Subsection 2.3.4).

2.3.1 Sensitivity of Surface Climate to UTLS Variability and General Circulation

The composition and thermal structure of the UTLS affect surface climate and its variability, through radiative and dynamical coupling. As mentioned in Subsection 2.2.1, the radiative forcing of surface climate strongly depends on the vertical distributions and gradients of greenhouse gases such as ozone and water vapour, aerosol and cirrus clouds in the UTLS. These distributions are determined by transport and mixing processes discussed in Subsection 2.3.2, by convective and chemical processes discussed in Subsection 2.3.3, and surface emissions discussed in Subsection 2.3.4. The radiative impact of composition changes in the UTLS, both locally and at the surface, have been found to depend not only on their vertical structure, but also on their latitudinal structure (Maycock et al., 2011).

Eruption of Mt. Pinatubo in June 1991 caused a major perturbation to UTLS composition. The volcanic aerosols that were ejected into, or formed within, the stratosphere were dispersed throughout the equatorial LS, producing significant warming there. The observed increase in the equator-to-pole temperature gradient in the LS of the winter hemisphere significantly changed atmospheric circulation patterns in the years after the eruption. The perturbations in the heat balance in the LS, although relatively small,

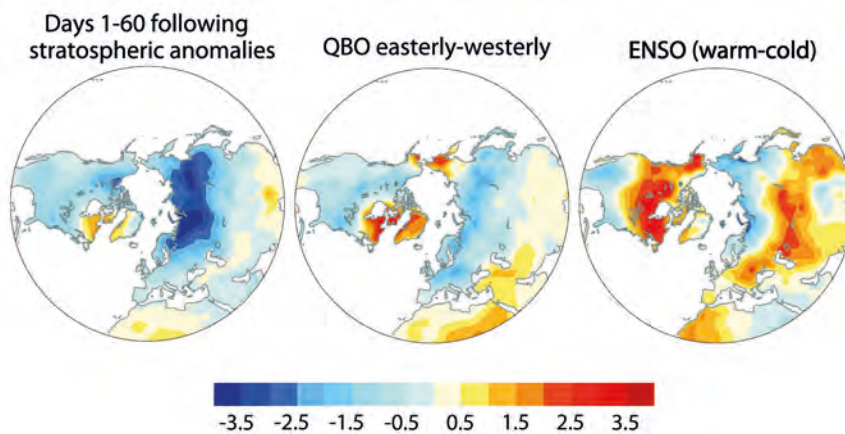


Figure 2.4. Differences in daily mean surface temperature anomalies observed between weak and strong vortex events at 10 hPa within 60 days following the event (left), between easterly and westerly phase of the QBO in January (middle), and between warm and cold episodes of ENSO during winter (January–March) (right). (Thompson et al., 2002; © American Meteorological Society. Reprinted with permission.)

also affected circulation in the troposphere and cooled surface temperatures (Stenchikov et al., 2002).

Climate models consistently predict a strengthening of the Brewer–Dobson circulation in response to greenhouse gas-induced climate change (Butchart et al., 2010), which would affect the transport of radiatively-active gases. Stronger upwelling would lead to a higher and colder tropopause in the Tropics, affecting water-vapour mixing ratios at the point of entry. The associated increase in downwelling in the extratropics would lead to a lower and warmer extratropical tropopause (Thuburn & Craig, 2000). As noted above, uncertainty in the modes of transfer of water to the stratosphere makes the effect of such changes on stratospheric water-vapour distribution difficult to predict. Furthermore, change in the stratospheric water-vapour source from methane oxidation has to be taken into account. It has been shown that a stronger Brewer–Dobson circulation would affect the UTLS ozone distribution, which could result in a positive radiative forcing from increased ozone in the UT specifically (Heggin & Shepherd, 2009a).

Global data on ozone, water vapour, methane, cirrus and aerosol are needed with sufficiently high vertical resolution to quantify the interactions between atmospheric composition and radiation.

The changes in ozone and greenhouse gases mentioned in the previous section project onto the dominant modes of dynamic variability in the stratosphere, i.e. the annular modes, and connect to surface climate (see Subsection 2.2.1 and Fig. 2.3). The Quasi-Biennial Oscillation (QBO), which is another mode of stratospheric variability and characterised by a downward propagating signal in tropical winds, creates a similar surface signature as the annular modes (Fig. 2.4). Another mode of internal variability in the atmosphere is the El Niño Southern Oscillation (ENSO), which is evident *inter alia* as an anomaly in surface temperatures in the Pacific Ocean. The ENSO exhibits a different signature in the northern hemisphere at high latitudes where the amplitude is similar but of opposite sign (Fig. 2.4). The ENSO has been shown to exert a strong influence on North American and European weather (surface temperature and precipitation) through teleconnections that are mediated by stratospheric wind anomalies (e.g. Ineson & Scaife, 2009). These studies imply that representing the stratosphere and downward dynamic coupling correctly in models could lead to improved forecast skills especially for seasonal weather forecasting. It is therefore important to understand the mechanism behind these modes of variability and how they are affected by climate change.

Through a similar process of stratosphere–troposphere coupling involving annular modes, the ozone hole has been shown to have a major impact on surface climate in the southern hemisphere, including a poleward shift in the subtropical jet, an increase in tropopause height and an increase in

precipitation (Son et al., 2008). These effects, which are mainly confined to austral summer following the breakdown of the Antarctic stratospheric vortex, exacerbate the effects of greenhouse gas-induced climate change. Model projections suggest that ozone recovery, as a consequence of the successful implementation of the Montreal Protocol, will lead to a reversal of these effects, which will then mitigate the effects of greenhouse gas-induced climate change during the summer, although it might accelerate surface warming over the Antarctic plateau. Such warming could also lead to a decrease in Antarctic sea-ice cover.

Wave breaking and dissipation in the UTLS are believed to cause other dynamic couplings to surface climate. A basic mechanism is that local temperature variations in the UTLS couple to wind speed variations via the thermal wind relationship; additional heating increases the static stability in this region, lowers the tropopause height, and modifies wave fluxes. Changes in the heat balance in the LS thereby couple dynamically to the troposphere and surface climate.

Global measurements of temperature are needed with sufficiently high resolution to characterise and quantify the mechanisms of dynamic coupling between the stratosphere and the troposphere in climate models.

2.3.1.1 Gravity-wave processes

Representation of gravity waves is necessary to model the coupling processes described above and in Section 2.1, and hence need to be included in any global model with a resolved stratosphere (Alexander et al., 2010). Gravity waves also contribute significantly to driving the Brewer–Dobson circulation. In fact, recent model studies (e.g. Butchart et al., 2010) suggest that parameterised orographic gravity waves and resolved Rossby waves are about equally important for forcing trends in the Brewer–Dobson circulation. These waves also play a critical role in forcing the QBO in equatorial zonal winds in the stratosphere (Dunkerton, 1997), which strongly influences transport and mixing of radiatively-active gases between the Tropics and mid-latitudes in the UTLS. Gravity waves, therefore, are a key player in the dynamic coupling between the stratosphere and the troposphere.

The representation of gravity waves in climate models is currently a major source of uncertainty. At present, most models use a physics-based parameterisation for orographic gravity waves, while the source strength and locations for non-orographic gravity waves are simply tuned to produce

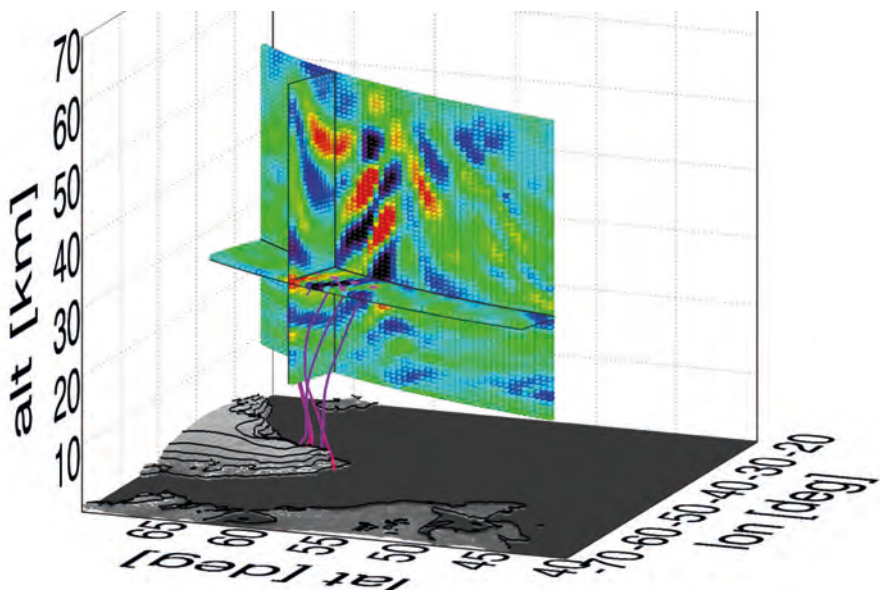


Figure 2.5. PREMIER sampling of 3D gravity-wave temperature-structures in the UTLS over Greenland. See text for explanation. (P. Preusse)

reasonable, representative temperatures and winds. Clearly, this situation is unsatisfactory because the parameterisations cannot respond directly to varying source strengths resulting from a changing climate (Fritts & Alexander, 2003). Recently, gravity-wave source parameterisations for fronts and deep convection have been implemented in a few General Circulation Models (GCMs) (e.g., Richter et al. 2010) using simplified approximations. While gravity waves have been inferred from satellite measurements of temperature fields, overall, the current satellite observations cannot provide the propagation direction, net momentum-fluxes, or net acceleration. In order to constrain gravity-wave drag parameterisations, it will be crucial to gain information on the separate effects of positive and negative momentum fluxes (associated respectively with positive and negative intrinsic phase speeds), and on their phase-speed distributions.

Global 3D temperature measurements are needed with sufficient vertical and horizontal resolution to determine gravity-wave amplitudes and horizontal and vertical wavelengths (wave-vector).

These concepts are illustrated in Figure 2.5. The simulated atmospheric temperature structures (background temperature profile subtracted) are interpolated European Centre for Medium range Weather Forecasting (ECMWF) meteorological data. Temperature values (coloured squares) are shown for a horizontal-height cross-section of the measurement along the flight track (one across-track sampling point only). The colour code is from -8K (purple) to $+8\text{K}$. The across-track sampling providing 3D information is shown at 25 km altitude. The 3D observations clearly allow identification of the dominant wave-fronts (perpendicular to the wave-vector). From this information, direction resolved momentum-flux can be derived, for the first time from satellite observations. In addition, the 3D dataset provides the information needed to trace back the dominant wave signal at each PREMIER sampling point to its sources. This is indicated in Fig. 2.5 for four selected sampling points (at 25 km altitude) with an along-track separation of 150 km. Each sampling point is connected with the source of its dominant wave signal by a purple line (tip of Greenland for all points). Note that the propagation directions indicated by the purple lines are not just straight lines, but have some curvature that must be taken into account in atmospheric models. From these quantities, global distributions of direction-resolved momentum-flux can be derived for the first time. By performing analysis using back-trajectories it may be possible to identify gravity wave sources as illustrated by the lines in Fig. 2.5.

This approach will facilitate the development of parameterisations of sources and effects of gravity-waves in models. In addition, such high-resolution data would be ideally suited to validating global weather-forecast models, such as the ECMWF model, as its resolution increases to capture an increasing fraction of the gravity-wave spectrum.

2.3.2 Trace-gas Exchange between Troposphere and Stratosphere

In the Tropics, transport of air is mainly upwards from the troposphere into the stratosphere, associated with the ascending branch of the large-scale Brewer–Dobson circulation (Fig. 2.1). This slow upwelling of air is balanced by poleward transport and net downwelling (timescale of years) in the extratropics. A major feature in trace-gas exchange in the tropical upper-troposphere is the Asian monsoon circulation, featuring a strong anticyclone extending from Asia to the Middle East (Fig. 2.6). Global observations of HCN, a pollutant produced by biomass burning, indicate that the Asian Monsoon provides an additional, more rapid pathway for air masses to reach the stratosphere (Randel et al., 2010; Fig. 2.8). In the UT, the anticyclone confines a region of pollution delivered by deep convection from the surface (e.g. Park et al., 2009) and influences the composition of the tropical tropopause layer

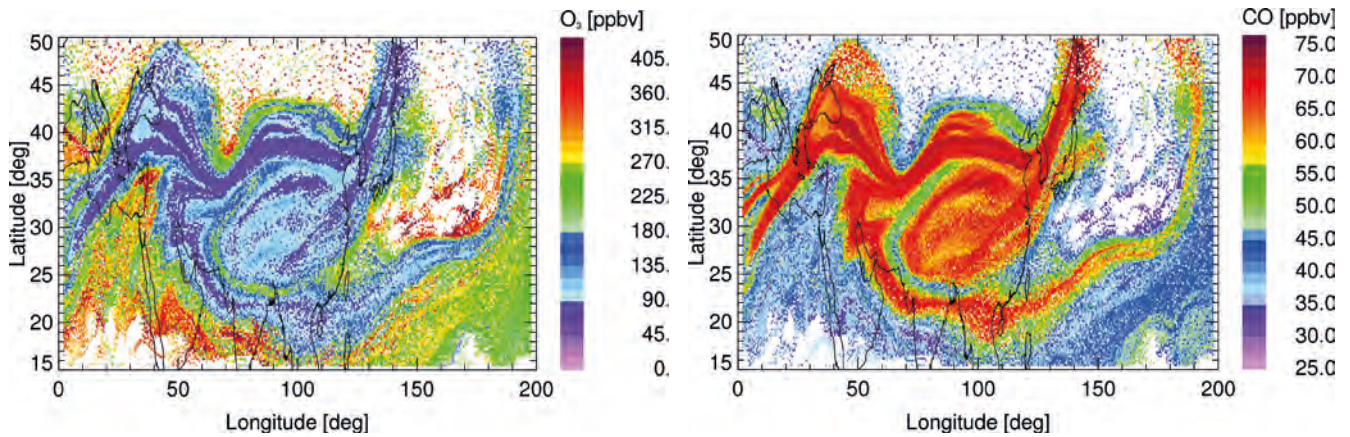


Figure 2.6. Distribution of ozone (left) and CO (right) in the upper Asian monsoon anticyclone (~18 km) for 9 August 2003 as simulated by the CLaMS model (e. g. Konopka et al., 2010). The monsoon has a strong influence on the composition of the TTL. ‘Young’ tropospheric air (low ozone and high CO values) results from fast convective upward-transport in the centre of the monsoon. Quasi-horizontal mixing of ‘older’ extratropical stratospheric air (high ozone values) into the TTL occurs at the edge of the highly variable anticyclone. (F. Plöger)

(TTL; Fueglistaler et al., 2009). The mixing ratios of H₂O, CO, HCN and other minor species in the TTL are imprinted on air entering the stratosphere much like the head of a tape recorder. Model simulations suggest that transport by the Asian monsoon could contribute significantly to the stratospheric water vapour budget (Subsection 2.2.2). Given the nature of the monsoon, the impacts are both seasonally and spatially highly variable (Randel & Park, 2006). Furthermore, ‘older’ extratropical stratospheric air is mixed equatorwards at the outer edge of the Asian monsoon anticyclone (Fig. 2.6), significantly affecting trace-gas budgets such as ozone and CO in the tropical TTL (e.g. Konopka, 2010). All these transport processes are associated with mesoscale 3D structures in trace gas fields (e.g. filaments) with spatial scales beyond the resolution of current satellite observations (e.g. Fig. 2.6).

In the extratropics, bidirectional quasi-horizontal transport of air across the edges of the subtropical jet (red wave-like arrows in Fig. 2.7) plays an important role in connecting the tropical troposphere (including the TTL) with the extratropical lowermost stratosphere (LMS) (light-blue shaded area in Fig. 2.7).

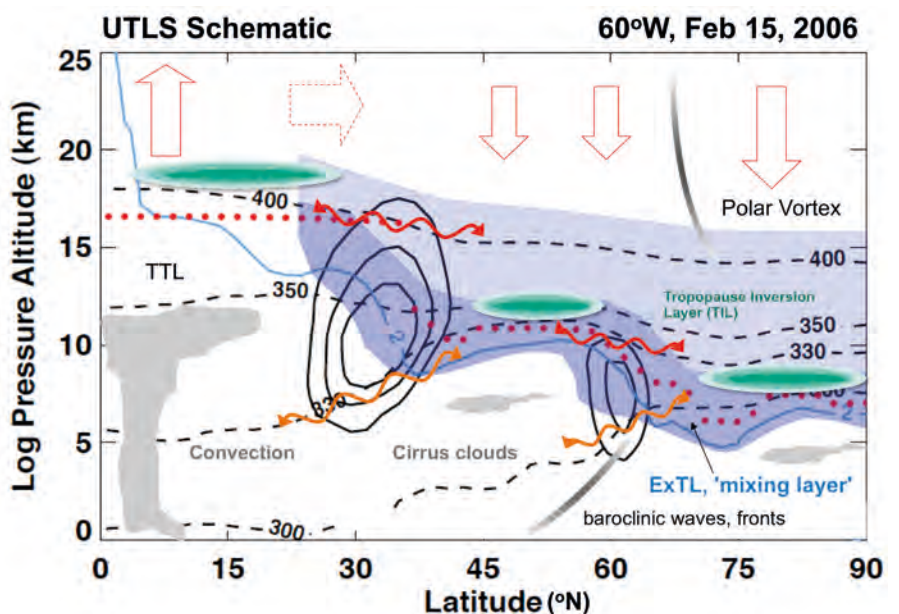


Figure 2.7. Stratosphere–troposphere exchange processes taken from Gettelman et al. (2011), showing: wind contours (solid black lines, 10 ms⁻¹ intervals), potential temperature surfaces (dashed black lines), thermal tropopause (red dots), potential vorticity surface (2 potential vorticity units, light blue solid line), extratropical-UTLS (dark and light blue), extratropical transition layer (ExTL, dark blue), clouds and fronts (grey), static stability contours in the tropopause inversion layer (TIL, green), quasi-isentropic exchange (wavy red arrows), cross-isentropic exchange (wavy orange arrows) and Brewer–Dobson Circulation (deep: solid red arrows, shallow: dotted red arrow).

The exchange processes involve medium- and small-scale structures such as tropopause folds in the vicinity of the subtropical jet stream (Sprenger et al., 2003) and filaments. Furthermore, this quasi-horizontal transport exhibits strong seasonal and interannual variability, related to the seasonally varying strength of the subtropical jet, which represents a transport barrier (Haynes & Shuckburgh, 2000). In addition to quasi-horizontal transport and mixing from the tropical UT, the composition of the LMS may also be significantly influenced by quasi-horizontal (isentropic) transport of polar filaments (and subsequent mixing) resulting from the springtime breakup of the polar vortex. Overall, mixing in this region of the UTLS (or likewise at the edge of the Asian monsoon anticyclone) can be understood as a scale cascade from synoptic-scale streamers over elongated filaments down to small-scale 3D turbulence.

Vertical, two-directional exchange between the troposphere and LMS also contributes to variability of composition in the extratropical UTLS. Moist convection (upward transport) or stratospheric intrusions from the LMS into the troposphere (downward transport) play an important role here. Convection and associated gravity-wave generation has been identified to inject boundary layer air directly into the LMS within several hours (e.g. Hegglin et al., 2004). In addition, radiative processes associated with the decay of anticyclones might also play a role in transport of air into the LMS. Transport from the LMS into the troposphere is a result of meso-scale processes associated with anticyclones, filaments, and cut-off low events.

A prominent feature in the extratropical UTLS that results from these exchange processes is the extratropical transition layer (ExTL), a region in the vicinity of the tropopause (Fig. 2.7) that is strongly influenced by stratosphere–troposphere exchange (Gettelman et al., 2011). The ExTL exhibits significant latitudinal and inter-hemispheric differences (Hegglin et al., 2009b). Several studies (e.g. Randel et al., 2009) suggest that the ExTL is key in forcing and maintaining the tropopause inversion layer (TIL) – a narrow region of strong static stability just above the thermal tropopause (Birner, 2006). While the relationship between the ExTL and TIL has been established on a climatological basis, much still needs to be learned about its temporal (daily) and spatial (longitudinal) variability (e.g. Erler & Wirth, 2011), and how it both reflects and influences the radiative and dynamic couplings between the troposphere and the stratosphere.

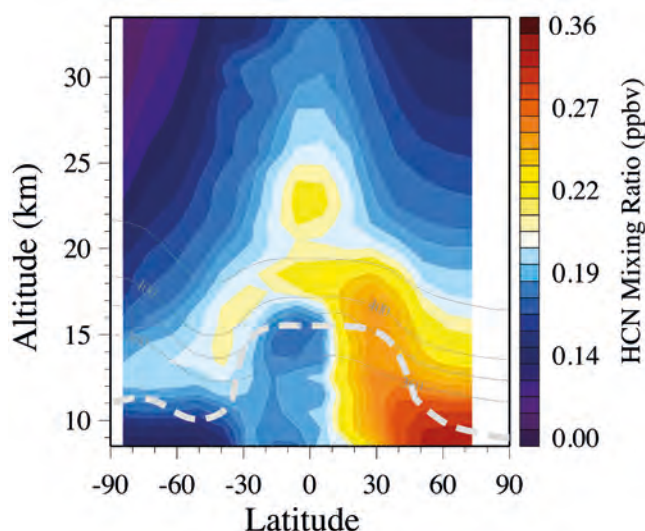
Current knowledge on the processes determining the structure and composition of the extratropical UTLS (and hence of the TIL and ExTL) is limited, owing to the observational gap between *in situ* measurements, which resolve small-scale features, and satellite measurements, which resolve synoptic-scale features.

Global 3D fields of water vapour, ozone, and transport tracers (e.g. CFC-11) are therefore needed with the required vertical and horizontal resolution to quantify transport processes controlling the composition and structure of the tropical and extratropical UTLS.

2.3.3 Impacts of Convection, Pyroconvection and Outflow on the UTLS

An important transport mechanism that gives rise to rapid changes in composition in the UTLS region is large-scale or organised rapid vertical transport or convection associated with storms ranging in scale from summer thunderstorms (cumulus towers) to large convective complexes, hurricanes and the Asian summer monsoon. In this manner, both long-lived gases (e.g. CH₄) and short-lived gases (e.g. CO, HNO₃, HCN, NO₂), which would otherwise be photochemically destroyed or removed in the boundary layer or lower troposphere, can reach the UT in much less than an hour: in some cases the cumulus towers can penetrate the LS as shown in Fig. 2.8. These transported species, together with water vapour, can significantly perturb the production

Figure 2.8. Latitude-height cross-section of zonally-averaged HCN from the ACE-FTS satellite instrument accumulated over the northern hemisphere summer (June–August). Profiles were acquired through solar occultation at one latitude per day in each hemisphere and the cross-section was accumulated as the latitudes of sunrise and sunset varied through the season. The light grey, dashed line denotes the average tropopause, darker grey lines denote potential temperature levels. The figure illustrates the role of the Asian monsoon in transporting the HCN-rich boundary layer air into the tropical LS. (W. J. Randel & M. Park)



of ozone. They also impact the formation of ice and cirrus clouds in the UT and its transport into the stratosphere, and in general alter the strength of the radiative forcing of the atmosphere.

There are other sources of rapid vertical transport in the troposphere. Unstable air, if triggered by intense heat release from forest or biomass burning, can also result in rapid uplift of biomass-burning products, i.e. gases, black and organic carbon, aerosols into the UT and LS (Fig. 2.9). This process is called pyroconvection and the outflow from pyroconvective plumes can significantly perturb the composition of the UTLS. In addition, the aerosols carried aloft can absorb incoming solar and outgoing thermal radiation, making the ambient air more buoyant and lofting the biomass burning products into the LS (Boers et al., 2010).

Evidence that pyroconvective plumes can reach the UT and in some circumstances the stratosphere is accumulating from aircraft and satellite observations. The altitude reached by the fire plume depends on fire intensity and meteorological conditions (Lavoué et al., 2007), and is quite variable. While in many cases, emissions are confined to the boundary layer, a significant fraction of smoke plumes directly reach the free troposphere (e.g. Guan et al., 2010), and extreme cases of direct injection into the stratosphere have been observed in boreal regions (e.g. Fromm et al., 2010). Both the injection height and the amount of matter burnt are important parameters for modelling these



Figure 2.9. A pyroconvection plume rising above the cloud tops. (A. Thielmann)

events to assess their impact on chemical tracer distributions (e.g. Generoso et al., 2007).

The modelling community has started to develop parameterisations for pyroconvection, but is limited by a lack of adequate composition data on a global scale to support extensive evaluations of the parameterisations. Recent work has highlighted that biomass-burning emissions need to be injected into the mid- and upper-troposphere to obtain agreement with measurements of HCN, CO or other trace gases by satellite instruments such as the Atmospheric Chemistry Experiment – Fourier Transform Spectrometer (ACE-FTS) (Lupu et al., 2009), the Tropospheric Emission Spectrometer (TES) and the Microwave Limb Sounder (MLS) (Gonzi & Palmer, 2010). Large-scale models have to rely on parameterisations constrained by higher-resolution models, which represent the detailed effects of the burning process (e.g. actual heat release and dynamics). Information on the underlying dynamics, fuel amounts and burning processes is carried in the chemical composition of pyroconvective plumes with which to improve parameterisations. Current satellite instruments such as the ACE-FTS can measure the gases produced by biomass burning but, due to sparse geographical coverage, can yield only a climatology of injection heights and emission yields.

Global observations of pyroconvective plumes are needed with the vertical and horizontal resolution required to characterise their injection heights, impacts on ozone production, on UTLS composition and on radiative forcing.

Over land in particular, convection can generate strong electric fields, which in turn generate lightning. The 6000K temperatures within the lightning bolts cause molecular nitrogen to thermally decompose, forming nitric oxide (NO). While the process is qualitatively understood, it is still not quantitatively understood and is difficult to be represented accurately in models. The amount of NO_x generated by lightning may be geographically dependent, as source strengths based on standard algorithms for North America, globally appear to be too small by about a factor of 4 (e.g. Parrington et al., 2008). It is also a strong function of model resolution, with global models aiming to reproduce only global averages correctly.

Global observations of nitrogen oxides are needed in the UT with the vertical and horizontal resolution required to differentiate lightning production from other sources and to determine their impact on ozone production and radiative forcing.

Volcanic eruptions sporadically inject material into the UT and also into the stratosphere. The Icelandic volcano, Eyjafjallajökull, caused major disruption to air travel in April 2010 by lofting ash above 5 km. Volcanic plumes entering the stratosphere, such as that from Mt. Pinatubo in June 1991, can affect the radiative balance and thermal structure of the stratosphere and also influence the surface climate (Subsection 2.3.1). Furthermore, the sulphate aerosol layer can provide surfaces for heterogeneous chemical reactions, which perturb chemical composition including the ozone layer.

Global observations are needed with the vertical and horizontal resolution required to locate precisely the altitudes of thin ash-layers and to quantify the injection of volcanic gases and ash into the UTLS and their impacts on composition and radiative forcing.

2.3.4 Processes Linking the UTLS to the Lower Troposphere

The lower troposphere, and the boundary layer in particular, is the source of many species that make up the composition of the troposphere and LS (Granier et al., 2011), with contributions from anthropogenic, pyrogenic and biogenic emissions, and also sporadic volcanic emissions. They can reach the free troposphere via the boundary layer by lifting in frontal systems, mesoscale storm systems and large-scale convection as outlined in Subsection 2.3.3. Plumes in the UTLS carry information about these surface emissions, and their

trajectories and chemical composition determine how pollution and air quality would potentially be affected on descent to the surface.

Atmospheric composition remains largely under-sampled in the free troposphere, even as observing networks are developing and improving (Laj et al., 2009). Besides dedicated field campaigns, observations remain scarce and there are large uncertainties with respect to the distribution and variability of, for example, ozone and its precursors in the free troposphere. *In situ* tropospheric observations are limited to geographical locations of ozone sondes and to aircraft profiles for species such as carbon monoxide, ozone, and water vapour from programmes such as Mozaic-Iagos (Marengo et al., 1998) or Caribic (Brenninkmeijer et al., 1999). Passive remote-sensing measurements from the ground are sparse while measurements from nadir-viewing satellites of species such as CO (Drummond & Mand, 1996), although abundant, have limited vertical resolution. As a result, there are several open questions regarding the chemical and dynamic processes that affect the variability of key trace gases such as ozone (Stevenson et al., 2006) and CO. This fundamentally limits our understanding of key environmental and societal concerns regarding the impacts of human activities at different geographical scales and time horizons, from air quality to climate issues. Current open questions revolve around long-range transport and removal pathways of pollution, on the estimates of regional-scale emissions and their associated trends, and on the tropospheric distribution of ozone, methane and key aerosol species together with their associated radiative forcings (e.g. Wild & Akimoto, 2001). Moreover, changes in atmospheric composition are intimately connected with climate change.

To significantly improve our understanding of processes controlling tropospheric composition, which operate on the mesoscale and are geographically

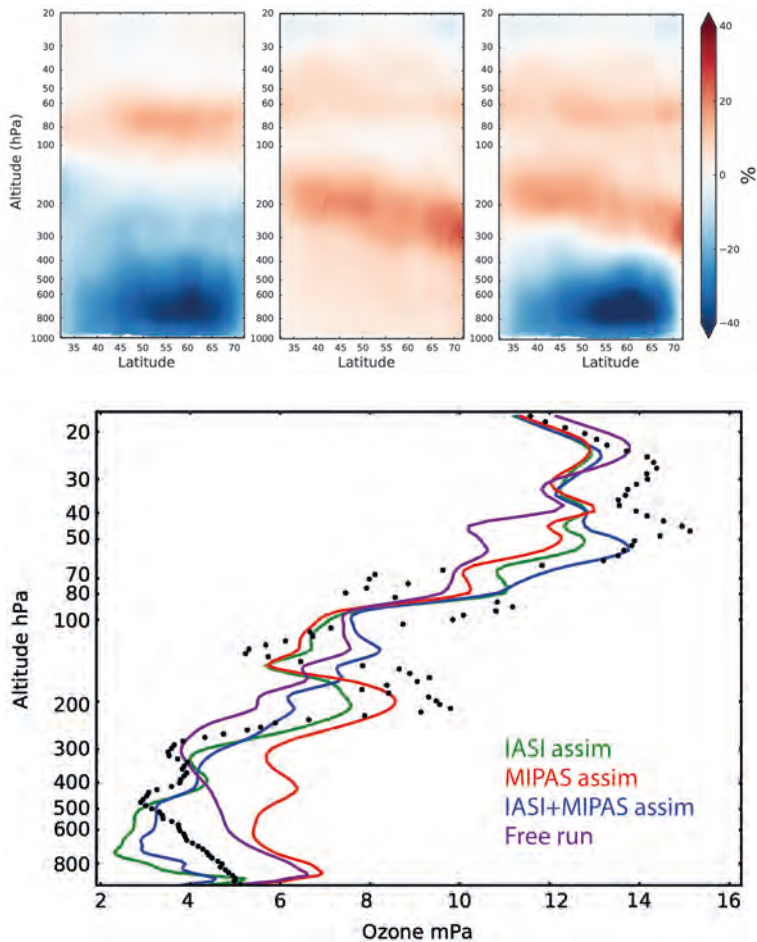


Figure 2.10: Top: monthly average (June 2009) meridional cross-section of ozone differences between analyses of tropospheric IASI (left), MIPAS limb (middle), and combined IASI and MIPAS ozone data (right) and the corresponding free-running model simulation (MOCAGE, Météo-France). This covers Europe and differences (blue and red) are expressed as a fraction of average ozone in the free-running model simulation (red: the assimilation of data adds ozone compared to the free run; blue: assimilation removes ozone). Bottom: example of comparison of model run and analyses with an independent ozone sonde (partial ozone pressure in mPa; Payerne, Switzerland, 1 June 2009). The separate assimilation of IASI (green) or of MIPAS (red) data alone improves the vertical structure of ozone compared to the free-running model (purple), but the simultaneous assimilation of both informations (blue) provide the best overall fit with the radiosonde (black dots). (J. Barre and V-H. Peuch)

widespread, global data of ozone, carbon monoxide, and nitrogen oxides (NO_2 , HNO_3 and PAN) with sufficient vertical and horizontal resolution are needed in the altitude range 6–25 km and which are collocated with operational meteorological observations from MetOp/MetOp-SG.

Contemporary chemical data assimilation systems allow the use of such information, derived from limb-emission sounders on research satellites, in conjunction with that from nadir-viewing sounders in the operational system, such as IASI and GOME-2 on MetOp, that have sensitivity in the mid-to-low troposphere. This is illustrated in Fig. 2.10, which shows synergy between limb and nadir measurements. The top panels compare monthly average latitude-pressure cross-sections for June 2009 of ozone analyses using tropospheric IASI ozone data only (left), MIPAS limb ozone profiles only (middle), and IASI and MIPAS ozone data together (right), in terms of the difference between each analysis and the corresponding free-running model simulation. The domain presented is for Europe, and the differences (blue and red) are expressed as a fraction of the ozone average values in the free-running model simulation. Red indicates that the assimilation of data adds ozone compared to the free run while blue indicates that the assimilation removes ozone. The bottom panel compares the model run and the analyses with an independent ozonesonde over Payerne, Switzerland. It is clear in this example that the benefits from the complementary measurement geometries can be exploited by contemporary chemical data-assimilation systems. In the future, these systems have the potential to provide ozone analyses that are well-constrained and accurate throughout the troposphere and stratosphere. Furthermore, systematic biases between models and the measurements revealed by the assimilation process carry information on dynamic and chemical processes in the model from which to identify where improvements are required. In addition, surface observations can be ingested by the assimilation system. This combination of surface observations with satellite measurements is expected to provide a powerful means to represent the distributions of key atmospheric compounds from the ground up through the troposphere and stratosphere.

To reduce the uncertainty in chemical weather forecast systems arising from inadequate representation of transport processes and surface emissions, and to improve model projections of air pollution in a changing climate, global vertically-resolved observations of the UTLS are needed that are collocated with MetOp/MetOp-SG.

In addition to process studies, such data should lead to an improved understanding of regional air pollution over areas of specific interest, and in particular over countries with fast-developing economies and populations such as in Asia. This will also allow for more accurate inversions of trace-gas emissions (e.g. CH_4), by providing better estimates on the values and variability of the UT and stratospheric contribution to total columns that are measured with nadir sounders.

2.4 Improving Medium-range to Seasonal Meteorological Forecasts

The expectation of extensive societal and economic benefits through provision of reliable medium-range to seasonal meteorological forecasts has been a prime motivation for meteorological research over the last few decades. By improving initial meteorological and chemical conditions for data assimilation systems in the sensitive UTLS region and by improving representation of the coupled dynamic, chemical and radiative processes in atmospheric models, as described in Section 2.3, the forecast ranges and skill of Numerical Weather Prediction (NWP) and Air Quality (AQ) systems will be substantially increased.

The UTLS is a region in which current meteorological and chemical analyses from data assimilation systems show persistent, systematic errors;

global observations of temperature, humidity, and ozone with high vertical and horizontal resolution would make a major impact in reducing these uncertainties. Until recently many NWP models have had very low resolution in the stratosphere, limiting their potential for long-range forecast skill (e.g. Roff et al., 2011; Marshall & Scaife, 2010). Increased resolution, together with the extension of NWP models to include detailed chemical processes (e.g. Flemming et al., 2009), sets the stage for much-improved jointly-produced meteorological and chemical forecasts. Previous assimilation studies with MIPAS or MLS temperature, humidity, and ozone data have highlighted how limb data is able to correct for errors in the analyses (e.g. Bormann & Thépaut, 2007). Global data in this height-range with denser sampling and higher vertical and horizontal resolution is needed for further advances.

In addition, tracers with a lifetime of more than a few weeks, for example, O₃, CO, CH₄ and CFC-11, contain implicit information on winds. Thus, high-spatial resolution measurements of such tracers will yield information on lower stratospheric motions, with the potential to improve the analysis of winds (e.g. Riishøjgaard 1996, Peuch et al., 2000).

Improved measurements in the UTLS will lead to two specific benefits for NWP. Firstly, improved analyses of the temperature structure in the tropopause region will improve forecasting of the intensification of mid-latitude weather systems. Secondly, improved stratospheric analyses offer potential to improve long-range (more than 1–2 weeks) tropospheric weather forecasts (Baldwin & Dunkerton, 2001; Thompson et al., 2002; Charlton et al., 2004). A recent study with the ECMWF NWP model (Jung et al., 2010) shows that relaxation of the northern hemisphere stratosphere towards observations leads to forecast error reduction primarily in high latitudes and over Europe. Other studies show that the stratosphere acts as a reservoir of long-term predictability (e.g. Orsolini et al., 2011) up to seasonal timescales. Together with information on ocean temperatures and on soil moisture, information on stratospheric dynamics and composition will therefore constrain the slow-varying boundary conditions for predictions of tropospheric weather and climate.

Furthermore, improved analyses of the LS would benefit the assimilation of radiance information from tropospheric channels on nadir sounders whose signals have a significant contribution from the stratosphere. Uncorrected errors in the stratosphere yield spurious information on the troposphere, with detrimental impact on forecast skill.

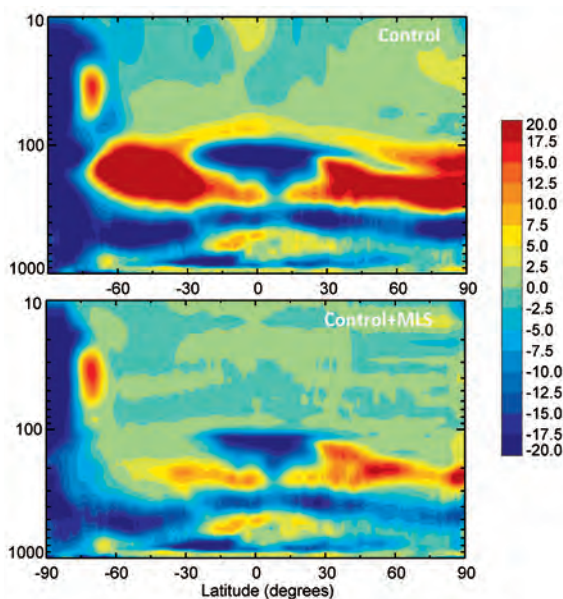


Figure 2.11. Latitude-pressure zonally averaged six-hour forecast errors for water vapour in July 2005 (in $100 \times \delta \ln(q)$, where q is specific humidity) for an experiment conducted with Environment Canada's operational NWP system. (Environment Canada, 2011)

Shortcomings in the representation of UTLS processes, for instance radiation, chemistry and gravity-wave parameterisations, give rise to large systematic errors in the stratospheric analyses of current NWP models. For instance, a better representation of the ozone field would improve modelling of radiation processes in this height-region.

Global observations are needed with sufficient vertical and horizontal resolution to improve fundamentally the representation of these UTLS processes in NWP models and, through data assimilation, to improve analyses and reanalyses.

Observing System Simulation Experiments (OSSEs) are useful for assessing and comparing the benefits of future or existing instruments in an idealised context. The output from a realistic ‘Nature Run’ is sampled according to the measurements characteristics of the instrument(s) studied, to provide synthetic observations. These synthetic observations are assimilated, and the resulting analysis compared to that from the same system but without assimilation of the synthetic observations (Control Run) and to the Nature Run, which provides the reference. Figure 2.11 presents latitude-pressure zonally averaged mean six-hour forecast errors for a modified water vapour parameter in July 2005 for an experiment conducted with Environment Canada’s operational NWP system. The Control Run and an OSSE for an instrument with the observational characteristics of MLS are compared to a Nature Run provided by ECMWF. The information provided by the limb instrument significantly reduces the short-term forecast errors in water vapour, especially in the UTLS region.

Global data on temperature and trace gases with high vertical and horizontal resolution in the UTLS will increase the skill and forecast ranges of NWP and AQ forecasts, as well as improving fundamental knowledge of processes controlling atmospheric composition and dynamics.

2.5 The Unique Contribution of PREMIER

Surface climate is particularly sensitive to the composition of the mid/upper troposphere and lower stratosphere, where thermal contrast with the surface is largest. Processes that control the composition of this height region and their links with climate are therefore of paramount importance and operate on scales ranging from planetary down to mesoscale. The representation of these processes in climate models has uncertainties mainly on the scales that are finer than can be observed from current or planned satellite missions. To resolve and quantify these processes – as required to test and improve the predictive capabilities of climate models – it will be essential to observe this height region globally in 3D on significantly finer vertical and horizontal scales than have previously been accessible from space. PREMIER will deliver these observations by means of advanced limb-emission sounding at infrared and mm-wavelengths (Chapters 4–7). These observations, in combination with new high-resolution whole-atmosphere models, will yield a unique perspective on processes occurring within the mid/upper troposphere and lower stratosphere (Chapter 3). By formation-flying to collocate and combine with nadir observations by MetOp/MetOp-SG, links to surface emissions (biogenic, pyrogenic, anthropogenic and volcanic), air quality and weather will also be quantified (Chapter 3).

PREMIER will bring into sharp focus the processes that control atmospheric composition in a height range that has particularly important links with climate and pollution.

Since no other limb-emission sounder is currently planned, PREMIER will uniquely meet specific Global Climate Observing System (GCOS) requirements for height-resolved monitoring of this atmospheric region, and will serve also as a demonstrator for this element of the space component of the Global Monitoring of Environment and Security (GMES) programme, as it evolves to meet the needs of the GMES Atmosphere Service post-2020 (Chapter 8).

→ RESEARCH OBJECTIVES

3 Research Objectives

The aim of the PREMIER mission is to quantify dynamic, radiative, and chemical processes controlling global atmospheric composition in the mid-troposphere to lower stratosphere (5–25 km), a region of particular sensitivity for surface climate. In addition, through combination with collocated observations by MetOp/MetOp-SG, PREMIER aims to quantify links with surface emissions and air pollution.

PREMIER will achieve its aim by resolving 3D structures of atmospheric composition and temperature in this region on finer scales than has previously been possible from space, permitting the following research objectives to be addressed:

Objective A: to quantify the impact of UTLS variability and the general circulation on surface climate

The distribution of radiatively-active gases in the UTLS affect surface climate directly through radiative forcing. They also affect the thermal structure and winds of this region, which impact surface climate indirectly through dynamic couplings between tropospheric and stratospheric circulations (Subsection 2.3.1). PREMIER will observe the fine-scale structure and variability in the distributions of radiatively-active gases, cirrus and temperature to investigate these radiative and dynamic couplings and to quantify their impact on surface climate.

Objective B: to quantify trace-gas exchange between the troposphere and stratosphere

Exchange of air between the stratosphere and troposphere plays a major role in the budgets and distribution of water vapour, ozone and other radiatively-active gases in the UTLS (Subsection 2.3.2). Transport tracers and temperature fields will be measured in 3D with the spatial resolutions needed to quantify quasi-horizontal transport, vertical transport by convection and gravity-wave breaking, and the influence of the Brewer–Dobson circulation.

Objective C: to quantify the impact of convection, pyroconvection and their outflow on UTLS composition

Surface emissions of trace gases and particulates, along with water vapour, can be lifted rapidly to the upper troposphere in convective or pyroconvective events (Subsection 2.3.3). PREMIER will observe indicators of convective, pyrogenic, biogenic and volcanic sources in the outflow plumes to differentiate sources and quantify their impacts on ozone production and the composition of the UTLS.

Objective D: to quantify processes linking the composition of the UTLS and the lower troposphere

The composition of the lower troposphere is governed by surface emissions, chemical and physical processes and transport occurring on a range of scales (Subsection 2.3.4). Combining collocated observations by PREMIER and MetOp/MetOp-SG will extend profiles of ozone, precursors and methane into the lower troposphere, to improve estimates of the tropospheric ozone budget, surface emissions and the impact of long-range pollutant transport on air quality.

PREMIER will achieve these research objectives by providing measurements to address specific scientific issues:

- *Variability of UTLS composition and its radiative feedback on surface climate (objective A):* The distributions of O₃, H₂O, cirrus and volcanic aerosols have a direct radiative impact on surface temperature. Surface climate is particularly sensitive to atmospheric composition changes in the UTLS, owing to the large temperature contrast with the surface. PREMIER will resolve mesoscale structures (50–100 km) in the UTLS distribution of O₃, H₂O, cirrus and volcanic aerosols. In combination with collocated MetOp/MetOp-SG observations, this will allow the surface temperature response to UTLS composition variability to be quantified.
- *The impact of the Asian monsoon circulation on the composition of the TTL and global UTLS (objectives B & C):* The upper tropospheric Asian monsoon circulation drives the budgets and variability of both water vapour and ozone in the TTL. The circulation allows pollutants from southern Asia to enter the TTL where they can be distributed globally throughout the UTLS. PREMIER will provide mesoscale observations required to quantify transport through the monsoon circulation and, in combination with collocated MetOp/MetOp-SG observations, convective uplift.
- *The impact of pyroconvection and volcanic eruptions on UTLS composition (objective C):* Biomass burning is responsible for copious emissions of trace gases and aerosols into the atmosphere. If the atmosphere is convectively unstable or the fire is sufficiently intense, such emissions reach the upper troposphere and sometimes even the lower stratosphere. PREMIER will observe the composition of these pyroconvective plumes, including HCN, which is produced from biomass burning alone, and CO. This will allow ozone production and radiative forcing from pyroconvective plumes in the UTLS to be quantified. Volcanic plumes of SO₂, sulphate aerosol and ash will be observed as they enter and evolve within the UTLS. Thin ash-layers that are not detectable by passive nadir-sounding, but are potentially hazardous to aviation will be located precisely in altitude.
- *The global tropospheric ozone budget (objectives B, C & D):* The tropospheric ozone budget is important for the oxidative or cleansing capacity of the atmosphere, surface air-quality and radiative forcing. The budget includes injection from the stratosphere, net chemical production and surface deposition. The individual terms are weakly constrained, even at the global scale, and current models differ quite significantly. PREMIER's highly-resolved UTLS ozone information will constrain the stratospheric injection term and, when combined with MetOp/MetOp-SG observations and information from ground networks, will constrain the tropospheric ozone budget.
- *Links to lower tropospheric pollution and surface emissions (objective D):* Industrial pollution is transported on intercontinental scales in the mid/upper troposphere by dynamic structures such as the 'conveyor belt'. Coupling of surface emissions and pollution with the composition of the mid/upper troposphere and lower stratosphere will be investigated by collocated observations from PREMIER in combination with MetOp/MetOp-SG observations of tropospheric ozone, carbon monoxide and nitrogen oxides. This combination will allow lower tropospheric distributions of CH₄ and shorter-lived gases to be resolved and estimates of their surface sources to be improved.
- *Links between stratospheric and tropospheric circulations, weather and climate (objective A):* Dynamic coupling between stratospheric and tropospheric

circulations has been shown to be a significant factor in the predictability of extreme cold events throughout the northern hemisphere. In particular, sources of internal climate variability such as the Northern Annular Mode, the Quasi-Biennial Oscillation, and the El Niño Southern Oscillation exhibit a pronounced stratospheric influence on tropospheric surface climate. PREMIER's observations of UTLS 3D temperature structure will allow dynamic coupling with surface weather to be quantified.

- *Gravity waves and mesoscale dynamics (objective A)*: Gravity waves play an important role in driving the stratospheric Brewer–Dobson circulation. In particular, they determine stratospheric wind distributions, which affect the propagation and dissipation of planetary waves within the stratosphere, thereby coupling large-scale and mesoscale dynamics. Owing to the lack of gravity-wave observations, models currently use parameterisations that represent the effects of gravity waves in an incomplete way. New information on momentum transfer by gravity waves and their sources to be derived from PREMIER's 3D observations of atmospheric temperature will significantly improve the accuracy of their parameterisation and the Brewer–Dobson circulation in climate models.

**→ OBSERVATIONAL
REQUIREMENTS**

4 Observational Requirements

4.1 Rationale for Global Height-resolved Observations from Space in 2019–23

PREMIER's scientific research objectives address interconnected geographical regions and cover the global atmosphere, so coverage from equatorial to polar latitudes is required.

A mission of at least four years is needed to observe interannual variability of the atmosphere in different phases of important climate modes such as the QBO, Arctic Oscillation (and related North Atlantic Oscillation) and ENSO. The data PREMIER would deliver are crucial and are needed in the 2019–23 timeframe to critically test and improve the representation of processes controlling atmospheric composition in future climate models where the troposphere and stratosphere will be integrated and vertical and horizontal resolution will be increased. Observations in this timeframe would also enable data to be better exploited from the advanced atmospheric nadir-sounders on MetOp-SG.

4.2 Geophysical Level-2 Data Requirements

4.2.1 Height-domain, Coverage, Spatio-temporal Sampling and Resolution

PREMIER primarily targets the UTLS region. This is defined as the part of the atmosphere where processes connect the troposphere with the stratosphere. The required altitude coverage ranges from ~4 km to ~25 km at polar latitudes to ~8 km to ~25 km in the Tropics. To connect processes occurring in the UTLS with those at higher layers, observations of temperature and certain trace-gases are also needed in the middle and upper stratosphere. To connect to the lower troposphere, i.e. below the UTLS range targeted by PREMIER, collocated observations are required from nadir-sounders on the operational MetOp/MetOp-SG platforms, with which PREMIER will fly in formation.

Height-resolved observations of the UTLS are required with global coverage (near pole-to-pole). The target vertical-resolution is 1 km for objectives A and D, to resolve vertical structure in radiatively-active gases and transported pollutant plumes, respectively. The target is 0.5 km for objectives B and C, to resolve mixing and small-scale transport processes on even finer scales. The threshold vertical-resolution is 1.5 km except within intense convective systems that exhibit strong vertical mixing. To resolve instantaneous structures in 3D down to mesoscale (defined here as 50–100 km), dense horizontal sampling is required along-track and across-track over a 360 km swath. This 3D sampling will reveal processes associated with mixing and convective outflow. To meet the research objectives, the target horizontal resolution is 25 km across-track and 50 km along-track and the threshold horizontal-resolution is 100 km. The duty-cycle is required to be 90% on a monthly basis. This will achieve uniform latitudinal and longitudinal coverage in about four days, to capture adequately the evolution of larger-scale structures and variability within a monthly timescale.

The middle and upper stratosphere are connected to the UTLS through overturning by Brewer–Dobson circulation, which itself is affected by propagation of horizontal momentum upwards from the UTLS from gravity waves and through the QBO. PREMIER is required to observe rapid downward propagation into the UTLS of stratospheric sudden warming and associated polar vortex disturbances, which occur over a period of several days. To capture

these phenomena and their impact on the UTLS (objective A) adequately, height-resolved observations of temperature, H₂O, O₃ and CH₄ are required to extend upwards through the stratosphere. Although uniform coverage of the middle and upper stratosphere is needed, horizontal and temporal sampling does not need to be as dense as in the UTLS. With the exception of temperature, for which the requirements are driven by gravity waves, vertical-resolution requirements are significantly less stringent (3 km threshold). A view of even higher altitudes (i.e. into the mesosphere) is needed for calibration purposes, and this geometry could potentially be exploited for additional science. Although objectives and requirements have not been formulated for the mesosphere, the added scientific value of this calibration mode would be evaluated and exploited.

The most important observational requirement for investigation of processes linking the UTLS with the lower troposphere (objective D) is to fly in formation with MetOp/MetOp-SG. This enables PREMIER's UTLS profile observations to be combined with collocated MetOp/MetOp-SG nadir-observations, most notably, of temperature, clouds, aerosols and the trace gases H₂O, O₃, CH₄, CO and NO₂.

4.2.2 Driving Geophysical Level-2 Data Requirements

Based on the scientific justification described in Chapter 2, specific scientific questions and a dedicated set of Level-2 data requirements were described in detail in the final Corsa study report (Kerridge et al., 2012) for each of the four mission objectives identified in Chapter 3. Table 4.1 presents a unified set of observational requirements summarised from four objectives. It shows the Level-2 products that 'drive', i.e. determine, the design of the mission.

The table incorporates temperature and composition data requirements for the targeted UTLS and also those for the middle and upper stratosphere (25–50 km) and for the lower troposphere (surface–6 km at mid-latitude), which is observed by the MetOp/MetOp-SG nadir-sounders. Certain requirements are limited to the troposphere, i.e. below the tropopause (denoted by TP). In cases where both relative (i.e. percentage) and absolute (i.e. volume mixing ratio) requirements are given, the least stringent requirement prevails, as determined by the vertical profile.

Temperature observations are required over PREMIER's full altitude domain with a precision of 0.5K target and 1K threshold. The precision requirements are driven by the science objective to characterise gravity waves through the whole stratosphere. For the other science objectives, the threshold temperature precision is 2K. For constituents, the required accuracy of a single observation (retrieved profile) is specified.

For water vapour, the target accuracy is 5% over the full altitude domain. Similarly for O₃, the accuracy requirements of 3% target and 8% threshold in the UTLS also apply above the UTLS. In the troposphere, where ozone mixing ratios are typically smaller than ~150 ppbv, a threshold of 30 ppbv is specified. For CH₄, the accuracy requirements differ substantially below and above the tropopause because variability, and hence the dynamic range (minimum to maximum), is much larger in the stratosphere. Above the tropopause the required accuracy is 10%, while in the troposphere the threshold requirement is 50 ppbv. For trichlorofluoromethane (CFC13, or CFC-11) which is a long-lived tracer required for characterisation of the transport and mixing processes addressed in objective B, a threshold accuracy of 30 pptv is specified, to resolve adequately a dynamic range in the UTLS between about 30 pptv and 300 pptv.

Requirements are specified for the shorter-lived constituents CO, HNO₃, HCN, NO₂ and peroxyacetylnitrate (PAN) whose distributions in the UTLS are indicative of chemical and transport processes and surface emissions addressed by objectives B, C and D. The CO accuracy requirements are more stringent in the LS (20 ppbv) than in the UT (40 ppbv) because the dynamic

range of stratospheric CO is much smaller. HNO₃ and HCN are required with threshold absolute accuracies of 1 ppb, and 200 pptv, respectively. HCN is a specific marker of biomass burning, which can be present throughout the UTLS, though measurements are only required when the concentration is elevated. The short-lived trace gases NO₂ and PAN are required in the UT for the investigation of long-range transport of air pollution and *in situ* lightning NO_y production in convective areas, when their concentrations are elevated (objectives C and D). Target (0.5 km) and threshold (1.5 km) vertical-resolutions for these shorter-lived gases are derived from objectives B and D, except for the threshold resolution on CO and HCN (3 km) which is derived from objective C. In addition to composition and temperature, it is required to observe light extinction in the UTLS along the line-of-sight (LOS). This characterises the physical properties of cirrus (ice-water content and ice-particle size) and other particulates that occur sporadically in the UTLS region (i.e. dust, smoke,

Table 4.1. Overview of the driving Level-2 data requirements for objectives A, B, C, and D.

Parameter	Driving Objectives	Altitude Range ⁽¹⁾ (km)	Targets		Thresholds	
			Along-track: 50 km Across-track: 25 km		Along-track: 100 km Across-track: 100 km	
			Vertical resolution (km)	Accuracy ⁽³⁾ (ppbv unless otherwise stated)	Vertical resolution (km)	Accuracy ⁽³⁾ (ppbv unless otherwise stated)
T	A	50–25	1	0.5K	1.5	1K
	A, B, C, D	25–6	0.5	0.5K	1.5	1K
	D	6–sfc ^(2,4)	<6	1K	6	2K
H ₂ O	A	50–25	1	5%	3	15%
	A, B, C, D	25–6	0.5	5%	1.5	10%
	D	6–sfc ⁽⁴⁾	<6	5%	6	10%
O ₃	A	50–25	1	3%	3	8%
	A, B, C, D	25–TP ⁽²⁾	0.5	25 ppb/3%	1.5	50 ppb/8%
	A, B, C, D	TP–6	0.5	15	1.5	30
	D	6–sfc ⁽⁴⁾	<6	15	6	30
CH ₄	A	50–25	1	10%	3	20%
	A, C, D	25–TP	1	5%	1.5	10%
	A, C, D	TP–6	1	25	6	50
	D	6–sfc ⁽⁴⁾	<6	25	6	50
CO	B, C, D	25–TP	0.5	10	3	20
	B, C, D	TP–6	0.5	20	3	40
	D	6–sfc ⁽⁴⁾	<6	45	6	90
HNO ₃	B, C, D	25–6	0.5	0.5	1.5	1
CFC-11	B	25–6	0.5	0.015	1.5	0.03
HCN	C	25–6	0.5	0.1	3	0.2
NO ₂	C, D	TP ⁽⁵⁾ –6	0.5	0.2	1.5	0.4
	D	6–sfc ⁽⁵⁾	<6	0.2	6	0.4
PAN	D	TP ⁽⁵⁾ –6	1	0.045	1.5	0.09
Extinction coefficient	A, C, D	25–6	0.5	10 ⁻⁴ km ⁻¹	1.5	2×10 ⁻⁴ km ⁻¹

⁽¹⁾ As covered by PREMIER limb observations down to ~6 km altitude at mid-latitude (i.e. down to 8 km at equator; down to 4 km at high latitude) and in combination with MetOp/MetOp-SG down to the surface.
⁽²⁾ TP = tropopause; sfc = Earth's surface.
⁽³⁾ Precision instead of accuracy is given for temperature.
⁽⁴⁾ Refers to lower-tropospheric column mean mixing ratio; i.e. 0–6 km at mid-latitude and 0–8 km in Tropics.
⁽⁵⁾ NO₂ and PAN apply only if above background.

volcanic ash and polar stratospheric-clouds). Ancillary data on cloud and aerosols in the lower troposphere are required from the MetOp/MetOp-SG sensors (Subsection 4.2.3).

4.2.3 Requirements for Ancillary Data

Ancillary data requirements for PREMIER most notably include the Level-1b and Level-2 products from MetOp/MetOp-SG for objective D, most importantly from IASI/IASI-NG, GOME-2/S5-JVNS and AVHRR-3/MetImage and 3MI (Subsection 4.4.4).

Other ancillary data requirements to generate PREMIER Level-2 products are of a more general nature, and principally include spectroscopic, meteorological and other input data for retrieval. Spectroscopic data (i.e. line positions, strengths, temperature-dependent pressure-broadened half-widths, lower-state energies and quantum assignments) needed for atmospheric radiative transfer calculations are determined from laboratory measurements and theoretical calculations and compiled in spectral databases. A priori information from the surface to the upper limit of the PREMIER range will be provided by forecasts or analyses from operational centres together with climatologies such as those developed through the MIPAS programme.

Products from other operational satellites flying concurrently, such as Sentinel-5 Precursor, Sentinel-3, Meteosat Third Generation (MTG) and the Joint Polar Satellite System (JPSS), though not required to generate PREMIER Level-2 trace-gas products, could contribute to scientific exploitation of the PREMIER Level-2 products, through the analyses of meteorological and surface variables from operational centres or directly. To investigate radiative, dynamic and chemical processes, which couple the UTLS and surface (objectives A, C and D), the highest quality ancillary data on meteorology and surface variables will be exploited.

4.2.4 Additional Level-2 Products

Trace gases additional to the mission drivers in Table 4.1, which could further augment but are not essential to fulfil the four objectives, are defined as ‘additional Level-2 products’. These should also be observed by PREMIER, either generally, or in particular conditions of elevated concentration, or by averaging, but do not influence the mission design. For example, tracers that have different lifetimes and different vertical gradients to CFC-11, such as N₂O, HCFC-22 or CFC-12, provide supplementary information to diagnose transport processes for objective B, whereas SF₆, which has a very long lifetime, is an additional indicator of interannual variability in the Brewer–Dobson circulation for objective A. The ratio of the heavy water isotope (HDO) to the main water isotope provides a further constraint on the hydrological cycle in the UTLS, most relevant to objectives B and C. Certain short-lived gases relate uplifted air masses in the UTLS to specific types of surface emission. For example, CH₃CN is produced only by biomass burning and therefore acts similarly to HCN as a marker, whereas isoprene (C₅H₈) is produced from biogenic sources and C₂H₂ is specific to vehicle emissions (objectives C and D). Other hydrocarbons such as ethane (C₂H₆) and secondary products such as methanol (CH₃OH) and formaldehyde (CH₂O) can lead to ozone production, although they are not specific to one type of source. Carbonyl sulphide (OCS) is usually a marker for oceanic emissions, however, concentrations can be greatly increased by volcanic emissions (objectives C and D). Elevated concentration of SO₂ in the UTLS is another important marker for volcanic emissions, to be related to sulphate aerosol and volcanic ash derived simultaneously from their extinction (objectives C and D). Trace gases of relevance to LS chemical processes at polar and lower latitudes include chlorine monoxide (ClO), chlorine nitrate (ClONO₂), methylchloride (CH₃Cl), bromine monoxide (BrO),

bromine nitrate (BrONO₂), methyl bromide (CH₃Br), dinitrogen pentoxide (N₂O₅) and peroxyxynitrous acid (HO₂NO₂) (objective A).

4.3 Geophysical Level-2 Data Requirements for Operational Applications

4.3.1 Generic Requirements Supporting GMES Atmosphere Service and NWP

The Global Monitoring for Environment and Security (GMES) programme activities will extend the current practise of NWP to atmospheric composition. By the time PREMIER launches, it is expected that global-scale operational systems in leading atmospheric forecasting centres will actually merge meteorology and atmospheric composition. Today, a few NWP centres already include stratospheric ozone in their operational suite, but the list of gas phase or aerosol species considered and the degree of coupling with meteorology (through radiation, cloud microphysics, assimilation) will increase considerably in the coming five years or so. Promising results were demonstrated in the context of the EU FP7 Monitoring Atmospheric Composition and Climate (MACC) project. The resolutions targeted for global-scale chemical application in the second half of the present decade are 50–100 km in the horizontal and around 1 km in the vertical in the mid-troposphere and above. As for the satellite meteorological data currently assimilated, detailed error and observational characterisations (e.g. averaging kernels) are required. While some centres will assimilate Level-1 data directly, it is expected that Level-2 data will constitute the bulk of the PREMIER data used. The most advanced systems, as the one currently developed at ECMWF (C-IFS, the extension of the NWP Integrated Forecasting System with on-line chemistry) will comprise detailed tropospheric and stratospheric chemistry representation, with thus a capability to assimilate all available chemical information.

4.3.2 Timeliness Requirement for Operational Applications

Operational applications in NWP centres are run round-the-clock to provide new analyses and refreshed forecasts generally every 6 or 12 hours (forecasts based on 00:00 and 12:00, or 00:00, 06:00, 12:00 and 18:00 UTC). For each analysis step, only the data falling within a certain assimilation window are taken into account. Currently, these assimilation windows are rather short and typically match the period between two consecutive forecasts, though windows of extended length (e.g. one day) are being considered for the future in some centres. Typically, each forecast is actually run two hours after its 'base date' (the end of the assimilation window). This cut-off time of typically two hours, together with the assimilation window, determines the timeliness requirements for operational applications: data taken more than {assimilation window + cut-off time} before start of the forecast run cannot be considered, while data older than the base date will not cover the entire assimilation window period. For these reasons, the timeliness required is three hours as a target with a threshold of five hours. In future, it can be foreseen that operational centres may extend this threshold.

4.4 Requirement for Limb-emission Sounding and Tandem Flying with MetOp

4.4.1 Introduction

To meet the stringent requirements (Subsection 4.2.2) demanded by the scientific objectives, requires 3D observations of a suite of trace constituents with unprecedented spatial resolution in the mid/upper troposphere and lower stratosphere. This calls for limb-emission sounding.

To meet requirements in quantifying the links to lower-tropospheric pollution and surface emissions (Section 4.2), and to support operational applications (Section 4.3), requires 3D high-resolution limb observations of the mid/upper troposphere and lower stratosphere collocated with MetOp/MetOp-SG nadir-sounding observations (Fig. 4.1).

The limb-emission sounding technique exploits the radiation thermally emitted in the atmosphere along the LOS of the instrument, which is directed towards the limb of Earth’s atmosphere (Fig. 6.1). The point on the LOS closest to the surface is called the tangent point. Under optically thin conditions, the tangent point is representative of the measurement location. Limb-emission geometry yields good vertical resolution because molecules in the LOS are concentrated in the layer immediately above the tangent point, firstly, because atmospheric density decreases exponentially with altitude and, secondly, because the LOS path-length through this layer is much longer than all higher layers of equivalent vertical thickness. It is worthwhile noting that limb-viewing geometry confers less advantage at shorter wavelengths since incoming solar photons can be multiply scattered in the lower atmosphere before being scattered in the limb-direction.

The horizontal resolution associated with a single limb-view or single set of tangent-heights is relatively coarse, owing to the long LOS path-length through the tangent-layer. For a vertical layer thickness of 1 km and homogeneous atmosphere, the horizontal resolution is several hundred km. However, by acquiring limb profiles more densely, the atmospheric structure can be resolved on finer horizontal-scales. Limb-sounding in the vertical plane of the satellite velocity vector with 50–100 km spacing along-track allows commensurate horizontal resolution to be achieved by tomographic (2D) retrieval schemes (Chapter 6). With finer along- and across-track sampling, clouds and plumes of

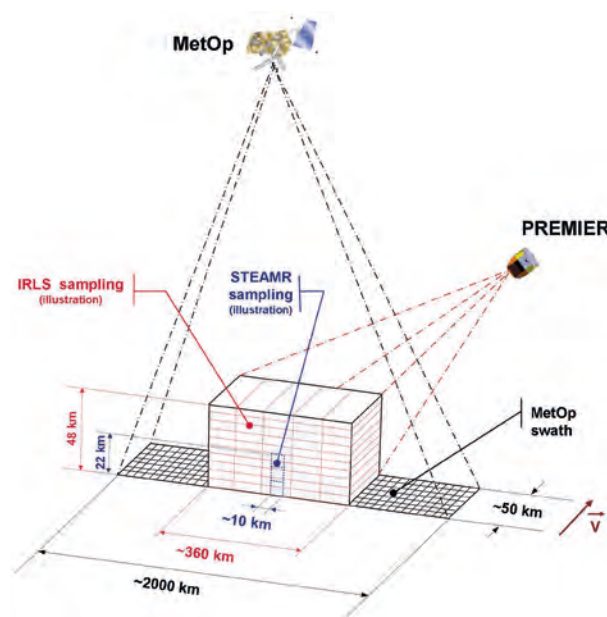


Figure 4.1. The PREMIER observation principle showing IRLS and STEAMR limb-viewing arrays in conjunction with MetOp/MetOp-SG nadir-sounders. (The numbers of samples are indicative only and the horizontal and vertical scales are not in proportion).

trace gases and particulates can be observed on correspondingly finer scales (Chapter 7).

Limb-emission sounding provides adequate geographical and seasonal coverage, since observations are possible at all locations during day and night. Observation in emission against the background of cold space rather than in absorption against the warm background of Earth's surface, whose temperature and emissivity are inhomogeneous and variable, is also advantageous for accuracy. Limb-geometry permits the measurement of trace gases in the UTLS which are too tenuous to be detectable in the shorter path lengths of nadir-geometry.

4.4.2 Atmospheric Limb Emission Sounding Heritage

Limb-emission sounding of Earth's atmosphere from space started with LRIR launched on NASA's Nimbus 6 in 1975, which employed filter radiometry in four infrared (IR) bands to determine global profiles of atmospheric temperature and pressure (from CO₂ emission in narrow and broad bands near 15 μm), water vapour (23–27 μm) and O₃ (9.6 μm) in the stratosphere and lower mesosphere (15–54 km) with a vertical resolution of ~3 km (Gille & Russell III, 1975). This was followed by a series of six IR instruments on four NASA satellites: LIMS (Gille & Russell III, 1984) and SAMS (Drummond et al., 1980) on Nimbus 7 (launched in 1978), CLAES (Roche et al., 1993) and ISAMS (Taylor et al., 1993) on UARS (launched in 1991), SABER (Russell III et al., 1999) on TIMED (launched in 2001) and HIRDLS (Gille et al., 2008) on Aura (launched in 2004), along with the CRISTA-1 and -2 flights (Offermann et al., 1999; Grossmann et al., 2002) on the space shuttle in August 1994 and November 1997.

This series of instruments progressively advanced our knowledge of the stratosphere and mesosphere as the number of constituents and geographical sampling density were increased, through use of cryogenic and mechanically-cooled quantum detectors in conjunction with increased spectral selectivity from narrow interference filters, pressure-modulation radiometry, Fabry-Perot and grating spectrometry. For example, the most recently deployed conventional filter radiometer, HIRDLS, had 21 channels between 6 μm and 17 μm and retrieved temperature and constituent profiles at 1 km vertical resolution and 100 km along-track resolution, and the CRISTA-1 and -2 grating spectrometer achieved a spectral resolving power of 500 ($\lambda/\Delta\lambda$) between 4 μm and 71 μm, 2.5 km vertical resolution and horizontal sampling of 200 km (along-track) × 600 km (across-track). The observed height-range was extended upwards into the lower thermosphere by CRISTA and SABER and downwards into the UT by HIRDLS.

A different technique, Fourier Transform spectrometry, was pioneered for IR-limb emission by ESA with MIPAS which was launched on Envisat. By observing the 4–15 μm range at very high spectral resolution (0.075 cm⁻¹ since September 2004, and 0.03 cm⁻¹ before) with low radiometric noise, up to 40 atmospheric trace-gases can be retrieved in the vertical range 6–68 km at 3 km vertical spacing and ~500 km along-track sampling (Fischer et al., 2008).

Limb-emission sounding at millimetre-wavelengths employs coherent detection of electromagnetic waves rather than incoherent detection of photons as used at IR wavelengths. The spectral resolution of techniques employed for coherent detection is intrinsically very high, so atmospheric lines can be fully-resolved and their pressure broadening can contribute height information provided that contiguous measurements are made over sufficient spectral bandwidths. Technology available in the 1980s provided spectral bandwidths sufficient to cover individual emission features in the mid/upper stratosphere and mesosphere, well-suited to investigate stratospheric O₃ and, in particular, its spring depletion in the Antarctic and Arctic.

The first such instrument, the MLS, was launched on UARS in 1991 (Barath et al., 1993) and provided the first space measurements of ClO. A similar

instrument, the MAS, flew three times on the Space Shuttle in 1992, 1993 and 1994 (Hartmann et al., 1996). These pioneering instruments were designed to profile the stratosphere, using narrow (~500 MHz) bandwidths at frequencies below 220 GHz (i.e. microwave and mm-wave). The first sub-mm radiometer in space was launched in 2002 on the Odin satellite (Murtagh et al., 2002, Frisk et al, 2003) and continues to function. Frequencies up to 580 GHz are employed for atmospheric measurements and also for studies of the interstellar medium. The higher frequencies, however, limited penetration into the troposphere because of the strong absorption by water vapour and oxygen. The Sub-Millimetre Wave Limb Emission Sounder (SMILES) (Inatani et al, 2000, Shiotani et al., 2002) operated on the International Space Station in September 2009–April 2010. While having much-increased sensitivity to trace-gas emissions through use of superconducting receivers, its frequency bands (625 GHz and 650 GHz) again restricted coverage to the stratosphere. A follow-up MLS instrument was launched in 2004 on NASA's Aura satellite (Waters et al., 2006). As well as adding sub-mm and THz bands to profile stratospheric Cl and Br compounds and OH, respectively, this includes broad channels in window regions near 190 GHz and 230 GHz, to extend profiling of several gases including H₂O, O₃, HNO₃ and CO into the upper troposphere for the first time.

4.4.3 Combining Advanced Infrared and Millimetre-wave Limb Sounders

To achieve the required advances in spatial sampling and resolution, PREMIER will need to deploy advanced IR and mm-wave limb-emission sounders in combination (see Fig. 4.1):

- The first satellite limb-imaging Fourier Transform Infrared (FTIR) spectrometer: Infrared Limb-Sounder (IRLS).
- The first satellite Millimetre-Wave Limb-Sounder optimised for UT sounding: Stratosphere-Troposphere Exchange And climate Monitor Radiometer (STEAMR).

IRLS and STEAMR will achieve the horizontal sampling density required along-track by observing at all tangent-heights simultaneously over the required vertical range through use of detector arrays, which will also ensure that tangent-point vertical spacings will be known to unprecedented accuracy. To deliver the required vertical resolution, the vertical field-of-view of IRLS will need to be comparable to that of High Resolution Dynamic Limb Sounder (HIRDLS) (~1 km), while the vertical field-of-view of STEAMR will need to be much narrower than that of Aura MLS in the upper troposphere. Two further innovations will be required of IRLS:

- To observe the limb simultaneously in a number of directions across-track, as well as in the vertical, through use of 2D arrays, to deliver 3D trace-gas observations with the required across-track coverage and sampling.
- To acquire data on a finer spacing along-track for cloud detection and improved spatial resolution in this direction.

4.4.3.1 Complementary sensitivities to trace gases, aerosol, cirrus and temperature

To meet PREMIER's requirements for sounding the mid/upper troposphere and lower stratosphere, the complementary attributes of IR and mm-wave limb

emission sounding need to be combined optimally, with respect to their very different sensitivities to cirrus clouds, aerosols and targeted trace gases.

The set of trace gases required by PREMIER (Table 4.1) will be covered through IR observations of CH₄, CFC-11, PAN and NO₂ in conjunction with mm-wave observations of CO and observations of H₂O, O₃, HNO₃ and HCN in both wavelength regions.

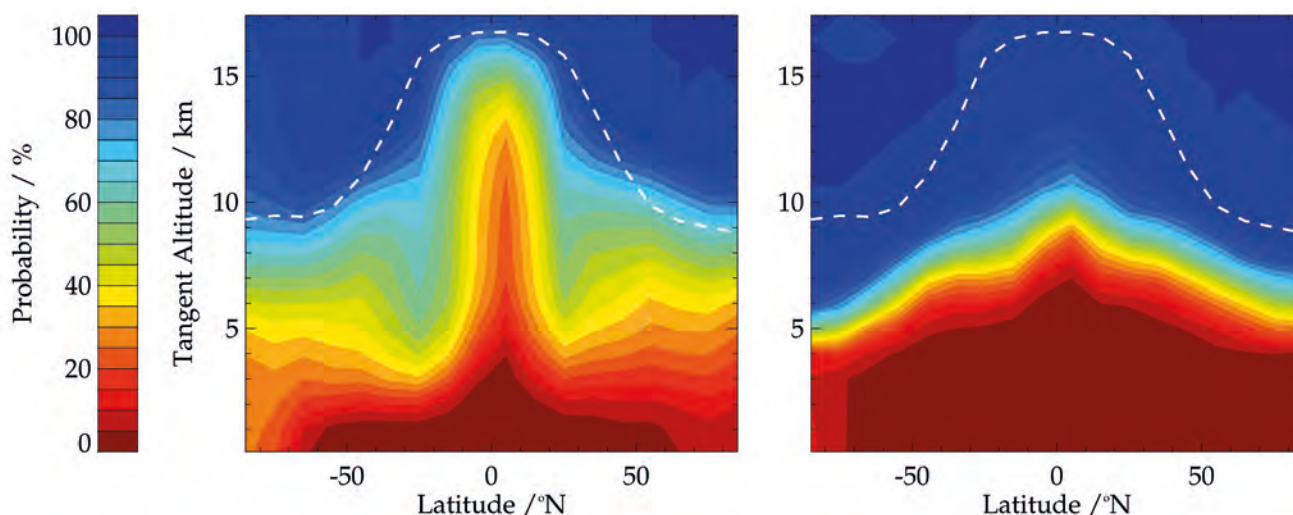
The additional species identified in Subsection 4.2.4 will all be observed as well. IRLS will observe organic compounds including ethane (C₂H₆), ethyne (C₂H₂), isoprene (C₅H₈) and methanol (CH₃OH) from uplifted surface emissions, additional tracers including SF₆ and aerosols (dust, smoke, ash, sulphate aerosol and polar stratospheric clouds). STEAMR will observe CH₃CN from biomass burning. Elevated concentrations of HDO and SO₂ will be measured by both IRLS and STEAMR. Halogens and nitrogen oxides of relevance to lower stratospheric chemistry at polar and lower latitudes will be observed by STEAMR and IRLS, respectively.

Trace-gas emissions at mm-wavelengths are not attenuated significantly by aerosols or polar stratospheric clouds (PSCs) and are attenuated much less by cirrus clouds than emissions at infrared wavelengths. Only cirrus clouds containing relatively large particles (>100 μm) can significantly attenuate limb-emission at mm-wavelengths. This means that trace gases can still be retrieved in the presence of most cirrus clouds. By contrast, cirrus size components <100 μm can be observed by infrared limb-sounding.

Limb-path transparency in IR and mm-wave window regions is illustrated in Fig. 4.2, which shows the annual mean probability of transmittance >20% at the two wavelengths as a function of latitude and height. These have been calculated from ECMWF analyses of temperature, humidity and cloud, in conjunction with Calipso/CloudSat information to verify representation on finer scales than the analyses. The impact of cloud on these calculated probabilities has been verified at IR and mm-wavelengths through comparisons involving the Envisat MIPAS cloud index and a CloudSat-derived global cloud database, respectively (Kerridge et al., 2012).

At mm-wavelengths, tropospheric penetration is controlled by water-vapour attenuation. Retrievals are generally confined to water-vapour mixing ratios

Figure 4.2. Comparison of limb transparency in infrared (left panel) and mm-wave (right panel) atmospheric windows to be exploited by PREMIER. The annual-mean probabilities of transmittance >20% calculated for ~12 μm and ~1 mm from ECMWF analyses of temperature, humidity and cloud are shown as a function of latitude and tangent-height. Transparency at mm-wavelength is controlled principally by humidity, which permits coverage of the upper half of the troposphere at all latitudes but restricts penetration into the mid-troposphere. IR wavelength however, is controlled by cloud, which restricts sampling of the equatorial UT while sampling down to the mid or lower troposphere is possible in cloud-free views. White dashed line indicates tropopause. (R. Siddans)



below ~300 ppmv, and therefore to the upper-half of the troposphere. Even in the Tropics, where cirrus is pervasive, annual mean limb-transmittance probabilities are still only ~10% lower than they would be in the absence of cloud.

In IR windows, tropospheric penetration is limited principally by clouds. In the absence of cloud, IR limb-sounding extends down to a level determined by water-vapour attenuation, typically ~8 km in Tropics, ~4 km at mid-latitudes and near-surface in arid polar regions.

For water vapour, ozone, nitric acid and hydrogen cyanide, the combination of IRLS and STEAMR observations therefore optimises sampling of the mid/upper troposphere and minimises bias owing to sampling cloud-free scenes only.

Atmospheric trace-gas emissions at mm-wavelengths arise from pure rotational transitions whereas at IR-wavelengths they arise from vibration-rotation transitions. Because the temperature sensitivity is much larger for vibrational transitions, IR spectra provide higher-precision temperature profiling, whereas trace-gas retrievals from mm-wave spectra are less sensitive to errors in knowledge of the temperature profile.

4.4.3.2 Collocation of IRLS and STEAMR observations

To combine STEAMR and IRLS optimally will need observations rearwards in the orbit plane, with yaw steering to offset east-west movement of the tangent-point due to Earth's rotation. IRLS will need to observe at multiple azimuth angles, including the orbit plane, with *a posteriori* knowledge of STEAMR and IRLS collocation to 0.5 km (target) and 1.0 km (threshold) in the vertical, half the IRLS sub-sampling distance across-track and 25 km along-track.

4.4.4 Combination of PREMIER Limb-emission with MetOp/MetOp-SG Nadir Observations

Nadir observations of trace gases have little or no vertical resolution but, in absence of cloud, have sensitivity down to Earth's surface. They can, therefore, be combined with PREMIER's vertical profiling of the mid/upper troposphere and lower stratosphere (Fig. 4.1) to enable links to lower tropospheric pollution and surface emissions to be quantified (objective D, Chapter 3, Section 4.2). The operational system planned for the PREMIER timeframe comprises nadir-sounders only (Chapter 8, Section 4.3).

MetOp currently provides the most powerful nadir-sounding capability for atmospheric composition. In the PREMIER timeframe, this will be superseded by MetOp-SG with advanced capabilities for IR spectrometry (IASI-NG), shortwave spectrometry (Sentinel-5 UVNS) and shortwave/IR imagery (MetImage and 3MI). Since MetOp/MetOp-SG is an operational system, it can be relied upon.

The benefit of combining PREMIER observations with collocated observations from the nadir-sounders on MetOp/MetOp-SG will be two-fold:

- Links to lower tropospheric pollution and surface emissions (objective D)
 - PREMIER's global distributions of O₃, H₂O, CO, CH₄, HNO₃, NO₂ and other trace gases in the mid-troposphere and above will be extended into the lower troposphere through combination with MetOp/MetOp-SG collocated data.
- Support to operational monitoring and forecasting applications
 - Trace-gas vertical profiles from PREMIER will improve substantially on the height-resolution of MetOp/MetOp-SG nadir-sounders in the mid/upper troposphere and lower stratosphere and also on their detection and characterisation of thin cirrus and aerosol layers.

For science exploitation in combination with PREMIER, Level-1 data and the following Level-2 data will be needed from MetOp/MetOp-SG:

- Cloud, aerosol and surface properties from AVHRR-3/MetImage and 3MI
- Temperature and humidity profiles from IASI/IASI-NG and AMSU/MWS
- Trace gases and aerosol from IASI/IASI-NG and GOME-2/Sentinel-5 UVNS

For use in combined retrieval schemes, MetOp/MetOp-SG observations will need to be closer in time than 1 min (target)/5 min (threshold) and span the swath of PREMIER IRLS, and *a posteriori* knowledge of their geographical collocation with respect to tangent-points of the PREMIER IRLS and STEAMR observations will need to be within 2 km along-track and across-track.

4.4.5 Exploitation of Data from Other Concurrent Missions

Opportunities to enhance further the scientific return from PREMIER through access to higher-level data from nadir-sounders on other satellites in different orbits could also be exploited, even though these are not required to achieve the mission objectives identified in Chapters 2 and 3. Some relevant possibilities include: Sentinel-5 Precursor and the US JPSS (both with 13:30 equator crossing times, cf. 09:30 for MetOp/MetOp-SG), Sentinel-3 (for height-integrated aerosol); MTG-S, MTG-I and other geostationary satellites over Asia and USA and the Canadian PCW/Phemos mission, which is designed to have frequent revisit times over high northern latitudes (Chapter 8).

4.5. Level-1b Data Requirements

In the following, requirements are denoted as target value [threshold value].

4.5.1 Level-1b Data Requirements for IRLS

Limb-emission sounding of Earth's atmosphere in the IR spectral region exploits the fact that most atmospheric molecules have allowed vibrational transitions and emit thermal radiation following Planck's law. The rotational-vibrational structure of these transitions is a characteristic signature of each molecule (Fig. 4.3).

As outlined in Subsection 4.4.1, limb geometry benefits from a cold space background and an inherently high-vertical resolution, although the resolution achieved in practice is sensitive to the vertical field-of-view width and vertical spacing of tangent-points. The overall accuracy of retrieved temperature and trace-gas profiles depends upon the noise-equivalent spectral radiance together with other uncertainties associated with the measurement and forward modelling of limb spectra, which have been investigated extensively for PREMIER IRLS (Kerridge et al., 2012).

The technical challenge for PREMIER IRLS is to advance Fourier transform spectrometry to achieve 3D high-resolution profiling of trace gases in the mid/upper troposphere and lower stratosphere, to meet PREMIER's demanding requirements (Table 4.1). Experience from the previous satellite limb-emission IR sounders (Subsection 4.4.2), particularly MIPAS, along with MIPAS-STR (Woiwode et al., 2011) and CRISTA-NF (Ungermaun, 2011) on high-flying aircraft and MIPAS-B (Friedl-Vallon et al., 2004) on stratospheric balloons, has provided the foundation for scientific and technical studies in preparation for PREMIER IRLS. The new airborne instrument, GLORIA-AB, is pioneering use of a 2D detector array for FTIR imaging of the limb to demonstrate this critical technological advance for PREMIER IRLS (Chapter 7).

The dual requirements for IRLS, to resolve dynamic processes and to detect tenuous trace-gases, lead to a two-mode concept for the IRLS instrument. In

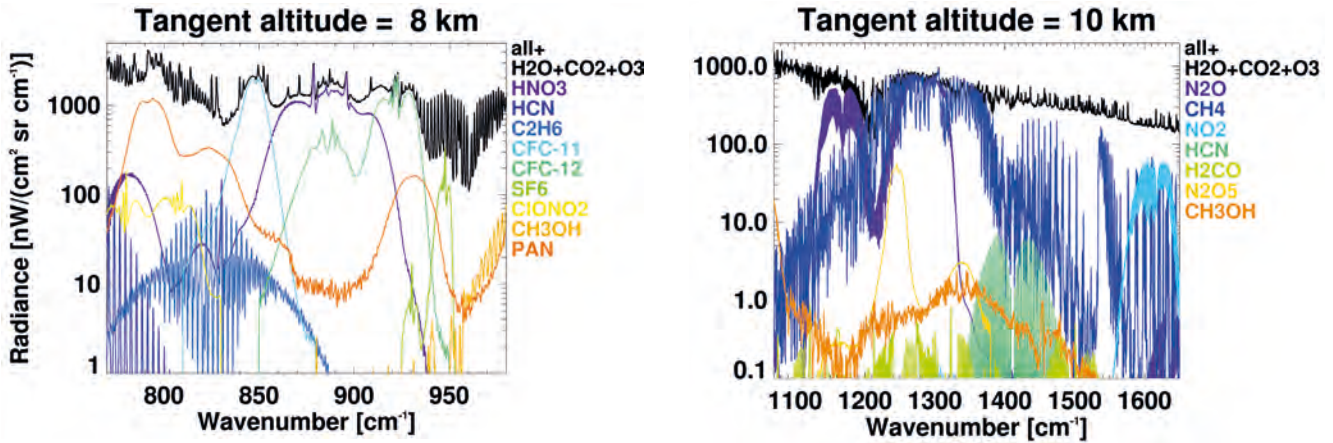
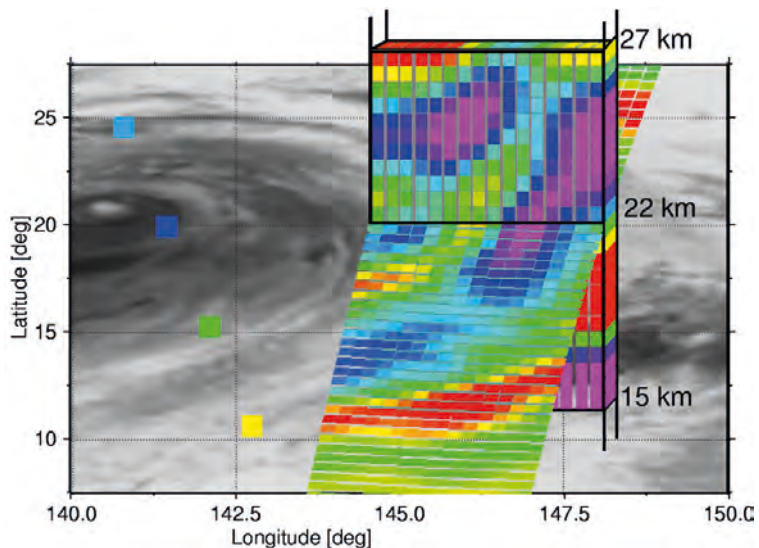


Figure 4.3. Typical spectra (calculated with the radiative transfer model KOPRA) for tangent altitudes of 8 km (IRLS Band A, left panel) and 10 km (IRLS Band B, right panel). The black curve at the top shows the sum of all contributions, i.e. the expected signal to be observed by PREMIER. The contributions of H₂O, CO₂ and O₃ (that actually dominate the spectra) are not shown individually. (M. Höpfner)

the dynamics mode (DM), the horizontal sampling is optimised, while in the chemistry mode (CM), the spectral resolution has been adapted for detection of trace gases with low concentration, identified in Subsection 4.4.3.1. The increase in horizontal sampling-density of IRLS in DM in comparison to MIPAS is indicated in Fig. 4.4. The dominant wave-fronts (perpendicular to the wave-vector) can be clearly identified by PREMIER. For comparison, the horizontal measurement track of MIPAS-Envisat is illustrated by four coloured squares on the left, each representing the horizontal position of one vertical profile measurement.

In the vertical dimension, the coverage comprises the region from the mid-troposphere up to the stratopause, thus ensuring adequate sampling of the higher atmosphere needed for analysis of atmospheric waves and coupling processes between UTLS and mid/upper stratosphere. The vertical sampling is equal for both modes (DM and CM) in the UTLS (0.6 [0.8] km). This ensures – in combination with a commensurate full width at half maximum (FWHM) of 0.7[0.9] km of the point spread function (PSF) – a vertical resolution of ~1 km for most atmospheric target quantities. In the across-track dimension, the IRLS viewing capability of 360 [240] km allows coverage of mesoscale atmospheric structures.

Figure 4.4. PREMIER sampling of 3D gravity-wave temperature-structures (background field subtracted) generated by a typhoon (grey-cloud image) as obtained from a mesoscale simulation. Temperature values (coloured squares) are shown for a horizontal cross-section of the measurement grid at 22 km altitude and for a vertical cross-section in the 15–27 km altitude region. The colour code is from -3K (purple) to +3K (red). MIPAS horizontal measurement track illustrated on the left. (L. Hoffmann and P. Preusse)



An optimal cloud detection and analysis is ensured for both measurement modes by requiring that sub-sample observations are available on-ground with the same spectral resolution as the main mode, and with a sub-sampling distance of ~12 [16] km across track, <50–100 km along track and 0.6 [0.8] km vertically. This information on cloud is augmented by requiring along-track highly-resolved (1 [12] km) data of the spectrally-integrated radiance.

The IRLS spectral coverage has been chosen such that on the long-wavelength side a CO₂ emission feature can provide high-precision pressure/temperature retrieval in the upper stratosphere and that an HCN emission feature is available. The high wavenumber limit is defined by the position of spectral signatures for the measurement of NO₂.

In order to retrieve Level-2 products at the required accuracy and high horizontal- and vertical-resolutions, and as the basis for retrieval of minor trace species, a very good radiometric sensitivity is required.

To meet the Level-2 requirements (Table 4.1), key instrumental quantities must be known with sufficient accuracies: (1) in the vertical dimension, the relative spacing of adjacent pixels and the PSF; (2) in the spectral domain, the wavenumber position and the form of the instrumental line-shape and (3) in radiometric space, the absolute accuracy and the sample-to-sample variation of the radiometric scaling factor and offset.

Tables 4.2–4.4 summarise some of the driving Level-1b requirements.

4.5.2 Level-1b Data Requirements for STEAMR

Due to pressure broadening and the water vapour continuum, spectral confusion increases with decreasing height below the tropopause. So to meet PREMIER's stringent requirements for sounding the upper troposphere, it will be necessary to resolve as cleanly as possible the emissions from target lines, interfering lines and underlying continua. To achieve this, contiguous spectral coverage over 12 GHz bandwidths is needed and separation of upper and lower side-bands is a desirable option (Fig. 4.5). The MARSCHALS airborne instrument has demonstrated UTLS limb-sounding of the mm-wave region targeted by STEAMR (Chapter 7).

In the mm-wave region the vertical sampling requirement must either be accomplished using scanning or a multibeam approach. To avoid rapid

Geometric Parameters	Value
Vertical coverage	4–52 km in polar regions, 8–56 km in tropical regions
Vertical Sampling	0.6 km [0.8 km] (lower half of altitude range) 1.2 km (0.8 km dynamics mode band A) [1.6 km] (upper half of altitude range)
FWHM of vertical PSF	<vertical sampling distance +0.1 km
Vertical PSF degradation from Earth's curvature and misalignment	Chemistry mode: <5% [10%] of vertical width of PSF Dynamics mode: <10% [15%] of vertical width of PSF
	1st neighbour <5 [15]%, 2nd neighbour <2 [7.5]%, 3rd neighbour <1 [4]%, 4th neighbour <1%, 5th neighbour <0.5%
Across-track sampling	Chemistry mode: 72 km [96 km] Dynamics mode: 24 km [32 km]
Along-track sampling	Chemistry mode: 50 km [100 km] (lower half of altitude range) 100 km (upper half of altitude range) Dynamics mode: 50 km
Horizontal coverage across-track	360 km [240 km]

Table 4.2: Geometric requirements for PREMIER IRLS Level-1b data.

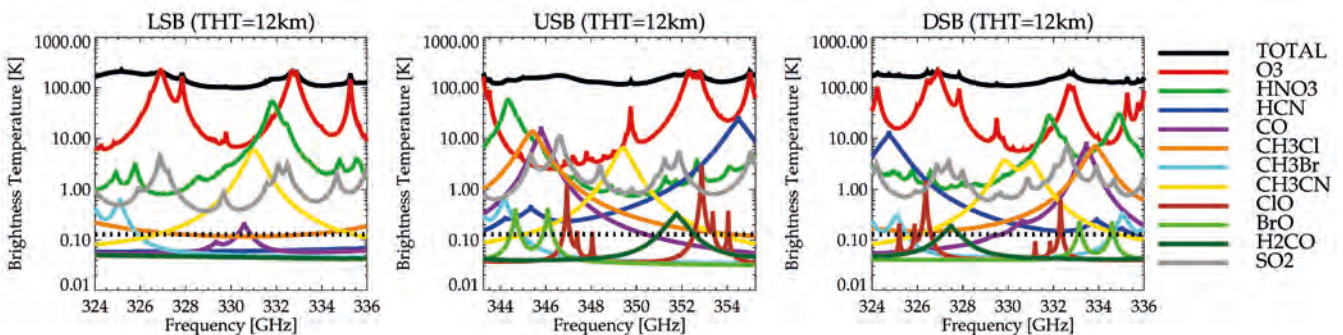
Table 4.3. Geolocation knowledge and stability requirements for PREMIER IRLS Level-1b data.

Geolocation Parameters	Value
Vertical geolocation knowledge	200 m [750 m]
Vertical geolocation knowledge between any two samples	100 m
Vertical geolocation knowledge between neighbours	15 m [25 m]
Vertical geolocation stability	60 m [100 m]
– within interferogram acquisition time in relevant frequency range	60 m [100 m]
– within horizontal sampling time	75 m [150 m]
Vertical co-registration	75 m [150 m] intra-band, 250 m interband; knowledge: 25 m [50 m] intra-band, 100 m interband

Table 4.4. Spectral and radiometric requirements for PREMIER IRLS Level-1b data.

Parameter	Value
Spectral coverage	Band A: 710 cm^{-1} [730 cm^{-1}] -1010 cm^{-1} [980 cm^{-1}] Band B: 1070 cm^{-1} [1100 cm^{-1}] -1650 cm^{-1}
Spectral resolution	Chemistry mode: 0.25 cm^{-1} [0.27 cm^{-1}] Dynamics mode: 1.58 cm^{-1} [1.73 cm^{-1}]
Spectral accuracy	Chemistry mode: 0.008 cm^{-1} Dynamics mode: 0.010 cm^{-1}
ILS characterisation	1% of width 1% of ILS maximum value
Radiometric accuracy	Quadratic sum of actual NESR, radiometric additive error and 1.5% of measured radiance
Radiometric scaling errors	0.15% [0.25%] (spatially and/or spectrally uncorrelated) 1% (spatially and spectrally and temporally correlated)
Spectrally varying radiometric errors	<4 $\text{nW}/(\text{cm}^2 \text{sr cm}^{-1})$ (CM) <1.5 $\text{nW}/(\text{cm}^2 \text{sr cm}^{-1})$ (DM)
Radiometric sensitivity	Chemistry mode: Band A: 2 [4.0-6.5] $\text{nW}/(\text{cm}^2 \text{sr cm}^{-1})$ Band B: 1.5-2.0 [4.0-6.5] $\text{nW}/(\text{cm}^2 \text{sr cm}^{-1})$ Dynamics mode: Band A: 0.8 [1.5-2.5] $\text{nW}/(\text{cm}^2 \text{sr cm}^{-1})$ Band B: 0.4-0.8 [1.5-2.5] $\text{nW}/(\text{cm}^2 \text{sr cm}^{-1})$ Ranges reflect the wavelength dependence of the requirement.

Figure 4.5. Limb brightness-temperature spectra in the STEAMR frequency bands calculated for 12 km tangent-height illustrating trace-gas emission features. Water vapour and continuum emission are included in the total, but not shown individually. Profiles are for typical mid-latitude conditions, except for SO_2 whose concentration is volcanically-enhanced. The left and centre panels show lower and upper side-band spectra individually, the right panel shows the superposed side-bands as measured by a double side-band (DSB) receiver. (D. Gerber)



scanning and improve sensitivity, the STEAMR Level-1b product will consist of sets of 14 calibrated and geolocated spectra corresponding to the beams of 14 independent receivers on the sky.

Table 4.5 presents the geometrical requirements for the STEAMR that are derived from the objectives and the driving Level-2 requirements in Table 4.1. The instantaneous field of view (FOV) plays an important role in the ability of the instrument to conform to the vertical-resolution requirements. Simulations have shown that the maximum width of the instantaneous field of view (IFOV) can be 3 km at the tangent-point on the limb if we are to achieve 1.5 km resolution in Level-2 products, although a smaller value leads to better constituent precision and a target IFOV width of 2 km has been set. With such a FOV oversampling is required to achieve retrieved profiles with ≤ 1.5 km vertical resolution. A compromise between vertical resolution and vertical coverage allows us to reduce the sampling from 1.5 km in the lower part of the range to 2 km above 16 km (polar)/20 km (equator). In order to achieve this dense vertical-sampling, receivers will be placed in two parallel columns with orthogonal polarisation. To minimise their difference in cloud sensitivity, the polarisation directions are required to be $\pm 45^\circ$.

Knowledge of the vertical geolocation of the spectra is specified to provide a sufficiently accurate a prior estimate to retrieve a pointing offset from the mm-wave spectra, and this suffices also for collocation with the IRLS for cloud screening. Retrieval studies (Kerridge et al., 2012) have indicated that the relative spacing between the beams is critical for accurate constituent profile retrieval and, therefore, there is a very tight requirement of 10 m on this knowledge. Table 4.6 summarises the driving geolocation knowledge requirements.

The choice of spectral region to observe is driven by the trade-off between the need to measure the target gases with the required precision, the vertical FOV width, which decreases with increasing frequency for a given the antenna size, and the need to observe in a frequency window in which the upper troposphere is accessible. The CO line near 346 GHz is a key driver for STEAMR, since this is ~ 6 times stronger than the 231 GHz line and accessible in the UT, whereas stronger, higher frequency lines are not. Spectral coverage is determined by the need to ensure that lines from important species can be distinguished. This is particularly important for a double-side band system and a judicious choice of local oscillator frequency is important. The second main driver is the need for good radiometric accuracy and precision. To distinguish spectral components from different gases in the UT, their signatures have to be measured over a broad frequency band and stringent requirements must be placed on all instrumental parameters that affect spectro-radiometric

Geometrical parameters	Polar regions	Tropical regions
Vertical coverage	4–26 km	8–30 km
Vertical sampling	1.5 km (4–16 km) 2 km (16–26 km)	1.5 km (8–20 km) 2 km (20–30 km)
Along track sampling	50 km	
Field of view FWHM	2 km [3 km]	
Antenna pattern knowledge	–30 dB [–26 dB] in main beam –35 dB in sidelobes	

Table 4.5. Geometrical requirements for PREMIER STEAMR Level-1b data.

Geolocation Parameters	Value
Vertical geolocation knowledge absolute	500 m [750 m]
Vertical geolocation knowledge relative between the beams	10 m [50 m]
Along-track geolocation knowledge	2 km

Table 4.6. Geolocation knowledge requirements for PREMIER STEAMR Level-1b data.

Table 4.7. Spectral and radiometric requirements for PREMIER STEAMR Level-1b data.

Parameter	Values
Spectral coverage	324.0–336.0 GHz (LSB) 343.25–355.25 GHz (USB)
Spectral resolution	10 MHz [25 MHz]
Instrument line-shape knowledge	–30 dB [–25 dB]
Sideband response knowledge	<35 dB [30dB]
Radiometric accuracy	<1K
Spectrally varying radiometric errors	<0.1K [0.25K]
Radiometric non-linearity	<0.5%
Radiometric sensitivity	0.25K [0.5K] DSB for 10 MHz channel

knowledge, be it sideband suppression or calibration accuracy. The most important spectral and radiometric requirements are given in Table 4.7.

→ SYSTEM CONCEPT

5. System Concept

5.1 Introduction

This chapter provides the technical description of the PREMIER mission, as derived from the preparatory activities in Phase-A, for implementation as an Earth Explorer in the frame of ESA's Living Planet Programme. It shows how candidate implementation concepts can respond to the scientific mission requirements defined in the previous chapters.

The system description is mainly based on the results of the work performed during parallel Phase-A system studies by two industrial consortia (EADS Astrium SAS, 2012; Thales Alenia Space Italy, 2012). When necessary, two implementation concepts (Concepts A and B) are described in order to present significantly different approaches capable of meeting the mission requirements. This applies to all the elements of the mission architecture with the exception of the mm-wave limb sounder instrument, which is based on the STEAMR concept being developed by Omnisys Instruments (Sweden) in the frame of a nationally-funded programme. In accordance with the PREMIER proposal, the programmatic scenario assumes that the STEAMR instrument will be provided as a Swedish national contribution to the mission.

After an overview of the mission architecture and the proposed orbit (Sections 5.2 and 5.3), the space segment is described in detail (Section 5.4) followed by the launcher, ground segment and operations concepts (Sections 5.5, 5.6 and 5.7). The overall mission performance is summarised in Chapter 7.

5.2 Mission Architecture Overview

The PREMIER main architectural elements are depicted in Fig. 5.1.

The space segment consists of a single satellite carrying two instruments: the infrared limb sounder, IRLS, and the STEAMR. The satellite flies in the same orbit as the MetOp satellite (or planned follow on) of the Eumetsat Polar System to achieve the required co-registration between the PREMIER limb



Figure 5.1. PREMIER mission architecture.

observations and the MetOp nadir observations. More precisely, PREMIER flies in loose formation with MetOp, some eight minutes ahead in a rearward limb-viewing configuration, which also minimises the risk of contamination and micrometeoroid impact for both instruments.

The baseline Vega launcher will inject the satellite into a phasing orbit from which PREMIER will manoeuvre into its nominal orbit, i.e. the MetOp one. As a backup, PREMIER is also compatible with the PSLV launcher in its full vehicle configuration.

The mission performs 3D observations of the atmosphere in the infrared (710–1650 cm^{-1}) and 2D observations in the mm-wave (320–360 GHz) spectral range and links atmospheric and surface processes by combining the PREMIER limb and MetOp nadir observations.

The PREMIER scientific data is delivered via an X-band downlink to a single high-latitude ground station (GS) in, for example, Svalbard (Norway), or, to two stations in, for example, Kiruna (Sweden) and Inuvik (Canada) in such a way to avoid orbits without contacts and meet the maximum five-hour latency requirement.

The IRLS is an imaging Fourier-transform spectrometer that combines the functions of spectrometer and imager with a cloud discrimination function. The IRLS operates in two mutually-exclusive operational modes, namely the dynamic mode (DM) and the chemistry mode (CM), with different spatial, spectral and radiometric performance. The DM focuses on observing atmospheric temperature and constituents at the finest spatial scale to study dynamic processes, while the CM provides observations of a wider range of trace gases at high spectral-resolution to investigate the transport and chemical processes controlling their distributions. The observation time per operational mode can be set in a wide range, namely between a quarter of an orbit and a month.

STEAMR is a millimetre-wave radiometer based on a tomographic multibeam limb sounding concept. It observes 14 tangent altitudes simultaneously and provides vertical and horizontal well-resolved information on the distribution of key UTLS constituents such as water vapour and carbon monoxide. The instrument design has heritage from the sub-mm wave radiometer on the Odin mission.

The ground segment uses the generic Earth Explorer ground segment infrastructure and is composed of:

- The Flight Operation Segment (FOS), which includes the Telemetry, Tracking and Command (TT&C) GS and the Flight Operations Control Centre.
- The Payload Data Ground Segment (PDGS), which includes the Science Data Acquisition Station, the Processing and Archiving Element and the Mission Planning and Monitoring Element.

5.3 Mission Analysis

The orbit selection, the formation flying control and the orbit maintenance are driven by the temporal and spatial co-registration requirements between PREMIER and MetOp:

- The PREMIER limb-sounding measurements must be temporally co-registered with the MetOp nadir observations to within five minutes.
- The ground projection of the centre of the PREMIER swath must be spatially co-registered with the MetOp Sub-Satellite Point (SSP) in the across-track direction to within 500 km.

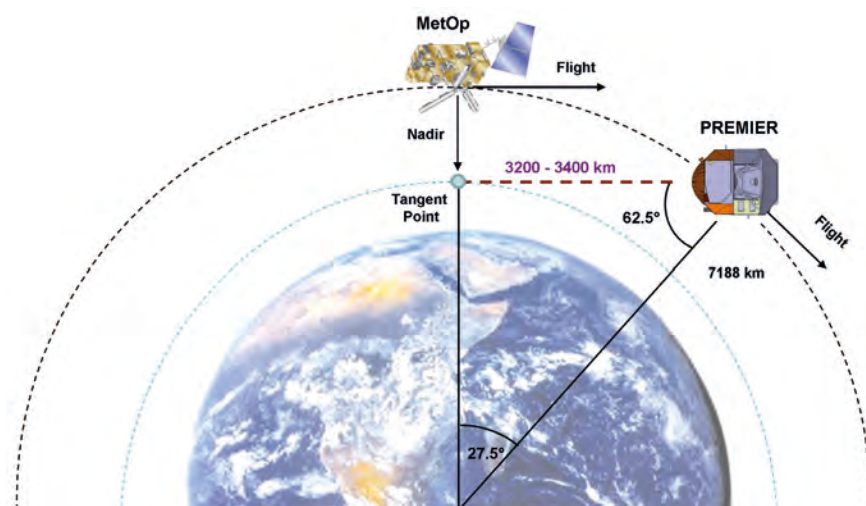


Figure 5.2. MetOp-PREMIER configuration.

Mean elements		Orbit characteristics	
Semi-major axis	7195.590 km	Repeat cycle	14+6/29
Eccentricity	0.0010247	Repeat cycle length	29 days
Inclination	98.721°	Orbits/day	14.207
RAAN	63.411°	Orbits/cycle	412
Arg. Perigee	90°	LTDN	09:30 hours
Mean anomaly	270°	Min. distance PREMIER-MetOp	3200 km
Elements as of 1 Jan 2019 at 00:00:00.00		Max. distance PREMIER-MetOp	3400 km

Table 5.1. PREMIER reference orbit and main orbit properties.

PREMIER fulfils the above requirements by flying in the Sun-synchronous MetOp orbit, at a reference altitude of 817 km, phased $\sim 27.5^\circ$ ahead of MetOp. The PREMIER-MetOp formation is sketched in Fig. 5.2. The Line of Sight (LOS) of both instruments has to be tilted $\sim 62.5^\circ$ with respect to the nadir direction to point to the Earth limb.

The PREMIER orbit has a repeat cycle of 29 days and a Local Time at the Descending Node (LTDN) of 09:30. The distance between PREMIER and the atmospheric limb at the tangent observation altitude oscillates with latitude between 3200–3400 km due to the elliptical shape of Earth. The orbital elements and other relevant orbit characteristics are summarised in Table 5.1.

In order to achieve the required relative position with respect to MetOp, PREMIER will be launched into an initial phasing orbit in the same orbital plane but at a different altitude, hence a different period, with respect to the reference MetOp orbit. The orbital period difference will cause a relative drift between the PREMIER and MetOp positions. Once the target position of PREMIER with respect to MetOp has been reached, an in-plane manoeuvre will be performed to modify the semi-major axis of the orbit and achieve the reference mission orbit altitude. The altitude of the phasing orbit will depend on the time available to drift into the nominal position. For a drift of 180° in 15 days, the phasing orbit will be around 9 km above the nominal one. The initial relative positions in orbit between PREMIER and MetOp will depend on the launch date within the MetOp orbit repeat cycle.

PREMIER will follow the same orbit correction strategy as MetOp to maintain the loose formation. The frequency of orbit manoeuvres will vary throughout the mission lifetime depending on the atmospheric density, a function of the solar activity, and hence depending on the launch date. For a

Figure 5.3. Variation of the reference orbit altitude throughout the mission lifetime for a launch on 1 January 2019 (top). Frequency of the in-plane (centre) and out-of-plane (bottom) orbit control manoeuvres. The bottom figure also shows the inclination control band (red).

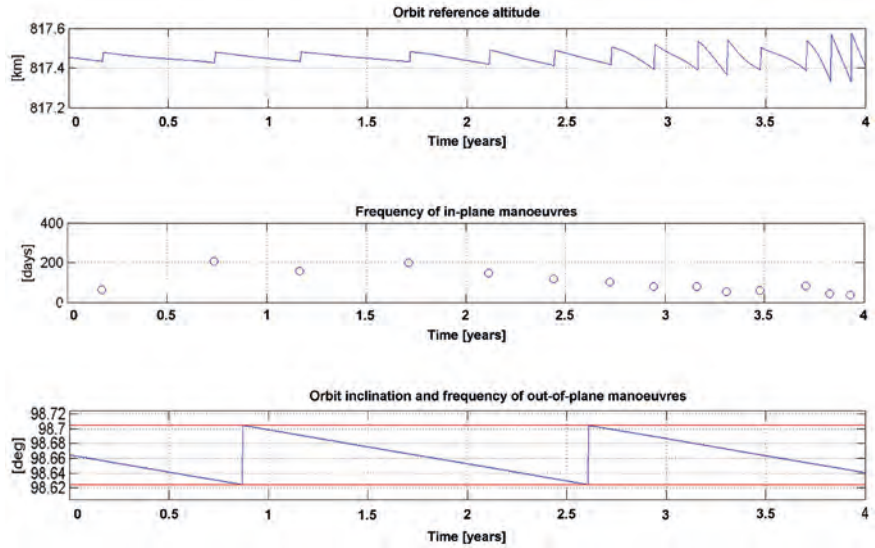
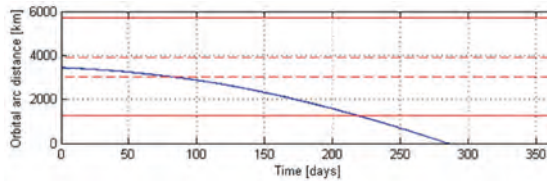


Figure 5.4. Evolution of the PREMIER–MetOp distance. The initial relative conditions correspond with the nominal PREMIER–MetOp position.



launch in 2019, as shown in Fig. 5.3, in-plane manoeuvres would be performed on average every three months, while inclination manoeuvres would be executed approximately once per year.

Figure 5.4 shows the evolution of the PREMIER–MetOp distance (in blue). The solid/dotted red lines represent the required threshold/target temporal co-registration band between the PREMIER limb-soundings and the MetOp nadir observations. Thanks to the similarity of the ballistic coefficient of the two satellites, the time needed by PREMIER to exit the formation control band is longer than the interval between orbit maintenance manoeuvres (Fig. 5.3) and therefore the formation between PREMIER and MetOp can be maintained with no need for dedicated manoeuvres in addition to the orbit control ones, only adapting the manoeuvre to take into account the formation flying repositioning needs.

PREMIER will fly in an orbit with a relatively high concentration of space debris. As a consequence, six collision avoidance manoeuvres per year are foreseen and the corresponding fuel budget has been allocated (Subsection 5.4.5.2).

PREMIER will fulfil the European Code of Conduct for Space Debris Mitigation by performing an orbit disposal manoeuvre at the End of Life (EOL) so that the satellite will reenter in the atmosphere in less than 25 years after the end of the nominal mission (Subsection 5.7.5 for more details).

5.4 Space Segment

5.4.1 Overview

The PREMIER space segment consists of a single satellite carrying the IRLS and the STEAMR instrument. The system configuration is based on an architecture identifying a payload module and a service module. The main constraints are

given by the dimensions of the Vega fairing, by the need for free rearward looking field of views (FOVs) for the limb observations and by the access to cold space views for cooling and instrument calibration purposes. Additional accommodation constraints arise from the need to protect the main and secondary STEAMR reflectors from direct Sun illumination during the nominal measurement modes.

Following the satellite configuration in Subsection 5.4.2, the payload concept is described in Subsection 5.4.3, and complemented with the description of the overall satellite subsystems and budgets in Subsections 5.4.4 and 5.4.5.

5.4.2 Satellite Configuration

The PREMIER satellite configuration design requires careful consideration of:

- The accommodation of the IRLS and STEAMR, so that both instruments have an unobstructed rearward view of the Earth limb.
- Instrument direct access to cold space for calibration and thermal control purposes, which requires the accommodation of both instruments on the cold-sky-facing panel of the satellite.
- The pointing and co-registration requirements, which favour isostatic mounting of both instruments on a common plate together with a startracker.
- The LOS stability, which requires minimisation of microvibrations.
- The need to protect the primary and secondary reflectors of STEAMR from direct illumination from the Sun to avoid permanent degradation. This requires the implementation of a sunshield.
- Launcher constraints, which require the ~300 kg payload to be placed such that the satellite centre of mass falls on the launcher axis within a given tolerance.
- Vega launcher fairing envelope, which limits the instruments and the overall satellite size and shape.
- Assembly, Integration and Testing (AIT), to ensure that the instrument integration and the platform integration are decoupled.

These constraints lead to two similar configurations where the satellite is about 3.7 m high and 1.75 m wide (Concept A) and 2.9 m high and 2.2 m wide (Concept B). Both are based on an architecture with separate service and payload modules. The two configurations are depicted in Figs. 5.5 and 5.6.

The service module provides the structural support for the payload and the sunshield. It contains all the platform subsystems required to support the nominal operations and survival of the satellite and payload as well as part of the IRLS subsystem electronics. It also supports a deployable single-wing steerable solar array that generates power for the instruments and the platform. The service module design minimises the generation and propagation of microvibrations, hence improving the IRLS LOS stability, by mounting the reaction wheels on dampers and aligning the axis of rotation of the solar array with the satellite pitch axis.

The payload module comprises the two instruments, IRLS and STEAMR, and a non-deployable sunshield protecting STEAMR from direct Sun illumination. The instruments are thermally decoupled from the service module and isostatically mounted on a dedicated Payload Interface Panel (PIP)

Figure 5.5. Concept A in deployed configuration.

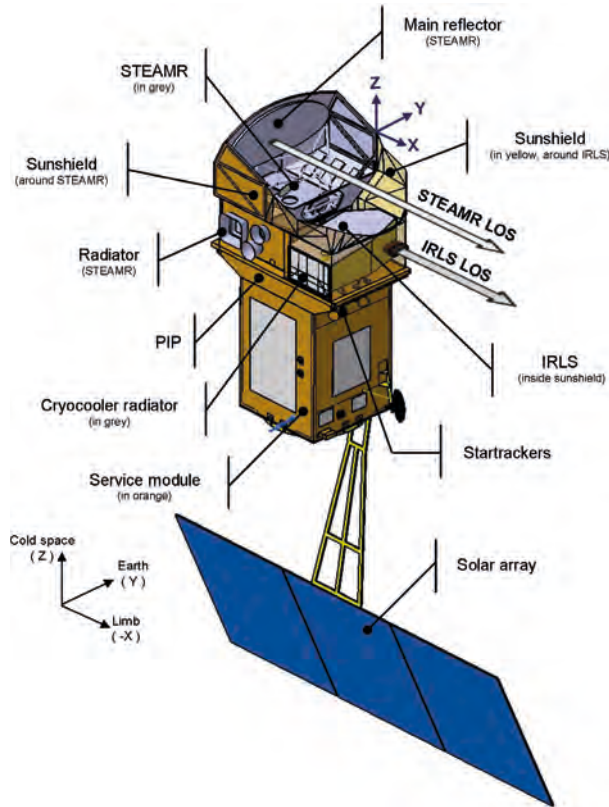
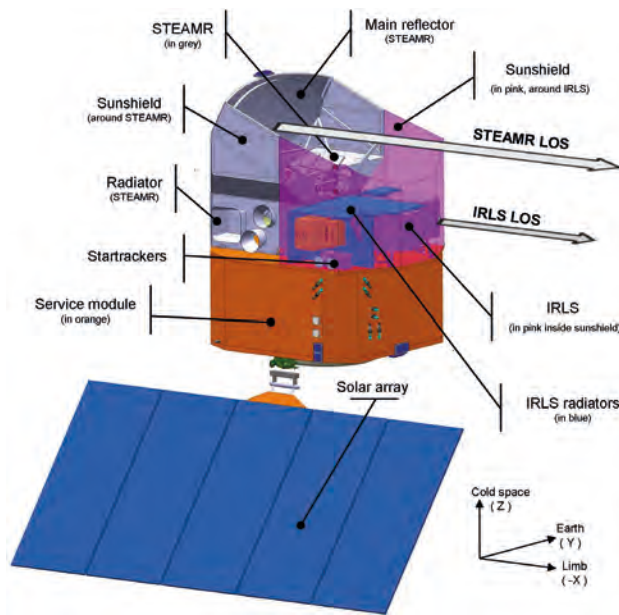


Figure 5.6. Concept B in deployed configuration.



in Concept A or on the top panel of the service module in Concept B. The PIP is a dedicated panel made in carbon fibre reinforced panel (CFRP) to reduce the thermoelastic distortion between the instruments and the startrackers, hence improving the pointing and co-registration performance by design.

The sunshield is a non-deployable structure divided into two parts (Figs. 5.5 and 5.6): the first is an integral part of the STEAMR structure and provides support to the instrument equipment; the second consists of a dedicated structure surrounding the IRLS and mounted on the PIP or the top panel (Concept A and Concept B respectively). The difference in the sunshield shape

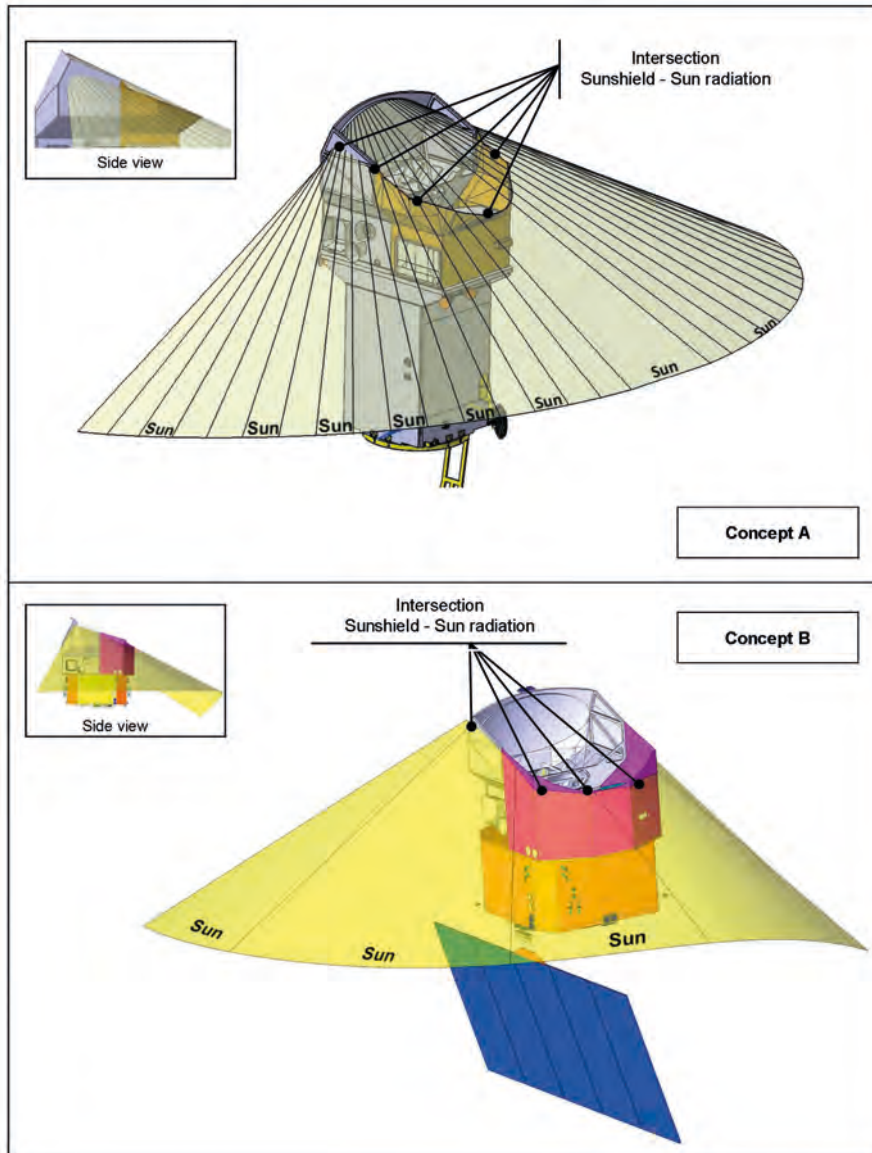


Figure 5.7. Sun envelope during nominal operations for Concept A (top) and Concept B (bottom).

between the two concepts is due to the different size of the IRLS. The sunshield around the IRLS consists of a mesh made of tubular elements and stiffening cables (Concept A) or a structure made of CFRP panels reinforced by a tubular rod frame (Concept B). In both concepts the outside of the sunshield is covered with high-efficiency multi-layer insulation (MLI) blankets that, together with the accommodation of the instruments on the panel of the satellite facing cold-space, provide a very stable thermal environment for STEAMR and for the IRLS.

Figure 5.7. Sun envelope during nominal operations for Concept A (top) and Concept B (bottom). 5.7 shows (in yellow) the Sun-viewing envelope of the STEAMR primary reflector during nominal operations. Radiation from the Sun is parallel to the envelope. The sunshield shades STEAMR by blocking the radiation that reaches the satellite below the envelope. Radiation above the envelope does not illuminate the STEAMR antenna and therefore there is no need to block it out.

5.4.3 Payload

5.4.3.1 Overview

The PREMIER payload consists of two instruments observing the Earth limb:

- The infrared imaging limb-sounder, IRLS
- The millimetre-wave limb sounder, STEAMR

The following sections address the observation principles, the description of the IRLS and the STEAMR instruments, starting with an overview of the instrument concepts, followed by a discussion on the impact of key requirements at Level-1b on the detailed definition of the instruments, which is presented by describing the main subsystems and the calibration strategy.

5.4.3.2 Observation principles

The IRLS is an imaging Fourier-Transform Spectrometer (FTS) combining the functions of a spectrometer and an imager with the ability to discriminate clouds. The IRLS provides two mutually exclusive measurement modes with different spatial, spectral and radiometric performance requirements (Table 5.2). The spectral range between $710\text{--}1650\text{ cm}^{-1}$ is covered by simultaneous observation of two spectral bands with a gap of about 90 cm^{-1} .

Figure 5.8 shows an illustration (not to scale) of the PREMIER observation principle, which is based on simultaneous limb observations by the IRLS and the STEAMR instrument. The observations are spatially and temporally co-registered with those performed by the nadir-viewing instruments on MetOp. The IRLS acquires bi-dimensional observations of the atmosphere (in red) centred on the MetOp swath, while STEAMR acquires mono-dimensional observations (in blue) centred on the IRLS swath. The along-track movement of the satellite and successive acquisitions provide another dimension to the observations.

The IRLS covers a swath of $\sim 360\text{ km}$ in the across-track direction and 48 km in the vertical direction. It achieves a vertical resolution better than 900 m in the lower part of the atmosphere by sampling at $600\text{--}800\text{ m}$. The vertical sampling in the upper part of the atmosphere varies between 800 m and 1.6 km (Table 5.2).

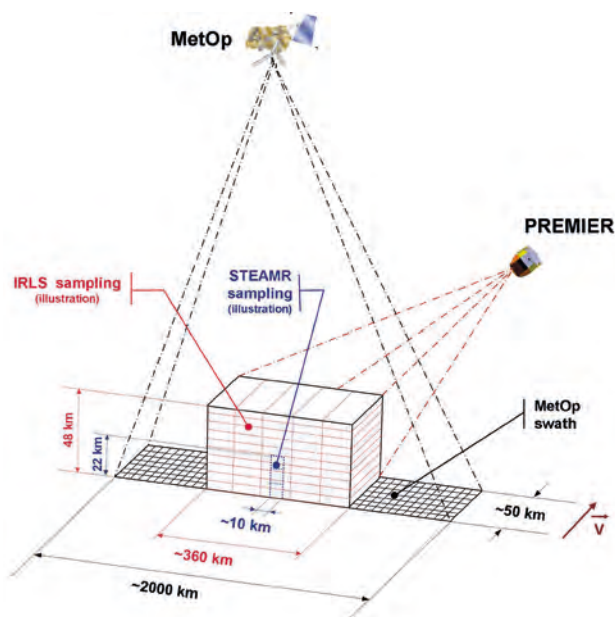


Figure 5.8. PREMIER observation principle.

The two operational modes provide high (CM) and medium (DM) spectral resolution. The required radiometric performance is met thanks to a larger across-track spatial sampling in CM than in DM. Spatial samples at the size needed are generated from the addition of elementary sub-samples of 16 km each.

Several along-track interferogram acquisitions are added to generate an elementary along-track sample acquisition of 50 km in length in both CM and DM.

The acquisition of spectra at the elementary spatial sub-sampling has two main advantages: it minimises the instrument self-apodisation so that no spectral resampling is required and enables a cloud-imaging function to discriminate cloud-contaminated (including thin clouds) sub-samples. This is achieved by a spectral analysis on the ground of the delivered sub-sample spectra with a dedicated algorithm that identifies altitude dependant signal anomalies owing to the presence of clouds. In this way, elementary cloud free sub-samples can be binned to create cloud-free samples at the target spatial sampling in CM and DM (see also Fig. 5.11).

The provision of spectra with a sub-sample size of 16 km facilitates the processing, since the self-apodisation function is weak enough so that no spectral resampling is required. Further processing on ground of the along-track change of the interferogram DC-level allows the identification of along-track variations of the signal generated by cloud presence with the subsequent possibility to flag the anomaly.

The STEAMR instrument provides spatially resolved (vertically 1.5–2 km and horizontally 50 km in the along-track direction) information on the atmospheric constituents by means of observations in the 320–360 GHz range. The STEAMR measurement concept is based on multibeam limb sounding in the orbital plane using Schottky-diode heterodyne receivers. The instrument limb view follows a staring concept, observing simultaneously an altitude range of 22 km with 14 beams spaced vertically: every 1.5 km in the lowest 12 km and every 2 km in the highest 10 km.

The general observation principles have been demonstrated by precursor airborne instruments to the IRLS and STEAMR. GLORIA is an imaging FTIR spectrometer with configuration similar to IRLS. It features a single band with a slightly reduced spectral range, but with higher spectral resolution. MARSCHALS, is a mm-wave limb-sounder that measures single side-band spectra in the STEAMR frequency range but with coarser resolution (200 MHz). The instruments flew together for the first time in a recent campaign on the high-flying Geophysica aircraft. A picture of the instruments accommodated in the Geophysica is shown in Fig. 5.9.



Figure 5.9. The GLORIA imaging FTS and the MARSCHALS millimetre-wave radiometer as accommodated inside the Geophysica aircraft.

5.4.3.3 IRLS

5.4.3.3.1 IRLS overview

The infrared limb sounder, IRSL, is an imaging FTS with heritage from previous instruments such as MIPAS, IASI and GOSAT. One of the main advances of the IRLS with respect to similar currently-operating limb sounders, such as MIPAS, is the extended FOV. MIPAS performs measurements with a single pixel at a vertical resolution of 3 km. In a single acquisition, the IRLS will observe a 2D-field providing information equivalent to ~1800 MIPAS acquisitions at about four times higher vertical-resolution (see also Fig. 4.4). This creates a very large volume of data, which must be pre-processed on board. Decimation of the interferograms allows the amount of data to be downlinked to be reduced significantly (factor ~10). The amount of spatial and spectral samples drives the detector readout frequency, the number of video acquisition chains and finally the data volume.

The IRLS provides two mutually exclusive measurement modes by making use of a single interferometer operated at two different strokes, and by adapting the acquisition times accordingly. The stroke requirements are well adapted to operate the interferometer in a two-sided interferogram acquisition mode. The core of the instrument is the interferometer mechanism, which benefits in both concepts of technology heritage from IASI and GOSAT.

The spectrum is acquired by scanning the optical path difference of the two split beams and by recording the interferogram generated by the two-beam interference. The scan is performed during an observation time in the order of one to several seconds. This means that the spectrum, which is derived on the ground by Fourier transformation of the interferogram, is an average of the scene radiance acquired during the interferogram dwell time.

Figure 5.10 shows the functional block diagram of the IRLS. The radiation emitted by the atmosphere is collected at the entrance of the instrument, which is protected by a baffle or by blades to minimise the collection of unwanted radiation from Earth. The pointing mirror reflects this limb signal towards the anamorphic front optics, which provides a uniform and almost rectangular beam (Concept A) or circular beam (Concept B) at the entrance of the interferometer. The beam is then split by the beam splitter and reflected by the corner cubes to generate interference between the reflected beams. The

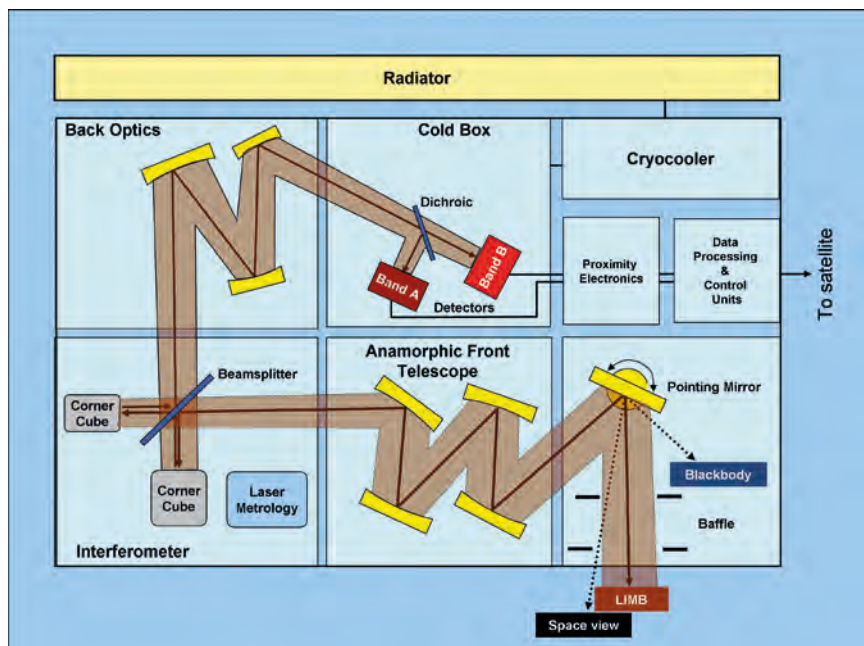


Figure 5.10. Block diagram of the IRLS with the individual sub-units arranged along the beam path.

light is then imaged by a back optics onto the focal plane inside the cryostat, cooled by active cryocoolers. Before the light reaches the detectors it is split into two bands by a dichroic beam splitter. The cryostat may contain further optical elements or even a complete re-imaging optics. The interference signal is recorded by two-dimensional detectors, one per band. The detectors instantaneously gather the full image of the limb scene for each interferogram scan position. The acquisition and the processing of the interferograms are performed by the data processing system.

Table 5.2. IRLS main Level-1b requirements.

Parameter	Requirement	
Operational mode	Chemistry Mode (CM)	Dynamics Mode (DM)
Instrument type	Imaging FTS	
Geometric Requirements		
Vertical coverage	48 km (4–52 km in polar regions, 8–56 km in tropical regions)	
Horizontal coverage	360 km [240 km]	
Vertical sampling distance	0.6 km [0.8 km] (lower half of the altitude range) 1.2 km (0.8 km DM band A) [1.6 km] (upper half of altitude range)	
Horizontal sampling distance	72–96 km	24–32 km
Horizontal sub-sampling distance (cloud imaging purpose)	12–16 km (can be relaxed by factor of 2 in upper half of altitude range)	
Along-track sampling distance	50 km [100 km]	50 km
FWHM of vertical PSF	700 m [900 m]	
Vertical width increase of FWHM	<5% [<10%] over 240 km of the swath	
Spatial cross talk (vertical)	1st neighbour <5 [15]%, 2nd neighbour <2 [7.5]%, 3rd neighbour <1 [4]%, 4th neighbour <1%, 5th neighbour <0.5%	
Spectral Requirements		
Wavenumber range	710 cm ⁻¹ [730 cm ⁻¹] to 1650 cm ⁻¹	
Band gap	Up to 90 cm ⁻¹ in the region 980–1100 cm ⁻¹	
Spectral resolution	0.25 cm ⁻¹ [0.27 cm ⁻¹]	1.58 cm ⁻¹ [1.73 cm ⁻¹]
Spectral accuracy	0.008 cm ⁻¹	0.01 cm ⁻¹
ILS characterisation	1% of width 1% of ILS maximum value	
Radiometric Requirements		
Noise Equivalent Delta Radiance (NEdL) @ Zero input Band A	2 [4.0–6.5] nW/(cm ² sr cm ⁻¹)	0.8 [1.5–2.5] nW/(cm ² sr cm ⁻¹)
NEdL @ Zero input Band B	1.5–2.0 [4.0–6.5] nW/(cm ² sr cm ⁻¹)	0.4–0.8 [1.5–2.5] nW/(cm ² sr cm ⁻¹)
Radiometric accuracy	<NEDL ² + (radiometric offset) ² + (0.015·measured radiance) ²	
Spectrally varying radiometric error (ghost)	<4 nW/(cm ² sr cm ⁻¹)	<1.5 nW/(cm ² sr cm ⁻¹)
Radiometric scaling error	0.15% [0.25%] (spatially and/or spectrally uncorrelated) 1% (spatially and spectrally correlated)	
Radiance range	133–240K blackbody radiance equivalent	143–240K blackbody radiance equivalent
Geo-location, LOS stability and spatial co-registration		
Vertical knowledge	750 m for a wavenumber range up to 710 cm ⁻¹	
Vertical co-registration	75 m [150 m] intraband 250 m interband	
Vertical co-registration knowledge	25 m [50 m] intraband 100 m interband	
Vertical geolocation stability	60 m [100 m] (within interferogram acquisition time) 75 m [150 m] (within horizontal sampling time)	

5.4.3.3.2 Observational requirements

The key IRLS observational requirements are summarised in Table 5.2. Threshold requirements are in brackets.

The following sections summarise the impact of the main Level-1b requirements on the instrument design.

Geometric requirements

PREMIER requires a maximum across-track view (swath) of ~360 km. The swath and the spatial sampling of the observed field drive the amount of data generated.

The vertical coverage at any point of the swath is 48 km from a reference minimum altitude tangent point that varies with latitude from 4 km at the poles to 8 km at the equator. To fulfil both requirements, the satellite's attitude will follow a latitude-dependent control law and, in addition, the detector array will be oversized to compensate for the curvature of Earth at the edge of the swath, which increases slightly the coverage at the centre (~52 km).

Since the vertical coverage is much smaller than the horizontal one, it is advisable to adapt the magnification of the front-optics in both directions. This measure rectifies the beam, allowing the use of conventional optics (corner cubes, beam-splitter and detector formats) and simplifying both the interferometer and detector configuration. The vertical resolution (better than 900 m) drives the vertical extent of the aperture, which is much larger than the horizontal one where the required sampling is 16 km. The swath width and the vertical resolution define the complexity of the optics. This is because the swath width determines the range of field angles that must be handled by the instrument, and the vertical resolution drives the maximum aperture extension and the magnification range of the optics.

The IRLS concepts must comply with the required spatial sampling and resolution in both DM and CM (Table 5.2). The higher vertical-heterogeneity of the atmospheric constituent in the lower half of the altitude range compared to the upper one leads to a different vertical resolution and sampling in the lower and upper halves of the FOV in CM. The broadening of the instantaneous FOV at the edge of the swath owing to Earth's curvature also affects the vertical resolution, that being the increase of the vertical resolution less than 10% within 120 km from the centre of the swath

The sample configuration is determined by the horizontal or across-track sub-sample size of 16 km or less, which determines the resolution of the cloud-imaging function, the generated data rate and the spectral quality of the instrument. With a sub-sampling size of 15 km, for example, a FOV of 360×52 km can be made up of 24 across-track sub-samples × 80 vertical samples, resulting in 1920 sub-samples. The target across-track sampling between 72–96 km in CM and between 24–32 km in DM can be achieved by spatial binning of the sub-samples. A picture of one possible configuration is shown in Fig. 5.11.

Spectral requirements

For an imaging FTS, the spectral resolution defines the Maximum Optical Path Difference (MOPD) and the degree of acceptable self-apodisation, and therefore the required level of pixel granularity. The IRLS optical design is optimised such that the beam divergence variation within the interferometer is very small, which makes the self-apodisation function almost negligible. Given the expected self-apodisation, MOPDs of ~2.5 cm and ~0.4 cm are required to achieve spectral resolutions of 0.27 cm⁻¹ and 1.73 cm⁻¹ in CM and DM, respectively.

The spectral accuracy is also demanding and requires a state-of-the-art thermally-stable interferometer concept, a stable instrument line shape across

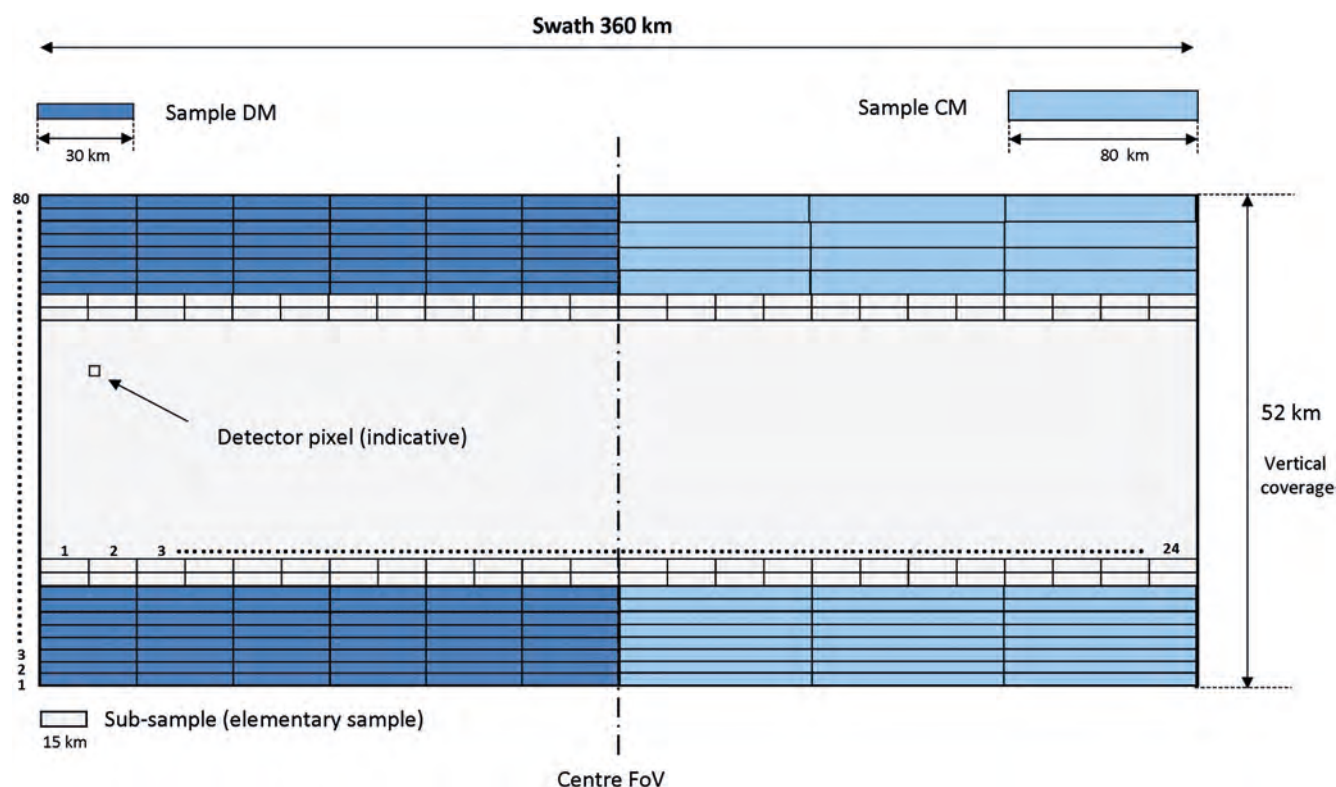


Figure 5.1.1. The sample and sub-sample concept. The CM and DM samples are generated by co-addition of several sub-samples. The left and the right part of the field are identical and have only been split here to show the configuration in DM and CM (exclusive modes). For CM and in band B, two vertical samples may be binned in the upper part of the atmosphere. The numbers 1–80 refer to the vertical sub-sampling numbering and the numbers 1–24 refer to the horizontal sub-sampling numbering.

the FOV, high optical-axis stability and accurate measurement of the variation in Optical Path Difference (OPD) during scanning.

The spectral range from 710–1650 cm^{-1} is covered by two spectral bands (Bands A and B) with an intermediate gap of 90 cm^{-1} in the spectral range between 980–1100 cm^{-1} . The cross-over of the dichroic beam splitter requires this spectral gap to make the separation in two bands. The splitting is beneficial for the radiometric performance, because it limits the spectral range of each band and thereby relaxes the requirements on key detector/focal plane characteristics (e.g. detector coating, detector charge handling capacity, signal band width, straylight separation). On the other hand, it requires a careful design to meet the interband co-registration requirement.

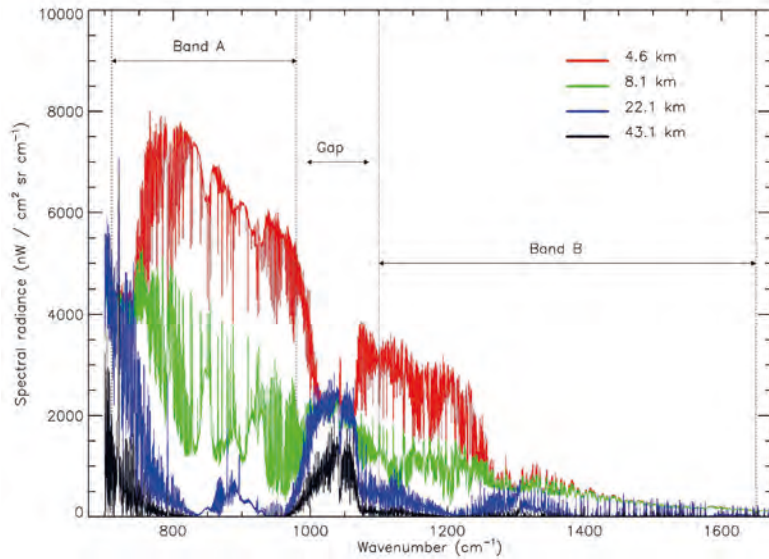
Radiometric requirements

The dynamic range to be covered by the IRLS must be compatible with the radiance emitted by the atmosphere in the relevant spectral bands within the observed altitude range. Representative atmospheric radiance spectra are shown in Fig. 5.12.

The scene radiance levels can vary by two orders of magnitude within the observed spectra. The dynamic and spectral ranges are directly linked since the FTS is exposed at Zero Path Difference (ZPD) to the radiation present within the full spectral range. The larger the dynamic and spectral ranges, the larger the charge handling capacity and the detection noise of the detector. The effective dynamic range requires detectors with large charge handling capacity operating at high readout frequencies.

The absolute radiometric accuracy is defined as the quadratic sum of the actual Noise Equivalent delta Radiance (NE Δ L), the radiometric offset error and 1.5% of the measured radiance. This requirement limits the total gain error

Figure 5.12. Atmospheric radiance spectra at four altitudes as expected to be observed by the IRLS. The total radiance of the observed spectra corresponds roughly to the radiance of a blackbody at temperatures in the range between 133K (high altitude) and 240K (low altitude). The spectra are calculated by using a one-dimensional radiative transfer (forward) model, RFM Version 4.25.



to 1.5% at the top of the dynamic range (low altitudes). For the low radiance observations (deep space or high altitudes), the absolute radiometric accuracy is determined by the offset and NEdL characteristics.

LOS pointing stability

Instability in the pointing of the instrument’s vertical LOS generates pseudo noise and a broadening of the FOV. Pseudo noise is understood in this context as a noise equivalent disturbance of the interferogram signal, and finally of the spectrum, which is generated by the modulation of the signal in the case of observing non-uniform scenes. A random oscillation of the LOS generates random noise that can be of the same magnitude as the instrument noise. Depending on their frequency, periodic oscillations will generate either line broadening or ghost lines.

A vertical LOS stability of 60–100 m within one interferogram dwell time, which is of the order of 1–7.5 s, is required to minimise the pseudo noise. The instrument is susceptible to pseudo-noise in a specific frequency range. As a result, microvibration and any other perturbations at frequencies between 0.2–500 cycles per interferogram in CM and between 0.2–2000 cycles per interferogram in DM are considered as critical and must be minimised by design.

A vertical LOS stability of 75–150 m within one horizontal along-track sample acquisition, which is of the order of 7.5 s, limits the FOV broadening. The requirement is not restricted to any frequency range, although the FOV broadening is mostly sensitive to low frequencies.

5.4.3.3 Instrument subsystems

This section describes the main subsystems of the IRLS.

Mechanical and thermal architecture

The instrument mechanical and thermal architectures are outlined in Fig. 5.13 for Concept A and in Fig. 5.14 for Concept B. The accommodation is driven by the high geometrical and thermal stability performance required to meet the pointing knowledge requirement (Tables 5.2 and 5.3). For both concepts, the instrument includes:

- A very stable optical bench to minimise thermoelastic distortions. It supports all the optical elements, the pointing mechanism, the interferometer and corner cubes and the cryostat. The optical bench is isostatically mounted on

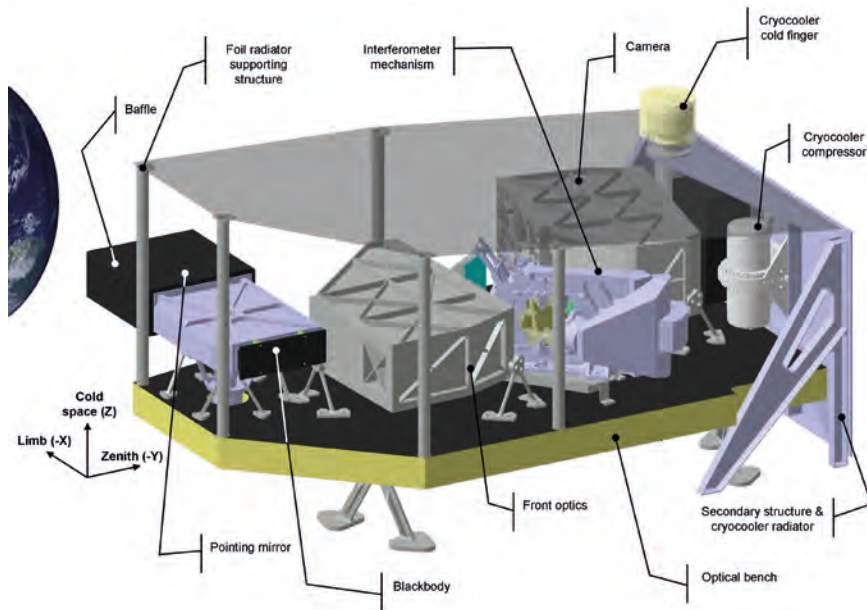


Figure 5.13. General overview of IRLS in Concept A showing all the sub-units.

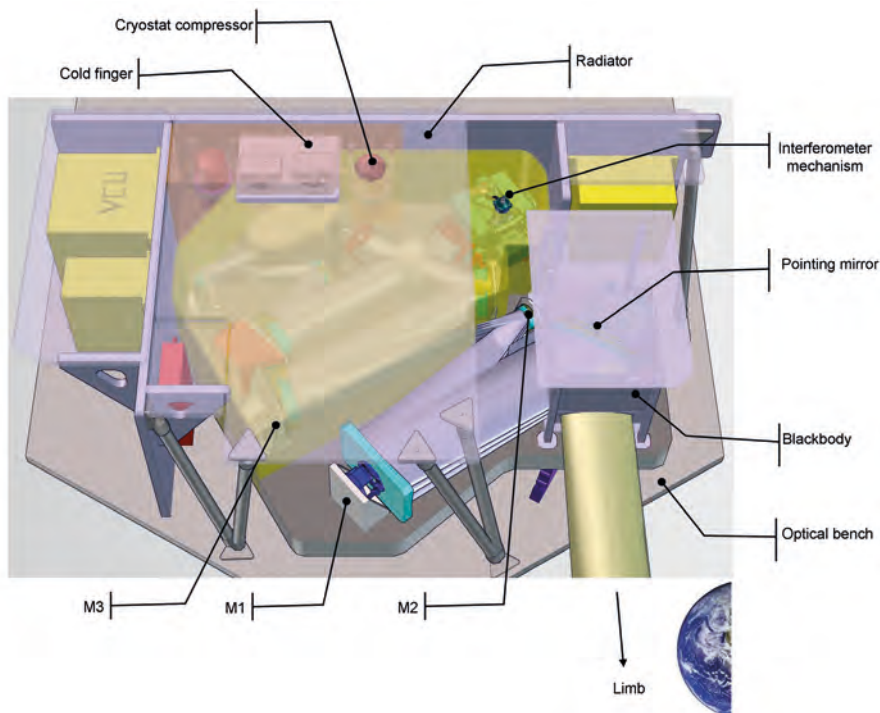


Figure 5.14. General overview of IRLS in Concept B. The picture indicates the mirrors (M1–M3) in the front optics. The instrument has several radiators, which all face into cold space, for the electronics, the optics and for the cold entrance compartment containing the pointing mirror.

the PIP in Concept A and on the top structure panel of the satellite in Concept B. The optical bench is kept at $\sim 240\text{K}$ for Concept A and at $\sim 293\text{K}$ for Concept B.

- An entry baffle minimising illumination of the instrument from the Sun and Earth.
- A blackbody accommodated close to the entrance
- A secondary structure made of aluminium panels supporting the cryocooler, which prevents the propagation of microvibrations to the optical bench. This secondary structure also supports parts of the electronics, which are covered with MLI.

- A top cover of the instrument that serves as a radiator.

The optical bench is made of aluminium for Concept A and of an aluminium honeycomb core with Carbon Fibre Reinforced Plastic (CFRP) skins for Concept B, which is a design inherited from IASI. The dimensions (height×width×depth) of Concept A is 0.6×1.15×0.8 m and 0.55×1.65×1.0 m for Concept B. The eigen-frequencies of the structures (first mode 35 Hz laterally and 75 Hz axially) are well above the requirements for both concepts.

The thermal control relies on passive cooling and on heating by thermistor lines, with the exception of the Focal Plane Assembly (FPA), where a cryocooler is needed to keep the temperature of the detectors in the cryostat at ~55K. The cryocooler has a dedicated radiator to evacuate several hundred mW of thermal power to cold space. In Concept A, almost all of the electronics are accommodated in the service module, whereas in Concept B the signal processing, the interferometer and the cryocooler control electronics are attached to a secondary structure of the payload module. The electronic modules are thermally isolated with MLI.

The instrument is operated at a temperature of about 240K (Concept A) or at ‘room temperature’, i.e. 293K (Concept B). A cold instrument generates little background radiation but requires a more complex assembly, integration and testing. Concept A is based on an athermal aluminium design to prevent deformation when cooled from room temperature to ~240K. The thermal control is based on an MLI tent with foil radiators supported by a tubular structure, which guarantees it will survive the rigours of launch. A second radiator dedicated to the cryocooler is accommodated on the zenith side. Concept B is kept at 293K with the exception of the entrance cavity so that the blackbody can be operated at a temperature of ~240K. A segmented radiator on top of the secondary structure is connected by heat pipes to the sub-units to enable the thermal control of the various subsystems, including the cryocooler. Both thermal control concepts benefit from extensive flight heritage.

Entrance aperture and pointing mirror

The instrument entrance aperture is not symmetrical since the required spatial resolution is more stringent in the vertical direction. A vertical aperture of at least 150 mm is needed. The horizontal aperture, between 25–40 mm, is not critical and determines the aperture area required to achieve sufficient signal throughput.

The pointing mirror is used to enable pointing to:

- the limb in normal acquisition mode
- deep space, for radiometric calibration including offset determination
- a blackbody, for radiometric calibration

These pointing directions can be realised either with a one-axis or a two-axes gimbal pointing mirror.

The geolocation knowledge and the minimisation of LOS jitters require a highly repeatable, accurate (to few arcseconds) and stable mirror pointing.

The blackbody is accommodated in the entrance cavity and is maintained at a constant temperature of 240K to provide a known reference radiance.

Front optics

The front optics are designed with an anisotropic magnification such that the rectangular field is transferred into an almost square (Concept A) or circular shape (Concept B) at the interferometer entrance. The anamorphic optical design reduces the beam divergence, distributing it almost equally within the interferometer. This allows the use of existing interferometer mechanisms and maintaining corner cube configurations and sizes. IASI, for example, uses corner cubes compatible with beams with a diameter of 80 mm, which is the

selected size for the IRLS Concept B. GOSAT accommodates 70 mm beams, which is slightly larger than for the IRLS configuration in Concept A.

Interferometer mechanism

Double pendulum (as GOSAT, Concept A) and linear (as IASI, Concept B) interferometer mechanisms have been identified as suitable candidates, because both can provide the required stroke and beam diameter. A double pendulum enables, using a rotational mechanism, the displacement of both corner cubes instead of only one as in the linear mechanism. The corner cubes move in opposite direction, so that the resulting path difference corresponds to two times the effective displacement. Both interferometer mechanisms are of similar complexity and need adaptation to fulfil the performance requirements, in particular for corner cube speed, trajectory and the related control accuracy. A single-point laser metrology system, which is used to determine the OPD, uses a sine and cosine interference signal to avoid fringe losses. It is based on a laser source providing a highly stable signal in the near-infrared spectral domain. Fibre optics collimate the laser beam and send it through the interferometer. The interferometer (corner cube) movement generates interference, which is measured by two photodiodes, and is then used to derive the actual OPD. Depending on the concept, a three-point measurement system can be considered to reduce the effect of lateral jitter that causes ghost lines in the generated spectra.

The stroke of the interferometer varies with the operating mode and hence the dwell time of the interferogram. In CM, the interferometer operates with a stroke of 2.5 cm leading to a dwell time of about 7.5 s for 50 km along-track sampling. In DM, a stroke of 0.4 cm leads to a dwell time 6.25 times shorter than in CM, assuming that the interferometer velocity remains constant. Since the along-track sample acquisition may be composed of several interferograms, the dwell time can be reduced if the interferometer operates at higher speed. The IRLS may then acquire and co-add several interferograms within one along-track acquisition period. This option leaves some freedom for the choice of the instrument configuration and the operational concept, since either constant or variable interferometer velocities can be selected.

The two interferometer mechanisms identified as baseline for the two concepts are shown in Figs. 5.15 and 5.16.

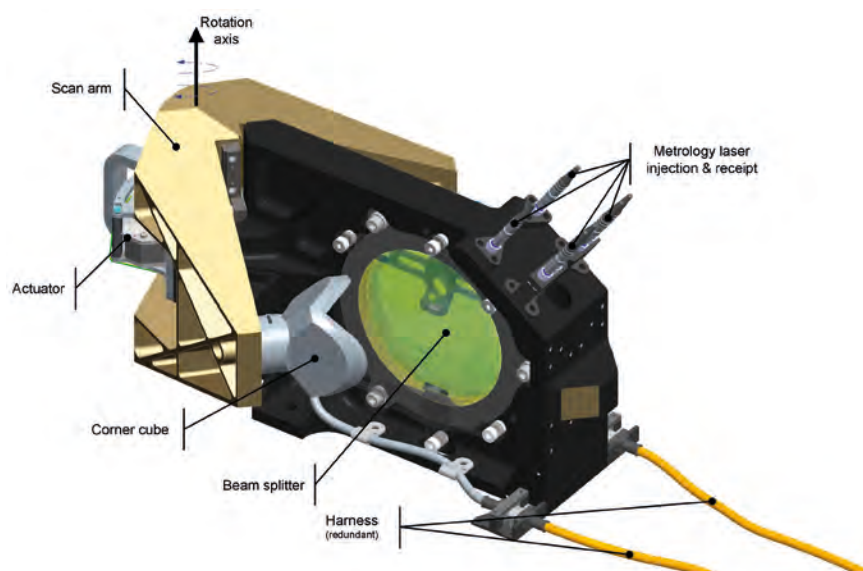


Figure 5.15. IRLS interferometer mechanism of Concept A, including the two corner cubes, the beam splitter and the interferometer mechanism.

Figure 5.16. IRLS interferometer mechanism of Concept B (left). Details of the interferometer mechanism (right).

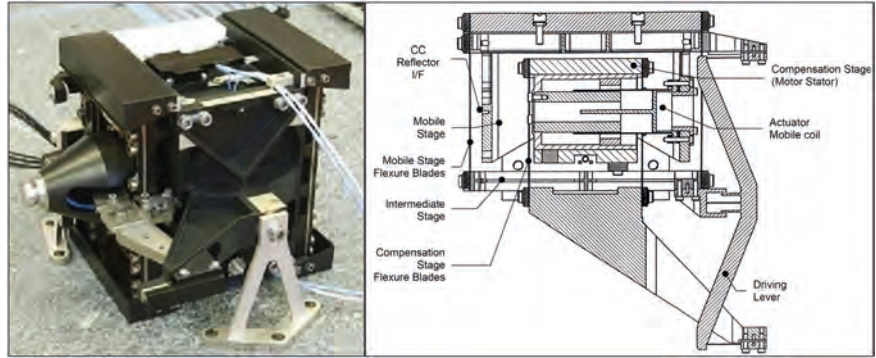
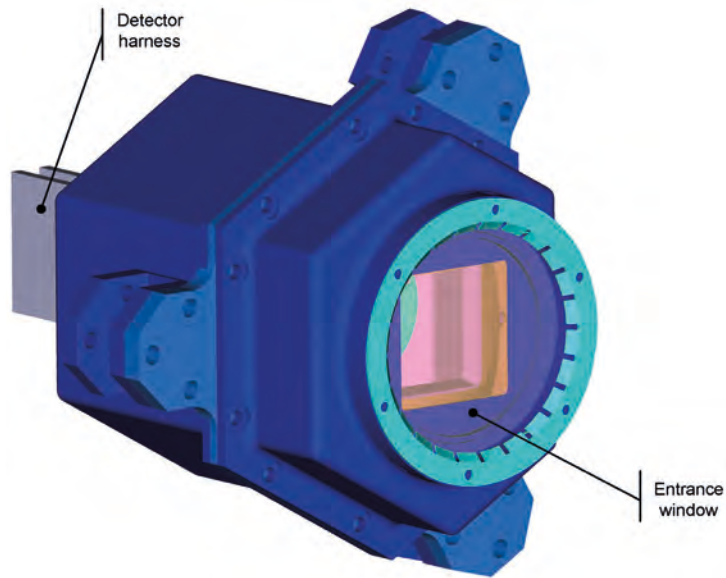


Figure 5.17. Cryostat design for Concept A, showing the entrance window and housing.



Back optics and cryostat

The back optics consist of a set of mirrors imaging the object into or onto the cryostat. The optics combination plus some compensation elements in the cryostat generate an image of quality close to the diffraction limit, which means that IRLS has good imaging performance and relatively low spatial cross-talk. The back optics generate an image matched with typical squared IR array detector formats. The cryostat subsystem provides the thermal isolation of the detector compartment, which must be kept at ~55K. Optical elements inside the cryostat, such as the dichroic beam splitter, are thermally isolated from the cryostat housing. The mounting structure and the wiring of the detectors are designed to minimise the heat load of the cryocooler. An example of the cryostat configuration for Concept A is given in Fig. 5.17.

Detectors

Suitable detectors are mercury cadmium telluride (MCT) complementary metal oxide semiconductor (CMOS) detectors similar to those currently under development for the MTG programme. The typical pixel pitch is 30 µm. The IRLS detector array format is significantly smaller than for MTG. Also the ‘macro-pixel’ configuration and the charge handling capacities are different.

A macro-pixel is a subset of detector pixels that has a combined integration capacity and that is readout as a single entity. For the IRLS, the macro-pixel is the set of detector pixels required to form the elementary spatial sub-sample (compare also Fig. 5.11). As a consequence, detector pixel defects have limited

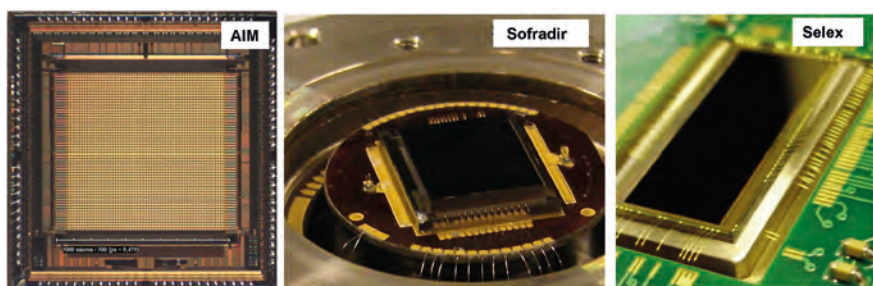


Figure 5.18. MTG IRS detectors: Detector ROIC from AIM (DE) is shown on the left. Detector test vehicle from Sofradir (FR) is shown in the middle and detector test vehicle from Selex (IT) is on the right.

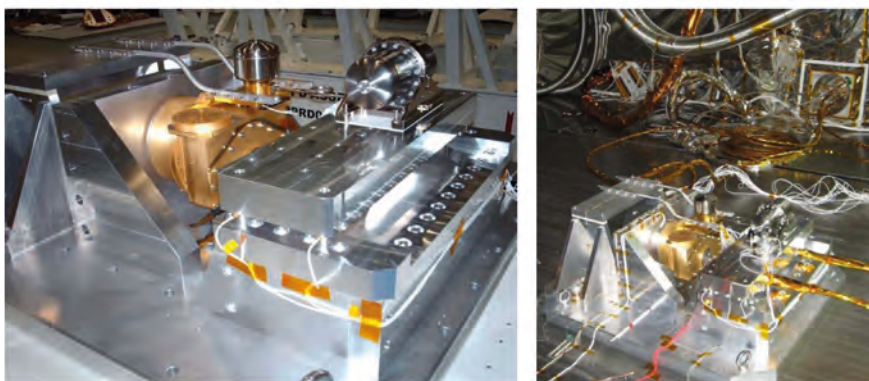


Figure 5.19. Large Pulse Tube Cooler EQM S/N002 integrated on a cryostat mock-up (left) and in a vacuum chamber (right) produced during the MTG pre-development programme.

impact on the performance of a complete sample and allow to maintain good data quality. The signal from a set of about 20 to 30 pixels is then binned and the charge is collected by a single charge capacitor for each sub-sample. Each single detector pixel can be switched on and off, as required to perform health checks, to remove malfunctioning pixels and to implement special operating modes of IRLS.

Static gain switching, in which the constant interferogram contribution is subtracted, and/or dynamic gain switching, in which only the white light peak is measured at a different gain setting, can be applied in order to reduce the charge handling capacity and therefore the detector noise.

In summary, the detectors will have to be customised by changing the detector mask and by redesigning the detector ROIC. Assuming 24 horizontal sub-samples and 80 vertical sub-samples, the IRLS requires 1920 sub-samples. If each sub-sample is made up of 30 detector pixels, then in total 57 600 detector pixels are required. As a consequence, the detector array has an area of less than 50 mm², about four times smaller than the MTG detectors. The cut-off wavelengths are 14 μm and 10 μm for Bands A and B, respectively. Both detectors are operated at about 55K in order to limit their dark current contributions (driven by Band A).

Cryocoolers

The detectors' required low temperature can only be achieved by active cooling. Stirling or Pulse Tube are possible cryocooler options, but must be optimised with respect to their operation to minimise power consumption and exported microvibrations. Coolers meeting the IRLS requirements are available from other programmes (e.g. MTG, Sentinel-3); the MTG cooler is considered as baseline. The cryostat accommodation requires careful thermal interfacing of the detector with the instrument structure to minimise thermal conductance. Although the instrument concepts are potentially compatible with a redundant cryocooler configuration, the current baseline is to use a single cooler, which has been found to be reliable for a mission lifetime of four years.

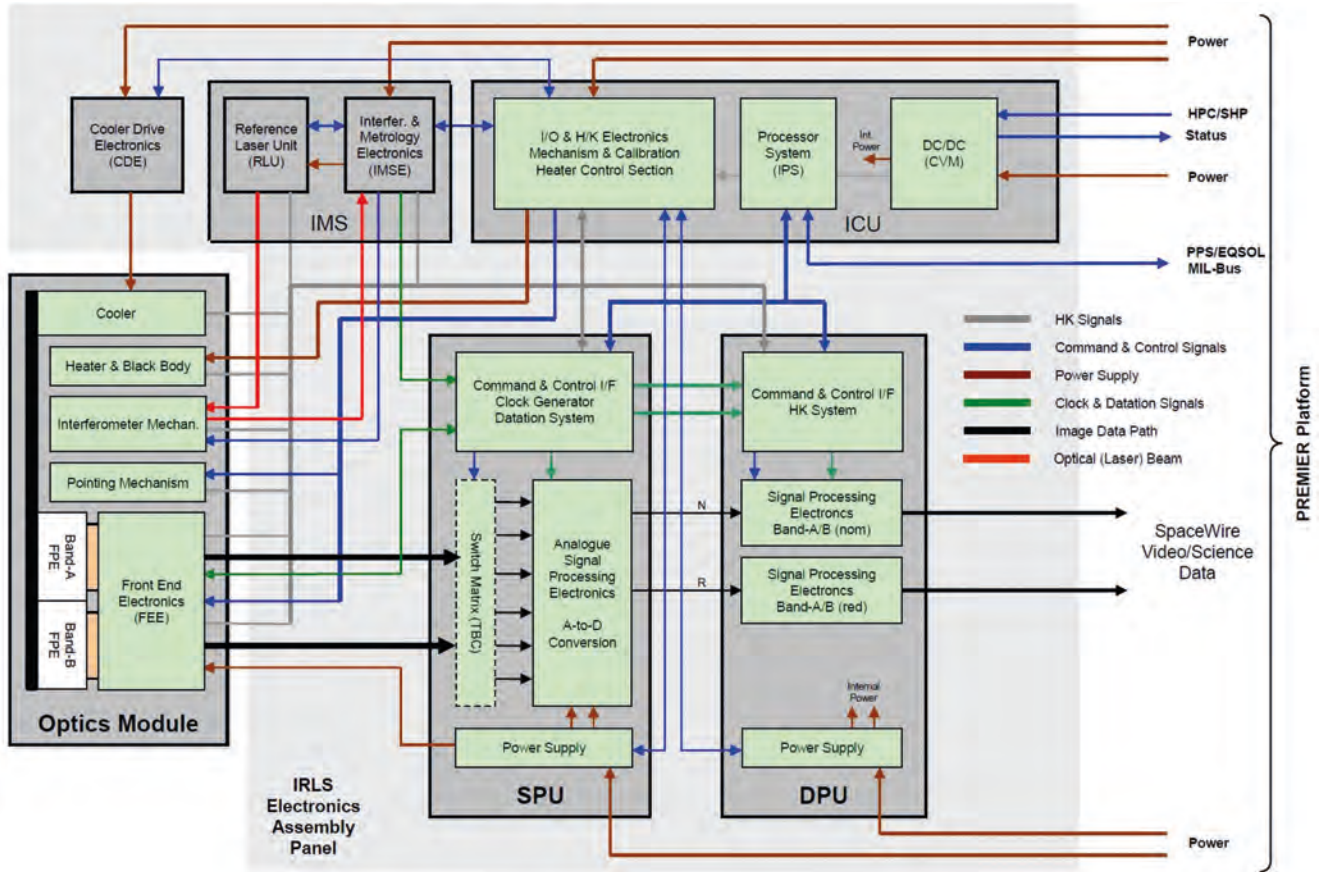


Figure 5.20. The electronic sub-units of the IRLS as derived within Concept A, SPU and DPU part of the service module.

Instrument electronics

The electronic architecture for Concept A is shown in Fig. 5.20. The figure also shows the distribution of the functionalities within the optical and the service module. The architecture of Concept B is similar except that the Signal Processing Unit (SPU) is located in the optical module as already mentioned. The detectors signals from both bands are distributed by the Focal Plane Electronics (FPE), which contain mainly the detector Read Out Integrated Circuits (ROICs). The signal is further pre-amplified by Front End Electronics (FEE) before it is sent to the SPU, where the analogue to digital conversion takes place. The IRLS performance relies on a 16-bit Analogue-to-Digital Converter (ADC) with low noise characteristics, operated at a sampling frequency of 2–4 MHz. There are multiple solutions that are compatible with the required performance of the video signal processing. The Data Processing Unit (DPU) performs the onboard processing. The Instrument Management System (IMS) controls the metrology system. The Instrument Control Unit (ICU) distributes the command signals and the power to the electrical sub-units and is in charge of the instrument thermal control. The IMS and the ICU are implemented in separate units to enable independent development and testing.

Onboard processing chain

The IMS takes care of the time sequences (synchronisation) and execution of all processing tasks. The interferometer metrology system and the two detectors' readouts need to be clocked synchronously and read out at a frequency of 4 kHz. The analogue signals are then digitised and transferred to a buffer for further processing in the DPU. The pixel readout rate is about 8 MHz, which requires using at least two output ports for each detector chain. The proximity electronics needs to be located close to the detectors to shorten the signal

lines, which are sensitive to noise from the environment. Other control and processing electronics can be physically placed in the service module. The exact split between the service and the payload module can be either before or after the video processing. In Concept A, the SPU is located in the service module, whereas in Concept B the signal processing is part of the payload module.

Onboard data processing.

The large data flow (~200 Mbit/s) generated at the output of the detector chains is transferred to the DPU, where the following processing steps are performed:

- Anomalies Detection: Cosmic rays or electrical anomalies can cause strong signal changes, which generate spikes within the interferogram. These spikes can either cause saturation of the signal or can lead to unusual slopes within the interferogram. Detection is possible by either linear or differential threshold limitation. A correction of the spikes is possible by interpolation or statistical fitting of the signal in between unaffected interferogram points.
- Non-linearity correction and bad pixel identification: Non-linearity is caused by the detector and by the proximity electronics. It is expected that the non-linearity is relatively stable and can be corrected by a look-up table, however future investigations will have to confirm this assumption. If required, a method for inflight non-linearity check and a look-up table for bad pixels will be established. The flagging of bad pixels will make use of algorithms based e.g. on comparing the pixel read-out at the white light peak.
- Binning of sub-samples: If a vertical binning of the sub-samples is required to restrict the data volume (e.g. upper part of the atmosphere), an offset or slope compensation must be performed to account for the different background and possible optic transmission differences.
- Interferogram resampling: The signal acquisition is based on constant time-sampling. Before the signal is further decimated, it is required to resample the interferogram on a fixed spatial reference grid. Several interpolation schemes are possible (spline, sinc or linear interpolation).
- Interferogram filtering and decimation: The amount of data can be reduced by applying a finite impulse response filter. This exploits the fact that the bandwidth of the acquired signal is larger than the bandwidth of the scene signal. The reduction factor is proportional to $\sigma_s/2(\sigma_2-\sigma_1)$ with σ_s being the wavenumber corresponding to the sampling frequency, σ_2 the maximum wavenumber (1650 cm^{-1}) and σ_1 the lowest wavenumber (710 cm^{-1}) of the scene signal. Since the signal is usually oversampled, also to minimise the detector charge handling capacity, the decimation factor is relatively high (~10).
- Data compression: Further reduction of the amount of data is possible since the dynamic range of the atmosphere is large and the signal content low at higher altitudes. Compression can be applied leading to further reduction by a factor of ~1.8.
- Provision of DC level: For cloud detection and discrimination, it is required to provide the DC level of the interferogram. A relatively simple algorithm is expected to be sufficient. The data will be provided with a sufficient number of bits so that the radiometric information content is maintained.

The onboard processing approach has heritage from previous missions (IASI and MIPAS). It is further assumed that fringe loss detection is not required since the metrology is based on a sine and cosine signal acquisition. The application

of all these onboard processes will reduce the onboard data production rate from ~200 Mbit/s to ~28.8 Mbit/s in Concept A and ~18.8 Mbit/s in Concept B. The onboard processing chain generates compressed interferograms for each sub-sample, which are then downlinked for further processing on the ground.

5.4.3.3.4 Instrument on-ground characterisation and in-flight calibration

Spectral and spatial response on-ground characterisation

The spectral and spatial parameters that have to be characterised on the ground are:

- The instrument line shape (ILS)
- The point spread function (PSF)

Both need to be characterised over the complete spectral range and over the complete FOV.

The ILS must be characterised to an accuracy of better than 1% of its maximum. The ILS accuracy depends on the determination of the optical axis, the corner cube trajectory and the PSF knowledge. The characterisation can be performed on the ground using a gas cell and lasers by comparing the instrument response to the input spectrum line shape. A similar process is performed in-flight by analysis of atmospheric emission lines and by the use of an ILS model.

The PSF determines the instrument spatial response to the observed target. Since the signal level varies drastically along the altitude range, a good knowledge of the PSF shape, up to ~100 km from its central peak, is required. The knowledge of the PSF shape has to be such that the integral outside ± 5 Full Width at Half Maximum (FWHM) is known with an accuracy better than 0.1% for errors uncorrelated between spatial samples. The shape of the PSF depends on the diffraction pattern, the detector convolution and the in-field/far-field scattering. To minimise scattering, an instrument providing a high level of cleanliness throughout the mission lifetime is required. The PSF shape must be characterised on-ground (e.g. characterising the response to a point source/knife edge measurement, supported by analytical models) because the large FOV prevents an in-flight characterisation to the required accuracy.

Spectral calibration

The spectral calibration consists of the characterisation of the instrument line shape, which depends on the knowledge of the:

- trajectory of the corner cube
- shape of the PSF
- shift of the optical axis

The interferometer metrology system is used to determine the position and trajectory of the corner cube, whereas the PSF shape is known by pre-launch on-ground characterisation.

The shift of the optical axis is determined by exploiting the imaging properties of the FTS through the analysis of the distribution of the spectral positions of one or several atmospheric emission lines (e.g. CO₂ line at 951.2 cm⁻¹ as shown in the left of Fig. 5.21) in every sub-sample across the observed field. The shift of the optical axis is retrieved by making a fit to the distribution of the line positions within the field (see Fig. 5.21 left).

The determination of the shift of the optical axis is performed using a statistically representative set of five consecutive observations in CM because of the higher spectral resolution of this operation mode compared to DM. Successful spectral calibration requires a relative spectral stability ($\Delta\nu/\nu$) better than 2.3×10^{-7} during the calibration sequence, which is achieved with a

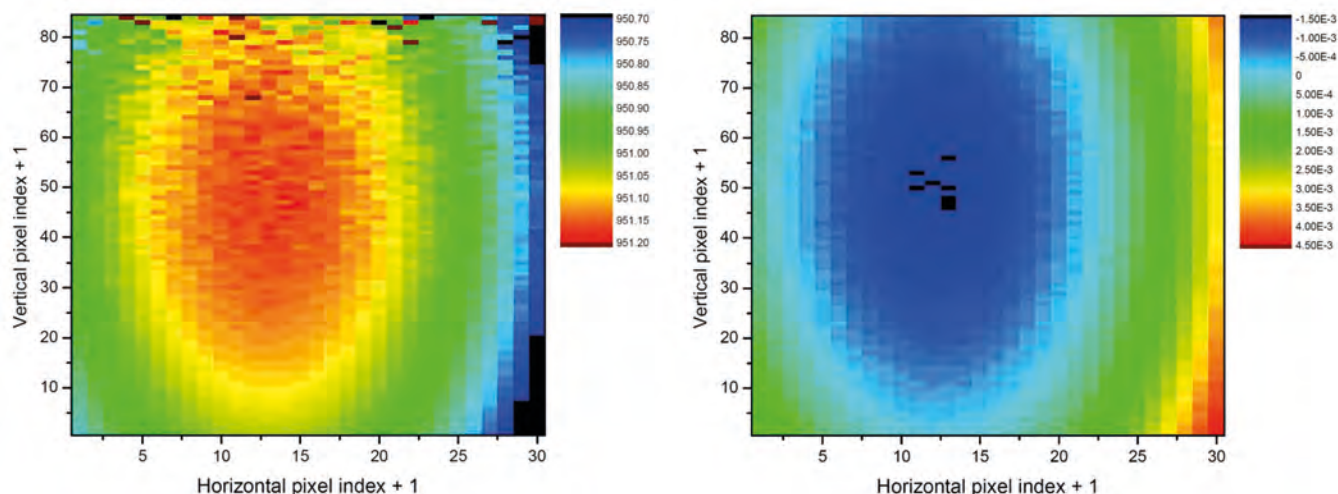


Figure 5.21. Result of a fit to the spectral positions of the CO₂ line at 951.2 cm⁻¹ (left). Residual error after correction of the shift of the optical axis as derived from the fit to the distribution shown on the left (right).

stable focal plane together with a high stability of the laser wavelength of the metrology system.

The total residual error after spectral calibration (e.g. corner cube trajectory, the PSF and the shift of the optical axis) is $\sim 5 \times 10^{-6}$ and meets the spectral accuracy requirement. Spectral calibration must be performed once per orbit given the expected high spectral stability of the instrument.

The spectral calibration performed in CM is also applicable to the DM. If the operation of the instrument in DM were longer than the interval between successive calibrations, the instrument should switch to CM, perform the spectral calibration sequence and change back to DM.

Radiometric calibration

The radiometric calibration consists of the determination of the radiometric offset and gain errors, both required to establish the relationship of the instrument radiometric response to the signal.

The main contributor to the radiometric offset error is the instrument background emission generated by variations of its internal temperature. The offset error is determined by periodic observations of cold space, which is a target providing zero radiometric signal.

The radiometric gain error is determined by observing a radiation source at a reference temperature. The IRLS observes periodically a blackbody at a temperature of 240K, which provides a signal corresponding to the maximum of the dynamic range.

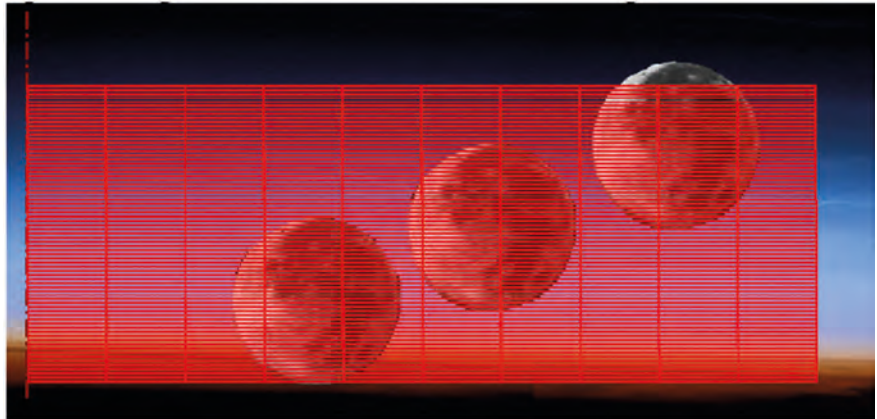
The radiometric offset calibration has to be performed several times per orbit to keep the radiometric offset error below $\sim \text{NEDL}/4$, as required.

LOS calibration

The main contributor to the LOS knowledge is the misalignment produced during launch and thermoelastic distortions in the instrument/optical bench.

An initial onboard altitude knowledge of ~ 750 m (i.e. about one vertical SSD) is required to obtain a vertical knowledge of the LOS better than 200 m by on-ground analysis of the atmospheric pressure and temperature information carried in the retrieved spectra. The requirement of 750 m is achieved by performing an inflight calibration of the LOS using the Moon as pointing target. The calibration is performed when the Moon's path crosses the PREMIER orbital plane by letting the Moon transit across the IRLS FOV (see Fig. 5.22).

Figure 5.22. PREMIER-Moon transition through IRLS FOV (red grid) for LOS calibration.



5.4.3.4 STEAMR

5.4.3.4.1 STEAMR overview

STEAMR is a mm-wave radiometer based on a tomographic multibeam limb-sounding concept taking heritage from the sub-millimetre wave radiometer flying on the Odin satellite.

Figure 5.23 shows the functional block diagram of STEAMR. An offset telescope system receives sub-mm radiation from the atmospheric limb. Additional optical elements (i.e. subreflectors and relay optics) fold the optical path, transform the elliptical antenna beams to circular beams and re-image them on the focal plane. Calibration devices can be viewed by rotating a switch mirror close to the secondary aperture stop (circular image of the primary/secondary).

The selection of the calibration unit is performed by a second rotating mirror, so as to select one of two cold-sky views, two reference loads at different temperatures or a signal source to calibrate the sideband ratio.

STEAMR observes 14 tangent points simultaneously in the altitude range 4–26 km over polar regions and 8–30 km over tropical regions. Fig. 5.24 shows the vertical and horizontal distribution of the 14 tangent points observed. Each of the blue and pink ellipses corresponds to one antenna beam and, as shown

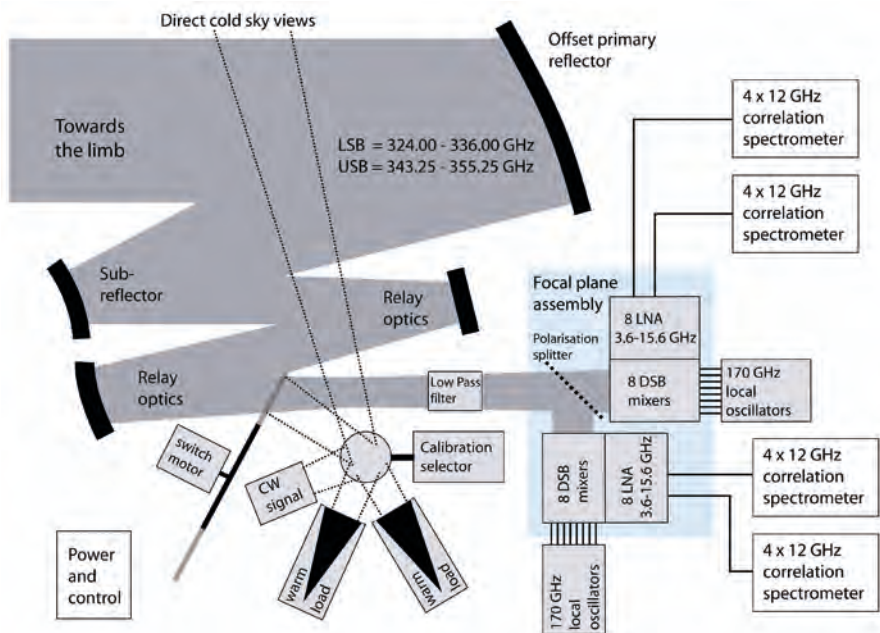


Figure 5.23. STEAMR functional block diagram.

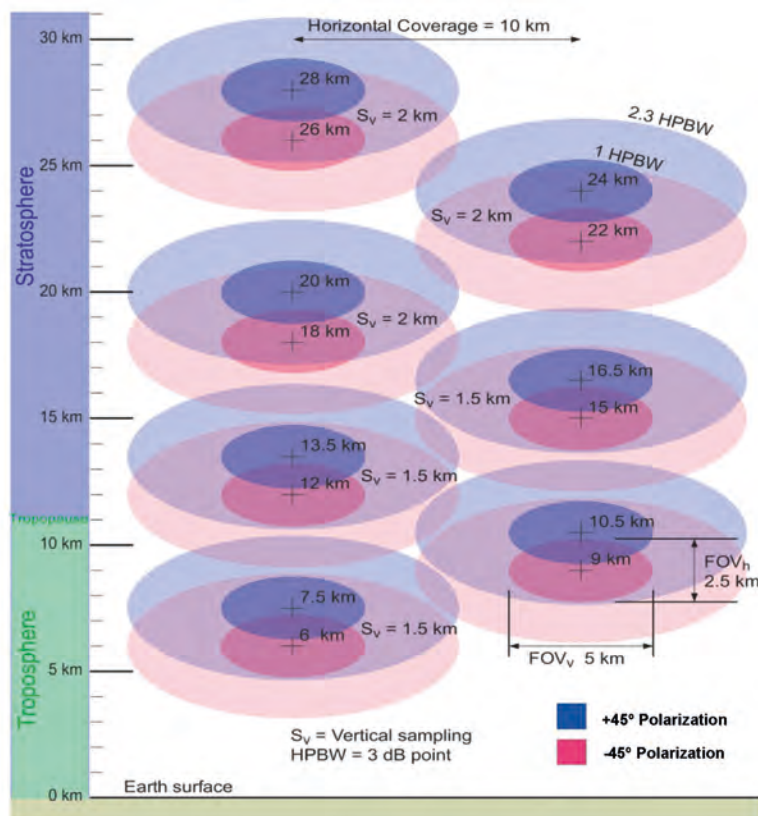


Figure 5.24. STEAMR vertical sampling. Each ellipse (blue and pink) represents one of the 14 simultaneous views of the limb.

in the figure, there is a vertical spatial overlap between the beams. Polarisation splitting is used to accommodate this overlap, with the blue beams polarised at $+45^\circ$ and the pink one at -45° . Individual, but identical, mirror-horn focal assemblies couple the signals into the waveguides of the 14 sub-harmonically pumped Schottky mixers integrated with the Low Noise Amplifier (LNA). The down-converted signals in the 3–16 GHz range are distributed, after amplification, to a set of autocorrelation spectrometers divided into four separate units to simplify the thermal control.

The receivers are grouped into units of four receivers each to simplify the signal distribution, design and test. The overall instrument design is composed of 14 double sideband (DSB) receivers and could, therefore, be augmented to either include two additional beams or to introduce sideband separation receivers for the two beams looking at the lower 10 km of the atmosphere.

5.4.3.4.2 Observational requirements

The key observational requirements of STEAMR at Level-1b are summarised in Table 5.3.

The following sections summarise the impact of the main STEAMR Level-1b requirements on the instrument design.

Geometric

The altitude range and the need for low antenna-beam sidelobe levels imply a telescope type suitable for wide-field imaging. The sidelobe level is also coupled to the level of the edge taper of the reflectors. Both the intermediate optics and the focal plane unit have been optimised to fulfil the 22 km altitude coverage requirement. Figure 5.25 shows the image quality achieved by STEAMR in the 22 km altitude range observed (all the beams fall to very low levels without strong sidelobes showing up).

Table 5.3. STEAMR main Level-1b requirements.

Parameter	Requirement	
Instrument type	mm-wave radiometer	
Number of beams	14 distributed vertically	
Geometric requirements		
Vertical coverage	22 km	
Vertical sampling	≤1.5 km lowest 12 km and ≤2 km highest 10 km	
Along-track sampling	≤50 km	
Antenna requirements		
Half-power beamwidth (FOV FWHM)	2 km [3 km]	
Knowledge of the antenna radiation pattern (ACAP)	Main beam ≤-30 dB [≤-26dB]	Side lobes ≤-35 dB
Sideband response knowledge	<35 dB [30dB]	
Receiver relative vertical position knowledge	10 m [50 m]	
Polarisation	±45° from the local vertical with ±5° accuracy	
Spectral requirements		
Spectral range	324.00–336.00 GHz (LSB), 343.25–355.25 GHz (USB)	
Spectral resolution	10 MHz [≤ 25 MHz] at -3 dB level	
ILS knowledge	-25 dB for every channel	
Radiometric requirements		
Radiometric sensitivity	0.25K [0.5K] at 10 MHz bandwidth at 250K scene temperature	
Radiometric accuracy	<1K	
Radiometric non-linearity error	<0.75K	
Spectrally varying radiometrically error	<0.1K [<0.25K]	
Geolocation requirements		
Vertical geo-location	500 m [750 m]	

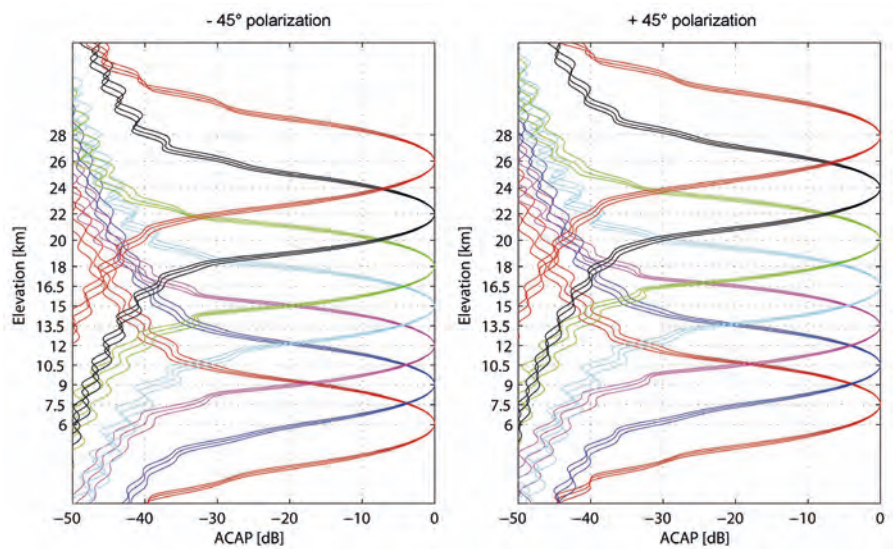


Figure 5.25. Azimuthally-collapsed antenna patterns for all 14 beams (+45° polarisation on the right, -45° polarisation on the left) calculated from simulations including the complete optical path.

The vertical resolution drives the antenna beam width and the sampling strategy. Narrow beam width and a sampling of 1.5 km in the lowest 12 km of the atmosphere and 2 km in the highest 10 km are needed. Half-power beam widths smaller than 3 km with a centre-to-centre beam separation of 1.5 km can be realised by arranging the beams in two columns and using orthogonal linear polarisation at $\pm 45^\circ$ from the horizon to minimise polarisation effects from the atmosphere, as shown in Fig. 5.24.

Spectral characteristics

The low altitude measurements drive the choice of the frequency region around 340 GHz, where the atmosphere is transparent. The pressure broadening effect of the low altitude spectral lines leads to the need for a large instantaneous bandwidth to be processed, while the simultaneous observation of atmospheric species drives the selection of the spectral bandwidth of the Intermediate Frequency (IF) chain and the design of the backend spectrometer. The bandwidth also determines the power consumption of the instrument and the receiver noise, which needs to be kept low to achieve high sensitivity.

The spectral resolution also has a large impact on the design of the backend spectrometer and the post-processing strategy. The number of lags to be processed is determined from the need to resolve the spectral features in combination with the processed bandwidth. The parallel processing of the multibeam system (14 beams in parallel) achieves the required high sensitivity.

Radiometric characteristics

The brightness temperature of the atmospheric limb signal depends on the altitude and frequency of the observation. It ranges from a few tens of K to about 250K, determining the dynamic range of STEAMR and the calibration strategy. Warm calibration sources at about 300K are needed, while cold calibration is achieved by looking at cold space.

The availability of Low Noise Amplifiers (LNAs) is the key to the selection of the IF. Including the LNA in the mixer block allows achieving low noise with large bandwidth.

5.4.3.4.3 Instrument subsystems description

This section describes the main subsystems of the STEAMR instrument.

Mechanical and thermal architecture

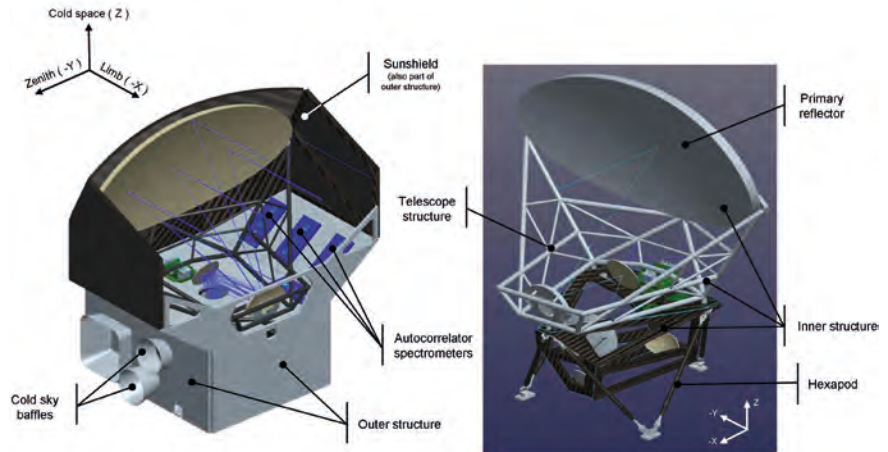
The STEAMR subsystems mechanical design is based on a primary inner structure and an outer secondary one. The primary inner structure consists of two elements:

- A highly accurate and stable CFRP structure holding the optics, the focal plane unit with mixers and the high frequency part of the local oscillators.
- A CFRP telescope with a tubular structure to hold the primary and secondary reflector mounted on top of the inner structure.

These two structural elements are isostatically mounted to the spacecraft interface by means of a hexapod with adjustable length (Fig. 5.26). The total mass of both structures is 14.7 kg (including margins). The lowest lateral (X direction in Fig. 5.26) eigen-frequency is 51.5 Hz, whereas the lowest eigen-frequency in the launch direction (Z in Fig. 5.26) is 65.4 Hz with 7% of the mass participating.

A mechanically-decoupled outer structure surrounds the inner one and provides protection from direct sunlight on the reflectors. It also shields the telescope from space debris and micrometeorite impacts. The electronic boxes are mounted on the inner sides of this outer structure. The outer structure also provides thermal isolation and helps to keep the correlation spectrometers and

Figure 5.26. Outer structure and protective cover with cold-sky baffles on the zenith direction and autocorrelation spectrometers in blue (left). Inner structure including telescope structure (light grey) mounted on the optical hexapod unit (black), both manufactured in CFRP (right).



the IF amplifiers at stable temperatures, with orbital variations of less than 1K. The total mass of the outer structure is 27.7 kg (including margins) and the lowest lateral eigen-frequency is 61.1 Hz, whereas the lowest eigen-frequency in the launch direction is 102.6 Hz with 10% of the mass participating.

The thermal design aims to provide a stable thermal environment for the instrument. It makes use primarily of passive means such as MLI attached to all external surfaces to shield from direct sunlight and Earth’s albedo.

The STEAMR telescope, i.e. the main reflector and the much smaller sub-reflector, is protected from direct sunlight by a sunshield. Its main purpose is to prevent the reflector from overheating. Furthermore, it allows the thermal gradients to be minimised, thereby reducing thermo-structural distortion and large temporal variations in the thermal signal background, both affecting performance. The size of the sunshield is minimised by making it part of the STEAMR instrument. This also allows independent testing of any interaction between the shield and the reflector beams.

The high-dissipating autocorrelation spectrometers are distributed on two white-paint radiators facing cold space. One additional small radiator with a baffle is mounted to face away from Earth and is connected by thermal straps to the focal plane unit with its mixers and LNAs (see Fig. 5.26). Internal instrument heaters are operated by the spacecraft to raise the temperature before switch-on as well as during cold phases (eclipse, LEOP and safe mode). Thermal simulations show that the autocorrelation spectrometers temperatures are maintained in the +10 to +20°C range and that the focal plane mixers with amplifiers can be kept at less than -30°C, with orbital variations less than 1°C.

Power

Four identical and internally redundant power supply units connect the instrument to the spacecraft power lines and control the power to each of the four radiometer blocks. Powering up of different subsystems and functions can either be commanded from the On-Board Computer (OBC) over the spacewire command link or by the internal power supply controller. This means that each block of four radiometer channels can be operated and tested individually. The maximum power in normal operating mode is 400 W including margins at EOL. The required heater power at start-up and during non-operating condition is ~100 W.

Optical design

The optical design, illustrated in Fig. 5.27, comprises three elements:

- The telescope with primary and secondary reflectors.
- Subsequent relay optics.
- The focal plane array.

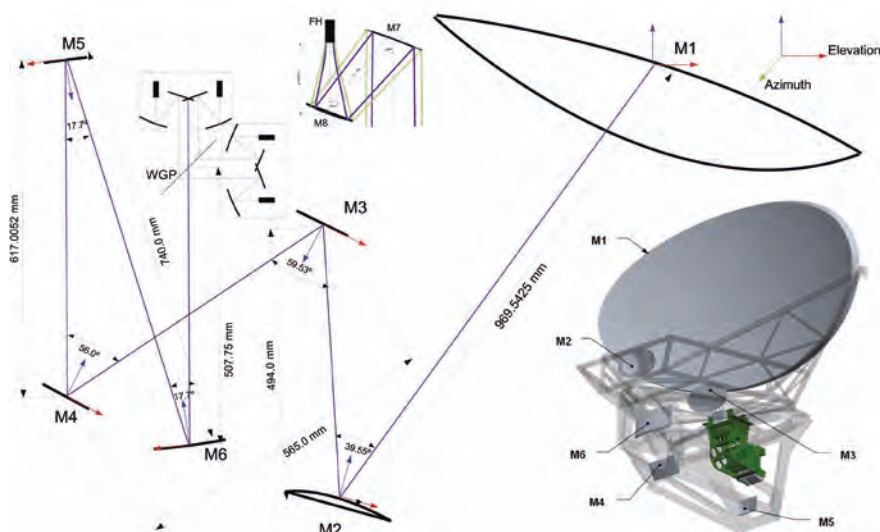


Figure 5.27. The optical path towards the limb is shown in scale. The optical path is split by polarisation just before the focal plane. The inserted CAD drawing at the bottom right shows the mirror placement and the focal plane unit in green.

The telescope is an off-axis Ritchey-Chrétien design with a hyperboloid primary reflector and a hyperboloid secondary reflector. The Ritchey-Chrétien design was preferred over the classical Cassegrain design as it provides better performance over a wide FOV by reducing third order coma and spherical aberration. The telescope therefore ensures high side-lobe suppression for off-axis beams, and is thus ideally suited for this application where all optics are off-axis. The complete telescope with support structure is made of highly stable CFRP, which was also used for Odin.

The geometry of the beams projected on the atmospheric limb is shown in Fig. 5.24. To increase spatial sampling, the 14 beams consist of two sets of seven beams, which are polarised orthogonally at $\pm 45^\circ$. The two sets of beams are highlighted in Fig. 5.24 with alternating red and blue colours. The spacing between the adjacent equivalently-polarised beams varies with altitude, with the lowest four beams having a relative sampling distance of 3 km and the upper three having a sampling distance of 4 km. With the overlap made possible using two orthogonal polarisations the spacing is reduced to 1.5 km and 2 km, respectively. To maintain the desired spatial sampling rate as illustrated above, the far-field antenna patterns require low sidelobes, thereby minimising cross-contamination of the adjacent beams. This is achieved with a uniform primary reflector edge taper of -25 dB.

The M3 and M4 relay mirrors are astigmatic reflectors that serve to fold and shape the incident beams in both amplitude and phase for the azimuth and elevation planes of the beams. These astigmatic surfaces are special types of bi-conic surfaces specifically designed for off-axis quasi-optical imaging, where the orthogonal curves of the surface in the astigmatic and elevation directions are described by two different off-axis conic geometries. They are fully astigmatic in the sense that the two incident focal points and two reflected focal points occupy different locations, thereby producing fully astigmatic beams. This essentially means that the reflectors, image elliptical beams to

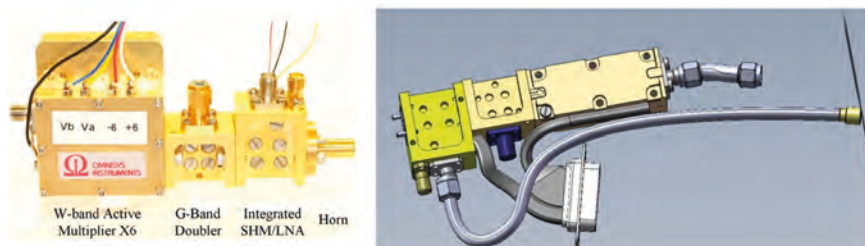
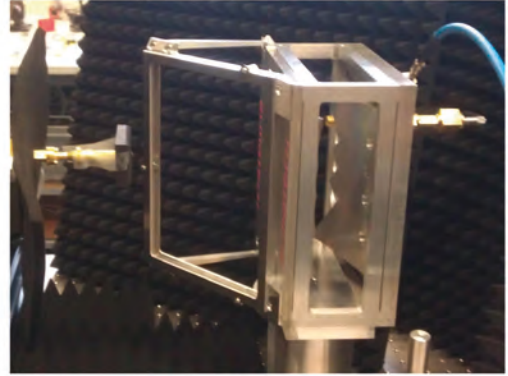
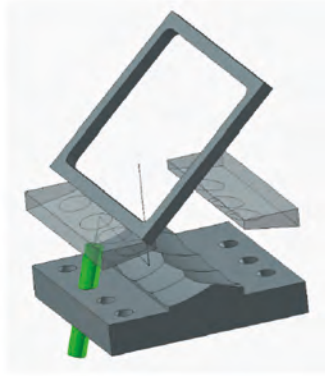


Figure 5.28. Existing receiver frontend prototype based on existing active multiplier used for the ALMA water vapour radiometers, passive doubler and DSB mixer with embedded LNA and mounted horn.

Figure 5.29. The M7 mirrors are all machined from the same structure that holds the feed horns, the two sets of M8 facet mirrors are on top. The drawing on the left shows a full set of seven receiver units with the LO mounted below the horns. The focal plane breadboard is on the right during near field testing at the Institute of Applied Physics (CH).



other elliptical beams. The combination of these reflector focal lengths and propagation distances creates an output plane where both the azimuth and elevation Gaussian beam amplitude radii are matched simultaneously, as are the azimuth and elevation Gouy phase shifts.

The M5 reflector is positioned at this output plane. This is a three-phase astigmatic reflector, where the orthogonal focal points on either the incident or the reflected side coexist. By intercepting the beams at the plane where they have both been circularised and matched in phase, they will propagate onwards with amplitude and phase symmetry. The M6 reflector serves to re-fold the beams to the focal plane, which is located behind reflector M3. The combined envelope of the beams is at a minimum between M5 and M6, which is where a rotating-chopper mirror can intercept the optical path.

The focal plane is now an image plane of the far-field, since the phase shift is 1.5π from the M1 reflector. At this plane, the beams are at their maximum mutual separation as defined from the far-field. The wave-front curvature of the focal plane is infinite, i.e. flat. This simplifies both design and testing. The optics of the focal plane unit (M7 and M8) couple the beams at the focal plane to the corresponding feed horns. The optical paths for each beam within the focal plane units are equivalent, being comprised of two paired off-axis conic reflectors.

Focal plane unit

The layout of one of the optical paths for the current model of the focal plane unit is shown in Fig. 5.29. The rim of the first facet, M7, is defined by the -18 dB amplitude radius, i.e. the level of mutual proximity of the beams at the focal plane

The design of the focal plane unit is based upon the heritage from the KOSMA telescope. These arrays were composed of monolithically-machined facet reflector arrays of paired off-axis reflectors that imaged the beams at the KOSMA telescope focal plane to their corresponding feed horns. The experience from these two designs has been used to arrive at a near-optimum design for the STEAMR focal plane unit.

Telescope

The telescope structure and its reflectors are made of highly stable CFRP while diamond-turned aluminium is used inside the instrument.

The baseline telescope has an aperture of 800×1600 mm and a surface accuracy of $10 \mu\text{m}$ RMS for both mirrors. The surface accuracy could be much worse than $10 \mu\text{m}$ while still meeting the specifications, but it is preferred to maintain very low sidelobes and, as a goal, to have the sidelobe below the required level of knowledge. This improves calibration accuracy thanks to better in-orbit antenna sidelobe characterisation.

The overall structure and accommodation of STEAMR is shown in Fig. 5.30 and Fig. 5.26. The telescope support structure must minimise the deformations

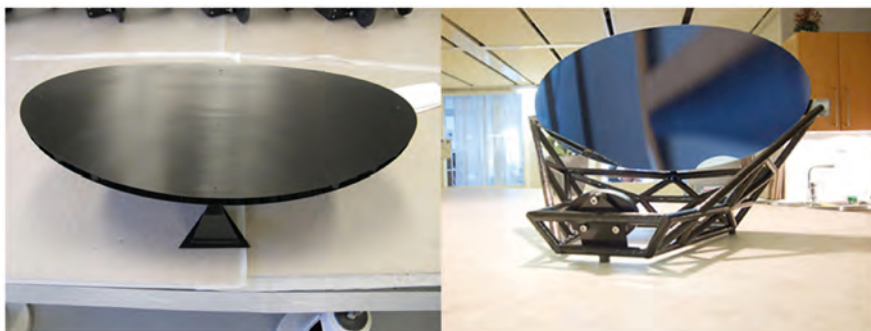


Figure 5.30. STEAMR telescope structure and mirrors, complete 1:4 scale prototype from Composite Mirror Applications (USA) with one micron RMS surface and, to the right, 1:2 scale prototype from Carbonia (SE) with $8\ \mu\text{m}$ surface accuracy.

caused by temperature variations and gradients. As a baseline, a CFRP tubular frame support structure is selected.

Calibration devices

The path from the mixers to the beam adjusting mirrors is interrupted by a rotating chopper. A lightweight flat Mylar mirror is mounted directly on the axis of a redundant drive stepper motor, which places this reflector into the beam path. A slower device, the switching mirror, provides two cold-sky directions and two calibration loads at two different temperatures, such as 250K and 320K. The self-emission of optical components before the switching mirror can be estimated by observing deep space via the telescope.

To calibrate the sideband ratio in-orbit, a tuneable line source with a high-frequency power detector using the existing LO design with an additional passive Schottky doubler, will be used. The latter only provides a relative calibration, but this is sufficient for determining the sideband ratio.

Mixers and amplifiers

The baseline mixers are at ambient temperature, DSB sub-harmonically pumped Schottky mixers with air-bridged planar diodes and integrated LNA. The LO is also mounted as close as possible to the mixers. The power consumption of each LNA and mixer unit is approximately 200 mW. Two mixer amplifiers prototypes have been built, both with performance around 1000K in terms of DSB receiver noise temperature (Fig. 5.31). Embedding the LNA within the mixer block is crucial to achieving high sensitivity combined with broadband IF operation. The IF signals are further amplified using commercially available amplifiers before being routed to the backend spectrometers.

Sideband separation mixers are being developed as a possible option. The selected LO design has enough power for sideband separation. This option would imply to double the IF and backend spectrometer output compared to the DSB baseline. Power would increase primarily with the number of IFs and correlator blocks used.

For the LO unit, a combination of frequency multipliers and power amplifiers is used, offering good reliability. The LO unit consists of a frequency-

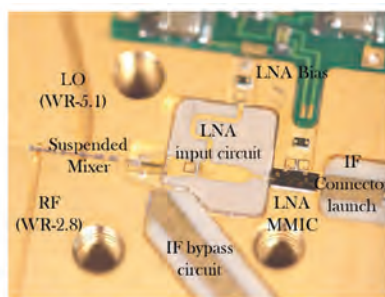
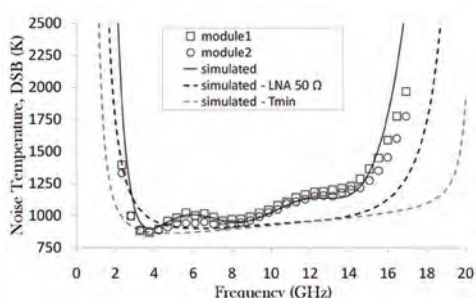


Figure 5.31. DSB receiver noise temperature from hot/cold measurements without optics. The difference with the simulation shows the potential for improvement by further optimisation (left picture). Open mixer block showing the sub-harmonically pumped mixer, LO waveguide, IF matching and MMIC LNA (right).

multiplied phase-locked voltage-controlled oscillators at 14 GHz, each driving four LO chains. Both the mixer LO and the back-end spectrometers will be locked to redundant high-accuracy oven-mounted crystal oscillators.

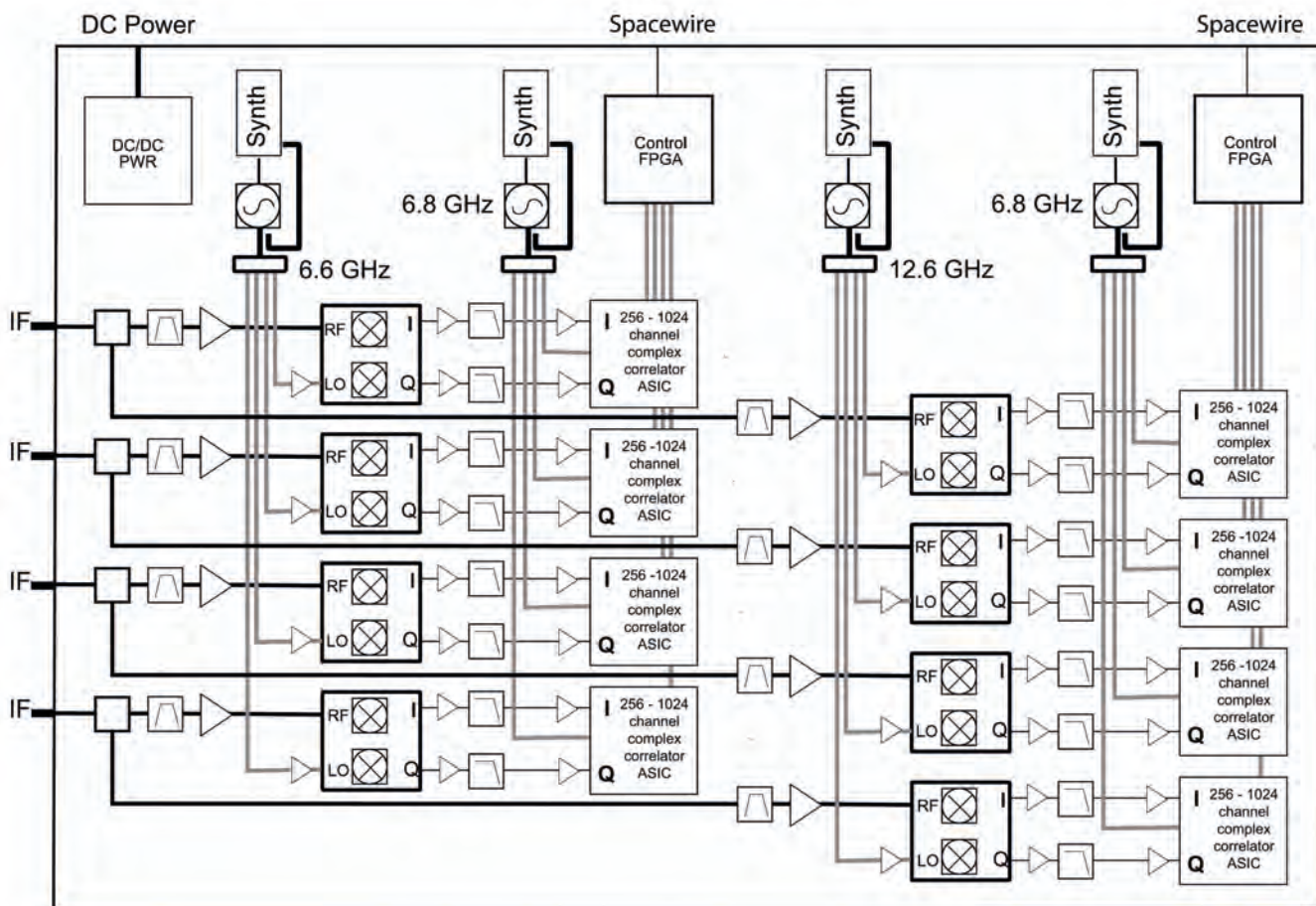
Back-end spectrometers

The back-end spectrometers are required to select and process the frequency regions surrounding the molecular lines of interest, synchronised to instrument pointing and reference switching. The 340 GHz region requires a bandwidth of 12 GHz. Given this large bandwidth, special consideration must be given to the power consumption and dissipation in the design of both the IF chain and the spectrometers.

For STEAMR, the spectrometers are set up to process 16x12 GHz bandwidth signals from the IF chain (lower and upper sidebands being superimposed in DSB). The spectrometer design is split into two very similar parts, each covering a bandwidth of 6 GHz. They are built processing four signal inputs (see Fig. 5.32). The IF spans 3.6–15.6 GHz. The developed spectrometer Application-Specific Integrated Circuits (ASICs) is used for both parts. The ASIC includes A/D conversion and both real and complex correlation using 256, 512, 768 or 1024 lags at the same time as the data is integrated on the chip.

One complete receiver path has been built, as shown in Fig. 5.33, to demonstrate the performance of the autocorrelation spectrometer with mixer and LO system. It has been tested, in cooperation with the Institute of Applied Physics (Bern, CH), on the Jungfrauoch mountain site. In February 2012,

Figure 5.32. Spectrometer block diagram for the four receiver channels. The input signal is split and filtered according to upper/lower IF-bands, amplified and sent to the IQ-converter. The I/Q signals are amplified and pass-band filtered before complex correlation in the HIFAS chip.



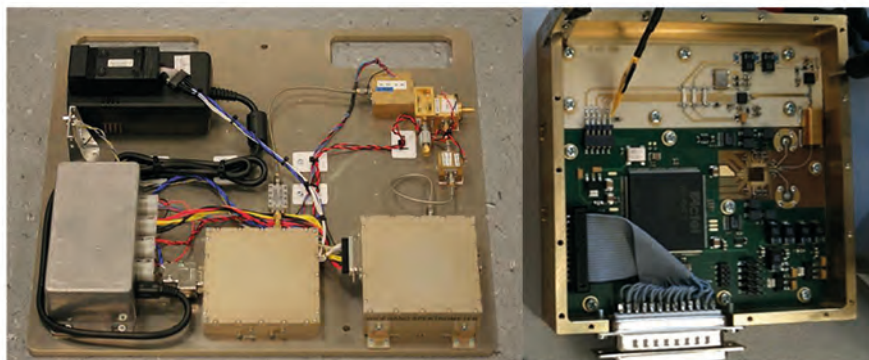


Figure 5.33. Assembled one-channel STEAMR breadboard. The photo shows a DC/DC converter (lower left), a 14 GHz LO source (middle), a 6 GHz bandwidth autocorrelation spectrometer (lower right, and open to the right). One early (with LNA separated) front-end can be seen connected to the 14 GHz source and the spectrometer.

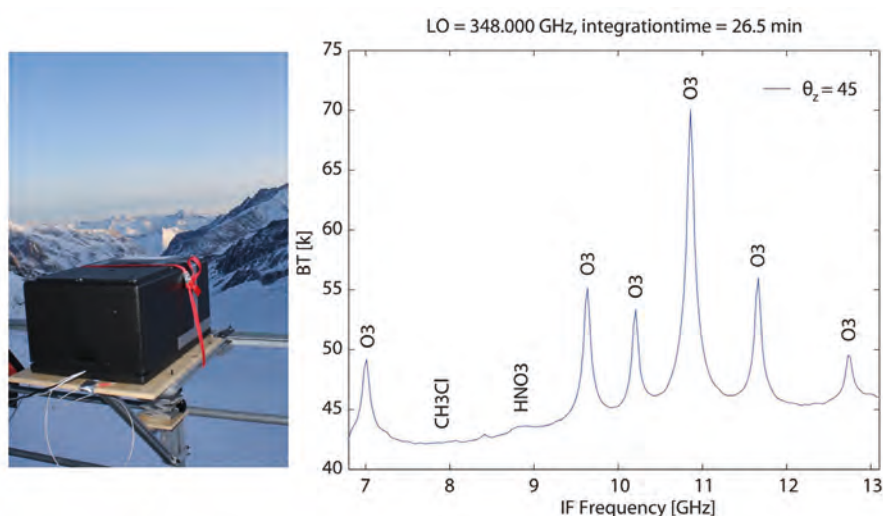


Figure 5.34. Breadboard receiver mounted on site in a protective cover at the Jungfrauoch mountain site (left). Double sideband STEAMR breadboard spectrum with an LO at 348 GHz and an IF band from 7–13 GHz. CH_3Cl , HNO_3 and O_3 lines are visible (right).

the first atmospheric measurements were carried out at an altitude of 3571 m with a STEAMR breadboard receiver. Observations were carried out with the breadboard DSB receiver developed by Omnisys Instruments (SE). The STEAMR FPA feed was used as a horn in conjunction with a specially designed focusing mirror and a flat switching mirror for different view angles. For calibration, a conical ambient temperature load was used with a nitrogen-cooled cold absorber. Figure 5.34 shows a picture of the STEAMR breadboard (left) and the measured spectrum (right).

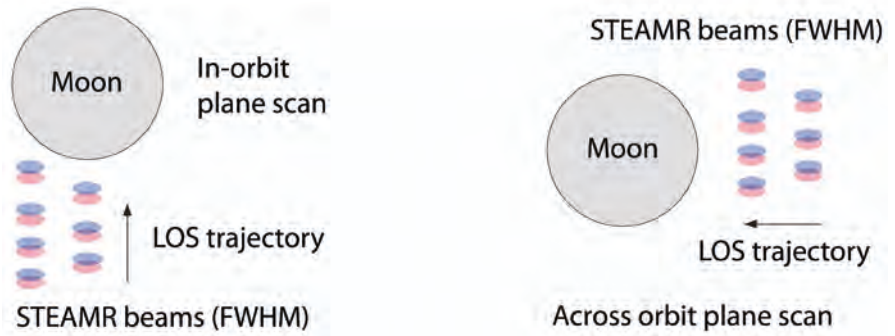
5.4.3.4.4 Calibration

The nominal measurement cycle of STEAMR is made by continuous measurements of the limb interrupted by reference calibration measurements. The receiver system processes simultaneously all frequencies and all limb altitudes observations, which are interrupted by the above mentioned interleaved calibration measurements.

The individual limb or calibration measurements can be set in steps of 0.1 s depending on the required along-track resolution or such to optimise in-orbit performance. For instance, a 4 s-long measurement could be split into eight half-second sub-integrations to allow post-processing corrections to be carried out in a shorter time.

Radiometric calibrations to determine the signal scale and the receiver noise are performed using views of cold space and of an onboard warm load. Calibration against the warm load, or reference loads, as used today in the Odin atmospheric observations, can be carried out around once per minute. The initial in-orbit check out will be used to determine the optimum time sequence for cold-sky and warm-load measurements. The onboard calibration

Figure 5.35. The set of receiver beams compared to the size of the Moon. The half-power beam level is indicated by the denser colour.



targets are validated by comparing with laboratory sources before launch. The atmospheric signal at higher altitude, together with an onboard signal source, will be used to establish the sideband ratio of the mixers.

Small differences in the zero level will occur owing to the different optical path via the telescope and the calibration mirrors. They will be measured using the spacecraft pointing to offset the limb view above any significant atmosphere and are expected to be very stable, therefore this only needs to be repeated on a time scale of days or weeks. All optics will have multiple thermal sensors allowing compensation to be carried out, also when temperature drifts are present.

In-orbit determination of the relative alignment of the LOS with respect to the attitude sensors can be performed by observing the Moon when it crosses the orbital plane (Fig. 5.35), thus twice per month. The vertical positioning of the beams can be determined by comparing the signal change as the LOS transits over the lunar edges. A nominal scan speed of 4° per minute provides sufficient sensitivity for LOS calibration, the error being about 36 m RMS, although lower speeds such as 0.4° per minute may be preferred to also allow the calibration of beam-to-beam positions.

5.4.4 Platform

5.4.4.1 Overview

The two platform concepts are similar and based on flight-proven designs with extensive reuse of off-the-shelf components. This section describes in detail each platform subsystem and provides the rationale for the architecture of the subsystems and the selection of components.

5.4.4.2 Structure

Besides the compatibility with the launcher environment, the PREMIER mechanical design is driven by the need to accommodate both STEAMR and IRLS within the limited volume available under the Vega fairing and by the instrument pointing constraints detailed in Section 5.4.2.

Figure 5.36 shows the two structural concepts proposed for PREMIER. They are designed to sustain the launch loads by providing a direct load path to the launcher. Concept A is a 1200 mm × 1200 mm × 1725 mm rectangular prism-shaped structure with four identical lateral panels linked to a base plate, where the Launcher Interface Ring (LIR) is attached. Every panel is attached to the other and to the base plate at two points with cleat connections. The panel based structure reduces weight compared to a traditional structural frame. Concept B is a 1745 mm × 2200 mm × 1100 mm rectangular-prism shaped structure, based on a well-proven design consisting of four lateral panels reinforced by means of internal shear webs. Lateral panels are chamfered

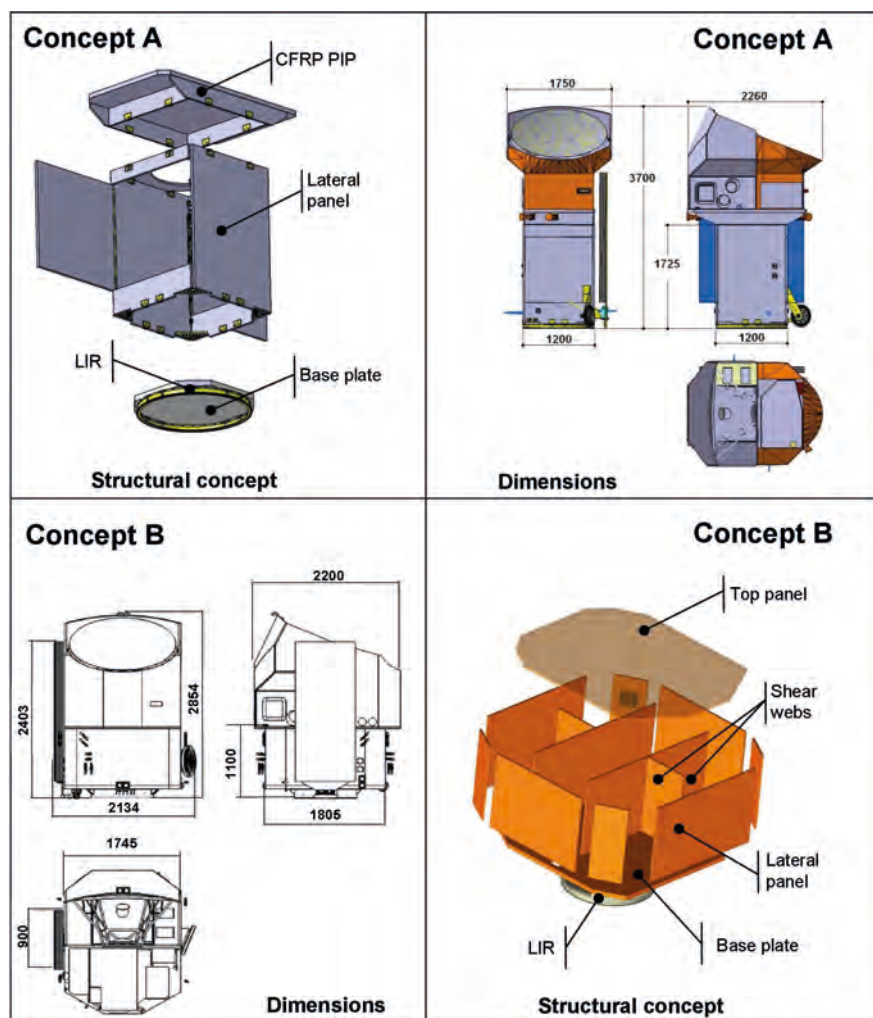


Figure 5.36. PREMIER structural concepts and satellite dimensions for Concept A (top) and Concept B (bottom).

for launcher accommodation optimisation with no impact on the structural strength.

The Finite Element Model (FEM) analyses showed first lateral modes at 18.8 Hz and 21.4 Hz and first axial modes at 60.6 Hz and 64.1 Hz, for Concept A and B respectively, therefore meeting Vega (with 15% extra margin) and PSLV requirements. Static analyses to assess the response of the structural concepts to quasi-static loads during launch have also been performed, confirming the adequacy of the proposed designs.

The IRLS performance is very sensitive to microvibrations from vibrating or rotating elements such as the Solar Array Drive Mechanism (SADM) and the reaction wheels, propagating through the structure. The impact of microvibrations on the stability of the instrument LOS can only be assessed with a very detailed FEM model, which will only be available in later phases. However, effective design measures to minimise the structural propagation of microvibrations have been considered, such as using elastomeric dampers in the reaction wheels and aligning the axis of rotation of the solar array with the pitch axis of the satellite.

Thermo-elastic deformations between the attitude reference and the instruments contribute to the instrument LOS absolute pointing error and to the LOS pointing knowledge error. Thermo-elastic analyses for a cold and a hot case, based on the expected extreme thermal environment conditions throughout the mission lifetime, confirm that the deformations stay within the allocated budget so that the overall instrument LOS pointing performance can be met with margins.

Both structural concepts use sandwich panels with aluminium skins and aluminium honeycomb. Two lateral panels can be opened to allow easy accessibility to all internal units, simplifying the AIT.

Equipment units are connected directly to the service module panels, with the exception of the propulsion subsystem, the reaction wheels and the antennas, which rely on dedicated secondary structures. The LIR is fixed to the bottom panel and has a 1194 mm diameter to interface with the launcher adapter.

The PIP is made of CFRP sandwich and it is attached to the satellite lateral panels by two point cleats per panel. Flexible blades have been added to each corner to improve the isostaticity of the PIP once mounted on the main structure.

5.4.4.3 Mechanisms

Both concepts make use of hold-down and release mechanisms to keep the solar array in the stowed position during launch and release for deployment. The deployment sequence for Concept A is shown in Fig. 5.37 and is divided into two steps, lasting 30 s in total. The first step employs spring devices and consists of the deployment of the solar array yoke and the central panel to achieve a fixed cant-angle that optimises the Sun incidence on the solar array. The second step also employs spring devices activated by a thermal knife and consists of the deployment of the lateral panels. For all these mechanisms reuse of existing flight-proven designs, or with minor modification if needed, have been considered.

An alternative solution using more complex regulated devices such as viscous dampers or electrical motors could also be envisaged to reduce shock during the deployment, if proven necessary.

Both concepts also use a SADM attached to the satellite bottom floor to rotate the solar array around the pitch axis. The SADM operates in micro-steps to minimise the generation of microvibrations. The SADM could use off-the-shelf flight-proven mechanisms such as the SEPTA-34C or the SEPTA-24 from RUAG (CH).

5.4.4.4. Thermal control

The main function of the thermal control subsystem is to guarantee operating and non-operating temperature ranges for all the satellite components. Thermal requirements are not critical for the PREMIER platform and can be

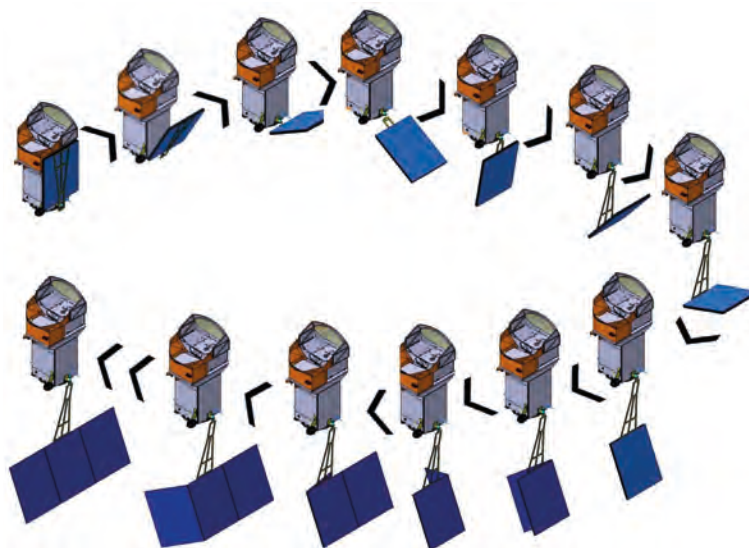


Figure 5.37. Deployment of the solar array in Concept A.

fulfilled by well-proven passive thermal control design, including heater lines and thermistors.

The PREMIER platform requires a maximum heat rejection power of about 680 W to reach thermal stability. This is achieved by using approximately 50% of the radiative surface on all four lateral panels, leaving sufficient design margins.

All internal units are painted in black and mounted on the platform walls by means of interface fillers and 3 mm-thick aluminium doublers to improve the conductive coupling with the radiators. Internal sidewalls are also painted in black to make the temperature of the internal cavities uniform, while MLI covers the non-radiative external surfaces of the platform.

Temperature sensors and heaters are placed in the units, payload bench and propellant tank to prevent excessive cooling during the cold phases (eclipses, LEOP and safe mode). Payload and satellite units require a maximum heater power of 350 W.

The IRLS and STEAMR have an autonomous thermal control (see Subsections 5.4.3.3 and 5.4.3.4.3) and are thermally decoupled from the platform by means of MLI insulation, both at the bottom of the instruments and on the top of the payload common bench, as well as by a low conductivity payload mounting structure.

The startrackers, accommodated on the payload common bench, are also thermally decoupled from their supporting structure to minimise thermal fluctuations along the orbit and hence reduce the pointing error.

The sunshield protecting STEAMR from direct sunlight and described in Section 5.4.2 is covered by MLI on the external surfaces, while the interior is either covered by MLI or by a combination of white paint and vapour-deposited aluminium Kapton foils to reject emitted/reflected radiation from Earth.

5.4.4.5 Electrical architecture

The PREMIER satellite features a rather conventional electrical architecture, inherited from similar low-Earth orbit (LEO) Earth observation satellites.

The system electrical architecture is illustrated in Fig. 5.38 and includes the following subsystems and equipment, with minor differences between the two concepts:

- Command and Data Handling, shown in green in Fig. 5.38, includes the OBC, for primary spacecraft command and control and dedicated platform and payload command-and-control, MIL-1553B data buses and Remote Interface Unit (RIU), catering for payload-specific interfaces and non-MIL-1553B platform equipment interfaces.
- Power Subsystem, shown in blue in Fig. 5.38, includes the Power Conditioning and Distribution Unit (PCDU), solar array, solar array drive electronics, battery and heaters.
- Tracking, Telemetry and Command (TT&C), shown in orange in Fig. 5.38, includes the S-band transponders, for realtime command, telemetry and ranging and the S-band antennas.
- Attitude and Orbit Control Subsystem (AOCS), shown in pink in Fig. 5.38, including the sensors and actuators.
- Payload Data Handling and Transmission (PDHT), shown in orange in Fig. 5.38, including the Mass Memory Unit (MMU) for storage of payload data, auxiliary data and platform telemetry and the X-band high data-rate downlink.

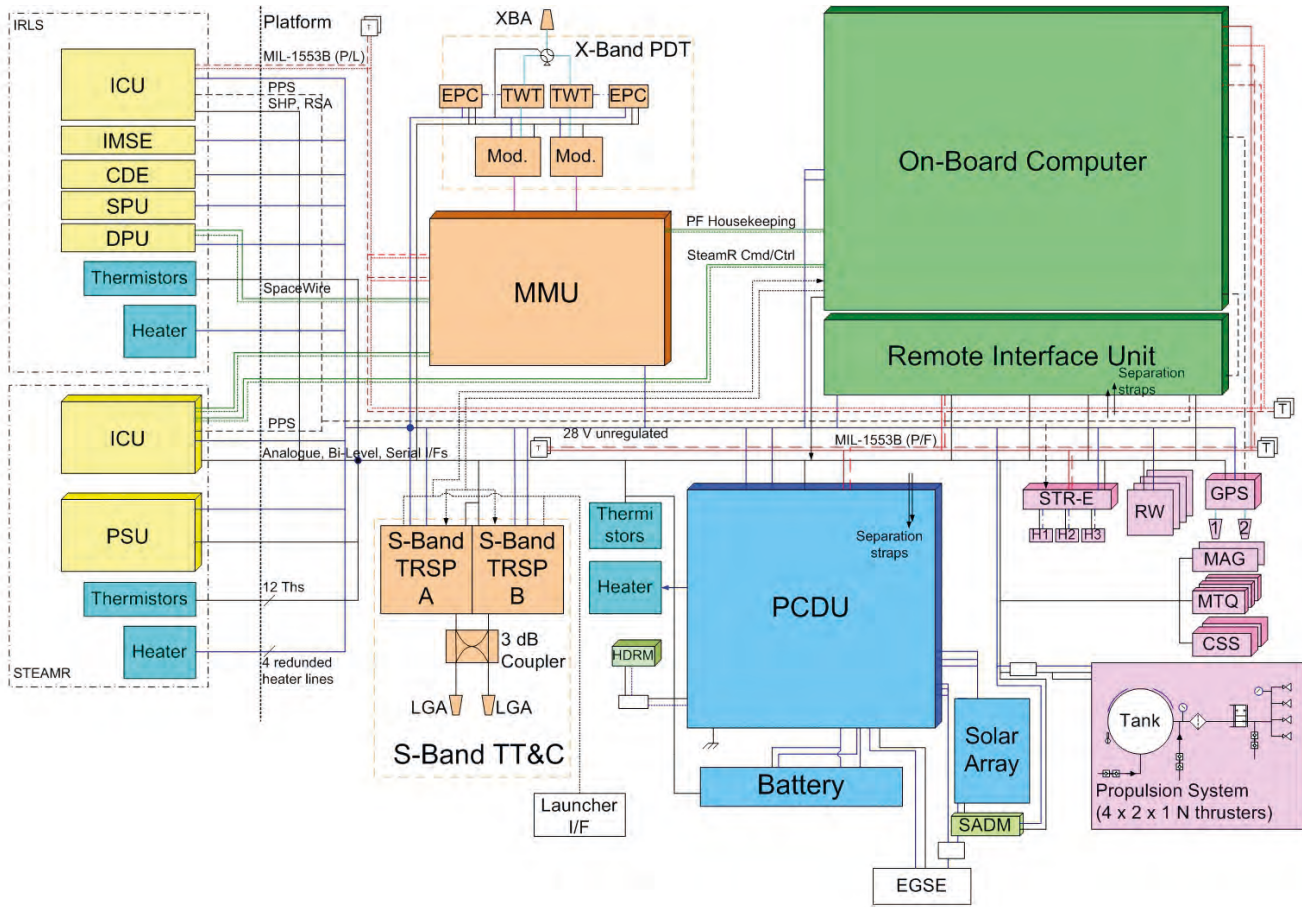


Figure 5.38. PREMIER top level electrical architecture.

- IRLS interface with the platform via a MIL-1553B bus. Discrete interfaces such as standard high power commands and relay status telemetry allows to control the ICU for switching on/off. Science data is provided by the IRLS DPU on redundant and fully cross-strapped spacewire link. Twelve power lines and five redundant heater supply lines, all protected by Latching Current Limiter (LCL), are provided by the PCDU.
- STEAMR is controlled by the OBC via a dedicated spacewire link for command and control. The satellite provides four power lines, four redundant heater lines and the associated thermistor, a time reference pulse and additional discrete on/off commanding capability with associated relay status telemetry to switch on/off the instrument control unit.

5.4.4.6 Command and data handling

The Command and Data Handling Subsystem (CDHS) provides the following functionalities:

- Overall satellite command and control including AOCs algorithms.
- Running the onboard autonomy and FDIR.
- Provision and distribution of ground and software issued commands to the satellite.
- Collection and storage of satellite house-keeping telemetry.
- Onboard time generation, synchronisation, maintenance and distribution.

The CDHS architecture is based on a recurrent concept with extensive heritage and consists of two units, the OBC and the RIU. The modular approach of separating the OBC from the mission-specific interfaces has the advantage of allowing reuse of existing hardware with minimal modifications, enabling early testing. Three redundant command and control buses are used: two MIL-1553B to connect to the platform units and the IRLS, respectively, and a spacewire for STEAMR.

The OBC acts as the command and control centre of both platform and payload, and is therefore the master controller of all communications on board, while all other units are remote terminals. The OBC communicates either on the nominal or redundant bus, while the remote terminals are listening in hot redundancy, to both busses.

The processing requirements of the OBC are within the typical range of a standard Earth observation LEO mission. All the onboard data processing and compression of the science data is carried out by the IRLS and STEAMR central electronics. Realtime housekeeping telemetry is acquired by the OBC and transmitted to the ground using the S-band downlink. The OBC hosts the onboard software and is based on a Leon-3 microprocessor (SCOC3) with a processing power above 15 MIPS in Concept A, and a Leon-2 microprocessor in Concept B. The computer also contains an internal 3.8 Gb memory, extendable to 16 Gb. A built-in monitoring and reconfiguration module ensures system level FDIR and triggers OBC reconfiguration and transition into Acquisition and Safe Mode, as necessary.

The OBC maintains and distributes the onboard time reference, which is synchronised to UTC GPS time provided by the GNSS receiver.

The RIU provides the interfaces between the OBC and the platform and payload units that do not use the MIL data bus. These include AOCS sensors and actuators, thermistors, heaters and the SADM.

5.4.4.7 Payload data handling and transmission

The Payload Data Handling and Transmission (PDHT) subsystem includes all equipment required to acquire, store and transmit the scientific data generated by the payload to the ground and consists of the Mass Memory Unit (MMU) and the X-band data downlink system.

The data flow starts from the instrument ICU, which ensures the transfer of data to the MMU for storage until the next ground station pass.

The MMU stores the payload data, auxiliary data required for payload data processing (e.g. position, velocity, attitude data) as well as the payload and platform housekeeping telemetry.

The Concept A MMU consists of two 1 Tb boards, which are used in cold redundancy to store the ~400 Gb of data generated during two consecutive

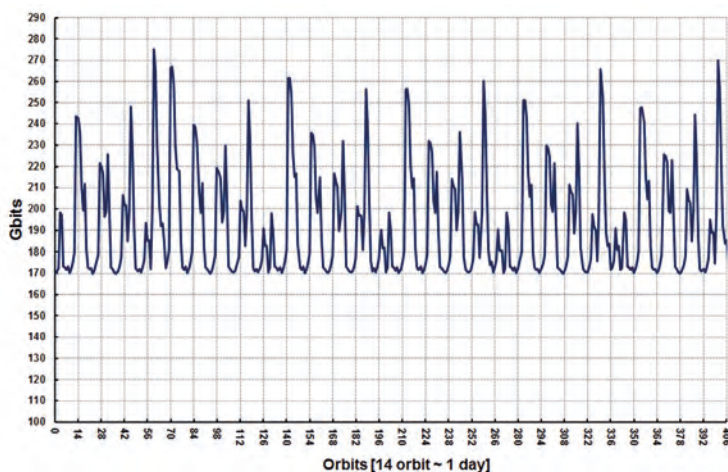


Figure 5.39. Mass memory usage for Concept A during repeat cycle assuming 100% duty cycle. Downlink in Kiruna and Inuvik.

orbits (assuming 90% duty cycle and including an extra 25% margin). The memory boards are based on NAND flash technology and are made compatible to the STEAMR spacewire link. Concept B foresees two MMU boards of 256 Gb each in cold redundancy based on SDRAM modules with advanced error detection and correction and latch-up protection to store ~260 Gb generated (assuming 90% duty-cycle and including an extra 25% margin) during two consecutive orbits. Differences in the amount of mass memory are due to the reuse of flight-proven solutions for cost saving reasons.

The X-band data transmission subsystem applies a QPSK modulation and coding to the bit stream at a rate of 270 Mbit/s. After amplification by the RF high-power amplifiers (TWTA), the RF signal is fed to the fixed isoflux X-band antenna through the waveguide redundancy switch.

In Concept B, the scientific data are downlinked to the Svalbard ground station, which is also used by MetOp. The compatibility of the PREMIER downlink with the same ground station as MetOp is ensured both by antenna geometrical aspects and by the use of different frequency bands. In Concept A, two ground stations are used: Kiruna and Inuvik. Both scenarios allow downlinking the data at every orbit to fulfil the five-hour timeliness requirements. The available time to downlink over an orbit repeat cycle is longer when using Kiruna and Inuvik than when using Svalbard only, which enables the use of a 270 Mbit/s system to downlink the larger amount of data generated by Concept A. Figure 5.39 shows the mass memory usage for Concept A.

5.4.4.8 Electrical power generation and energy storage

The electrical power subsystem supports the following functionalities:

- Generation of power
- Energy storage
- Power regulation and distribution to all equipment

The total power consumption is fairly constant through the orbit since the instruments operate continuously. As a result the electrical power architecture follows a simple design and a cost effective ‘Direct Energy Transfer’ (DET) power conditioning. However, the continuous data acquisition requires a relatively large power generation and storage to cope with the payload and platform needs during eclipse. As a result, the electrical power subsystem is designed to handle a constant power generation of 2.3 kW and a fairly constant power consumption of 1.5 kW.

The PCDU is responsible for distributing power from the solar array and the battery to the platform and payload equipment, providing power control and battery charge control. A DET power conditioning scheme comprising a classical Sequential Shunt Switching (S³) regulator, similar to the ones used in satellites such as Seosat and Sentinel-3, has been selected as a baseline. The PCDU distributes power via single power lines that are protected by folding and/or latching current limiters. Critical equipment, namely the OBC and the S-band transponder, is connected through resettable current limiters, which maintain power to the protected unit even after anomaly.

Both concepts use a non-regulated 28 V power bus compatible with the IRLS and STEAMR power needs.

Power is generated by a single-wing deployable solar array, which rotates around the satellite pitch axis by means of a SADM attached to the bottom floor of the satellite. The solar array is composed of three or five panels using triple-junction Gallium-Arsenide cells with a Beginning of Life (BOL) efficiency of 28%. The area of the deployed solar array is close to 11.5 m² and provides 2.3 kW at EOL. The solar array is canted with respect to the orbital plane to maximise the energy production throughout the orbit.

The battery consists of lithium-ion stackable decks, which benefits from heritage of missions such as Sentinel-2 and SAR Lupe. An off-the-shelf ABSL battery with the capacity of ~160 Ah, providing the required storage margin, has been selected for both concepts.

5.4.4.9 Telemetry tracking and command

The TT&C subsystem provides S-band communication capabilities between the spacecraft and the ground station. Two omni-directional antennas ensure a communication link for all possible attitudes of the satellite in nominal and non-nominal conditions. The subsystem provides the following functions, compatible with the applicable ESA standards:

- Command reception function, for reception and demodulation of commands sent from the ground station.
- Telemetry function, for modulation and transmission of realtime housekeeping data to the ground.
- Ranging and Doppler tracking functions providing range and range-rate information as a backup of the onboard GNSS receiver data for orbit determination in the event of emergency.

The TT&C functions are implemented via a traditional architecture using a functional chain consisting of two S-band transponders connected to two S-band low gain antennas via a 3 dB hybrid splitter/coupler. The receivers are used in hot redundancy while the transmitters are used in cold redundancy. Two circularly polarised, low-gain hemispheric S-band antennas mounted on the service module meet the requirement for 4π steradian coverage in the fully deployed satellite configuration, as shown in Fig. 5.40.

The command uplink includes two operation modes: a PCM/PSK/PM modulation scheme supports 4 kbit/s data rate and is used in nominal operations when only few telecommands per pass are needed. The second mode uses a SPL/PM modulation scheme and provides a data rate of 64 kbit/s for larger software updates.

The telemetry downlink includes two operation modes, a PCM/PSK/PM modulation scheme supports 25 kbit/s data rate and parallel ranging and Doppler

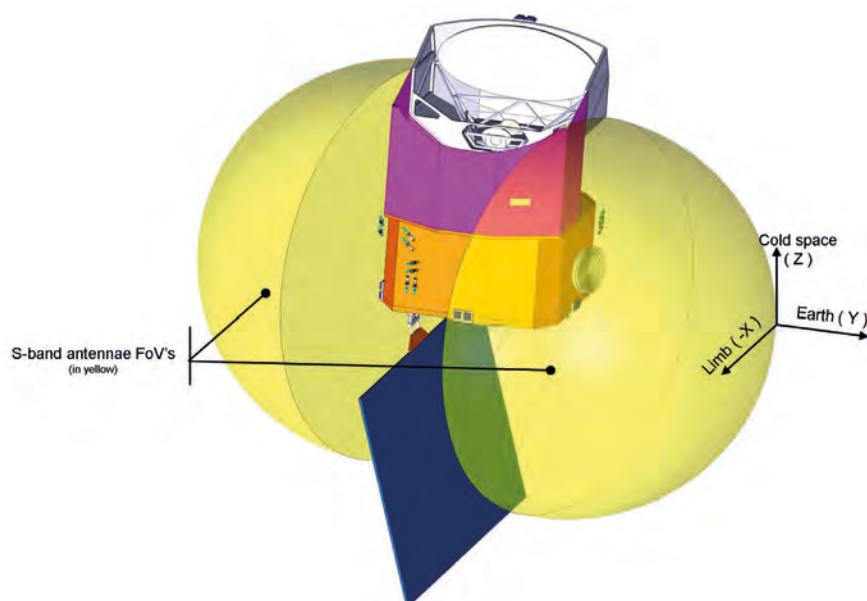


Figure 5.40. PREMIER S-band TT&C outline.

tracking. The second mode provides a data rate of 1024 kbit/s supporting the dump of recorded HKTM in emergency but with no ranging capabilities.

5.4.4.10 Attitude Orbit Control System (AOCS)

The PREMIER AOCS concepts are based upon four distinct modes of operations. All modes are implemented in software and are distinguished by the suite of hardware (sensors and actuators) used. A more detailed description of the main modes follows:

5.4.4.10.1 Initial acquisition mode

This mode is active as of satellite separation from the launcher and aims at reducing the residual satellite angular momentum, acquiring the attitude necessary for starting the solar power generation and ensuring the required shadowing of STEAMR. In this mode, the solar array is automatically deployed just after the satellite detects separation from the launcher. Subsequently, the AOCS is initialised and the satellite is controlled in safe mode, described below.

5.4.4.10.2 Normal mode

This mode is in charge of attitude control during nominal operation, i.e. when the instruments perform the scientific observations and during instrument calibration. The attitude control is performed by reaction wheels. Both concepts use a gyro-less approach, providing the realtime attitude and angular rate estimate using startrackers and Kalman filters. Concept A uses a three-head startracker while Concept B uses a two-head startracker. Momentum management is continuously performed with the magnetic torquers. This mode also supports the pitch manoeuvre required for the instruments LOS and deep-space calibration.

5.4.4.10.3 Orbit control mode

This mode is in charge of performing any in-plane and out-of-plane orbit manoeuvres during the commissioning phase, the nominal phase and the EOL phase. All the manoeuvres are performed using thrusters. For Concept B, no slew manoeuvres are needed to perform orbit control manoeuvres owing to the thrusters configuration. In Concept A, reaction wheels are used to perform a slew manoeuvre before and after the thrust to properly orient the satellite. Attitude control during the thrust phase is performed by pulse-off modulation in Concept B and via the reaction wheels for Concept A.

5.4.4.10.4 Safe mode

The safe mode is activated by the FDIR in case of major failures that cannot be recovered autonomously onboard. In this mode, only the vital satellite functions are maintained and the spacecraft is put into safe conditions, where it is able to survive for a time only limited *a priori* by the consumables. The satellite is controlled in a Sun-pointing attitude and stabilised via a slow spin around the pitch axis. The safe mode relies, as much as possible, on sensors and actuators not used in other modes. The determination of the attitude is performed using the Sun sensors, magnetometers and gyros in Concept B and using the Sun sensors and magnetometers in Concept A. The magnetometers provide Earth magnetic-field measurements for efficient operations of the magnetic torquers, which are used together with the thrusters as attitude control actuators. For Concept A, thrusters are only used when critical conditions/pointing are encountered, in particular to avoid illumination of the STEAMR reflectors.

Sensor	Number	Characteristics	Redundancy
Sun sensors	2 sets × 6	±80° FoV	Cold redundancy
Gyros	2	ARW 0.1–0.2°/√hr Scale Factor <2000 ppm	Cold redundancy
Magnetometer	2	3-axis	Cold redundancy
Startracker	2	Random Error <8" Bias <8"	Hot redundancy
GNSS	2	Position <10 m 3D in real-time	Hot redundancy
Reaction wheels	4	Momentum 30 Nms Torque 215 mNm	Hot redundancy (4 wheels on)
Magnetorquers	1 set × 3	250 Am ²	Hot redundancy

Table 5.4. AOCs Equipment characteristics for Concept B.

A summary of the AOCs equipment for Concept B is given in Table 5.4. Similar units have been selected for Concept A with the exception of the gyros.

PREMIER requires at least four reaction wheels to allow the required three-axis control with adequate robustness. A four reaction-wheel pyramidal configuration provides balanced capacity on every satellite axis and is tolerant to a single wheel failure. In nominal mode, PREMIER performs a sinusoidal yaw steering manoeuvre with an amplitude of about 4° and a period of one orbit to compensate for east-west movement of atmospheric tangent-points caused by Earth's rotation and to ensure that the relative velocity between the instrument and the observed target is aligned with the instrument LOS to facilitate the tomographic retrieval from successive observations along the orbit track. The yaw steering causes the PREMIER swath to oscillate horizontally around the MetOp orbital track. A pitch manoeuvre is also required to point the instrument LOS at the required altitude along the orbit.

The transition to the safe mode attitude is driven by the need to keep STEAMR out of direct illumination from the Sun. The STEAMR secondary reflector must not be illuminated for more than 35 s during non-nominal operation to avoid permanent deformation. The secondary reflector is illuminated only within a ±6° solid angle with the vertex at the centre of the main reflector. To fulfil such requirements, Concept B uses of a redundant set of thrusters devoted only to perform the transition to safe mode attitude using angular rate measurements delivered by a coarse gyro.

The safe mode strategy for Concept A is based on a hybrid mode using a B-spin control based on the use of magnetometers for attitude sensing and magnetotorquers to dampen the angular rate. Thrusters are only used to rapidly dampen angular rates exceeding a given threshold. The efficiency is not optimal because the required torques are computed, based on magnetometer measurements instead of gyros. The time to reach the safe mode attitude can be longer than 35 s and a Sun avoidance strategy must be implemented. Whenever the Sun illuminates the STEAMR reflectors, the thrusters are activated to provide a torque normal to the satellite spin axis and to the Sun direction. The angular-rate measurement will be estimated from Sun-sensor data. The robustness of this approach requires further consolidation. Alternative solutions might include defining a threshold on the derivative of the magnetic-field measurement or adding a coarse gyro, as in Concept B.

5.4.4.10.5 Propulsion

The PREMIER propulsion subsystem is used for orbit acquisition and maintenance throughout the mission, EOL disposal manoeuvre and for attitude control in initial acquisition mode and safe mode. Orbit control manoeuvres are

required throughout the mission to maintain the required orbit and formation with MetOp.

For both concepts, the propulsion subsystem is a conventional mono-propellant system using hydrazine (N_2H_4), pressurised at 24 bars with helium and operated in blow-down mode. The propellant tank is the same tank as used on Sentinel-2, with a capacity of 132 kg (Concept A) or a modified LEO-bus-1000 tank, with 111 kg capacity (Concept B) have been considered. Both tank options provide sufficient propellant capacity to satisfy the mission needs with all the required margins (Table 5.5).

The propulsion subsystem for Concept B relies on sixteen 1 N thrusters divided in two branches of eight thrusters. A branch will be used as nominal orbit control actuators, while the second set of thrusters will be devoted to the safe mode, in line with the design recommendation of using different actuators for the safe mode. In case of failure, each branch can provide redundancy for the other. Figure 5.41 shows the thrusters configuration for Concept B.

A plume impingement analysis has been successfully performed to assess the risk of contamination of critical components such as external MLI, solar array, startracker optics, radiators, RF antennas, STEAMR reflector and IRLS optical aperture.

5.4.4.11 Radio frequency and electromagnetic compatibility

The STEAMR instrument is extremely sensitive to interferences in 3.8–16 GHz and the 320–360 GHz frequency range. As a consequence, adequate isolation between STEAMR and the main and secondary lobes of the S- and X-band downlink antennas must be provided. Furthermore, the radiated electric-field intensity reaching STEAMR components from 30 Hz to 18 GHz shall be kept below 1 V/m. A preliminary analysis has been performed to assess the impact of the S- and X-band antennas as well as other equipment, such as the magnetotorquers or the cryocooler compressors electronics. The results show values from the X-band antenna slightly over the requirements, without taking into account the effect of the sunshield and of the satellite structure. If the results are confirmed by more detailed analysis in later phases, extra shielding will be placed in the structure and the sunshield to meet the required performance.

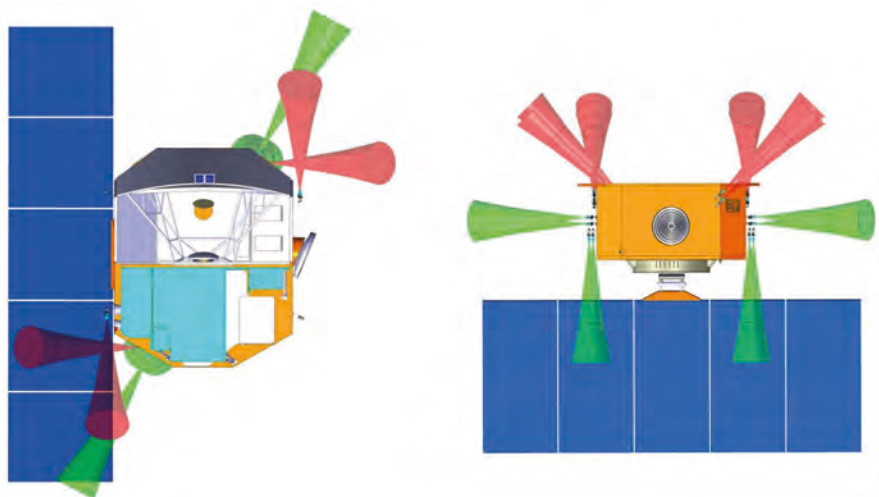


Figure 5.41. Thruster configuration in Concept B.

	Concept A	Concept B
Platform total	644	552
Payload total	250	292
Dry mass total	894	844
System margin	134	127
Dry mass with margin	1028	971
Propellant	97	84
Wet mass	1125	1055
Launcher performance	1240	1240
Launcher adapter	88	76
Launch margin	27	109

Table 5.5. Mass budgets for Concepts A and B [kg].

5.4.5 Budgets

5.4.5.1 Mass Budgets

Table 5.5 reports the mass budgets for the two concepts studied, including the following maturity margins:

- Harness: 30%
- Completely new developments: 20%
- New developments derived from existing hardware: 15%
- Existing units requiring minor/medium modification: 10%
- Existing units: 5%

An additional 15% margin at system level has been applied to protect against unpredictable mass evolutions and/or mass balancing needs. The differences on the platform mass of the two concepts result mainly from the use of a 40 kg PIP and a different estimation of the harness mass leading to ~30 kg more. Differences in payload mass are consequence of the two different designs. The launcher performance and margins refer to the Vega baseline launcher.

5.4.5.2 Delta-V budget

The delta-V budgets for the two concepts are shown in Table 5.6. Differences in the delta-V for the orbit injection correction and formation flying acquisition come from different launch and formation flying acquisition strategies, with Concept A using a more conservative approach than Concept B.

Differences in the delta-V for the deorbit manoeuvre come from the use of different atmospheric and deorbiting assumptions.

	Concept A	Concept B
Orbit injection correction and formation flying acquisition	36.3	24.4
Orbit maintenance	32.1	21.7
Collision avoidance	6.4	12.4
Safe mode and Sun avoidance	2	4
Deorbit manoeuvre	64.3	85.6
Total	141.1	148.1

Table 5.6. Delta-V budgets for Concepts A and B [m/s].

Table 5.7. Power budgets (average values) for Concept A and B [W].

Operating Mode	Concept A	Concept B
Safe Mode	677	631
S/C Nominal + P/L On+ Downlink ON	1544	1552
S/C Nominal + P/L On	1379	1350
S/C Nominal + P/L Standby	587	717

Table 5.8. Mass memory sizing for Concepts A and B.

	Concept A	Concept B
Instrument data rate [Mbit/s]	28.8	18.8
Downlink rate [Mbit/s]	270	270
Average instrument duty cycle [%]	90	90
Mass memory requirement [Gb]	400	260
Mass memory size EOL [Gb]	2000	512

5.4.5.3 Power budgets

The power budgets for the different operation modes are detailed in Table 5.7.

	Concept A	Concept B
Roll [μrad]	150	73
Pitch [μrad]	30	15
Yaw [μrad]	150	145

Table 5.9. AKE for Concepts A and B.

5.4.5.4 Data rate and volume

The data rate and volume budgets are presented in Table 5.8.

	Concept A	Concept B
Roll [μrad]	200	145
Pitch [μrad]	50	29
Yaw [μrad]	200	290

Table 5.10. APE for Concepts A and B.

5.4.5.5 Pointing and geo-location

Table 5.12 summarises the main error contributors, the sources of errors, the assumed types of error and their relationships with the observation requirements. The table is the basis for the allocation of maximum allowable errors to the different contributors and for deriving the AOCS performance requirements detailed in Tables 5.9, 5.10 and 5.11. The performance achieved by the proposed AOCS is detailed in Chapter 7.

The allocation made for the Absolute Knowledge Error (AKE) for both concepts is shown in Table 5.9.

The allocation for the Absolute Performance Error (APE) for both concept is shown in Table 5.10. The pitch axis requirement drives the AOCS critical requirement, and the allocation in both roll and yaw varies between the two concepts due to the different strategies adopted for apportioning errors to the different contributors.

	Concept A	Concept B
Roll [μrad]	24	97
Pitch [μrad]	12	19
Yaw [μrad]	24	195

Table 5.11. RPE for Concepts A and B.

The Relative Performance Error (RPE) is shown in Table 5.11. The pitch axis requirement drives the AOCS performance and the allocation in both roll and yaw varies between the two concepts due to the different strategies adopted for apportioning errors to the different contributors.

5.5 Launcher

The baseline launch vehicle for PREMIER is Vega, launched from Kourou, French Guiana. PREMIER will be the sole passenger on the launcher due to its relatively large size and launch mass. Concept A uses the 1194-mm LVA, developed for Sentinel-2 (Fig. 5.42). Concept B uses instead the standard 937-mm LVA, although this results in a lower height available under the fairing because of increased height of this LVA, which limits the satellite height under the fairing.

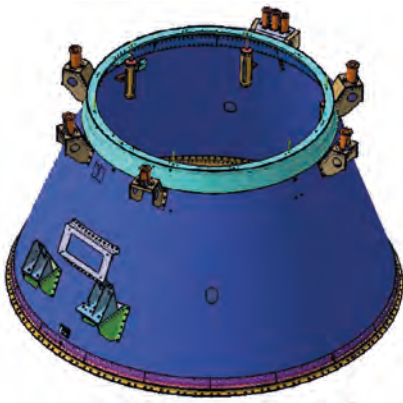
Scientific/ Observation requirements	Macro-error contributors	Sources of error	Class
IRLS/STEAMR geo-location knowledge	On-ground satellite orbit determination (OGOD)	Position measurement error	Gaussian random process
IRLS/STEAMR geo-location knowledge	On-ground satellite attitude determination (OGAD)	Attitude measurement error	Gaussian random process
IRLS/STEAMR geo-location knowledge, IRLS/STEAMR co-registration knowledge and IRLS/ STEAMR coverage	Knowledge of the relative attitude between OGAD reference frame and IRLS measurement reference frame	STR thermo-mechanical deformation	Time bias, harmonic signal
		STR-IRLS thermo-mechanical deformation	Time bias, harmonic signal
		IRLS thermo-mechanical deformation	Time bias, harmonic signal
		IRLS pointing calibration error	Time bias
		IRLS pointing mirror repeatability	Gaussian random process
IRLS/STEAMR geo-location knowledge and IRLS/STEAMR co-registration knowledge	Residuals of the IRLS focal plane calibration/mounting errors	Residual of the IRLS focal plane calibration	Gaussian random process
IRLS/STEAMR geo-location knowledge and IRLS/STEAMR co-registration knowledge	Knowledge of the relative attitude between OGAD reference frame and STEAMR measurement reference frame	STR thermo-mechanical deformation	Time bias, harmonic signal
		STR-STEAMR thermo-mechanical deformation	Time bias, harmonic signal
		STEAMR thermo-mechanical deformation	Time bias, harmonic signal
		STEAMR pointing calibration error	Time bias
IRLS/STEAMR geo-location knowledge and IRLS/STEAMR co-registration knowledge	Residuals of the STEAMR focal plane calibration/ mounting errors	Residuals of the STEAMR focal plane calibration	Time bias
IRLS/STEAMR co-registration knowledge	Actual attitude between IRLS and STEAMR	On-ground alignment error between IRLS measurement reference frame and IRLS alignment cube	Time bias
		Launching and environmental changing effects on IRLS	Time bias
		IRLS thermo-mechanical deformation	Time bias, harmonic signal
		Payload mounting plate thermo-mechanical deformation	Time bias, harmonic signal
		Launch effects on the relative attitude between IRLS and STEAMR	Time bias
		STEAMR thermo-elastic deformation	Time bias, harmonic signal
		Launching and environmental changing effects on STEAMR	Time bias
		On-ground alignment error between STEAMR measurement frame and STEAMR alignment cube	Time bias
IRLS/STEAMR co-registration knowledge	Attitude control error	Attitude control error	Gaussian random process
IRLS/STEAMR coverage knowledge	Synchronisation/time-tagging between IRLS and time in OGAD/OGOD	Synchronisation of the IRLS with OGAD/ OGOD	Gaussian random process
IRLS/STEAMR coverage	Synchronisation/time-tagging between STEAMR and time in OGAD/OGOD	Synchronisation of the STEAMR with OGAD/OGOD	Gaussian random process

Table 5.12. Summary of the main error contributors, sources of errors, types of error and their relationships with the observation requirements.

Table 5.13: Launch vehicle performance and margins [kg].

Launcher	Performance	Wet mass	Margin
Concept A			
Vega	1152	1125	27
PSLV full vehicle	1400	1125	275
Concept B			
Vega	1164	1055	109
PSLV full vehicle	1400	1055	345

Figure 5.42. Vega 1194-mm LVA interface.



The backup launch vehicle is the Indian PSLV full vehicle launcher, lifting off from Sriharikota Island, India. The PREMIER satellite is compatible with both launchers requirements.

The capacity of the two launchers is listed in Table 5.13. The Vega performance has been reduced by 100 kg from the figure quoted in the Vega User Manual (Arianespace, 2006) to take into account the current uncertainty in the injection performance. For both launchers, the reported performance also includes the launcher adapter mass. The Vega performance shows limited mass margins, while for PSLV the margin is more comfortable.

Figure 5.43 shows the accommodation of Concept A (left) and B (right) in the dynamic envelope of the Vega fairing. The clearance for both concepts is about 2 cm and is driven by the non-deployable sunshield on top of the IRLS for Concept A and by the size of the IRLS/STEAMR for Concept B.

Figure 5.44 shows the accommodation of Concept A (left) and Concept B (right) in the dynamic envelope of the PSLV fairing. The margins are close to 20 cm.

5.6 Ground Segment and Data Processing

5.6.1 Overview

Following the approach of developing a multimission ground segment, the current generation of Earth Explorer ground segments has been designed, built and integrated using generic components configured or adapted to each satellite. This approach will apply also for the Earth Explorer 7.

5.6.2 Ground Segment Elements

The PREMIER ground segment consists of two main components, namely the Flight Operation Segment (FOS) and the Payload Data Ground Segment (PDGS), as shown in Fig. 5.45.

The FOS includes the TT&C ground station and the Flight Operations Control Centre. The TT&C ground station provides the following main functions:

- Housekeeping telemetry acquisition
- Telecommand uplink
- Satellite tracking
- Data connection to the Flight Operations Control Centre

During LEOP, operations are supported by a dedicated ground station network. This uses Estrack core and enhanced stations where possible.

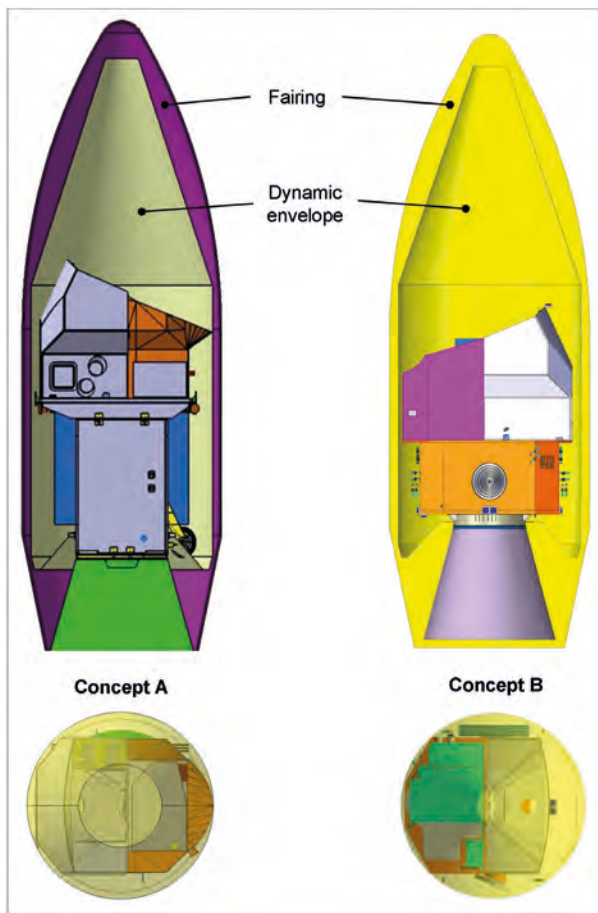


Figure 5.43. Accommodation of PREMIER in the Vega fairing for Concept A (left) and Concept B (right).

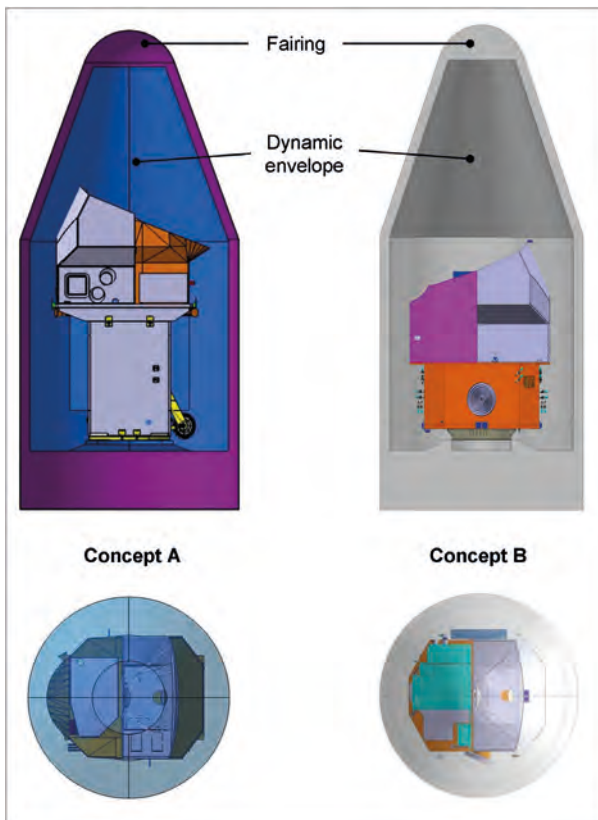


Figure 5.44. Accommodation of PREMIER in the PSLV fairing for Concept A (left) and Concept B (right).

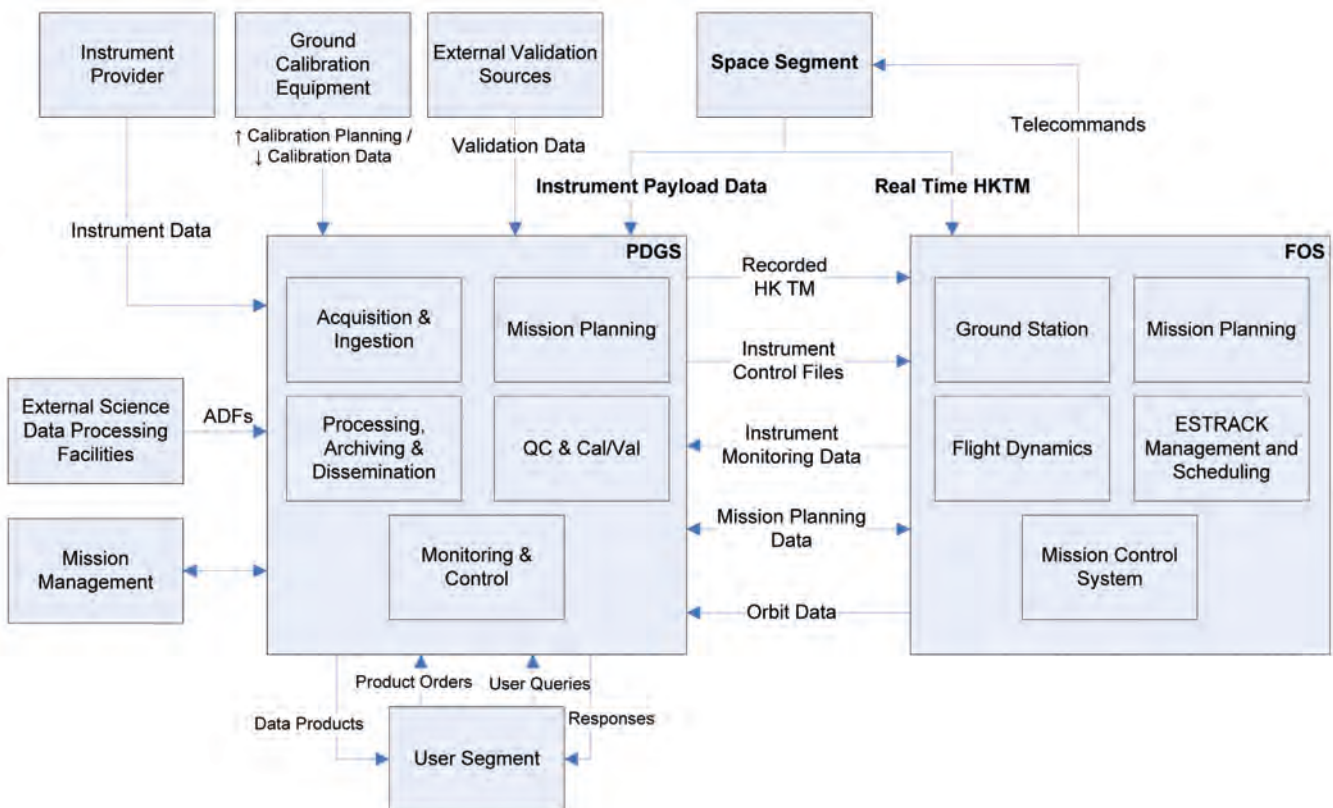
The Flight Operations Control Centre, based at ESA-ESOC, will provide the following main functions:

- Satellite monitoring and control
- Flight dynamics and manoeuvre planning
- TT&C ground station network control
- Overall satellite operations planning
- Onboard software maintenance
- Mission simulation
- FOS supervision
- Spacecraft system data distribution
- Interface with the launch site for LEOP

The PDGS is primarily responsible for receiving the science data from the satellite, applying the appropriate processing algorithms and delivering the resulting products to the users. It consists of the following functions:

- Payload data acquisition and ingestion function for downlink of science data telemetry
- Processing function
- Archiving function
- Dissemination function
- Mission planning function
- Quality control and Calibration/Validation (Cal/Val) function
- Monitoring and control function
- User services

Figure 5.45. PREMIER ground segment architecture.



5.6.3 Flight Operation Segment

The FOS is strongly based on existing ESA hardware and software infrastructure, adapted where necessary for PREMIER.

5.6.3.1 TT&C

The baseline S-band TT&C ground station is located in Kiruna (SE). No modification to the Kiruna ground station equipment is needed to support PREMIER. The primary data source for orbit determination in the routine operations phase is the onboard GNSS receiver. Ranging and Doppler tracking will be used as a backup for orbit determination in emergency operations.

The principal task for TT&C passes in routine operations is telecommand uplink. Realtime housekeeping telemetry will also be acquired during these passes, but is not a driver for the minimum number of required passes. The TT&C ground station is not dedicated to PREMIER, but shared with other missions. Allocation planning – for both TT&C and PDGS – is performed by the Estrack Management and Scheduling System (EMS) in cooperation with the Mission Planning System (MPS). EMS also generates the detailed operation schedules executed by Estrack ground station monitoring and control systems.

5.6.3.2 Mission control system

The Mission Control System (MCS) is based on the Earth Explorer MCS (EEMCS), which is an extension of SCOS-2000. The EEMCS is continuously upgraded with the functionality needed for specific missions. For PREMIER a certain degree of customisation of the system (including some functional modifications) is likely to be necessary according to satellite design, ground interface specifications, the final operations concept, and the existing capabilities of the EEMCS at the start of implementation.

5.6.3.3 Flight dynamics

Flight dynamics is a service provided to missions that delivers orbit information and event files to the various planning entities as well as the orbital predictions used by the Estrack ground stations. It also generates command sequences that are transferred to the MCS directly or via the MPS. Flight dynamics receives spacecraft monitoring data, including GNSS tracking data, and – for emergency operations – ranging and Doppler tracking measurements performed by the ground stations via the MCS. Information about the MetOp orbit is also needed. This is gathered by the PREMIER FOS in order to plan the orbit and formation flying maintenance manoeuvres.

5.6.3.4 Mission planning system

The FOS MPS is based on the Earth Explorer MCS mission planning kernel. It generates schedules for execution by the MAS as well as command sequences for up-link to the satellite. The MPS will require configuration of mission-specific rules and constraints. As for the MCS, some functional modification is likely to be needed but the need for any specific modification cannot be identified at this stage.

Estrack Management and Scheduling is responsible for planning ground station allocation to missions supported by Estrack, and generation of detailed ground station schedules.

5.6.3.5 Simulator

The spacecraft simulator is built using the SIMSAT infrastructure, the existing ground models and the generic dynamics and space environment models. Spacecraft subsystem models will in general need to be developed specifically for PREMIER, though reuse will be possible for heritage subsystems already modelled in predecessor simulators. The onboard flight software is executed on an emulator.

5.6.3.6 FOS operation and implementation

The mission operations will be automated, as far as is reasonable, to minimise risk and to contain the size of the operations team. Operations support is restricted to normal working hours, i.e. five days per week. Out of normal hours, on-call engineers can be alerted automatically should a serious anomaly be detected. A serious anomaly is one that threatens system availability, such as significant data loss or a danger to the health of the spacecraft. The latter should, in principle, be excluded thanks to the spacecraft autonomy. Other anomalies will be investigated during working hours.

Contacts with the FOS ground station via the TT&C will be limited to those necessary for mission plan up-links. A single S-band TT&C ground station, assumed to be located in Kiruna, with one contact per day is assumed. In view of the low frequency of TT&C contacts, regular spacecraft health monitoring is assured via recorded HKTMs, downlinked in X-band and forwarded to the FOS from the PDGS. Frequency and latency are not critical, but nominally the TM would be acquired at each pass and forwarded as a single file after reception. No near-realtime planning is required.

During LEOP, operations are supported by a dedicated ground station network (see Section 5.7). This uses Estrack core and enhanced stations where possible (depending on the chosen launch site). In general, the ground segment architecture is fixed and heavily based on the existing ESA hardware and software. As apparent from the analysis of requirements, however, there is a desire to limit the cost of operations by reducing TT&C access to the spacecraft while increasing the level of onboard autonomy.

Regardless of the operations model selected for the nominal phase, the FOS development will still have to prepare for all reasonable eventualities. However, moving towards support in office hours only and automated monitoring and alarming during nights and weekends is a natural evolution of the operations concept. Apart from this, the design of the FOS is familiar in terms of the functional blocks to be used: the MCS will be based on the MCS Earth Explorer kernel, the Mission Automation System will execute control procedures and schedules, the NAPEOS extension to the ORATOS platform will be used for GNSS data processing, a simple Mission Planning System will be developed from infrastructure elements or an existing Earth observation mission and, in general, the ESA Ground Operations System (EGOS) infrastructure will be employed.

Daily operations will be characterised by the heavy use of orbit-tagged telecommands. Thus, only a simple, weekly FOS mission planning will be required, with no realtime re-planning, or out-of-hours support. In addition, in order to reduce the number of commands to be sent to an absolute minimum, the use of On-Board Control Procedures (OBCP) will be maximised. The only external input to the FOS mission planning, apart from the PDGS, will be the MetOp manoeuvre notifications from Eumetsat. The manoeuvres required to follow the MetOp orbit will be performed at the same time as the orbit control manoeuvres from MetOp and they will be adapted to take into account the formation flying repositioning.

5.6.4 Payload Data Ground Segment

This section details the main functions and the specific features of the PREMIER PDGS.

5.6.4.1 Main drivers

The main performance requirements driving the architecture and operation of the PREMIER PDGS are:

- Data latency: the PREMIER mission has a near-realtime (NRT) delivery requirement to the end users. A goal of three hours and a threshold of five hours are defined for the data latency, i.e. (from sensing to Level-1b data being available to users). This requirement will mainly drive:
 - the data rate needed for the X-band downlink
 - the network of X-band stations,
 - the available processing times of each Level-1b product.
 - the delivery times to the final users.
- Volume of archive data: a substantial volume of data of about 700 TB for four years of operation for Level-0 and Level-1b alone needs to be archived for the PREMIER mission.

5.6.4.2 Ground stations

Science data along with recorded HKTm downlink will be performed via X-band at the ground stations. Antennas with a figure of merit of at least 31 dB/K are required to support the downlink rate of 270 Mbit/s.

The NRT requirement means that least one downlink per orbit has to be implemented so as to limit ageing of data onboard to about 100 minutes. The actual number of required stations also depends on the onboard data generation rate. With the lowest estimated IRLS rate (18.8 Mbit/s), a single high-latitude station such as Svalbard is sufficient to ensure 100% of the data with a maximum latency of three hours (goal). On the other hand, under the high IRLS data-rate scenario (28.8 Mbit/s) a station like Svalbard can only support 47% of data in less than three hours after sensing and a constellation of multiple stations such as Kiruna/Inuvik is considered to support the three hours latency goal for 78% of the science data. The threshold requirement of maximum latency of five hours is fulfilled for 100% of the scientific data in both cases.

5.6.4.3 Processing

Taking into account onboard ageing of data, the fulfilment of the NRT requirement allows for 75 minutes of ground latency for the three-hour goal and 195 minutes for the threshold of five hours. The ground latency is mainly driven by transmission delays between ground stations and the processing centre and the Level-1b processing time.

Assuming conservatively (for the period when PREMIER will fly) a ground link capacity of 34 Mbit/s at the Svalbard station and up to 16 GB of science data per orbit, 63 minutes are required to transfer them from the downlink station to the processing centre. This leaves very little time if processing activities are performed sequentially based on data chunks of one orbit to meet the goal NRT requirement. A viable solution is to transmit the data in slices of, say, 10 minutes, and to process these slices as soon as they are received at the processing centre, so that transmission and processing overlap.

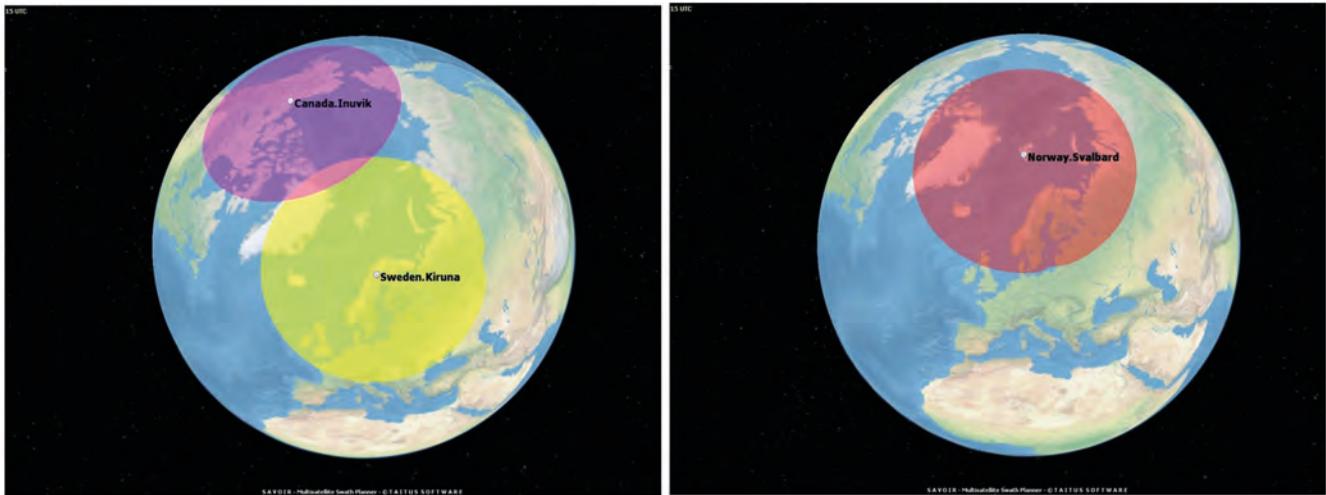


Figure 5.46. Ground visibility maps. Kiruna and Inuvik (left). Svalbard (right).

With this streaming approach, an estimated time of 40 minutes can be allocated to the Level-1b processing. Based on experience with MIPAS, this would require a CPU capacity of 6 GFLOPS for the IRLS Level-1b processing. The STEAMR Level-1b processing is assumed to require an additional 600 MFLOPS. Considering the capacity of already existing processors, this is not considered to be a critical factor.

5.6.4.4 Payload planning

This function is in charge of defining the plan of activities for both the STEAMR and IRLS instruments. It is also in charge of planning X-band downlink activities over acquisition stations.

The payload planning function supports both:

- Mission Time Line (MTL) type of planning i.e. where the time of execution of an onboard command is triggered by an absolute time
- Mission Position Line (MPL) where execution time is specified by an orbit number and a position along that orbit usually in the form of an argument of latitude.

In the case of PREMIER, the payload and downlink planning are expected to rely on MPL planning only. Payload plans are expected to cover one week of activities and to be forwarded to the FOS two weeks in advance of the planned week.

The payload planning function is driven by the operation of the two exclusive IRLS modes, DM and CM. The baseline is to share the IRLS science measurements equally between the two modes, although the minimum duration of each mode is one quarter of an orbit and the maximum one month.

5.6.4.5 User services

ESA pursues a policy of developing a multimission infrastructure for the distribution of data products to end users. It is assumed that such multimission user services will be extended to handle PREMIER data products and end users.

The user services will support data product discovery, access and visualisation as well as general information on the status of the mission status

and the help desk. Several user categories will be supported through different interfaces including web-based client for offline access to a limited number of products and more automatic interfaces such as FTP for the systematic distribution of NRT products to operational users.

5.6.4.6 Archiving

The function provides systematic mid- and long-term archiving of PREMIER products and auxiliary data. This function also interfaces with the services to provide access to products and auxiliary data to users.

The data volumes have been estimated and are identified in Table 5.14. The long-term archive will implement backup policies to ensure that no data are lost.

5.6.4.7 Reprocessing

Besides the reprocessing of limited reference datasets usually handled by the main processing facility, systematic bulk reprocessing following, for example, upgrades of the processors on the ground is supported by a separate infrastructure. In view of the important CPU resources required over a limited amount of time by bulk reprocessing campaigns, the current trend is to procure reprocessing as a service relying on shared resources.

5.6.4.8 Calibration/validation

The main functions of the Cal/Val facility are:

- Processing of inflight calibrations measurements and update of calibration parameters used by the processors (in the form of auxiliary data files) as required. For PREMIER, this covers radiometric (offset, gain) and pointing calibration for the STEAMR and IRLS instruments, as well as spectral calibration of the IRLS instrument.
- Identification and characterisation of deviations based on the processing of inflight calibrations or vicarious measurements that may trigger payload planning requests (e.g. additional inflight calibrations) or possibly processor evolutions.
- Support to Cal/Val users (e.g. provision of special calibration products).
- Configuration control of the instruments calibration databases.

5.6.4.9 Instruments performance and monitoring

The quality control function provides the continuous assessment of the quality of the PREMIER products and ensures that the products meet a minimum level of quality prior to their distribution. The function is generally split into several sub-functions:

- A near-line service in charge of systematic control of all generated products prior to their distribution to users.
- Offline tools allowing specialised operators with the support of external experts to perform manual analysis of specific products triggered, for example, by feedback from users or reports generated from the systematic screening.

Product type	Volume (TB for 4 years)
Level-0	380–460
Level-1b	260

Table 5.14. Level-0 and Level-1b data volumes for archiving.

- The quality control function is supported by the long loop sensor performance function, which allows monitoring of key parameters of the payload and trends such as ageing effects.

5.6.4.10 Monitoring

The main objective of the monitoring function is to ensure that the PDGS fulfils its objectives, in particular, in terms of performance and availability so that the mission requirements can be met.

The following high-level aspects to be monitored can be anticipated.

- Data circulation (interfaces between the various facilities)
- Data dissemination (interfaces between the PDGS and external entities including users)
- Telemetry acquisition versus planning
- Production versus planning and acquisition
- Level-1 data latency (end-to-end) including availability aspects.
- Archiving completion

5.6.4.11 Deployment

The final selection of the PDGS Facilities and hosting centres is generally performed through open competition at the beginning of Phase-C/D.

As a consequence, no explicit assumption concerning the list of PDGS centres and their locations is provided in this report. In view of the data latency requirements, the studies have nevertheless already outlined important aspects concerning:

- Acquisition stations: need for a high-latitude station such as Svalbard or two stations such as Kiruna and Inuvik.
- Link between acquisition stations and processing centres: a capacity of at least 34 Mbit/s will be required.

5.6.5 Mission Data Processing

Data processing is divided into two independent chains, one for the IRLS and another for STEAMR.

5.6.5.1 IRLS

The IRLS data processing chain is divided between an onboard and an on-ground processing chain (Subsection 5.4.3.3.2). Figure 5.47 shows the main steps of the on-ground chain, whose objective is to produce spectrally and radiometrically calibrated spectra from raw interferograms. The main steps are the following:

- From raw downlink data to Level-0
 - Decoding and error correction: The data is decoded and checked for inconsistencies to detect possible transmission errors. Error flags are detected and transferred to enable further processing limitations.
 - Decompression and interferogram reconstruction: In this step the lossless compression process, which is performed onboard to reduce the amount of data to be downlinked, is reversed. Data compression/decompression is effective if the compression zones of the interferogram are well known. Raw decompressed interferograms either in DM or CM are obtained at

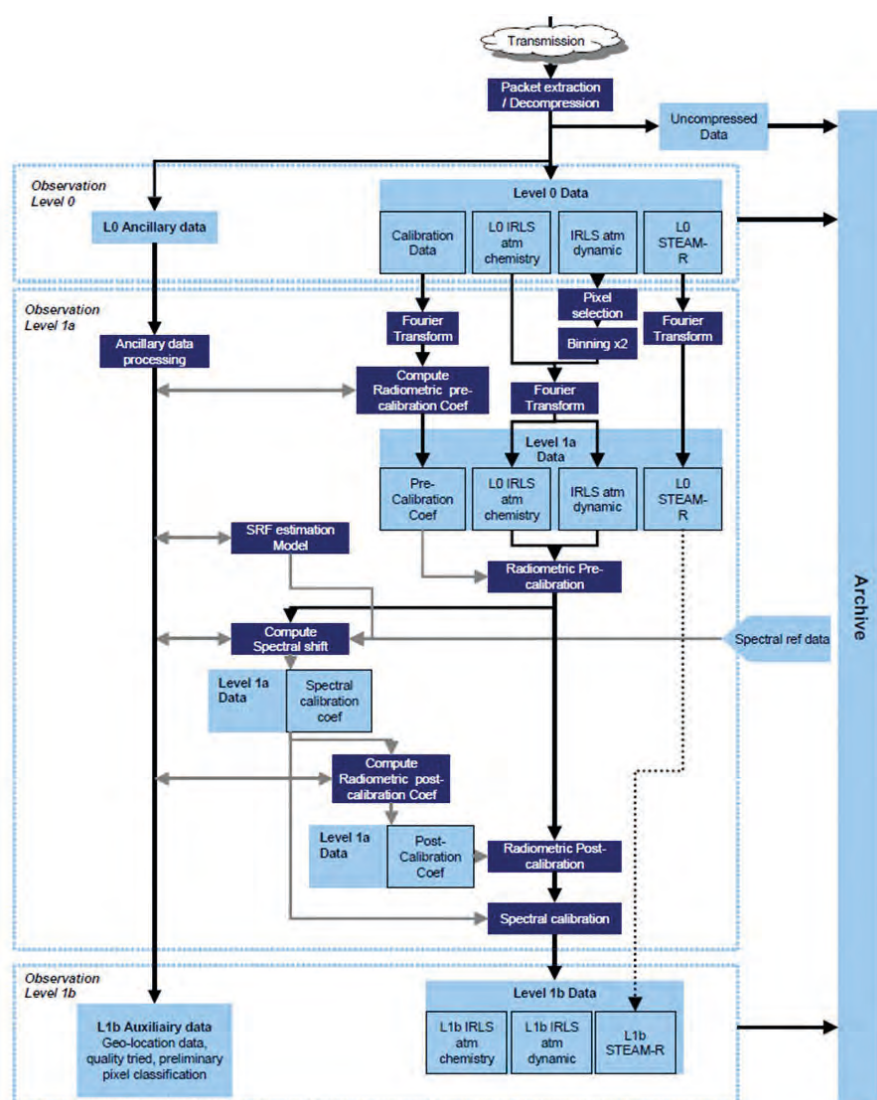


Figure 5.47. Overview of the IRLS ground processing chain.

the end of this step (Level-0 data). Calibration and ancillary data is also de-compressed for use in further steps.

- From Level-0 to Level-1a data: This step consists of building the raw spectra and appending to it the radiometric and spectral calibration parameters. The sequence is as follows:
 - Sub-sample selection and binning: It consists of the application of the cloud-detection algorithm following a selection of cloud free sub-samples and their subsequent binning into samples.
 - Fourier transformation: The interferograms are converted into complex spectra by means of a fast Fourier transformation.
 - Computation of radiometric calibration coefficient: The offset and slope radiometric coefficients are computed from the cold space/blackbody observations. Spectral filtering is applied to reduce the radiometric noise affecting the calibration measurements.
 - Estimation of the spectral response function: The spectral response function is obtained using the on-ground characterisation and the in-flight instrument information.
 - Computation of the spectral shift: Spectral shift computation is performed on atmospheric lines as discussed in Subsection 5.4.3.3.4.

- Data quality analysis: The data of the spatial samples are analysed to verify compliance with the data quality requirement.
- From Level-1a to Level-1b data: This step consists of applying the radiometric and the spectral calibration coefficients to the raw spectra to obtain Level-1b data. It follows the sequence:
 - Radiometric correction: A correction is performed where the radiometric offset of the spectrum is subtracted before the spectrum is calibrated by multiplying it by the slope or radiometric gain coefficient. Then the real part of the spectra is extracted.
 - Spectral calibration and resampling: Spectral shift coefficients are used to resample the spectra to a common spectral grid. Re-sampling is performed on the raw oversampled spectra using spline interpolation.
 - Ancillary data appended: Ancillary data (e.g. geolocation) is appended to the radiometrically and spectrally calibrated spectra for further Level-2 processing.

5.6.5.2 STEAMR

The processing of raw STEAMR data to calibrated, geolocated and time stamped spectra with uncertainty information and diagnostics takes place in four main stages. The process is supported by a database of instrument information that may have been generated before flight or through in flight calibration and characterisation procedures. The steps are as follows:

- Collection of data: Here the data from the instrument itself including time stamped spectra and housekeeping data such as the temperatures of the reference loads, temperatures of telescope component, mechanism settings etc. are gathered and written to the database. In addition relevant information from the spacecraft housekeeping and the post-processed spacecraft and instrument pointing information including orbital position are logged with their timestamps.
- Signal reconstruction: Since the AutoCorrelation Spectrometers (ACS) uses 1.5 bit digitisation the autocorrelation functions need to be corrected for this fact. Relevant information on the digitisation levels and the statistics of the signals received is provided in the instrument housekeeping data. Each of the four cross correlation function generated by the spectrometers is independently corrected and they are then combined to provide the final correlation function and Fourier transformed in the to power spectral density. These spectra are timestamped at the middle of the integration time and stored and marked with the observed source.
- Calibration and error estimation: Because of the high degree of amplification used in microwave radiometers they are sensitive to gain variations and require careful calibration. The basic principle is a two-point calibration using known sources, one of which is a cold space view that at these frequencies essentially provides zero power. Gain variations are corrected by regularly viewing a source of known brightness. This can be cold space or an onboard source. Calibration consists of interpolating the hot and cold sources in an optimal manner to the times of the acquisitions of the atmospheric spectra. The time window, over which reference spectra are interpolated and the manner in which they are weighted, can be adjusted to provide the best performance give the characteristics of each receiver. Contributions from the antenna and other components are modelled and verified through observations of cold space through the antenna as well as the calibration

ports. Statistics of the calibration procedure, such as noise and variations of gain, are stored as input to later processing.

- Geolocation: For each recorded spectrum, spacecraft pointing and position data are interpolated to the timestamp. Using information from the instrument database on the relative pointing of each beam the spectrum is geolocated in the manner that best suits the Level-1b to -2 processing stage.

5.7 Operation and Utilisation Concept

5.7.1 Overview

The operational profile of the PREMIER mission includes the following phases:

- LEOP and commissioning
- Nominal operations
- Contingency operations
- Disposal

A description of each phase is presented in the following sections.

5.7.2 LEOP and Commissioning

The LEOP covers the period from switch-over to internal power on the launch pad until the satellite is in its deployed configuration, in the nominal orbit and with the AOCS operating in Normal Mode. The PREMIER LEOP is estimated to last five days as a minimum and can be divided in two phases. The first phase starts with liftoff and ends with the separation of the satellite from the launch vehicle. The second phase, when the satellite is autonomous, lasts until Sun-pointing acquisition.

The first phase is launcher-controlled. Activities during the launcher-controlled phase are limited to monitoring a few satellite health parameters acquired by the launcher and transmitted together with the launcher telemetry. The duration of this phase depends on the selected launcher, and ranges from 15 minutes to roughly 90 minutes. A typical sequence of events during the first phase is:

- The launch is at night.
- The fairing is jettisoned 4 min after liftoff when the launcher is still in eclipse.
- The launcher exits eclipse about 22 min after liftoff. It is then illuminated by Sun for 71 min. During this illuminated phase, the launcher is able to control its attitude to prevent Sun illumination of the STEAMR main reflector.
- After reentering eclipse, separation is performed.

The second phase starts with an automatic sequence that leads to a safe mode attitude, where the satellite can remain as long as necessary. This phase comprises the following onboard activities:

- Detection of separation from the launcher (through dedicated separation-detection device).
- Solar array deployment.
- Platform units switch on and AOCS initialisation.

- Rates damping.
- Sun-direction search and Sun-pointing acquisition.

Although this sequence is fully automatic and requires no contact with the ground, it is possible to define the timing of activities so that critical activities are performed when in visibility of a support S-band ground station. This may be the case for the solar array deployment.

Once this sequence is completed, the ground takes over for the preparation of normal mode transition. Transition into normal mode is commanded by the ground during one of the S-band contacts. The commissioning phase then starts. The commissioning phase concerns both platform and payload and lasts up to one month. This phase includes the complete characterisation of the performance of the platform, payload and ground segment to verify that the system is ready for the transition into the routine operational phase and that the instrument calibration and validation activities can be started.

The first part of the commissioning phase will be used to perform in-orbit functional and performance tests of all the platform subsystems. Upon completion of the platform commissioning activities, the spacecraft will be in the operational attitude and orbit with the AOCS in normal mode. At this point, the commissioning of the IRLS and STEAMR can begin.

During the payload commissioning phase the following activities will be performed:

- Pointing calibration for IRLS using stars and the Moon and for STEAMR using the Moon and Jupiter.
- Spectral calibration of the IRLS instrument using atmospheric data
- Radiometric calibration of both IRLS and STEAMR.

PREMIER will also achieve its nominal position in the same orbit as MetOp. Therefore, the required in-plane and out-of-plane manoeuvre from the launch orbit to the MetOp orbit will be performed.

5.7.3 Routine Operations/Calibrations

During the operational phase, both instruments acquire data permanently except during the calibration periods and the orbit maintenance manoeuvres.

Calibrations are performed periodically, as shown in Table 5.15, and must be taken into account in the mission planning:

The attitude-change manoeuvres have small amplitude, however the date and time of these manoeuvres have to be selected to avoid direct Sun illumination on the STEAMR main reflector.

In addition, the nominal mission planning includes the following activities:

- Weekly orbit determination and upload of the updated orbit parameters.
- Computation and upload of on/off commands for the S-band transceivers consistently with the predicted S-band passes.
- Computation and upload of scientific data download commands for the predicted X-band passes.

A new mission plan is expected to be produced every week and will cover a period of two weeks.

Instrument	Calibration	Duration	Period of occurrence	Operational impact
IRLS	Radiometric (cold Space)	<1 min	10 min	Internal (pointing unit inside IRLS)
	Radiometric (blackbody)	~5 min	1 day	Internal (pointing unit inside IRLS)
	Pointing (stars)	50 min	1 month	2° pitch bias on the satellite attitude
STEAMR	Pointing (Moon)	50 min	30 days	2° pitch bias on the satellite attitude and scan of target
	Spectral	50 min	1 year	

Table 5.15. Calibration manoeuvres.

5.7.4 Contingency Operations

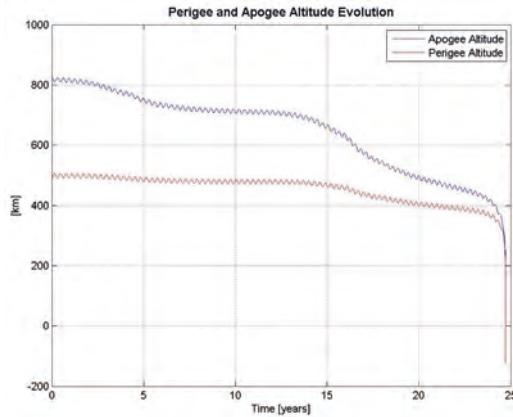
The PREMIER satellite is designed to survive for up to 72 hours without intervention from the ground a single failure occurs. A hierarchical FDIR concept will manage the onboard detection and recovery of failures. In case of major failures, the FDIR triggers the satellite transition into safe mode.

The FDIR design follows a well-established concept based on failure criticality levels and on the corresponding FDIR intervention:

- Level 1: This is the lowest level of the FDIR and covers internal unit failures managed by the unit itself. The mission is not impacted by the recovery actions performed.
- Level 2: At this level some dedicated onboard software monitoring are implemented to detect local failure at unit level. The associated recovery actions to resolve the failure in an adequate manner are generally to switch off the failed unit and in most of the cases to switch on the redundant one in the current operating mode. Typical examples of FDIR Level 2 implementations are AOCS equipment failures.
- Level 3: This level is defined to safeguard the payload whenever the nominal operations are no more possible. In this case the scheduled payload operations are interrupted. Generic recovery actions are defined in order to isolate failures of both the avionics and the Payload. The failures managed by the FDIR level 3 are mainly :
 - Failures of the payload
 - Under voltage of the power bus, which needs disconnection of the non-essential loads
 - Propulsion function failures
- Level 4: This level is defined to safeguard the satellite whenever the failure severity and criticality cannot be managed at the lower FDIR levels. The detection of such cases is performed by the on board computer and handled by the Reconfiguration Units which are the highest on board instance to react on failures. The satellite enters safe mode, the payload is switched off and only the equipment required to ensure the survival of the spacecraft is kept active. In this mode the satellite is placed in a Sun-pointing attitude where it can wait for ground intervention.

The FDIR is design such that the survival of the satellite has priority over the availability of mission data during all phases of the mission lifetime.

Figure 5.48. Perigee and Apogee altitude evolution.



All FDIR functions implemented in the onboard software are triggered by parameter values stored in the On-Board Computer. These functions can be enabled or disabled via TC from ground and may be adapted and set according to the operational needs. A history log stores all FDIR data for investigation on ground. The FOS has the final overall control over all failure recovery activities even if the satellite performs them autonomously.

5.7.5 Disposal

The European Code of Conduct for Space Debris Mitigation requires that a satellite must reenter the atmosphere within 25 years after the end of nominal operations. For PREMIER, this will require a series of orbit manoeuvres to be performed at the end of the mission's lifetime, aimed at lowering the altitude of perigee to 490 km.

Figure 5.48 shows the evolution of the apogee and perigee altitude for PREMIER once the disposal manoeuvre has been performed.

After the last manoeuvre, all satellite units are switched off. The satellite then remains uncontrolled and enters the off-mode upon full battery discharge.

**→ SCIENTIFIC DATA
PROCESSING AND
VALIDATION CONCEPT**

6 Scientific Data Processing and Validation Concept

6.1 Introduction

This chapter outlines the principles and state-of-the-art processing of scientific data from contemporary satellite limb-emission sounders and nadir-sounders, the advances in data-processing schemes to be made for PREMIER and the validation concept. Methodologies for retrieval of atmospheric constituent distributions (i.e. Level-2 products) from spectral radiances (i.e. Level-1 products) are briefly described along with data assimilation. These retrieval and assimilation schemes will produce the data to be exploited scientifically to meet PREMIER's objectives, and by operational centres to demonstrate the added value of PREMIER data.

6.2 Atmospheric Composition Retrieval

6.2.1 Limb-Emission Sounding

Atmospheric emission sounding in IR and mm-wave regions offers a number of advantages, notably measurements can be made regardless of solar illumination and, therefore, globally through the day and night. The radiance seen by the instrument (see Fig. 6.1) is given by:

$$I(\nu) = I_{\infty}(\nu) e^{-\tau(\infty, \nu)} + \int_0^{\infty} k(s, \nu) B(\nu, T) e^{-\tau(s, \nu)} ds \quad (6.1)$$

where $I(\nu)$ is the radiance at frequency ν , s is the distance along the observation path, I_{∞} is the intensity at the far boundary of the observation path, $k(s, \nu)$ is the total absorption coefficient summed over all species, T is the physical temperature, τ is the optical depth given by:

$$\tau(s, \nu) = \int_0^s k(s, \nu) ds \quad (6.2)$$

and B is the Planck function.

Figure 6.1 shows the LOS through the atmosphere for a single limb path. The contribution to observed intensity, $I(\nu)$, at frequency ν from a given atmospheric layer, $\delta I(\nu)$, is proportional to the path length through that layer, δs , the Planck function evaluated at the temperature of that layer, $B(T, \nu)$, and to the absorption coefficient within that layer, $k(s, \nu)$. The latter is a function of the absorbing trace gas concentrations and their spectroscopic parameters as well as pressure and temperature within the layer. The contribution from this path segment to the observed intensity is reduced according to the transmittance

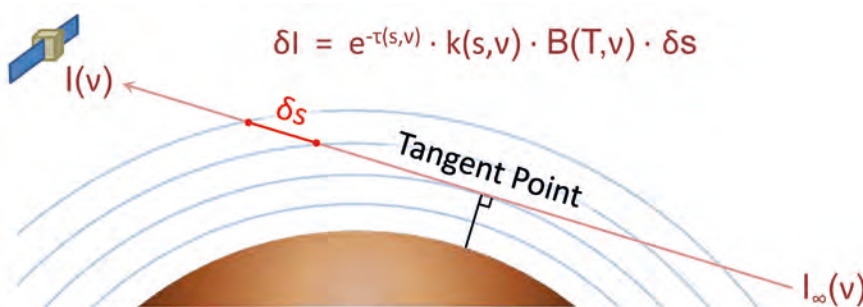


Figure 6.1. The LOS through the atmosphere for a single limb path. For full explanation see text. (D. Gerber)

$\exp(-\tau(s,v))$ between the path segment and the satellite, which depends upon the distribution of absorbing gases, pressure and temperature over the path. The path segment through the shell closest to the tangent-point is much longer than all the other path segments, so the observed intensity is typically weighted strongly towards the tangent-layer contribution, and likewise for all other limb-paths.

In limb geometry, $I_\infty(v)$ is the cosmic background radiation, which is very small and stable by comparison to the path-integrated atmospheric emission term. As the effective path length ds through each atmospheric layer is longer than the vertical path length through that layer, sensitivity to weakly-emitting species is greater for limb- than nadir-geometry. Because path length through a layer increases rapidly towards the tangent-point, which is the lower bound to the integral, weighting functions for limb-views are strongly-peaked at their tangent-points so, if closely-spaced in tangent-height, offer intrinsically high vertical-resolution in comparison to nadir-sounding.

The principles and mathematical basis for inversion of measured limb-emission spectra to obtain the distributions of temperature or trace gases is very well established. One of the most common approaches is optimal estimation (Rodgers, 2000), whereby *a priori* information is combined with information inherent to the measured radiances, with a weighting inversely proportional to their respective error covariances.

A non-linear form of the optimal estimation is given in Eqs. 6.3 and 6.4.

$$x_{i+1} = x_i + (S_a^{-1} + K^T S_y^{-1} K)^{-1} [K^T S_y^{-1} (y - y_i) - S_a^{-1} (x_i - x_a)] \quad (6.3)$$

$$S_x = (S_a^{-1} + K^T S_y^{-1} K)^{-1} \quad (6.4)$$

x_i and x_{i+1} are the atmospheric state-vectors retrieved from the i 'th and $i+1$ 'th iterations and x_a is the *a priori* estimate of the state-vector from independent sources, such as climatology or a model forecast.

y is the vector of measured limb spectral radiances, y_i is the vector of forward model predictions of limb spectral radiances for the atmospheric state x_i .

K is the matrix of Jacobians (i.e. derivatives of y_i with respect to x_i) evaluated at the atmospheric state x_i , and K^T is its transpose.

S_y , S_a and S_x are the error covariance matrices for, respectively, the measurement vector, the *a priori* state-vector and the retrieved state vector.

Iteration commences from a linearisation point, x_0 , which can be estimated from retrievals at neighbouring locations or *a priori* information, and continues until a convergence criterion is met, specified in terms of deviation between the vectors x_i and x_{i+1} . The retrieval is deemed satisfactory if the measured radiances have been fitted to a level consistent with the measurement error covariance matrix and is consistent with the *a priori* estimate at the level expected from its covariance matrix.

6.2.1.1 State-of-the-art

In terms of retrieval methodology, the PREMIER IRLS can be viewed as a fusion of the IR emission limb-sounders High Resolution Dynamics Limb Sounder (HIRDLS, high vertical-resolution) and MIPAS (large spectral bandwidth, high spectral-resolution). The methodologies for retrieval of atmospheric parameters from these instruments are discussed below.

For analysis of HIRDLS data, a single processing scheme is in use (R. Khosravi et al., 2009), while in the MIPAS case, besides the ESA operational Level-2 processor (Raspollini et al., 2006) scientific Level-2 processing schemes exist at several institutions (e.g. Karlsruhe Institute of Technology:

v. Clarmann et al., 2003; Univ. Bologna: Carlotti et al., 2006; Oxford University: www.atm.ox.ac.uk/MORSE; University of Leicester: Moore et al., 2010).

A characteristic that these processors have in common is that atmospheric parameters are retrieved by fitting simulated radiances, as calculated with radiative transfer models, to the observations. By application of iterative non-linear retrieval schemes (e.g. Eqs. 6.3 & 6.4), the atmospheric quantities are modified in such a way that the simulated measurements fit optimally to the observations in terms of minimisation of a quadratic cost-function, usually subject to a constraint from *a priori* information or other regularisation. As a standard approach, target quantities are retrieved in sequential steps, whereby temperature/pressure or temperature/pointing is the first step, followed by trace gases in decreasing order of typical magnitudes of their contributions to the spectral radiance. In parallel with the target quantities, additional parameters are often co-retrieved to increase the quality of the fit and decrease deteriorating effects on the target quantity. These can include spectrally interfering atmospheric traces-gases and aerosols and instrumental parameters such as offsets in radiometric or spectral calibration. Other differences between the processors are related to the radiative transfer models used, including atmospheric discretisation, the spectral regions selected, the choice of the constraint, the representation of the retrieved profiles (i.e. pressure levels or geometric altitude levels and their vertical spacings, e.g. tangent points) (e.g. Kiefer et al., 2010).

A major difference between HIRDLS, a conventional filter radiometer, and MIPAS, an FTIR spectrometer, is the number of their spectral samples. HIRDLS has 21 channels of several cm^{-1} width, whereas MIPAS measures about 50 000 spectral elements in the $700\text{--}2400\text{ cm}^{-1}$ range (Fischer et al., 2008). For HIRDLS, limb-path transmittance functions spectrally-averaged over each channel are pre-computed through line-by-line calculations for a comprehensive range of atmospheric conditions and a look-up table used in the retrieval processor. Figure 6.2 shows a latitude/pressure cross-section compiled from ozone profiles produced by this scheme for an orbit segment of HIRDLS data. For MIPAS, a set of spectral microwindows are pre-selected for each target constituent to maximise information content from that constituent over the vertical range and minimise sensitivity to spectral interference from other constituents, other radiative transfer uncertainties (spectroscopic line parameters, departure from local thermodynamic equilibrium) and

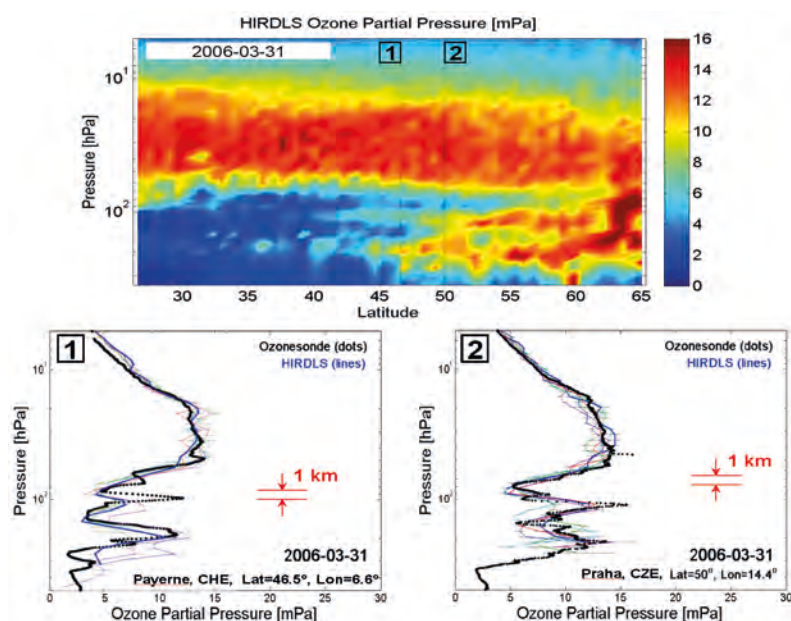


Figure 6.2. This HIRDLS retrieved ozone cross-section shows a multilayer intrusion of low-ozone tropospheric air into the lower stratosphere over Europe in spring 2006. Individual profiles retrieved by HIRDLS are also shown in comparison to ozonesonde profiles at two locations (Payerne and Praha) indicated in the cross-section. These show that vertical structure associated with the intruding layers of tropospheric air has been captured well by HIRDLS. PREMIER aims to match HIRDLS' 1 km vertical resolution, while improving structure retrieved along-track by applying tomography (not available to HIRDLS which views at a fixed 45° azimuth angle) and adding the third, across-track dimension. (B. Nardi & J. Gille; see also Pan et al., 2009)

instrumental uncertainties. Microwindows of width several cm^{-1} are selected for each target gas.

Horizontal inhomogeneities are also handled in different ways. In 1D schemes, based on representing the atmosphere as a set of homogeneous, concentric vertical layers and retrieving a single vertical profile from each limb-scan, errors are minimised either through adaptive selection of spectral windows or by accounting explicitly for horizontal gradients within the forward model. In 2D schemes, a whole atmospheric cross-section (vertical \times horizontal) along the orbit track is retrieved in a single step from the set of limb-scans which span that cross-section. Such schemes employ a 2D radiative transfer model, such that horizontal and vertical variations can be modelled explicitly (Kiefer et al., 2010, and references therein for MIPAS and Khosravi et al., 2009, for HIRDLS).

A common element of all IR schemes is to pre-screen cloud-contaminated observations, which simplifies radiative transfer modelling for temperature and trace-gas retrievals and increases computational efficiency. Criteria and methods for cloud screening differ depending on the level of stringency required, which also depend on which parameters are co-retrieved with target species (Massie et al., 2007, Spang et al., 2004). Moving beyond the detection of clouds/aerosols to support temperature/trace-gas retrievals, cloud properties are also retrieved: cloud top height/pressure, cloud/aerosol extinction, cloud ice-water content, polar stratospheric cloud composition and size information on PSC and cirrus clouds (e.g. Massie et al., 2007, Spang et al., 2010, Höpfner et al., 2006, Mendrok et al., 2007).

Retrieval schemes for satellite limb-emission sounders operating in the mm-wave region employ the same principles and mathematics as those in the IR, and are also similar in practice. The state-of-the-art is described for the Odin Sub-Millimetre Radiometer (SMR) (Urban et al., 2005), the Sub-Millimetre Wave Limb-Emission Sounder (SMILES) (Takahashi et al., 2010, Brito et al., 2011) and Aura MLS (Livesey, 2006). The Aura MLS 2D retrieval scheme was actually the first practical implementation of such a scheme. One practical difference for the mm-wave arises from intrinsically high spectral resolution and comparatively narrow bandwidths of the heterodyne technique, which accommodate monochromatic line-by-line computation of the radiative transfer equation for fitting over the full mm-wave spectral bands, rather than the microwindow approach employed for FTIR. Practical differences arising from the longer wavelength itself are: much lower sensitivity to cirrus, for which less stringent cloud-screening procedures are needed, and use of O_2 rather than CO_2 as a well-mixed gas for temperature profiling and pointing.

Differences in retrieval schemes for the mm-wave limb-sounders, which have flown previously, are principally owing to their selections of frequency bands and their noise performances. SMILES being cooled to 4K and using a superconducting detector gives by far the best precision; allowing retrieval of minor stratospheric gases (e. g. BrO) from individual scans. Selection of limb scanning patterns also has a significant influence, with MLS profiles being retrieved (by a 2D scheme) at ~ 200 km spacing along-track, while SMR and SMILES retrieve profiles at ~ 600 km and ~ 300 km intervals, respectively. Slightly different strategies are used in the inversion procedures. SMILES and SMR use geometric altitude as the vertical coordinate and one pointing bias is retrieved from the spectra, while MLS places the spectra on a tangent pressure grid first, either by using the O_2 spectra or the pressure information inherent in strong spectral lines. Different techniques are also used to deal with uncertainties in the water vapour continuum absorption. Large particles in ice clouds can perturb limb radiances either upwards or downwards. For SMR a technique that uses only the extinction of radiation by cloud ice when observing low tangent heights has been developed (Eriksson, 2007), while MLS uses all tangent heights. The most significant uncertainty in retrieving cloud ice is knowledge of the cloud-affected fraction of the beam.

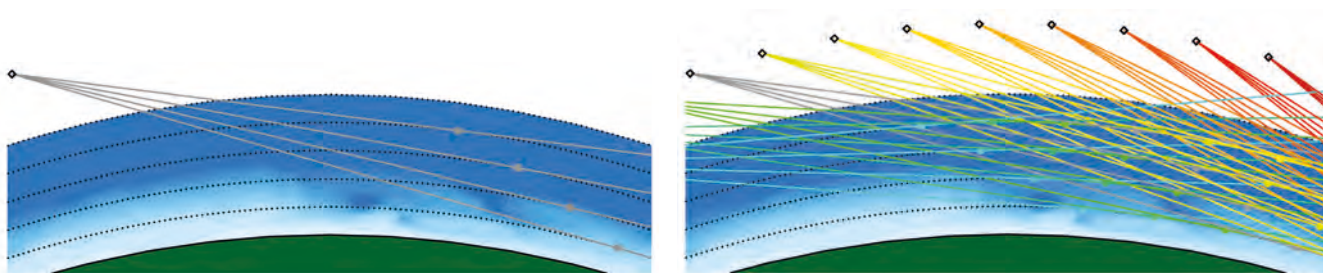


Figure 6.3. The tangent-paths for a vertical array viewing rearwards in the plane of satellite motion. The left panel is for a single measurement period and the right panel is for a series of consecutive measurements. For a conventional limb-scanner, a single vertical-profile is retrieved from an individual limb-scan and atmospheric layers are assumed to be homogeneous, i.e. horizontal variations within an atmospheric shell are neglected in the radiative transfer model. For a tomographic approach, measurements are closely spaced along the orbit track so a given volume of air is viewed from different directions and a 2D atmospheric cross-section is retrieved from the set of limb-views. The radiative transfer model represents horizontal and vertical structure in temperature and constituents. The PREMIER IRLS 2D detector array will sample a number of azimuth angles simultaneously, adding the third dimension (across-track). (R. Siddans)

6.2.1.2 Advances for PREMIER

The PREMIER IRLS will provide truly 3D observations by combining high vertical-resolution (1 km), sampling across-track (25 km for dynamics mode) over a ~360 km-swath and dense sampling along the flight track (50 km for dynamics mode). To fully exploit the horizontal resolution along flight track from overlapping lines of sight (Fig. 6.3), sophisticated 2D tomographic retrieval algorithms will be implemented.

Practical implementations of 2D tomographic retrieval schemes for the large-scale retrieval of atmospheric constituents from satellite measurements were first realised by Ridolfi et al. (2000) for MIPAS and Livesey et al. (2006) for MLS. To exploit the potential of the horizontal measurement density of PREMIER IRLS, it is obvious to follow in these footsteps. Memory and CPU power typically scale with the second or third power of the number of elements in the measurement vector (y) and/or retrieval state-vector (x). If the measurement error covariance matrix, S_y , is assumed to be diagonal, elements of matrices such as $K^T S_y^{-1} K$ can be accumulated sequentially and matrix operations can be limited to the dimension of S_x , which is much smaller though large nonetheless. Current retrieval processors calculate matrix-matrix products and matrix inversions to produce solutions along with diagnostic quantities. These operations limit the size of the state-vector which can be handled at one time (i.e. the length of each segment of an along-track cross-section). The speed of the radiative transfer model is not a limiting factor if fast radiative transfer methods are combined with analytical or algorithmic computation of derivatives (e.g. Francis et al., 2006; Ungermann et al., 2011).

However, recent developments allow to circumvent the abovementioned limitations by using iterative solvers, sparse storage and individual diagnostics (e.g. Livesey & Read, 2000; Ungermann et al., 2010). The most costly operation for tomographic retrievals then becomes the production of diagnostic quantities such as the averaging kernel matrix rather than solving the optimal estimation equations. As an alternative to the exact calculation of diagnostics, approximate methods (e.g. Flath et al., 2011) have been successfully applied to tomographic problems from other fields.

To demonstrate some of these challenges, Fig. 6.4 compares the overall memory consumption and runtime for three example retrievals adjusted to conditions of the IRLS dynamics mode. The number of retrieved quantities is given as n , while the number of observations is given as m . Panel (a) shows that employing sparse techniques can reduce the required memory by more than two orders of magnitude. Panel (b) shows the reduction in computation time for a Jacobian matrix using a fast radiative transfer model via either finite

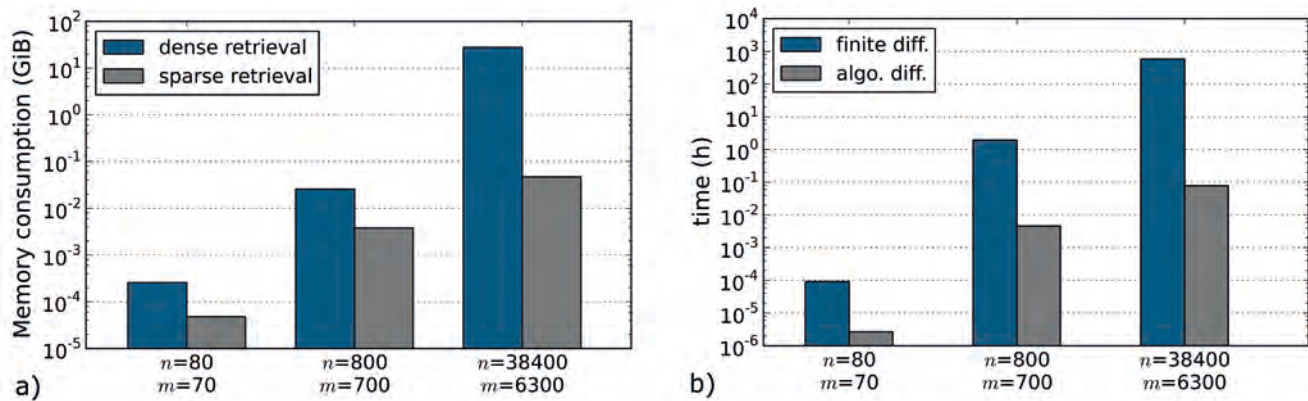


Fig 6.4. Reduction of memory consumption (left) and computational time (right) by advanced techniques for three test cases. The variable n denotes the number of atmospheric quantities and m the number of radiance observations. For explanation see text. (J. Ungermann)

differences or the adjoint method. The numbers chosen in the figure are typical for the IRLS dynamics mode. The columns on the left correspond to a 1D single-target retrieval employing one micro-window only. The number m represents the total number of observed radiance values in the vertical profile, n indicates the number of retrieved values included in the retrieval (a profile of 70 values in the altitude range of the observation and 10 above). Although n may be larger than m , the degree of freedom (independent results) is limited by the number of observations (m). The middle columns show the same for a 1D retrieval of 10 target species employing 10 micro-windows. The columns on the right show the conditions for a 2D retrieval employing a sequence of 90 profiles. The number of retrieved quantities (n) is comparatively high, because we assumed that a horizontal oversampling by a factor of 4 provides the best result. This has been shown in a retrieval study investigating the detectability of gravity waves by PREMIER (Ungermann et al., 2010). The scale for both plots is logarithmic.

The approach sketched in Fig 6.4 has the largest impact on the dynamics mode, which is most time consuming (compared to the IRLS chemistry mode and STEAMR). First performance studies indicate that multi trace-gas retrievals are feasible on a small to mid-size cluster (considerably faster than in real time). Real-time simple diagnostics are also already feasible on similar hardware.

Processing time will be minimised in practice by first performing 1D retrievals, to provide the linearisation point from which 2D tomographic retrievals would proceed, and thereby confining the number of iterations required. The linearisation point and *a priori* for 1D retrievals will combine information from earlier PREMIER retrievals and operational analyses.

For STEAMR, as for the IRLS, tomographic inversion tools will be refined to achieve the highest data quality, while being less demanding computationally owing to the smaller measurement vector, y . To achieve the required tropospheric retrieval accuracy, STEAMR spectral fitting will need to separate target spectral lines as cleanly as possible from interfering lines and retrieve frequency-dependent *continua* due to water vapour, dry air and cirrus, which would be facilitated by separating upper and lower side-bands.

Use of arrays by IRLS and STEAMR will minimise retrieval errors from uncertainty in knowledge of tangent-point vertical spacings. Instrumental parameters, which vary between array elements, are accommodated in the retrieval state-vector (Kerridge et al., 2012).

6.2.1.3 Advances for PREMIER through infrared and mm-wave

PREMIER will be the first satellite mission designed specifically to exploit the complementary attributes of IR and mm-wave limb-emission sounders (Section 4.4.3) that have been demonstrated in several airborne campaigns (Chapter 7). To exploit the complementary sensitivities of IRLS and STEAMR to aerosols and cirrus and thereby optimise sounding of the mid-upper troposphere for trace gases observed in common (H_2O , O_3 , HNO_3 and HCN), approaches will be developed to combine information from the two sensors in the retrieval domain as well as in the assimilation domain (Section 6.3). Once consistency of the individual sensors is verified, one of two parallel approaches will be applied in the retrieval domain which are equivalent in terms of their theoretical information content in an optimal estimation framework (e.g. Rodgers, 2000). The baseline approach will be to combine Level-2 data from the two sensors post hoc. The alternative is to use distributions retrieved from STEAMR as *a priori* information for IRLS. In the presence of cirrus or aerosol of significant IR limb-opacity (e. g. smoke, dust, ash), the IRLS retrieval would add information at altitudes above. In their absence, the IRLS retrieval would extend information deeper into the troposphere than the STEAMR lower limit.

6.2.2 Nadir-sounding and Limb–Nadir Synergy

Schemes to retrieve atmospheric trace-gas distributions from satellite nadir-sounding observations are well-advanced in Europe, following the launches of ERS-2 (1995), Envisat (2002) and MetOp-A (2006). Operational Level-1b and Level-2 processors have been established in each case to produce data for subsets of important target gases. The focus of scientific activity is currently on: (a) refining radiometric calibration and retrieval algorithms for individual trace gases and sensors to achieve accuracies required for designated essential climate variables in ESA's Climate Change Initiative; (b) developing retrieval schemes for additional, detectable gases (e.g. Clerbaux et al., 2009) and (c) combining collocated observations from different types of sensors to (i) optimise vertical resolution (IR and shortwave spectrometry) and (ii) represent better cloud, aerosol and surface properties (high-resolution visible/IR imagery).

Further advances are planned for Sentinel-5 Precursor (S-5P), which is due to be launched in 2015, to exploit denser spatial sampling and much-improved short-wave IR measurements of CH_4 and CO . For Sentinel-5 UVNS and companion MWS, Infrared Sounder (IRS), Visible and Infrared Imager (VII) and 3MI sensors, due for launch on MetOp-SG around 2020, dedicated Level-2 processors will be developed to exploit the observational advances of these individual sensors and their combination. These developments will be designed to take full advantage of increased processing power and data capacity available at that time. Production of Level-1 data and a fraction of Level-2 data for these operational satellite missions will be performed in near-real time to serve the needs of the GMES Atmosphere Service and NWP operational centres for forecasting applications.

We can therefore be confident that Level-1b and Level-2 processors for the MetOp-SG sensors will be in an advanced state of readiness by the time of launch, for exploitation in combination with PREMIER.

Schemes are being devised to combine information from limb- and nadir-sounders on Envisat and MetOp (Ceccherini et al., 2010) and on NASA's Aura (Ziemke et al., 2011) in the retrieval domain as well as the assimilation domain (Sections 2.3.4, 6.3 and 8.3). Although these pioneering schemes have begun to indicate the potential of the limb–nadir combination, an important limitation is that neither Envisat, MetOp nor Aura provide observations that are well

collocated in space or time, which PREMIER-MetOp/MetOp-SG is designed to accomplish.

As for the mm-wave–IR combination outlined in Subsection 6.2.1, two parallel approaches will be pursued, which are equivalent in terms of their theoretical information content in an optimal estimation framework. However, in this case, there is expected to be substantial benefit from adopting retrieved distributions from the limb-emission sounders as *a priori* information for the nadir-sounders, since this will constrain the vertical distributions of trace gases through the stratosphere and mid/upper troposphere. This will enable independent, collocated information from the nadir sounders to be concentrated below the limb-range, i. e. the lower troposphere. Simulations in Chapter 7 show quantitatively the positive impact on retrieval of (lower) tropospheric O₃, CH₄, CO and HNO₃ of PREMIER limb-emission observations in combination with MetOp-SG nadir observations.

6.3 Data Assimilation

Data assimilation methods have been used since the early days of NWP, in the 1950s (see for instance Cressman, 1959). Data Assimilation (DA) refers to a range of mathematical procedures of varying complexity that allow information from different sources, observations, numerical models or any other prior information to be combined and provide numerical fields that are consistent with all of these, within their statistical error margins. Lahoz et al. (2007) describes DA as the procedure to ‘find the best representation of the state of an evolving system given measurements made and prior information on the system, taking account of errors in the measurements and the prior information’. Data assimilation has been particularly important for meteorological forecasting as it is an initial value problem: the quality of the forecast principally depends upon the quality of the atmospheric state at the initial instant. Methods have been made gradually more complex to consider varied observations types simultaneously (satellites, aircraft, sondes, surface sites), and also to ingest data at the right time and to account for the vertical and horizontal sensitivities of the measurements.

There are two main classes of DA methods: sequential (observations are taken into account one after the other as they occur) and variational (observations taken within a certain time window are used at the same time to minimise a cost function, which quantifies the mismatch between the different sources of information). Bayesian estimation, as described for instance in (Rodgers, 2000), provides a rigorous mathematical approach to data assimilation. However, its implementation for realistic full-scale geophysical systems is not tractable, owing to the size of these systems, so drastic simplifying hypotheses have to be made. The most commonly used algorithms, such as optimal interpolation (OI), variational techniques (3D- or 4D-var) or Kalman Filter and Smoother, are based upon statistical linear estimation. This assumes that the systems are linear and that the errors are Gaussian. Ensemble assimilation methods (such as the Ensemble Kalman Filter) are also increasingly used; they assess statistical properties of the system using the spread of an ensemble of realisations of the system, basing upon a Monte Carlo mathematical approach. All these techniques are used operationally in NWP centres worldwide, providing meteorological forecasts of ever increasing skill and accuracy owing to improvements in observing systems and models as well as DA techniques (Simmons & Hollingsworth, 2002).

Lahoz et al. (2007) reviewed similarities and differences in DA applied to meteorology and atmospheric composition, focusing, in particular, on stratospheric applications. Work on this topic only started in the 1990s (Austin, 1992), while observational data had been available for a decade or more, in particular, observations of stratospheric ozone both from radiosondes

and satellites. A key reason for the delay was that computer power was not sufficient for 3D chemistry-transport models to provide prior information of sufficient resolution and quality or to cope with the size of the 'state', which is much larger in the case of atmospheric composition than meteorology. However, chemical-data assimilation has been developing very fast in the last ten years. (Geer et al., 2006) presented the first international intercomparison of analyses (the result of DA) of ozone profile data from Envisat-MIPAS, which involved more than ten groups.

There is thus already extensive experience in Europe and in the international community to take advantage of satellite Level-1b data (radiances) or Level-2 data (profile, column) on the main atmospheric constituents. The benefit is primarily to fill information gaps (Lahoz et al., 2007) resulting from the fact that the observing systems provide discrete information in both time and space. DA thereby extends the range of process studies that can be conducted with satellite observations and models. As an example, El Amraoui et al. (2008) investigated dynamic and chemical processes in the polar stratospheric vortex during the unusually cold winter 2004–05, using ozone and N₂O data from Aura-MLS. Tools of the type needed to assimilate PREMIER limb-sounding data and to deliver the expected benefits on the different science foci of the mission are available. Furthermore, advances are expected in methodologies, data handling and computer power by the time of PREMIER and MetOp/MetOp-SG (2019–23). They will allow refinements of the current chemistry-transport and NWP models and assimilation systems in better horizontal and vertical resolutions and better representation of coupled radiative, dynamic, microphysical and chemical processes.

DA tools are used not only to add value to raw observational datasets, but also to diagnose issues in observation streams. In the process of DA, observations are compared to prior model estimates. This provides a means to monitor the quality of data by detecting jumps, anomalous values or biases. Monitoring the quality of data assimilated in current NWP systems is now an integral part of the work of operational centres, who feedback routinely to space agencies and other data providers when suspect data are detected. The developments around GMES allow operational activities to be foreseen for atmospheric composition, by transferring the current practices of NWP to this new application field. The required timeliness for PREMIER data will allow the resulting observations to enter operational data assimilation systems, in particular at the ECMWF but also in a range of centres in Europe and worldwide. Feedback will therefore be readily available to monitor data quality, in the context of the wider Global Observing Systems for atmospheric composition (see Chapter 8). The analyses obtained with PREMIER data will also extend validation by allowing comparisons with a range of independent remote-sensing or *in situ* measurements which are not collocated in space and time with those of PREMIER; very much in the manner used by Geer et al. (2006) to compare assimilated Envisat-MIPAS data with the Halogen Occultation Experiment (HALOE) and ozone sondes measurements.

A range of DA methods and tools will be used to exploit fully the unique value of the PREMIER observations: to address the scientific objectives of the mission; to contribute to validation and to provide data quality metrics for continuous monitoring throughout the mission.

6.4 Validation Concept

Data validation techniques for limb-emission sounders are well-established. However, validation of PREMIER data on the fine spatial scales required will be challenging. It will need to be based on correlative data from airborne instruments that are at least equivalent in terms of their spatial resolution, precision and accuracy. Established and new techniques for PREMIER are

described below. Prior to validation, self-consistency checks will be performed. For example, the across-track mean and variability of IRLS limb-radiances (Level-1) and retrieved geophysical quantities (Level-2) will be assessed and coincident profiles of temperature, H₂O, O₃, HNO₃ and HCN retrieved by IRLS and STEAMR will be compared for cloud-free conditions. PREMIER validation activities will be planned well before launch and will address pre-launch activities, self-consistency tests, identification and selection of the most appropriate validation techniques, organisation of dedicated validation campaigns and data base management.

6.4.1 Established Techniques for Limb-emission Sounders

The aims of atmospheric profile validation are: (a) to determine, understand and potentially correct any bias and (b) to quantify the precision independently and compare with that estimated from the PREMIER data (e.g. v. Clarmann, 2006). Validation strategies have to consider:

- The validation measurements should have been validated independently and fully-characterised in terms of error estimation and averaging kernels.
- The coincidence criteria for validation must be defined. For validation measurements that are not precisely collocated in time and space, either interpolation has to be applied, e.g. by trajectory modelling or by data assimilation (Section 6.3) or recourse has to be made to compare on a statistical basis.
- Consideration of the different vertical (and horizontal) averaging kernels of both PREMIER observations and validation measurements will be crucial.

Extensive validation exercises have been performed for e. g. Envisat-MIPAS operational and scientific data products (ACP, 2006). Typical validation measurements are identified below according to the carrier/platform:

- Ground-based observations mainly comprise remote-sensors e.g. installed at the Network for the Detection of Atmospheric Composition Change (NDACC) sites. They range from highly-resolved profiles by active instruments (lidars for T, O₃ and H₂O) to poorly-resolved vertical distributions or columns of many trace gases retrieved from solar occultation FTIR, MW-radiometers or UV-visible Differential Optical Absorption Spectrometers (DOAS).
- Airborne sensors (sondes, high-altitude balloons and aircraft) deliver horizontally- or vertically-highly resolved one-dimensional datasets for temperature, humidity or ozone and also for other trace species such as CH₄ and N₂O. Figure 6.2 illustrates the use of ozonesondes to validate vertical structure at two locations in the associated HIRDLS cross-section. Remote-sensing data from balloon and high-flying aircraft using the UV-visible, mid/far-IR emission/solar occultation or microwave spectral regions contribute with a variety of trace gases, extending the 1D *in situ* observations to 2D cross-sections along the flight path. In order to get optimum coincident datasets, special validation campaigns including airborne instruments have been coordinated for MIPAS by ESA.
- Commercial aircraft observation programmes such as MOZAIC, CARIBIC and IAGOS provide non-coincident *in situ* observations for statistical comparisons.
- Satellite sensors, principally other limb-sounders, have also contributed significantly to MIPAS validation. Coincidences between observations from different satellites are rare. However, statistical satellite-satellite

intercomparisons have proven useful for identifying biases. For PREMIER, spatial resolution will have to be downgraded for comparisons with other satellite sensors.

6.4.2 New Techniques for PREMIER

Previous limb-emission sounders have used telescopes with scanning mirrors or 1D detector arrays to obtain vertical profiles with restricted horizontal sampling and so validation focused strongly on vertical profile aspect. Observations by the precursors to PREMIER IRLS and STEAMR (Gloria-AB and Marschals, respectively) from an aircraft such as Geophysika flying up to an altitude of 20 km can be made with appropriately high horizontal-resolution (<25 km) as well as vertical resolution (< 1 km) for validation of PREMIER data in the UTLS region. Measurements by completely independent *in situ* techniques on airborne platforms such as Geophysika or HALO (up to 14 km) can offer even higher resolution either vertically or horizontally. By adopting a dedicated flight pattern, these high-flying aircraft have potential to validate 2D and 3D structures in PREMIER UTLS data.

Campaigns will need to be planned for geophysical situations where high spatial-variability can be expected. By the time of PREMIER, observations from high-flying manned aircraft will be augmented by those from unmanned aerial vehicles (UAVs) such as NASA's GlobalHawk and the EuroHawk, which will provide much longer flight durations and ranges.

To validate the temperature structure associated with gravity waves, lidar and rocketsonde data will also be used. Hemispheric distributions of momentum flux in the lower stratosphere will be compared, for example, to values derived from super-pressure balloons.

For the validation of small VOCs (including e.g. H₂CO and CH₃OH), very compact and sensitive proton-transfer-reaction mass spectrometers are being developed for *in situ* measurements from commercial (e.g. CARIBIC) and research (HALO) aircraft (Brito & Zahn, 2011), in addition to existing techniques for C₂–C₈ compounds (see e.g. Baker et al., 2011). Similarly, a new diode-laser spectrometer for *in situ* measurements of water vapour and its isotopic variations (²D, ¹⁸O) is already routinely operated on CARIBIC (Dyroff et al., 2010), while a second version for HALO has been constructed and will make its first flight in summer 2012.

**→ PERFORMANCE
ESTIMATION**

7 Performance Estimation

7.1 Background

The capability of PREMIER to address the scientific objectives identified in Chapter 3, and also to serve the operational applications identified in Chapter 8, has been assessed at three levels: firstly, the performance of the system concept described in Chapter 5 has been assessed in relation to the Level-1b requirements specified in Chapter 4 (Section 7.2); secondly, retrieval simulations have been performed on the basis of these sensor specifications and estimated errors on individual profiles have been compared to the Level-2 requirements defined in Chapter 4 (Section 7.3) and, thirdly, the scientific impact of retrieved constituent and temperature fields has been quantitatively assessed in case studies (Sections 7.4 and 7.5). The performance assessment described in this chapter draws upon results from ESA funded scientific studies (*CORSA*, Kerridge et al., 2012; *Impact*, Riese et al., 2011 and *Gravity Wave*, Preusse et al., 2012) and nationally-funded scientific activities as well as information from the Phase-A industry studies (EADS Astrium SAS, 2012; Thales Alenia Space Italy, 2012) and the end-to-end performance simulator development (GMV 2012) and results from the Swedish nationally-funded STEAMR programme. Furthermore, precursor airborne infrared and mm-wave limb-sounders have been used in dedicated campaigns to demonstrate new observing capabilities of the PREMIER mission. Results from the March 2010 campaign (*PREMIER_Ex*, Spang et al., 2011; Cortesi et al., 2011) are included in Section 7.4.

7.2 Level-1b Performance

7.2.1 Introduction

This section presents the main system and instrument (IRLS/STEAMR) Level-1b performance achieved by the mission concepts described in Chapter 5. It compares the expected performance against the requirements and provides, when relevant, justification or further explanation on key performance parameters. Subsection 7.2.2 discusses the data latency and the mission availability, followed by the IRLS and STEAMR performance in Subsections 7.2.3 and 7.2.4, respectively. Subsection 7.2.5 shows the geolocation, LOS stability and co-registration performance and finally Subsection 7.2.6 discusses the end-to-end performance simulator.

7.2.2 System Performance

7.2.2.1 Data latency

The data latency at Level-1b is the time elapsed from the onboard acquisition of the data to the availability of the processed data in the ground segment. The latency is broken down into three contributors: the time between the onboard acquisition and the downlink at the ground station; the time required to send the data from the ground station to the PDGS and finally the time required at the PDGS to process and store the data.

During an orbit repeat cycle (29 days), a specific point of Earth's atmosphere is observed several times with different latency. Figure 7.1 shows the worldwide distribution of the maximum (top) and minimum (bottom) data latency over a repeat cycle for Concept A; 99.7% of the observed geographical area has a

Figure 7.1. Worldwide distribution of the maximum (top) and minimum (bottom) data latency for the Kiruna and Inuvik ground station scenarios.

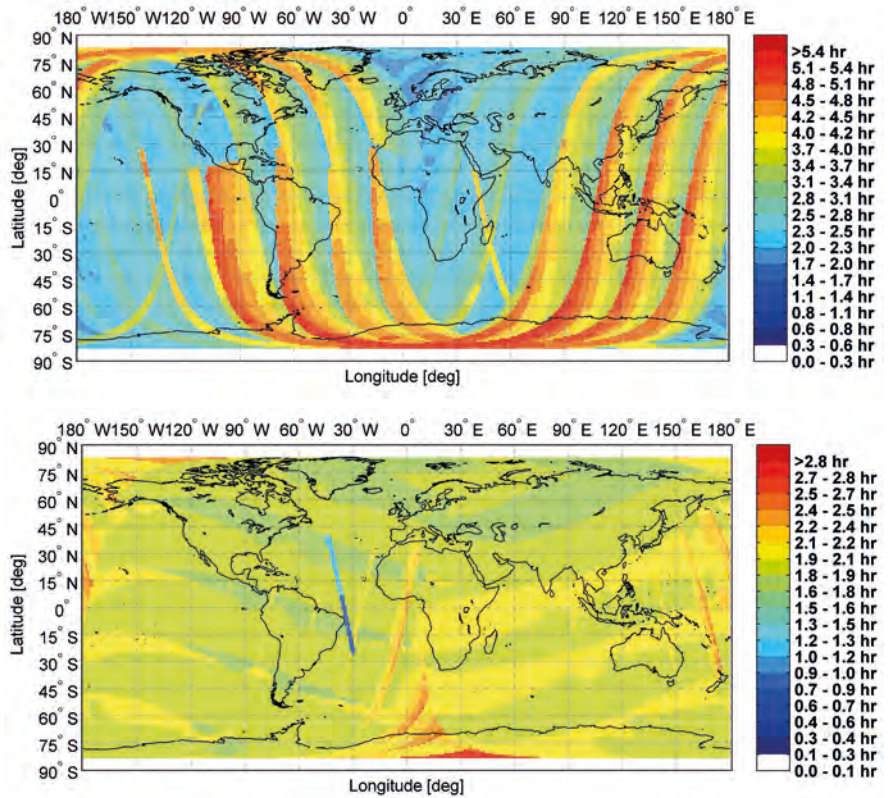
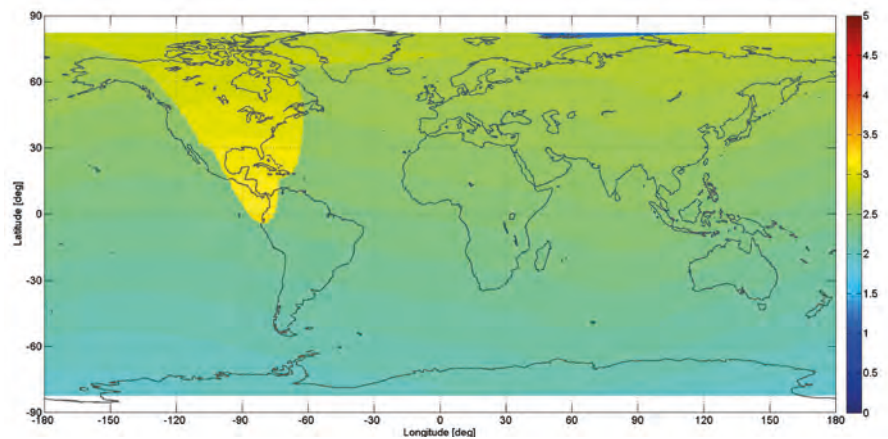


Figure 7.2. Worldwide distribution of the maximum timeliness for the Svalbard ground station scenario.



maximum latency better than five hours, while 78.63% has a minimum latency better than three hours.

The estimate of the processing time for both concepts has been based on the processing times of similar existing instruments, while the ground data transmission speed is based on capabilities today, which are expected to have improved by 2019.

The data latency requirement is met for both concept scenarios under current assumptions on ground station processing capabilities.

Figure 7.2 shows the worldwide distribution of the maximum data latency over a repeat cycle for Concept B; 95% of the observed geographical area has a maximum latency better than 3 hours, while the remaining 5% is better than 3.5 hours.

7.2.2.2 Mean operational availability

The mean operational availability is defined as the percentage of time during which the system (space segment and ground segment) acquires and delivers Level-1b data simultaneously for IRLS and STEAMR. The mean operational availability includes deterministic (e.g. calibration, orbit maintenance) and statistical data outages (e.g. owing to safe mode occurrence, recoverable hardware anomalies).

The average mean operational availability over four years is estimated to be about 90%.

7.2.3 IRLS

7.2.3.1 Overview

This section presents the main performance of IRLS at Level-1b achieved by the baseline concept described in Chapter 5. The requirements and performance are compared, an explanation of the achieved performance is provided and the feasibility, margins and criticalities, if any, are highlighted.

7.2.3.2 Geometric performance

Table 7.1 summarises the main geometric requirements and achieved performance. All the geometric requirements are met, including the increase in vertical width if a special detector macro-pixel configuration is implemented for Concept A.

7.2.3.2.1 Coverage and sampling

PREMIER IRLS will observe the same range of altitudes (48 km corresponding to 4–52 km at the poles and 8–56 km at the equator) throughout the entire swath. This requires slightly oversizing the instrument FOV in the vertical direction to take account of the effect of Earth's curvature. As a result, the total vertical coverage achieved is in the range of 50–52 km.

A vertical sampling distance of better than 700 m will be realised by the optics magnification, and by a corresponding match of the detector configuration. Horizontal sampling distances are multiples of 15 km or 16 km corresponding to the smallest detector macro unit. The along-track sampling distance of 100 km in CM and less than 50 km in DM will be realised by an adaptation of the interferogram acquisitions and subsequent on-track binning.

The vertical width increase results from the fact that the orthogonal detector configuration does not account for the curvature of Earth, and as a consequence a horizontally extended detector macro-pixel will broaden the vertical PSF. Current concepts are compatible with the requirement in CM, but to achieve the performance in DM it is necessary to apply a shift of samples at detector pixel level, which requires a special format of the detector for Concept A.

7.2.3.2.2 Spatial resolution and PSF

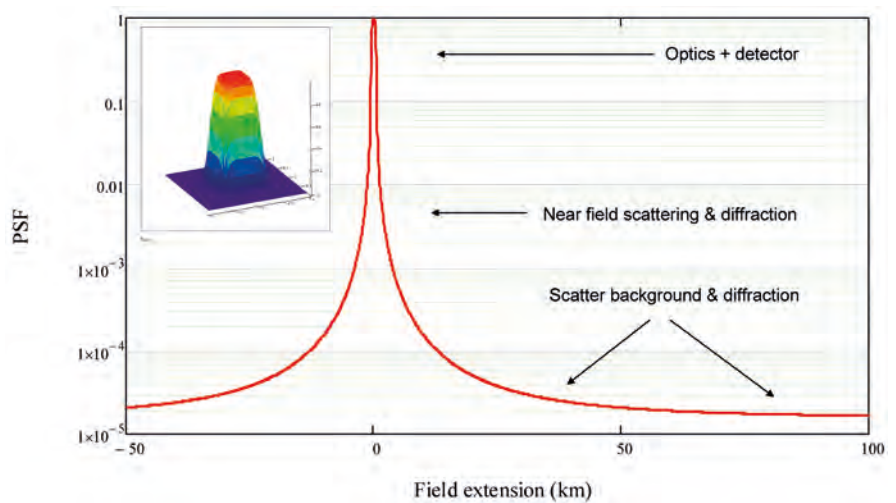
A vertical resolution of less than 900 m is achieved by a vertical sampling of about 700 m, an aperture with a vertical extension in the order of 150 mm, and an optical design such that the imaging performance is close to the diffraction limit.

Figure 7.3 shows the PSF including the near-field and the far-field contribution. It is presented on a logarithmic scale because the PSF drops down by several orders of magnitude and the far-field sensitivity is as important as the near-field sensitivity. The far-field and the near-field contributions lead

Geometric parameter	Requirement	Performance Concept A/Concept B
Vertical coverage	48 km	50–52.5 km
Horizontal coverage	360 km [240 km]	352–360 km
Vertical sampling distance CM	0.6 km [0.8 km] (lower half of the altitude range)	≤0.7 km
	1.2 km [1.6 km] (upper half of altitude range)	≤1.4 km
Vertical sampling distance DM	0.8 km Band-A [1.6 km] (upper half of altitude range)	<0.7 km (Band-A) <1.4 km (Band-B)
Horizontal sampling distance CM	72–96 km	≤96 km
Horizontal sampling distance DM	24–32 km	≤32 km
Horizontal sub-sampling distance CM and DM	12–16 km	≤16 km
Along-track sampling distance	50 km [100 km] CM	100 km
	50 km DM	50 km
FWHM of vertical PSF	0.7 km [0.9 km]	≤0.85 km
Vertical width increase CM	<5% [10%]	<7%
Vertical width increase DM	<5% [10%]	12–22%
		≤10% with special detector format
Spatial cross talk (vertical)	1st neighbour	≤8.7%
	2nd neighbour	≤2.2%
	3rd neighbour	≤1.2%
	4th neighbour	<0.6%
	5th neighbour	~0.5%
Vertical co-registration	75 m [150]m intraband 250 m interband	80 m 250 m
	25 m [50 m] intraband 100 m interband	50 m 100 m

Table 7.1. Summary of the main geometric requirements and achieved performance.

Figure 7.3. The vertical PSF of IRLS with indications of the dominant contributors. The insert (top left) shows the 2D response of a single detector pixel on a linear scale that corresponds to the area very close to the peak (up to ~1 km).



to a certain degradation of the PSF compared to the ideal diffraction limited performance in the angular range up to a few degrees.

The PSF shown in Fig. 7.3 has been constructed from results of the optical design simulations and the straylight analysis performed during Phase-A. The PSF will change slightly with the field location (altitude). The basic shape is determined by the diffraction limit and the detector response. Mirror roughness and contamination affect the near- and far-field contribution in a similar manner and generate an almost flat contribution to the PSF. The baffle scattering and other effects such as ghosts from the optics, which can deteriorate the PSF, have been minimised in the optical designs and are not included in the figure.

7.2.3.2.3 Spatial cross-talk

Assuming that the instrument is exposed to a black-and-white (illuminated/not illuminated) scene with the edge between white and black placed in the middle of a pixel '0', then the spatial cross-talk is defined as the percentage of radiation, seen by the pixels that are not illuminated, compared or normalised to a fully illuminated pixel. The cross-talk is calculated by the convolution of the PSF with this step-function and the corresponding analysis of the true instrumental step-function to derive the signal (cross-talk) seen by the neighbouring pixels.

The cross-talk computation is further illustrated in Fig. 7.4 where the PSF shown in Fig. 7.3 is convoluted with an ideal step-function. The resulting cross-talk values up to 35 km away are plotted in the figure. According to current assumptions, the cross-talk requirements are fulfilled as can be seen in Fig. 7.4 by comparing the instrument response to the step-function with the green dots/line, which correspond to the goal requirements.

7.2.3.2.4 Interband/intraband spatial co-registration

Spatial co-registrations are formulated as interband and intraband co-registration, ensuring that the registrations of different spectral features are related to the same target.

Intraband co-registration (between two spectral channels of the same band) depends on the capability of the instrument and its optics to propagate the radiation independently of its wavelength. Aberrations alter the image formation and prevent perfect co-registration. The optical designs have been analysed with respect to their susceptibility to aberrations, and it has been shown that they are compliant with the intrachannel requirements as given in Table 7.1.

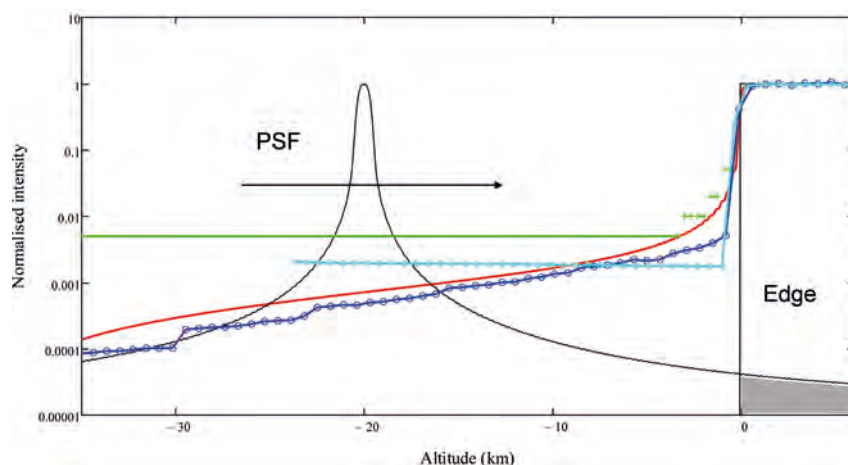


Figure 7.4. The convolution process and resulting instrument response to a step-function located at the centre of pixel 0 (red). The PSF is convoluted across the edge and the overlap with the edge step is integrated across a field of ± 40 km. The edge-function is compared to a ray-tracing simulation, which shows the contribution from light scattering (blue). Cross-talk requirements are indicated by the green dots and line.

Spectral parameter	Requirement	Performance
Wavenumber range	710 cm ⁻¹ [730 cm ⁻¹] to 1650 cm ⁻¹	710 cm ⁻¹ to 1650 cm ⁻¹
Band gap	Up to 90 cm ⁻¹ in the region 980–1100 cm ⁻¹	980/1010–1070 cm ⁻¹
Spectral resolution	≤0.25 cm ⁻¹ [0.27 cm ⁻¹] (CM) ≤1.58 cm ⁻¹ [1.73 cm ⁻¹] (DM)	≤0.26 cm ⁻¹ ≤1.67 cm ⁻¹
Spectral accuracy	0.008 cm ⁻¹ (CM) 0.01 cm ⁻¹ (DM)	0.008 cm ⁻¹ (CM) 0.01 cm ⁻¹ (DM)
ILS characterisation accuracy	1% of width	≤0.3%
	1% of ILS maximum value	<1%
ILS asymmetry	<5%	<4%

Table 7.2. Summary of the main spectral requirements and achieved performance for both Concepts A and B.

Interband co-registration (between two spectral channels of different bands) requirements are more difficult to meet than the intraband co-registration. It is affected by the misalignment between the focal plane assemblies of Band-A and Band-B, and the back optics located after the dichroic beam splitter inside the cryostat. An interband co-registration of 25 m corresponds to a focal plane misalignment of the order of 3 μm. Concepts A and B are both expected to meet the threshold knowledge requirement of 50 m by means of a high thermal and mechanical stability for the focal plane (Chapter 5) and by performing in-flight observations with both bands of well-structured targets such as the Moon, so that correlation between the obtained images in both bands can be revealed.

7.2.3.3 Spectral performance

7.2.3.3.1 Wave number range, number of bands and band gap

A wave number range down to 710 cm⁻¹ has been implemented. The band gaps are slightly different for the two concepts. The transition range is limited to about 70–90 cm⁻¹, which is considered small but feasible. A deeper analysis is required on the spectral band splitting properties of the dichroic beam splitter to investigate and predict the expected performance in more detail.

7.2.3.3.2 Spectral resolution

The CM drives the spectral performance requirements. The spectral resolution is not seriously compromised by the instrument self-apodisation and the target value of 0.27 cm⁻¹ in CM can be met even with a stroke less than 2.5 cm. The spectral sampling interval will be slightly above 0.2 cm⁻¹ in CM. A comparison of the ideal ILS of a sub-sample at the location of the optical axis compared

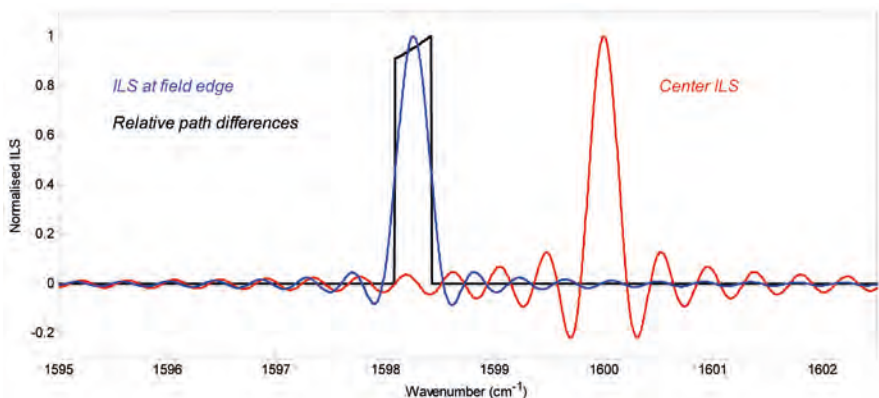


Figure 7.5. Comparison of the normalised ILS for a centre sub-sample and an edge sub-sample. The relative path difference contributions for a sub-sample (distribution within the sub-sample area) also are shown.

Radiometric requirement	Requirement	
Mode	CM	DM
Noise Equivalent Delta Radiance (NEdL) @ Zero input Band-A	2 [4.0-6.5] nW/(cm ² sr cm ⁻¹)	0.8 [1.5-2.5] nW/(cm ² sr cm ⁻¹)
NEdL @ Zero input Band-B	1.5-2.0 [4.0-6.5] nW/(cm ² sr cm ⁻¹)	0.4-0.8 [1.5-2.5] nW/(cm ² sr cm ⁻¹)
Radiometric accuracy	$< \text{NEdL}^2 + (\text{radiometric offset})^2 + (0.015 \cdot \text{measured radiance})^2$	
Spectrally varying radiometric error (ghost)	$< 4 \text{ nW}/(\text{cm}^2 \text{ sr cm}^{-1})$	$< 1.5 \text{ nW}/(\text{cm}^2 \text{ sr cm}^{-1})$
Radiometric scaling error	See Table 7.4	
Radiance range	133-240K blackbody radiance equivalent	143-240K blackbody radiance equivalent

Table 7.3. Summary of the radiometric requirements.

to the ILS that is effectively generated by a sub-sample of $0.8 \text{ km} \times 15 \text{ km}$ at the edge of the field is illustrated in Fig. 7.5. The simulation assumes an ideal detector response.

According to the analysis taking all known error contributors into account, the ILS width and asymmetry, and the ILS knowledge are expected to be compliant with the requirements. Losses of the instrument sensitivity owing to detector pixels, which if malfunctions will be switched off, can be compensated by modelling. Due to the relatively large sub-sample being composed of more than 20 detector pixels, the sensitivity to pixel losses is relatively low. The spectral characterisation accuracy is expected to be well below 1% and the spectral accuracy better than 0.008 cm^{-1} in CM, and better than 0.01 cm^{-1} in DM as described in Chapter 5.

7.2.3.4 Radiometric performance

Table 7.3 summarises the main radiometric requirements for CM and DM. Performance is compliant with requirements.

7.2.3.4.1 NEdL performance

The Noise Equivalent delta Radiance (NEdL) is computed using detailed and mature radiometric noise models developed during Phase-A. The instrument noise levels depend mostly on the instrument pupil size, its total spectrally dependant transmission, the operational temperature, the dynamic range of the signal, and on the noise of the instrument detectors and electronics. The

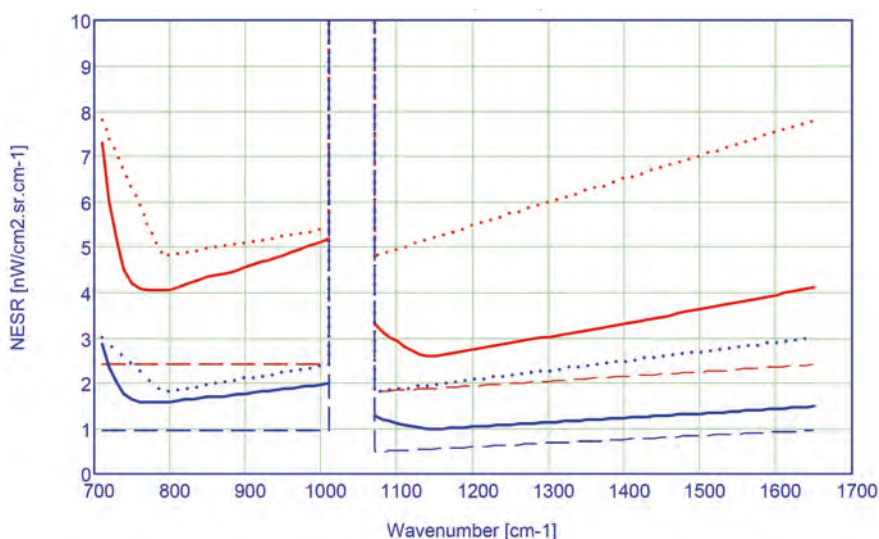


Figure 7.6. Concept A NEdL for an input scene radiance equivalent to the radiance of a blackbody at 240K. CM is shown in red and DM in blue, goal requirement as dashed lines and threshold requirement as dotted lines.

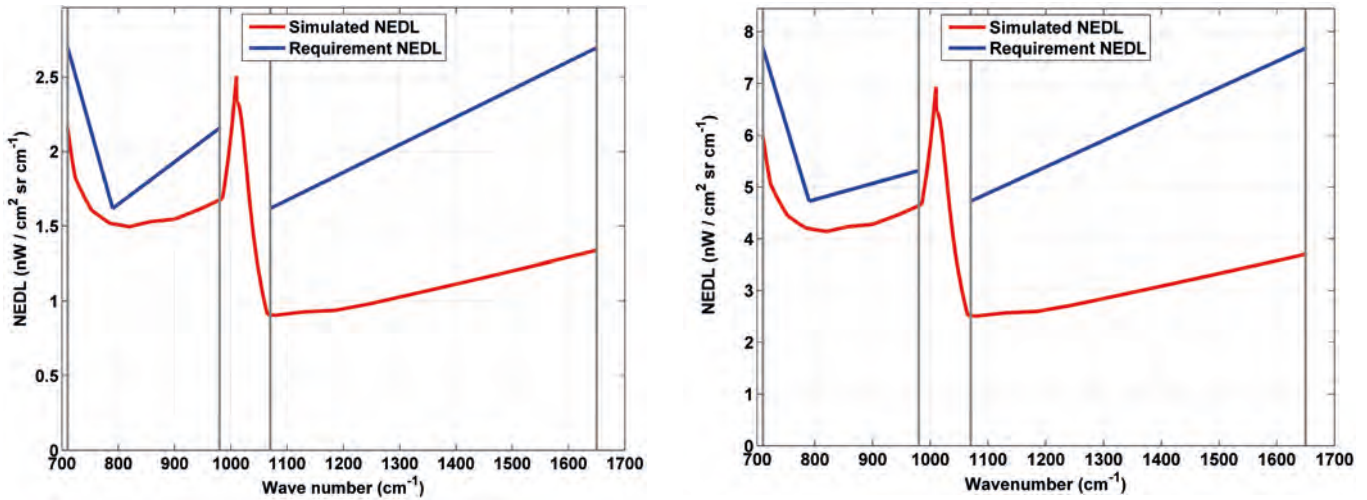


Figure 7.7. NEΔL of Concept B for an input scene radiance equivalent to the radiance of a blackbody at 240K. DM on the left and CM on the right.

results of the calculation of the NEΔL in DM and CM are presented in Figs. 7.6 and 7.7 for Concept A and B.

The instrument operational temperature plays a key role in the NEΔL performance, since emission from the instrument can generate a dominant noise contribution to the NEΔL. If the temperature is 240K instead of 293K, the NEΔL improves considerably. The evaluation in Phase-A concluded that both concepts, which operate at 240K and 293K respectively, are compliant with the NEΔL requirements.

7.2.3.4.2 Radiometric accuracy

The NEΔL, the radiometric offset and the scaling error contribute to the radiometric accuracy. The NEΔL has been discussed above. Offset errors can be corrected by measuring the offset through deep space calibration. Therefore, the dominant error for the radiometric accuracy is the scaling error, for which a dedicated requirement has been formulated. Scaling errors are due to changes in the instrument radiometric response or inaccuracies in the calibration sources. They alter the instrument radiometric response depending on the input radiation level. Scaling errors can be classified in spatial, spectral and temporal errors, and can also either be correlated or uncorrelated. The requirement is shown in Table 7.4.

Spatially correlated errors are the blackbody temperature measurement error, the absolute temperature knowledge and the knowledge of the emissivity.

Spatially uncorrelated errors are the detector non-linearity and the gain variation of the amplification chain and can vary randomly pixel by pixel

Temporally varying errors can potentially be corrected during the retrieval process if the change induced in the instrumental response is not random

Table 7.4. IRLS scaling error requirements.

Radiometric scaling error (requirement)		Spectrally correlated	Spectrally uncorrelated
Temporally correlated	Spatially correlated	1.00%	0.15% [0.25%]
	Spatially uncorrelated	0.15% [0.25%]	0.15% [0.25%]
Temporally uncorrelated	Spatially correlated	0.15% [0.25%]	0.15% [0.25%]
	Spatially uncorrelated	0.15% [0.25%]	See NESR

(i.e. they are correlated). Therefore, the tolerance to correlated errors is much higher than to uncorrelated errors. The error analyses, including all known contributors, led to the conclusion that the goal requirements can almost be fulfilled. However, careful attention has to be paid in future phases to the dominating errors: non-linearity of the detectors and accuracy of the knowledge of the blackbody temperature. A stable and well-known blackbody is as critical as an accurate characterisation of the non-linearity of the detectors to meet the requirements.

Spectrally-varying radiometric errors are errors generated from ghosts appearing in the ILS as a result of modulations during the interferometer scan. Such modulations can be caused by micro-vibrations and a corresponding lateral movement of the corner cube(s). The effect is similar to the LOS jitters and will cause pseudo-noise. Analysis of the requirements shows that the lateral shift must be limited or measured and corrected to achieve knowledge of the corner cube lateral jitter of about 5 nm. This can be achieved with a three-point metrology; however the performance and degree of compliance of a simpler single point metrology still has to be investigated in more detail (Chapter 9).

7.2.4 STEAMR

7.2.4.1 Overview

This section presents the main performance of STEAMR at Level-1b achieved by the baseline concept described in Chapter 5. The requirements and performance are compared, an explanation of the achieved performance is provided and the feasibility, margins and criticalities, if any, are highlighted.

7.2.4.2 Geometric performance

The main STEAMR geometric requirements and achieved performance are summarised in Table 7.5. The vertical coverage and sampling are determined by the arrangement of the individual beams in the focal plane as an image of the far-field of the telescope. The along-track sampling is determined by the repeat time of the limb measurements.

Figure 7.8 shows the overlaid dual-linear polarisation beam patterns at 323.6 GHz, 339.6 GHz and 355.6 GHz, calculated using the GRASP 9 physical optics software package including all optics from horn to telescope. Crosses mark the beam centres at the three frequencies, and the elevation scale is for mid-latitudes. The figure demonstrates the vertical sampling and coverage directly as it comes from the simulations.

7.2.4.3 Antenna performance

The full set of ACAPs at three frequencies from which the FWHM values have been derived is shown in Fig. 5.25.

The diffraction patterns change with frequency and show some variation with the beam position generated by the instrument optics, but the FWHM stays below 2.9 km in all cases. The antenna patterns fall nicely with no high sidelobes as expected from the low edge taper on the telescope in combination

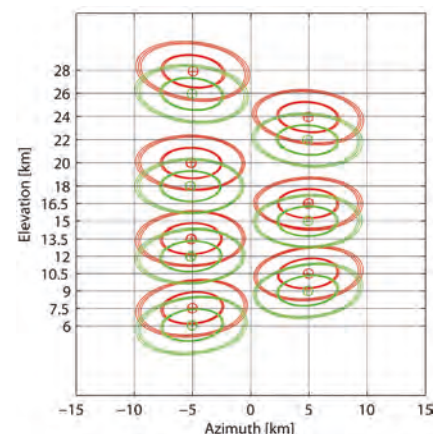


Figure 7.8. Overlaid dual-linear polarisation beam patterns at 323.6 GHz, 339.6 GHz and 355.6 GHz as computed using GRASP 9. Orthogonal linear polarisations in green and red with contours at -3 and -10 dB.

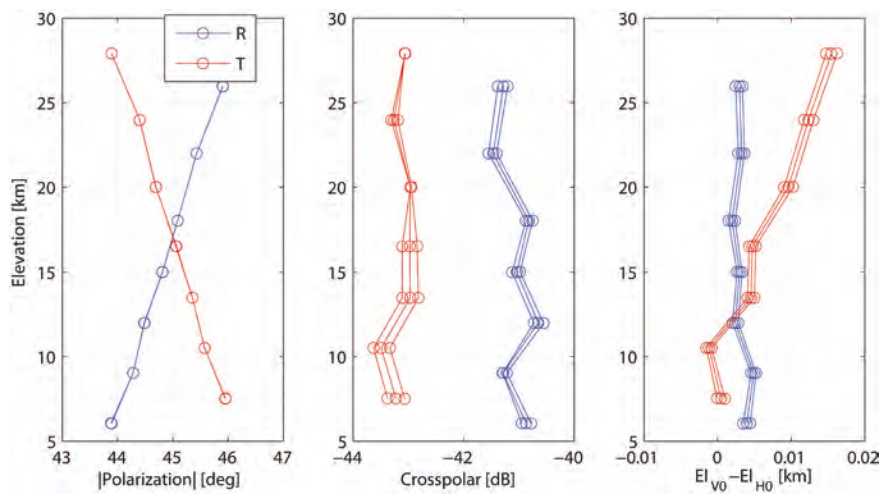
Geometric Parameter	Requirement	Performance
Vertical coverage	22 km	22 km
Vertical sampling	<1.5 km for lower 12 km, <2.0 km for upper 10 km	1.5 km for lower 12 km 2.0 km for upper 10 km
Along-track sampling	<50 km	50 km

Table 7.5. Summary of main STEAMR geometric requirements and the estimated performance.

Antenna Parameter	Requirement	Performance
Half-power beam width (ACAP, FOV FWHM)	2 km [3 km]	323 GHz FWHM = 2.55–2.88 km 339 GHz FWHM = 2.44–2.76 km 355 GHz FWHM = 2.35–2.64 km
ACAP knowledge	Main beam ≤ -30 dB Side lobes ≤ -35 dB [≤ -26 dB]	Main beam -35 dB Side lobes -35 dB
Side lobe level (ACAP)	≤ -25 dB	-28 dB
Receiver relative vertical position knowledge	Overall knowledge ≤ 750 m Beam to beam ≤ 50 m	In-orbit instrumental error is 36 m Pre-launch error is 31 m
Polarisation accuracy	Angular accuracy: $\pm 5^\circ$	2.2°

Table 7.6. Summary of STEAMR main antenna requirements and the estimated performance.

Figure 7.9. showing change of polarisation angle, cross-polar level and deviation from intended beam centre to actual with altitude. 'R' refers to a $+45^\circ$ polarisation and 'T' refers to a -45° polarisation.



with the averaging process in the ACAP calculation. By pushing the outer sidelobes below -35 dB the instrument becomes less sensitive to assumptions about the antenna patterns improving the final calibration of the data. Near-field scanning, such as the one from Nearfield Systems Inc (US), is used on the ground during development and testing to determine both individual antenna patterns and alignment. The test facility will be set up in or close by the STEAMR integration site. Once in orbit, the edge of the Moon can be used to verify beam alignment with errors of about 36 m (68% confidence interval). The instrument has some rotation of polarisation angle with altitude but remains at $44-46^\circ$.

7.2.4.4 Radiometric performance

The main radiometric performance of STEAMR is detailed in Table 7.7 and specifies the required sensitivity for calibrated data, the accuracy of the measurements, the amount of non-linearity and the level of spectrally varying disturbances.

The radiometric sensitivity is dominated by noise sources in the signal mixer and LNAs. Measurements of the receiver noise from the baseline mixers with embedded LNA show a maximum temperature of 1400K. A typical measurement cycle last ~ 6 s, (4 s for limb pointing, 1 s for cold sky view and 1 s for 300K warm load view), which results in 6 warm and 6 cold views every 38 s. As a consequence and assuming 15% absorptive loss in the optics, a radiometric sensitivity of 0.5K and 0.4K is obtained in the upper and lower

Radiometric Parameter	Requirement [K]	Performance [K]
Radiometric sensitivity (DSB)	≤ 0.5	0.5
Radiometric accuracy	< 1	0.5
Radiometric non-linearity error	< 0.75	0.3
Spectrally varying radiometric error	0.25	0.2

Table 7.7. Summary of STEAMR main radiometric requirements and the estimated performance.

part of the IF range respectively. If the mixer/LNA are cooled to -20°C the receiver noise is expected to drop by 10%. Tests performed using a breadboard show a stability of up to 40 s as shown in the Allan variance plot (Fig. 7.10). The measurement cycle is assumed ~ 6 s, much shorter than the 40 s shown. Ground testing is influenced by air turbulence, however based on experience from Odin it is expected that conditions will provide better stability. Much of the instabilities results from overall gain changes owing to slow temperature variations. The slow gain variation can be fitted by splines or polynomial functions and used as part of the data processing.

The sensitivity in terms of the required signal to achieve a SNR of one in one second is shown in Fig. 7.11. The calculation was made including 250K from the limb, time loss and noise contributions from cold sky and internal calibration loads for a measurement cycle of 6.3 s or 50 km covered distance. The nominal resolution with 512 lags or 22 MHz and also reduced to 256 or 44 MHz are both shown. The requirement of 0.5K at 6.3 s and 10 MHz corresponds to 0.85K at 1 s and 22 MHz.

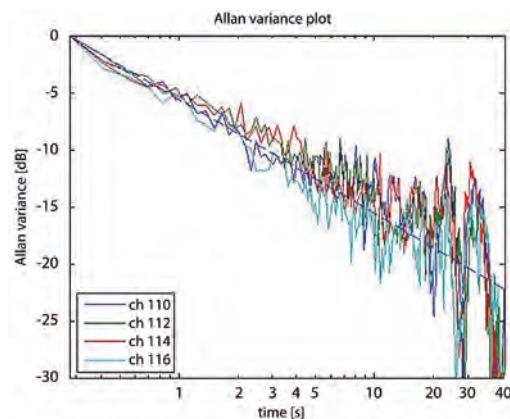


Figure 7.10. Allan variance plot of the output at four different backend frequencies with breadboard mixer starting at a warm calibration load. The dashed line shows the result for white noise.

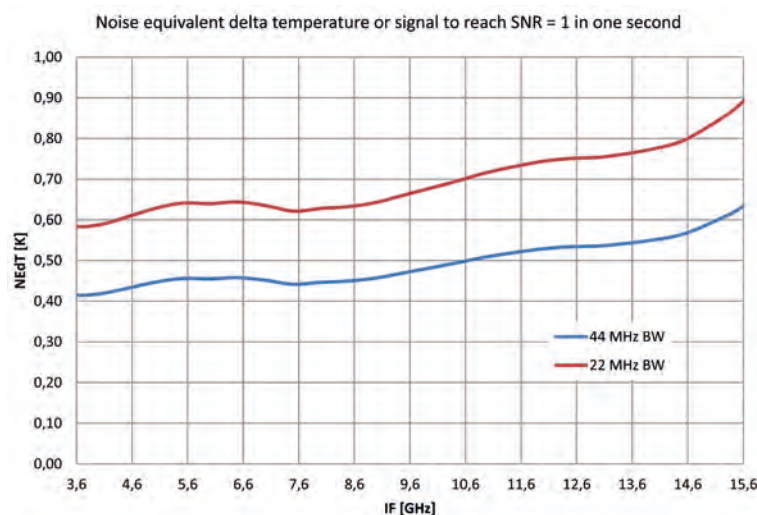


Figure 7.11. The NEqT for two different spectral resolutions calculated for the conditions of a full 6.3 s measurements cycle, but degraded and presented for an acquisition time of 1 s.

Table 7.8. Radiometric error sources.

Error source	Error [K]
PT 100 accuracy allocated to error	0.1
Temperature sensor to surface error	0.05
10% remnant of 1K standing waves	0.1
0.1% error in coupling to 300K load	0.3
0.1% error in emissivity of 300K	0.3
Error from 300K load calibration with sideband ration uncertainty to -30 dB	0.3
Uncertainties in emission from optics	0.1
Non-linearities in IF	0.03
Non-linearities in backend	0.3
Total calibration error (RMS)	0.6

A low radiometric non-linear design is preferred over the correction of the measurements. The non-linearity is dominated by the performance of the autocorrelation spectrometer. Components operated in compression are also an important source of non-linearities. All elements in the IF chain have more than a 20 dB margin to their 1 dB compression point resulting in a gain compression factor below 0.0001, which corresponds to a 3mK error for a 300K dynamic range. Tests using a spectrometer with the HIFAS ASIC have shown that it is possible to maintain a linearity of 0.0005 for a 3 dB range (corresponding to a signal of 1000K for STEAMR). A conservative relaxation by a factor of two gives 0.001 and an error of 300mK for 300K range.

Two types of calibration loads are used, cold sky and 300K load. The radiometric accuracy depends on the temperature accuracy of the calibration loads at 340 GHz and the linearity of the RF chain. The design of the PREMIER radiometric calibration subsystem is very similar to the one of the ALMA instrument, therefore performance is expected to be of the same order or better due to vacuum. The specifications for the ambient temperature ALMA calibration loads are 0.3K, emissivity of 0.998 and coherent scattering less than -55 dB. IAP has measured (A. Murk et al., 2008) the final prototypes and averaged over angles of incidence from -10° to 10° the backscatter at 350 GHz is around -68 dB. The emissivity of the conical target is better than 0.9999.

All optics are equipped with multiple temperature sensors to allow the emitted signal to be estimated. A 0.5K sensor error per optical element corresponds to ~50mK radiometric error in both cold sky and limb views thanks to the use of low emissivity optics. Table 7.8 shows the sources of the radiometric calibration errors, which leads to a total error of 0.6K.

The total effect from uncorrected standing waves towards calibration sources and remnant atmospheric lines correspond to 0.2K including margins. The level of artefacts from leakage between sidebands in the autocorrelator can be computed by considering the strongest lines present in the limb spectra at 250K. The phase has been estimated using the ACS breadboard as phase detector showing that a relative phase accuracy of 2° can be achieved with a corresponding sideband rejection of -35 dB. This would make a 250K spectral line appear as a 0.08K artefact before data processing.

7.2.4.5 Spectral performance

The main spectral performance of STEAMR is detailed in Table 7.9. There are two preferred spectral ranges; one compatible with a high IF and one with a low IF, both in combination with double-sideband and separated- sideband operation. The lower IF is preferred due to better sensitivity linked to availability of low noise amplifiers. The spectral resolution is specified as the

Spectral Parameter	Requirement	Performance
Spectral range	DSB Frequency range: From 324.0 GHz to 336.0 GHz (LSB) and from 343.25 GHz to 355.25 GHz (USB)	324.000 GHz to 336.000 GHz (LSB) 343.250 GHz to 355.250 GHz (USB)
Spectral resolution	≤ 25 MHz	16.0 MHz resolution from the sinc function or 22.0 MHz with Hamming or 24.0 MHz with Hanning smoothing
ILS knowledge	≤ -25 dB	-30 dB
Sideband response knowledge	< -30 dB	-30 dB

Table 7.9. Summary of STEAMR main spectral requirements and the estimated performance of the baseline concept.

FWHM of Level-1b data and could be viewed as to include both smoothing or not. The ILS sets the level to which the instrument response should be known. The sideband response knowledge is relative from one sideband to another as a ratio.

The required spectral range in double-sideband mode is shown in Fig. 7.12. The 12 GHz IF bandwidth is split into two times 6 GHz by the autocorrelation spectrometer each processing 512 lags to meet the required spectral resolution. The ILS can be measured using standard lab equipment and is close to the theoretical ILS. The line source used to measure the sideband ratio has a built-in power detector and will also be tested extensively on the ground to provide a very accurate measurement in orbit. It is expected that the sideband ratio is a smooth function that can be measured with high resolution.

Figure 7.13 (left) shows the frequency response of the breadboard autocorrelation spectrometer after transforming. Figure 7.13 (right) shows the small deviation existing between the autocorrelator spectrometer output and a perfect sinc function. These results correspond to 256 lags, while the nominal operating mode will use 512 lags, hence the spectral resolution is better by a factor of two.

The effect of applying Hanning smoothing, as shown in Figure 7.14 (left), reduces the depth of spectral sidelobes while broadening the main response.

Figure 7.14 (right) shows a measurement of the channel response at a signal frequency of 347.5 GHz and at an IF of 7.5 GHz. The measured channel widths for the two cases are within 0.1% at the 3 dB and 6 dB points, i.e. no significant impact from the LO phase noise. The signal to noise is better than -30 dB and systematic effects should be possible to measure better than -30 dB with standard equipment. The use of waveguides has the advantage of cutting off low frequencies and it is sufficient to sweep in frequency from 250 GHz. The absolute accuracy of the frequency response will be determined by the onboard frequency reference with all parts locked to the same frequency standard.

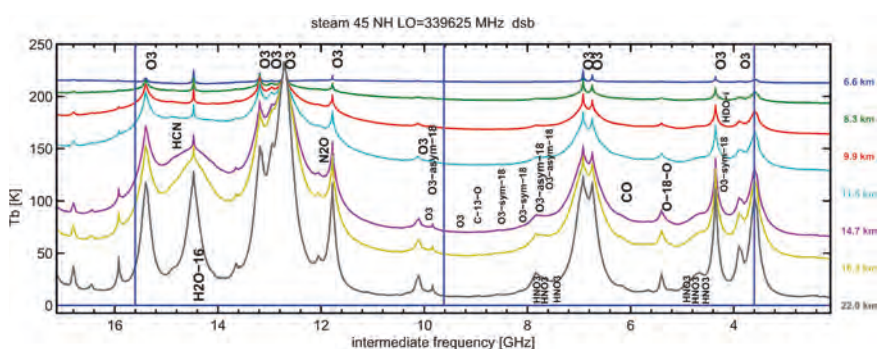


Figure 7.12. Required spectral range in double sideband mode.

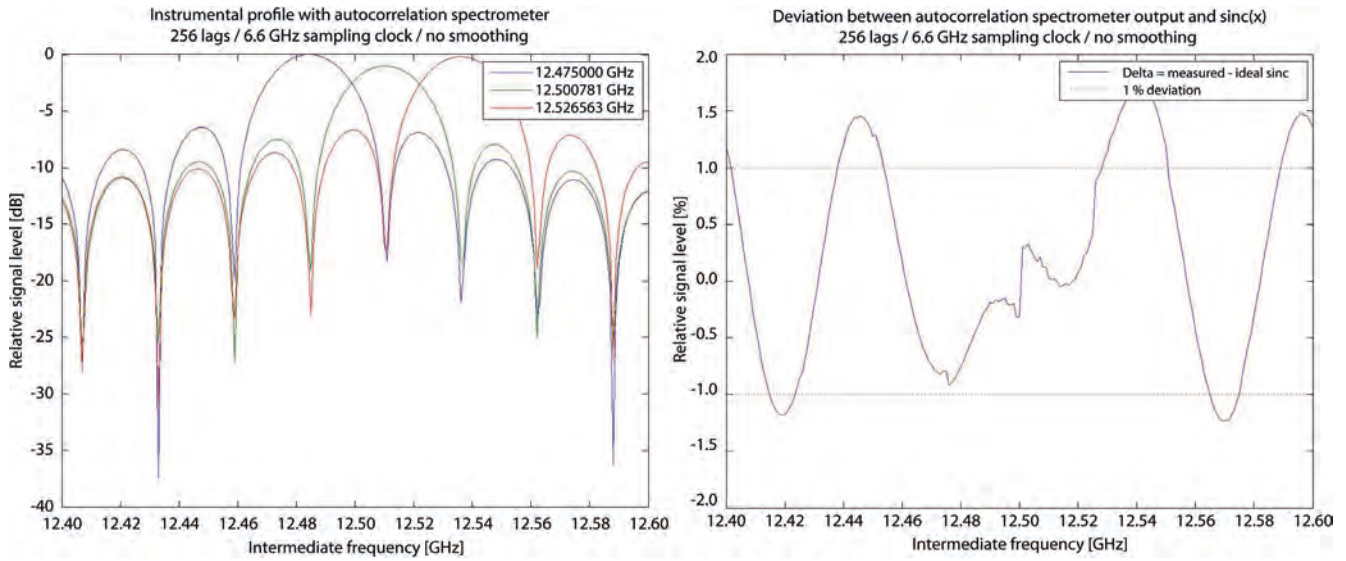


Figure 7.13. Measured raw frequency response after transformation from time to frequency domain (left). Difference between autocorrelation spectrometer output and sinc function (right). As can be seen, the difference is very small.

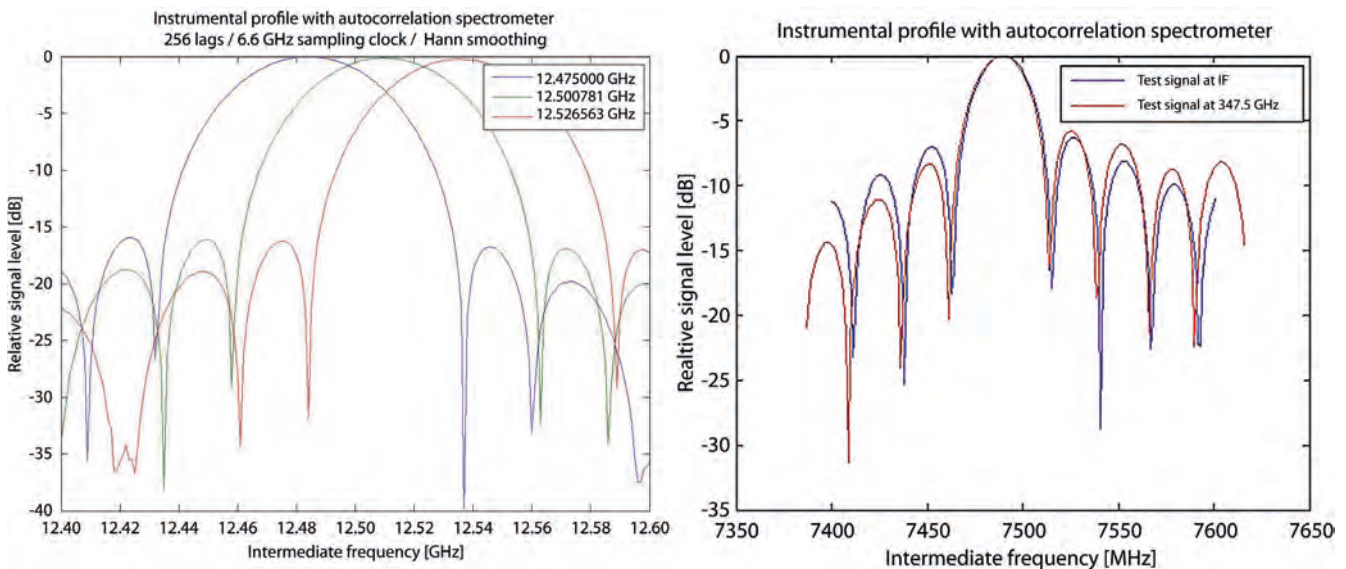


Figure 7.14. Effect of Hanning smoothing (left). Instrument response measured at IF of 7.5 GHz and a signal frequency of 347.5 GHz (right). The same number of lags, 256 and a sampling clock of 6.6 GHz was used in all cases. By using 512 lags rather than 256 lags the resolution improves by a factor of two.

7.2.5 Geo-location, LOS Stability and Inter-instrument Co-registration

Table 7.10 summarises the main system related co-registration, geo-location and LOS stability requirements for the IRLS and STEAMR.

7.2.5.1 Vertical knowledge

The threshold vertical knowledge requirement is set at 750 m for both IRLS and STEAMR. As described in Chapter 5, the error contributing to the vertical knowledge are: the on-ground orbit determination (OGOD), the on-ground attitude determination (OGAD), the knowledge of the relative attitude between OGAD reference frame and the IRLS/STEAMR measurement reference frame,

Parameter	Requirements [m]		Performance mean value [m]	
	IRLS	STEAMR	IRLS	STEAMR
Vertical knowledge	200 [750]	500 [750]	≤350	≤580
Vertical stability (within interferogram acquisition time)	60 [100]	N/A	100	N/A
Vertical stability (within along track sampling time)	75 [150]	150 [300]	148	<150
Vertical spatial co-registration knowledge between instruments	500 [1000]		≤700	

Table 7.10. Geolocation, LOS stability and instrument co-registration requirements summary.

the residuals of the IRLS/STEAMR focal plane calibration mounting errors, and the synchronization/time-tagging between the IRLS/STEAMR in OGAD/OGOD.

The contributions to the vertical knowledge of each error have first been estimated either by analysis or heritage. Monte-Carlo simulations have then been performed to obtain mean values over time. The performance achieved after this analysis is better than 350 m for the IRLS and better than 580 m for STEAMR for both mission concepts.

7.2.5.2 Vertical stability

For IRLS the threshold vertical stability within an along-track sampling dwell time is set at 150 m for a confidence interval of 99%, while the requirement is more relaxed for STEAMR. The errors contributing to the vertical stability are: attitude control errors, reaction wheel mechanical noise, IRLS cooler vibrations, as well as mechanical momenta coming from actuation of the pointing mirror, corner cube, SADM, the STEAMR calibration device, and from the reaction resulting from the solar array flexible modes.

The estimation of each error has been performed either by analysis or heritage and errors have been considered as fully correlated. The performance achieved after this analysis is better than 150 m.

7.2.5.3 Vertical co-registration between instruments

The threshold vertical co-registration knowledge between IRLS and STEAMR is set at 1000 m. The error estimations for each macro error contributors to the total vertical co-registration have been performed based on design or on heritage. Monte-Carlo simulations have also been performed to obtain mean values over time. As a result the performance achieved in vertical knowledge is better than 700 m.

7.2.5.4 LOS stability and pseudo-noise

LOS instabilities are a consequence of micro-vibrations originating from moving parts of the satellite. Pseudo-noise is the result of the LOS instability and the high vertical heterogeneity of the atmosphere. The assessment of its effect as a noise contributor requires the analysis of the impact of micro-vibrations (e.g. random or sinusoidal) on the modulation of the measured interferogram and the corresponding error of the spectrum at Level-1b (Subsection 7.2.6).

Major contributors to the LOS stability are the harmonic frequencies of the RW, which are at this stage assumed to be at 33 Hz, 97 Hz and 249 Hz; the cryocooler at 60, 120, 180, 240, 300, 360, and 420 Hz, and the SADM actuation at 1.7 Hz. Random vibrations are expected to have a minor effect in comparison with the harmonics and are at this point neglected. The amplitude of the RW and the cryocooler harmonic perturbations is assumed to be ~0.5 arcsec while the amplitude of the SADM perturbation is ~1.5 arcsec. All these perturbations

are combined to model the LOS stability over time (Figure 7.15) in a worst-case scenario by assuming a common node at time T=0, which means that all frequencies are almost in phase.

Figure 7.15 shows the LOS evolution for two seconds. The LOS instability is less than ± 100 m peak to peak in a time span equal to the interferogram dwell time, which meets the threshold requirement. The pseudo-noise generated by such LOS instability is presented in Subsection 7.2.6 as part of the end-to-end simulator description.

7.2.6 End-to-end Simulator Description and Results

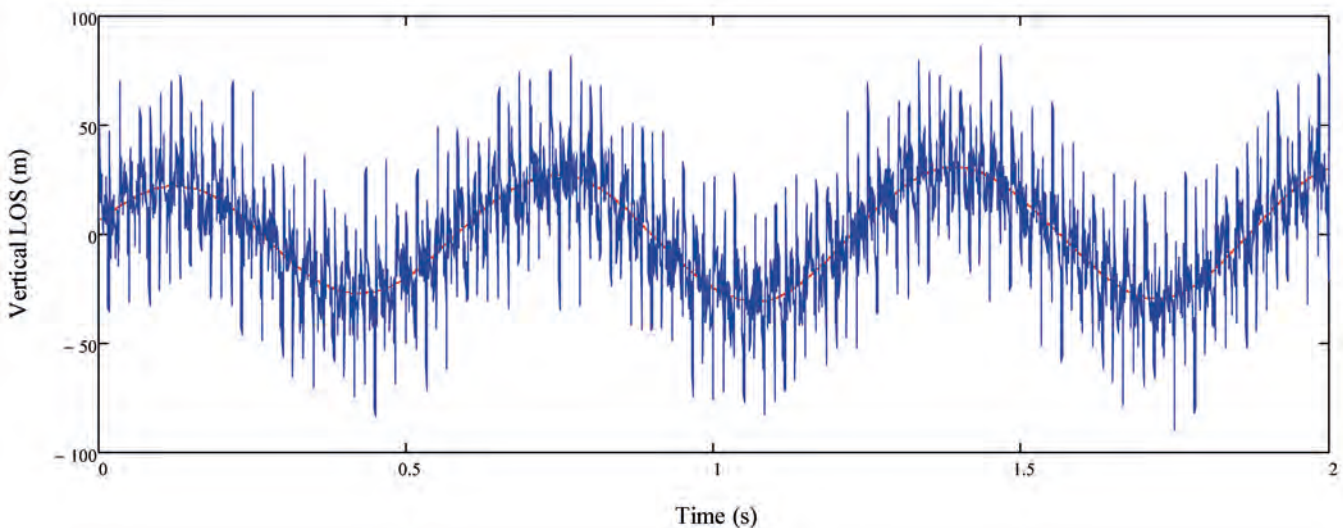
The PREMIER end-to-end (E2E) mission performance simulator generates Level-1b spectra and Level-2 data products using detailed instrument and retrieval models together with realistic error sources. Figure 7.16 shows the simulator high level architecture, which includes the following modules: two IRLS (OSS#1 and 2 in grey) for Concept A and B, STEAMR (also in grey), an atmospheric scene generator (SG), the Level-1b to Level-2 processing, and the performance evaluation (in red on top) module, which is used as a tool to compare simulation outputs with the inputs.

The atmospheric scene generator creates 2D atmospheric scene from user-defined constraints using a reference forward model with heritage from MIPAS.

Each IRLS module comprises following models:

- AOCS/SC: simulates the attitude and position of the satellite including LOS pointing and stability errors.
- AOCS/IRLS coupling: provides the discrete IRLS input radiances for every sub-sample taking as input the reference LOS and the corresponding atmospheric scene as generated by the AOCS and the SG modules, respectively.
- IRLS instrument: models the IRLS response and generates raw interferograms at sub-sample level using as input the discrete IRLS radiance provided by the AOCS/IRLS coupling model. It models the most relevant instrument errors, and also the spectral and radiometric calibration procedure.

Figure 7.15. 'Time series' of the vertical LOS position at the limb during a period of 2 s as generated from the composition of the expected harmonics frequency perturbations (blue). The SADM LOS perturbation is shown in red.



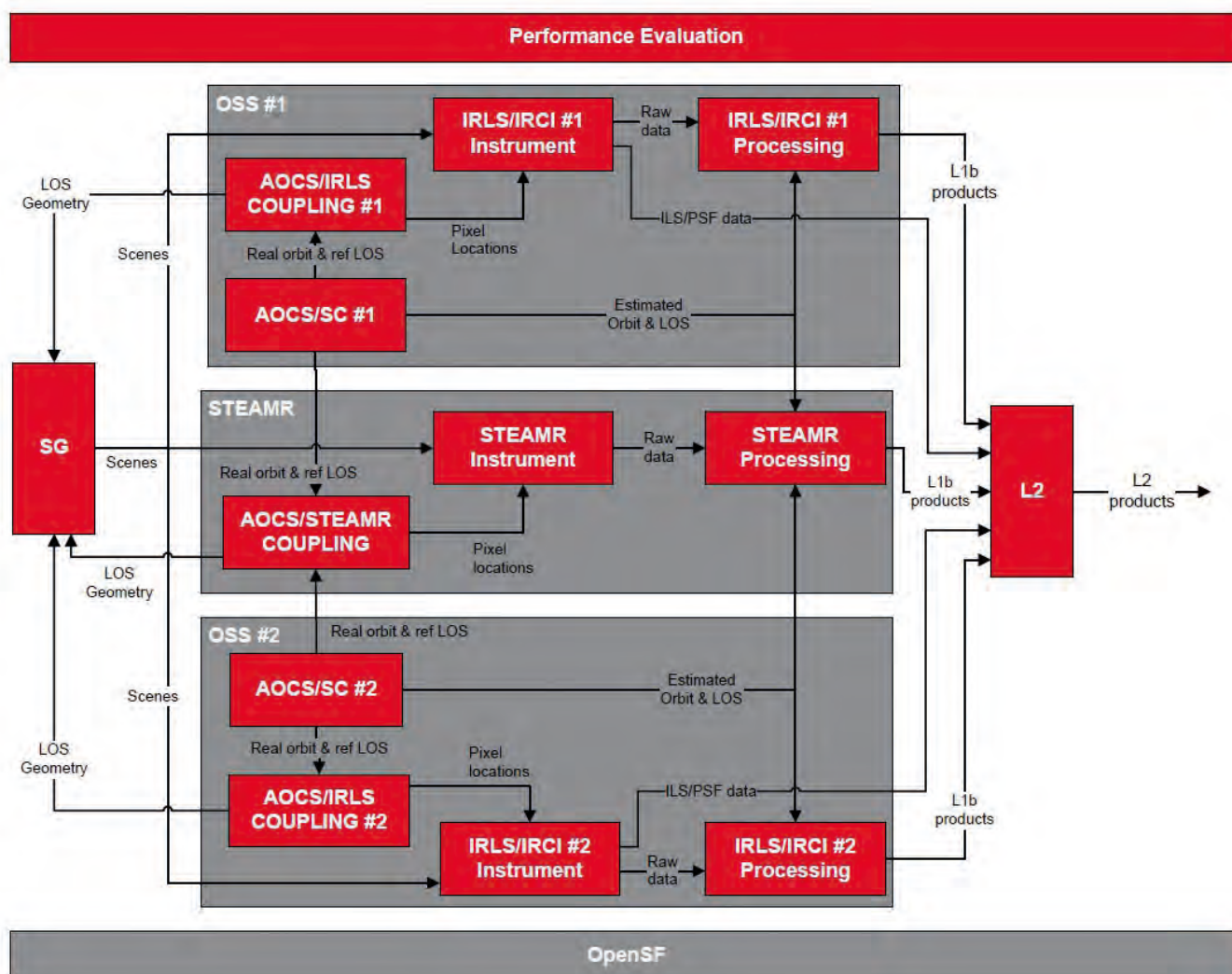


Figure 7.16. PREMIER E2E simulator performance simulator block diagram.

- IRLS processing: models the onboard and on-ground processing chains and generates Level-1b products (spectra) using as input the raw interferograms generated by the IRLS instrument model.

The STEAMR module comprises of the following models:

- AOCS/STEAMR coupling: derives from the reference LOS the corresponding views of the instrument to the atmosphere, providing the input radiances for each STEAMR channel.
- STEAMR instrument: simulates the STEAMR response including the most relevant instrument errors.
- STEAMR processing: models the onboard and on-ground processing and generates Level-1b products (spectra).

The Level-1b to Level-2 processing module generates vertical profiles of chemical species (e.g. O₃, H₂O), temperature and pressure using as input Level-1b spectra generated by the IRLS and STEAMR modules.

Open SF is used as a generic simulation framework where models and product retrieval tools can be plugged in using a well-defined and documented integration process.

Two examples of the end-to-end capabilities assessing the compliance of the system to the mission requirements at Level-1b are shown in Figs. 7.17 and 7.18.

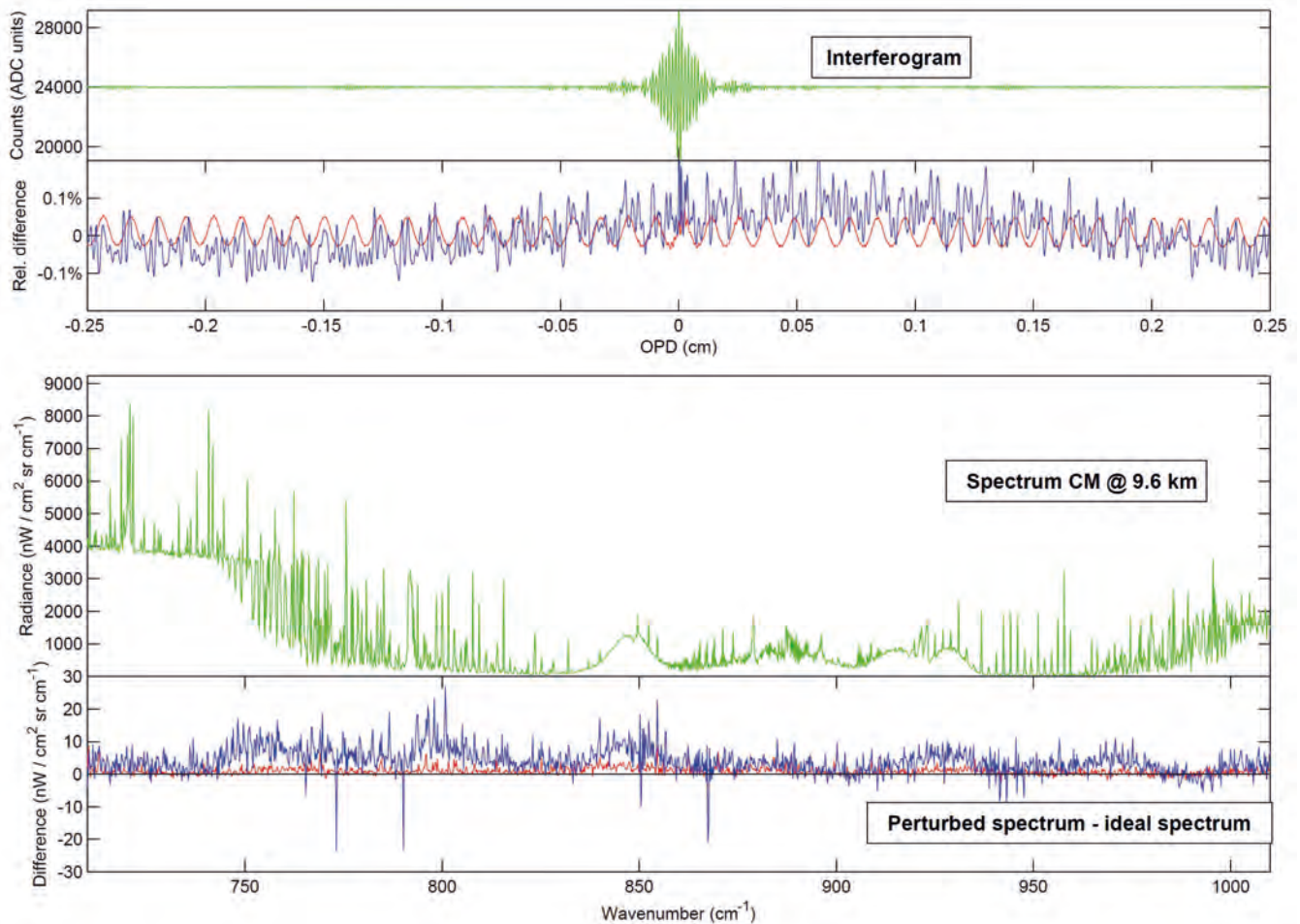
Figure 7.17 (top) shows the simulated unperturbed interferogram (in green) for CM Band-A at an altitude of 9.6 km and the difference with two perturbed interferograms, one resulting from a LOS instability with a frequency of 60 Hz (red) and one for the simulated time series (blue) as described in Fig. 7.15.

Figure 7.17 (bottom) shows the unperturbed Level-1b spectrum in green and the difference to the perturbed spectra below, which are understood as pseudo-noise. The RMS error is typically $4.1 \text{ nW/cm}^2 \text{ sr cm}^{-1}$, and the background generation can be of the order of $10 \text{ nW/cm}^2 \text{ sr cm}^{-1}$. The simulated pseudo-noise is in the order of the instrumental noise in Band-A CM. However, the actual behaviour of the LOS stability can only be assessed once a detailed structural design is made and analysed in further development.

Further analyses on Level-1b and Level-2 using the end-to-end simulator are planned during the Phase-A extension.

Figure 7.17 (top) shows the unperturbed Level-1b spectra for three of the 14 STEAMR beams corresponding with the tangent altitudes of 27.5, 16.0 and 5.6 km in blue, green and red, respectively. Figure 7.17 (bottom) shows the difference between the unperturbed spectra at each altitude and another one generated with a beam-to-beam position error knowledge of 75 m. At the lowest altitude, the noise introduced by the position error (red in bottom figure) is small; however at higher altitudes (green in bottom figure), the error accounts

Figure 7.17. Top: unperturbed interferogram for CM Band-A at an altitude of 9.6 km (green) and difference with perturbed interferograms generated by introducing a 60 Hz (red) perturbation and a set of ten frequencies (blue). Bottom: unperturbed spectrum (green) and difference between unperturbed and perturbed spectra for 60 Hz (red) perturbation and a set of ten frequencies (blue).



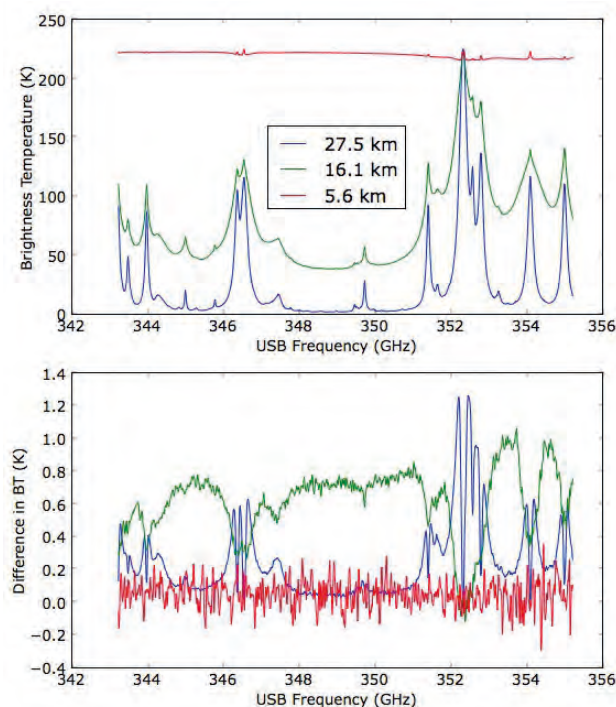


Figure 7.18: Results from the STEAMR end-to-end simulator. The upper panel shows representative spectra and the lower panel the differences when the pointing is misaligned by 75 m.

up to a 1K change in brightness temperatures, confirming the need of an accurate beam-to-beam position knowledge.

7.3 Individual Profile Retrievals

7.3.1 Introduction

The performances of IRLS and STEAMR have been assessed on the basis of individual profile retrievals simulated for example profiles and their respective Level-1b specifications and by propagating identified errors. These simulations employed state-of-the-art radiative transfer models and optimal estimation retrieval schemes for both sensors, and both IRLS modes. Confidence in their robustness and reliability has been gained by performing a number of simulations on a common basis with several independent schemes (Kerridge et al., 2012). The assessment has drawn on knowledge of the latest ‘generation’ of IR and mm-wave limb-sounders (i.e. MIPAS, HIRDLS, SMR and MLS). Instrumental errors have been identified, quantified and propagated for one example atmospheric profile for each of IRLS and STEAMR, with particular attention to specifications and errors associated with use of IR-detector arrays and mm-wave receiver arrays in place of limb-scanning (Subsection 7.3.2). Based on error estimates for the example atmospheric profiles and identified error mitigation procedures, compliance to Level-2 requirements is assessed and summarised in Subsection 7.3.3.

7.3.2 Estimated Errors on Retrieved Profiles

Simulations for the IRLS are for a tangent-height range of 6–50 km (mid-latitude) for temperature, H_2O , O_3 and CH_4 , which are required over that extended range, and otherwise from 6–25 km, with a nominal, i.e. un-refracted, vertical sampling distance of 0.7 km below an altitude of 30 km and 1.4 km above, except for dynamics mode in Band-A for which it was 0.7 km over the whole range. They have been performed on a common basis for the dynamics and chemistry modes using the optimal estimation method (Chapter 6).

The retrieval grid had 1 km vertical spacing below 30 km, and 2 km above, except for dynamics mode temperature retrieval for which it was 1 km over the whole range. Pressure for a single reference level was retrieved jointly with temperature, H₂O and O₃, and a continuum profile was also retrieved independently for each selected spectral interval (microwindow). A loose *a priori* uncertainty was selected for each variable (100% in VMR, 10K in temperature, 10% in pressure, 0.1 km⁻¹ in continuum), resulting in vertical resolution (i.e. averaging kernel vertical widths) commensurate with spacings of the retrieval grid. The microwindows were selected using a procedure which minimised the retrieval ‘baseline’ error, which reflects Noise Equivalent Spectral Radiance (NESR), uncertainties in concentrations of spectrally interfering gases, and uncertainties in retrieved temperature profile and reference pressure. Instrumental errors listed in Table 7.11 were propagated linearly, with particular attention to the degree of correlation between vertical samples and between spectral samples (Kerridge et al, 2012).

Error analyses for either the DM or CM for a mid-latitude example are shown in Figs. 7.19 (a)–(e) for temperature and trace gases specified in Table 4.1. The figures show the baseline error estimate (full black curve), which combines instrument noise (NESR) with uncertainties from spectral interference and, for trace gases, propagation of temperature and pressure retrieval errors. Instrumental errors are estimated by linear propagation. The RSS total curve (dashed grey curve) is an estimate of the total error, which combines the baseline and all instrumental errors on a root sum square (RSS) basis. In each case, the breakdown of errors is shown in addition to the baseline and ‘RSS total’ error. The threshold (dashed red line) and target (solid red line) Level-2 requirements are also shown. For temperature, H₂O, O₃, CH₄, CFC-11 and HNO₃, errors have been analysed for both modes. For NO₂, PAN and HCN errors have been analysed for the CM only. Additional trace gases for which observations by PREMIER would be desirable (Chapter 4) have also been assessed, but are not shown. It is noteworthy that the NESR is generally found not to be the limiting error. Retrievals in DM are more sensitive than in CM to knowledge of instrument line shape (i.e. skew and spread), due to the coarser spectral resolution. Knowledge of skew is potentially significant to absolute accuracy of temperature retrieval in the mid/upper-stratosphere, though not to retrieval of vertical or horizontal structure. Because the temperature profile and reference pressure were only retrieved from Band-A in this analysis, trace gases with microwindows in Band-B (i.e. H₂O, CH₄, NO₂ and PAN) can be affected by errors in knowledge of the pointing offset between Band-A and Band-B in addition to other errors. Errors in knowledge of pointing or radiometry which vary randomly from one vertical sample to the next can also be significant.

Simulations were performed for STEAMR with 25 MHz resolution for a tangent-height range of 6–28 km with nominal (i.e. un-refracted) sample spacings of 1.5 km at 6–18 km and 2 km at 18–28 km. Temperature and pressure profiles were retrieved simultaneously, assuming hydrostatic equilibrium, with profiles of continuum, H₂O (from spectral line), O₃, CO, HNO₃, HCN and additional gases. The parameters were retrieved on a vertical grid with 1.6 km steps up to 21 km and progressively decreasing resolution above, including altitudes close to the 14 tangent-heights in the limb-view range. For ozone, a retrieval grid with 1.8 km resolution up to 23 km was used. A vertical pointing-bias, spectrometer frequency shift, and an offset on the sideband ratio were retrieved jointly with the geophysical variables. A noise equivalent brightness temperature (NEBT), of 0.35K (DSB) was adopted. Instrumental uncertainties were propagated linearly and are listed in Table 7.12.

Error analyses for STEAMR for an example equatorial profile are shown in Fig. 7.20 for temperature and trace gases specified in Table 4.1. The random error estimate (solid black curve and circles) represents instrument noise (NEBT) combining system noise and random gain fluctuations, and the uncertainties of all spectrally interfering gases. Instrumental errors are

Code	Definition	Value
Spatial Requirements		
STRAY	Ignore PSF contributions beyond 3rd neighbour	N/A
PSF	Knowledge of the PSF	1% within FWHM, 0.2% within 5×FWHM
PSF VU	Vertically uncorrelated component of PSF knowledge	0.5% within FWHM, 0.1% within 5×FWHM
STRAY VU	Straylight beyond 5×FWHM	0.05%
POI	Absolute vertical geolocation knowledge	750 m
POI VU	vertical geolocation knowledge between adjacent vertical samples	15m
JITTER	Geolocation stability	Jitter time series
POI BU	Vertical co-registration knowledge between spectral bands	40 m (1 σ uncertainty)
POI SU	Co-registration knowledge within spectral band	25 m
Spectral Requirements		
SHIFT	Spectral calibration accuracy	CM: 0.008 cm ⁻¹ DM: 0.010 cm ⁻¹
SKEW	ILS function characterisation (asymmetric distortion)	1% of ILS maximum (0.5% for apodised ILS)
SPREAD	ILS width characterisation	0.3% (0.15% for apodised ILS)
Radiometric Requirements		
NESR	Noise Equivalent Spectral Radiance	(according to Subsection 4.5.1)
GAIN	Radiometric gain error, fully correlated	1%
GAIN SU	Radiometric gain error, spectrally uncorrelated	0.15%
GAIN BU	Radiometric gain error, band uncorrelated	0.15%
GAIN VU	Radiometric gain error, spatially uncorrelated	0.15%
OFF	Radiometric additive (offset) error, fully correlated	NESR/4
OFF VU	Radiometric offset, vertically uncorrelated	CM: NESR/10 DM: NESR/4

Table 7.11. Instrumental errors included in the IRLS retrieval performance assessment.

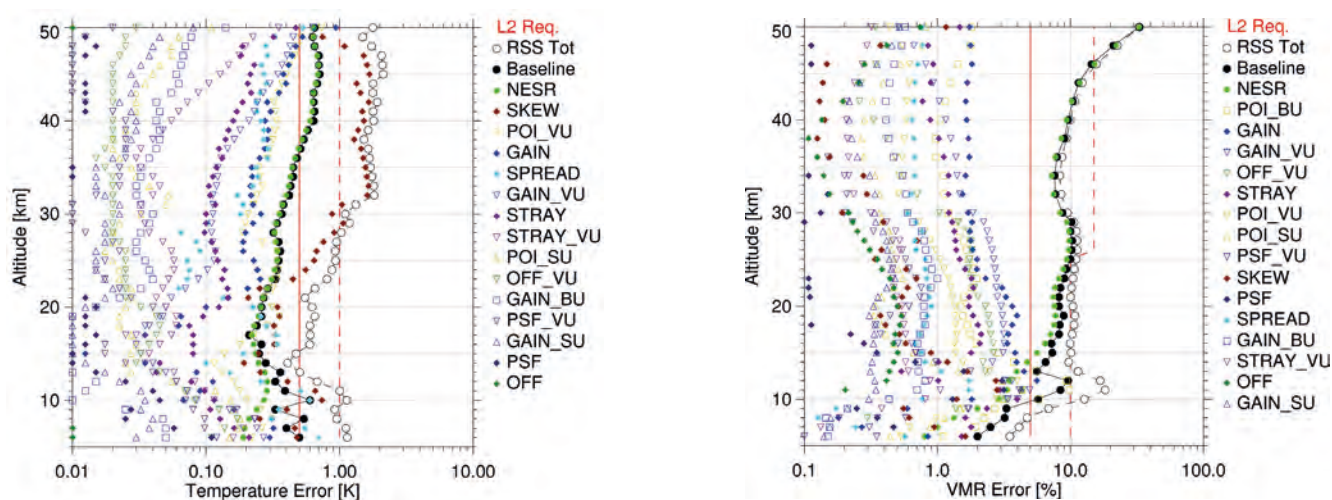


Figure 7.19(a). Error components for IRLS (DM) profile retrieval of temperature (left) and water vapour (right) for a single mid-latitude profile. (A. Dudhia)

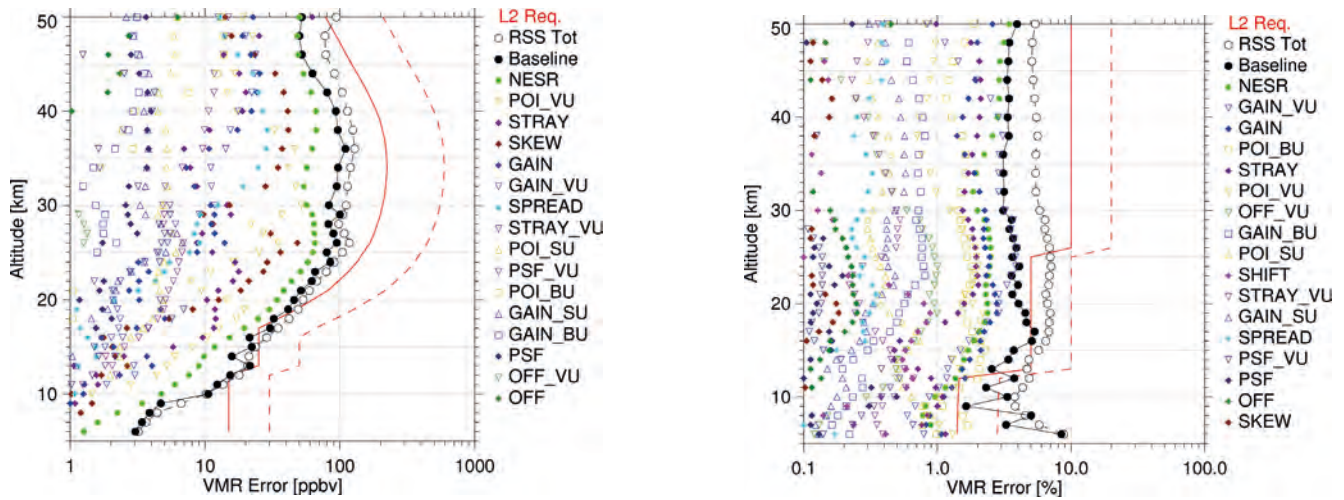


Figure 7.19(b). Error components for a single mid-latitude profile of O₃ (left) and CH₄ (right) for IRLS CM. (A. Dudhia)

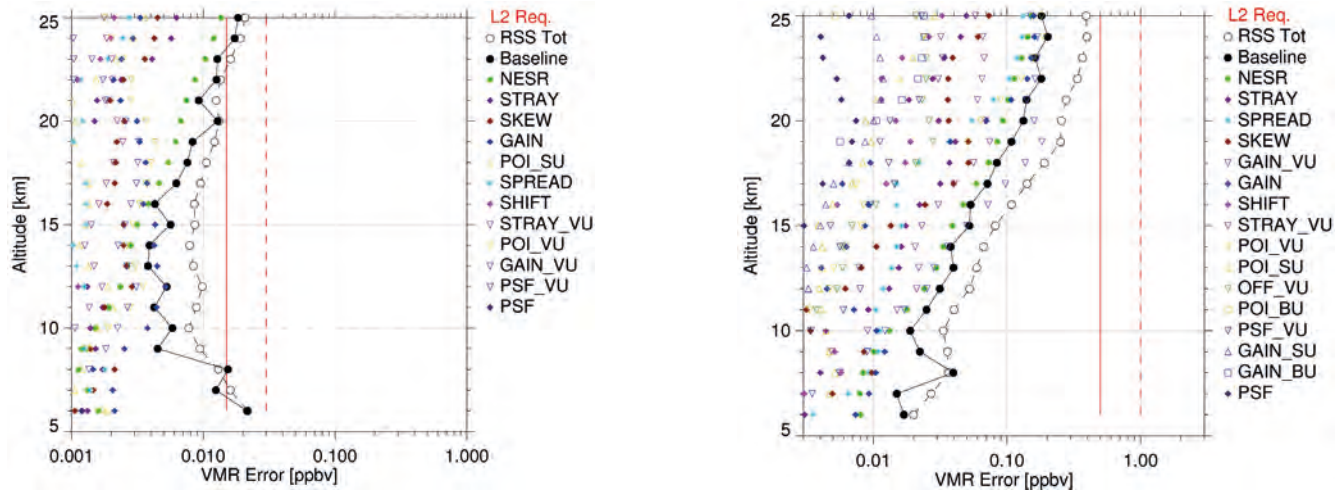


Figure 7.19(c). Error components for a single mid-latitude profile of CFC-11 (left) and HNO₃ (right) for IRLS DM. (A. Dudhia)

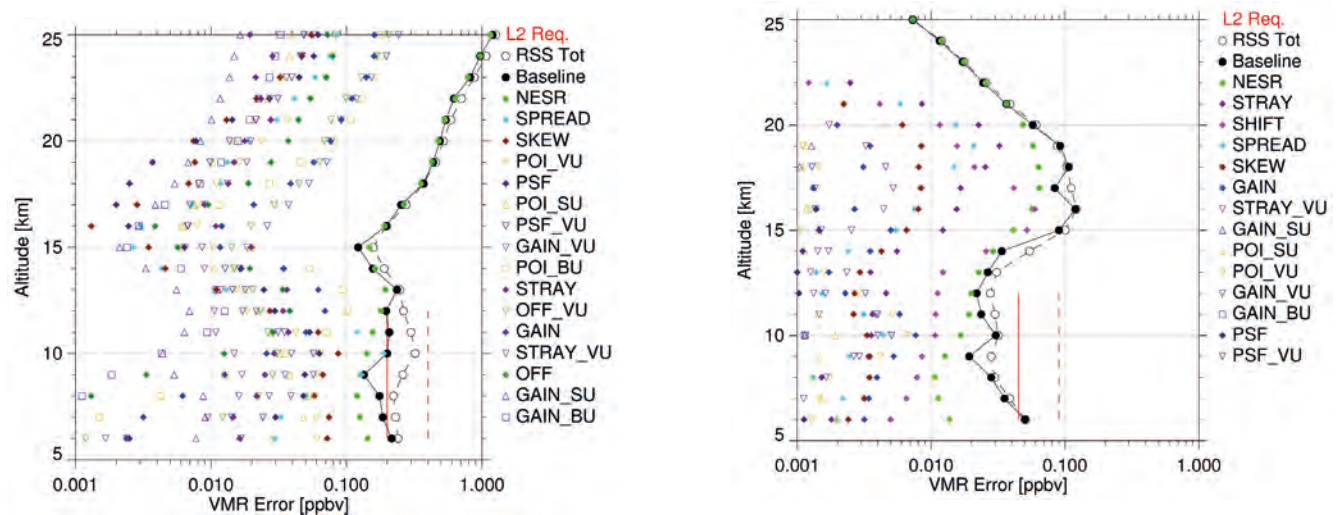


Figure 7.19(d). Error components for a single mid-latitude profile of NO₂ (left) and PAN (right) for IRLS CM. (A. Dudhia)

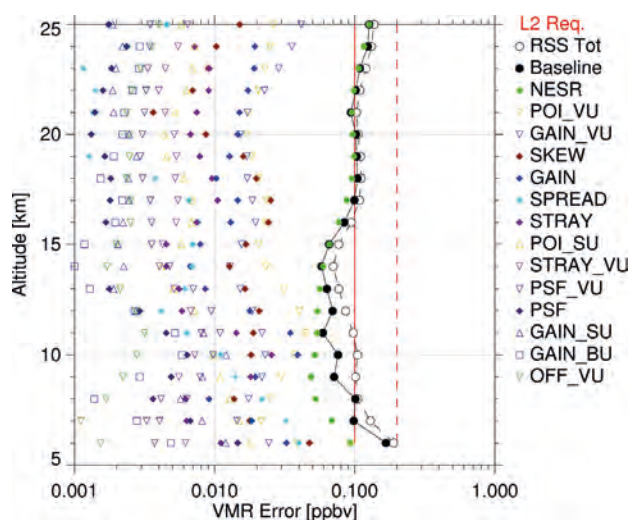


Figure 7.19(e). Error components for a single mid-latitude profile of HCN for IRLS CM. (A. Dudhia)

estimated by linear propagation. The RSS total curve (dashed black line and circles), is an estimate of the total error, combining individual components on an RSS basis, as for IRLS. The threshold (dashed red line) and target (solid red line) Level-2 requirements are also shown. Similar analyses have been performed also for additional trace gases for which observation by PREMIER would be desirable (Chapter 4), but are not shown here.

The accuracy requirements for target variables specified in Table 4.1 are compared in Fig. 7.21 to performance estimates for an atmospheric profile for IRLS (mid-latitude) and STEAMR (equatorial), taking into account instrument specifications which have been assessed during Phase-A (Chapter 5 and 7.2). For the mid-latitude profile, Level-2 requirements are met by IRLS baseline errors and also generally by the RSS of all errors. An exception is H_2O at the tropopause, where the mixing ratio is lowest and the fractional error requirement therefore particularly stringent. For H_2O , significant contributors in the case of the CM are vertically-uncorrelated pointing and gain errors. In the case of the DM, ILS skew (asymmetry) and spread (width) are significant, see Fig. 7.19(a). Other exceptions for the DM are ozone around 18 km and temperature in the upper stratosphere, where skew is again significant. Errors such as these are expected to be stable and therefore amenable to mitigation in-flight through identified procedures. Moreover, the baseline temperature error, which incorporates the random components, complies with the Level-2 requirement on precision. For the example equatorial profile, Level-2 requirements are met by STEAMR random errors down to ~ 10 km, although for

Code	Definition	Value
Radiometric and spectral requirements		
Random	Statistical error (NEBT, gain fluctuations)	0.35K
CAL L	Calibration, linearity error	0.6K
CAL M	Calibration, multiplicative (gain) error	0.05% (0.15K)
CAL B	Spectrally varying radiometric error	0.2K
SIDEB	Sideband response characterisation error	-30 dB
Spatial requirements		
ANT M	Antenna, main beam knowledge	0.25% (-26 dB)
ANT S	Antenna, side-lobe knowledge (relative to -20dB)	1% (-20dB)
DRIFT	Geolocation, linear vertical drift	50 m/s (300 m)
POI R	Interbeam pointing knowledge	10 m

Table 7.12. Instrument errors included in the STEAMR retrieval performance assessment.

O₃ this is for 1.8 km grid spacing. Below this altitude, water vapour attenuation increasingly limits precision in all cases. The Level-2 requirements are not fully met by the RSS totals for temperature, H₂O and O₃ where errors in spectral baseline contribute significantly, see Fig. 7.20(a) and (b). While radiometric non-linearity limits temperature accuracy, the random error complies with the Level-2 requirement on temperature precision, see Fig. 7.20(a).

The effect of a propagated error on retrieved profiles can vary, depending on the temperature and constituent profiles. Figure 7.22 illustrates the influence of atmospheric variability on estimated H₂O and O₃ error profiles in relation to the set of Level-2 requirements specified in Table 4.1. Although the variability is considerable, accuracy requirements are seen to be met for this set of profiles, except in very small areas where H₂O or O₃ mixing ratios are particularly low or where sharp discontinuities occur in their profiles and requirements formulated as percentages are therefore especially challenging. The plots in Fig. 7.22(a) show the difference between retrieved values (accounting for

Figure 7.20(a). Error contribution for single retrievals of an equatorial temperature profile (left) and water vapour (right) using STEAMR. The errors are described in Table 7.12. The solid black curve represents the instrument noise (e.g. system noise, random gain fluctuations plus uncertainties from spectrally interfering gases). The dashed black line corresponds with the RSS estimate of the total error. The threshold (dashed red line) and target (solid red line) Level-2 requirements are also shown. (J. Urban)

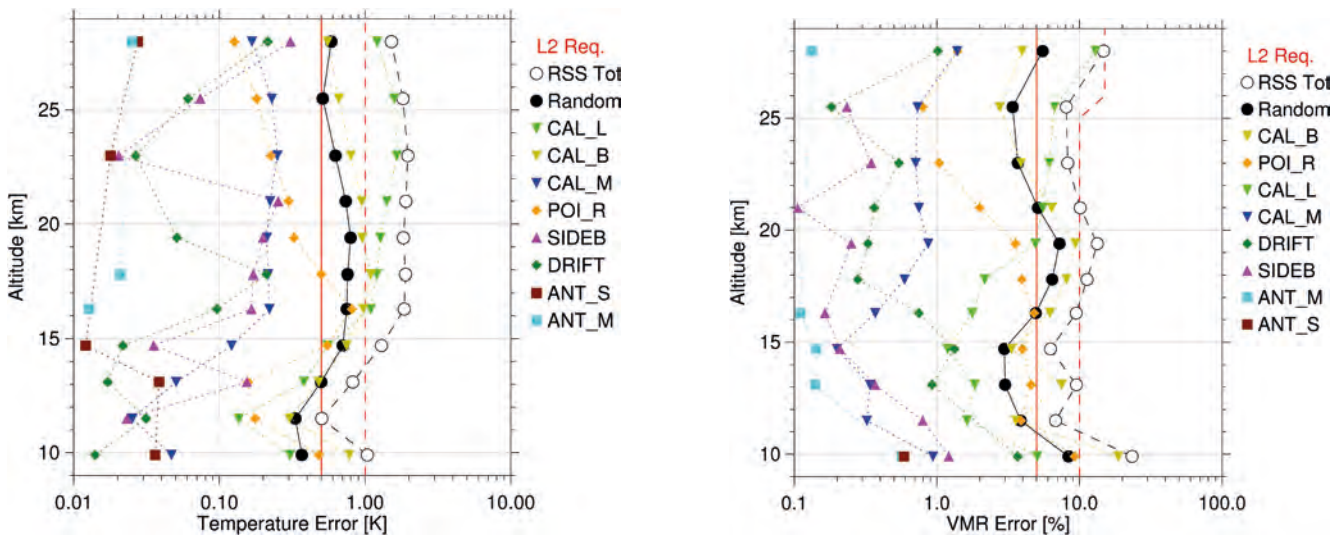
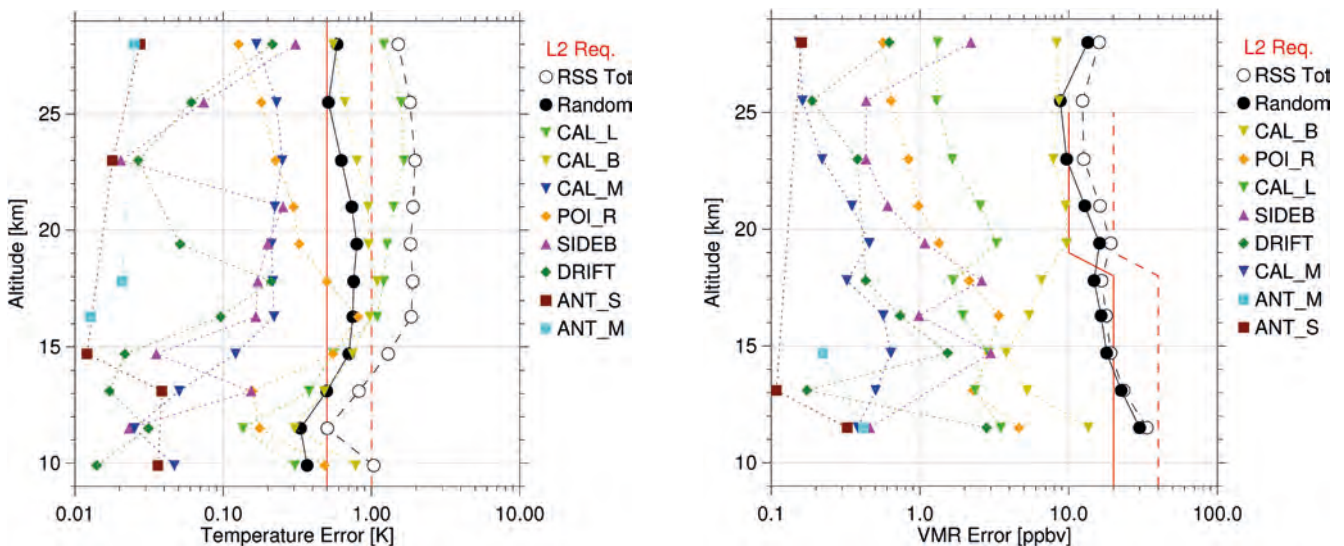


Figure 7.20(b). Error components for single equatorial profiles of ozone (left) and carbon monoxide (right) for STEAMR. (J. Urban)



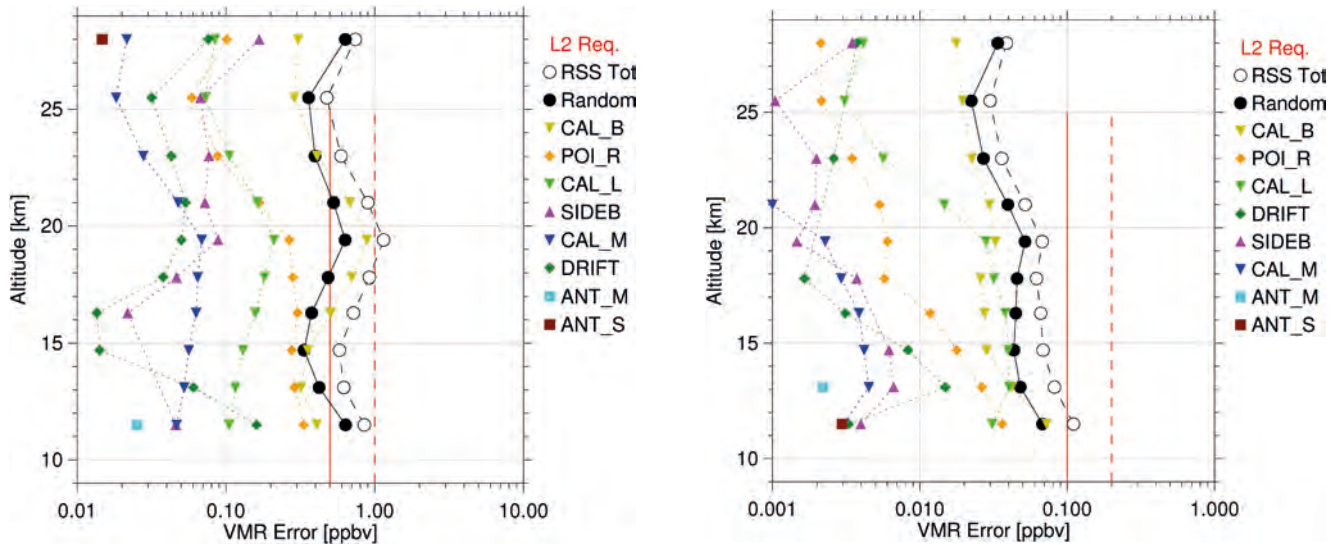


Figure 7.20(c). Error components for single equatorial profiles of nitric acid (left) and HCN (right) for STEAMR. (J. Urban)

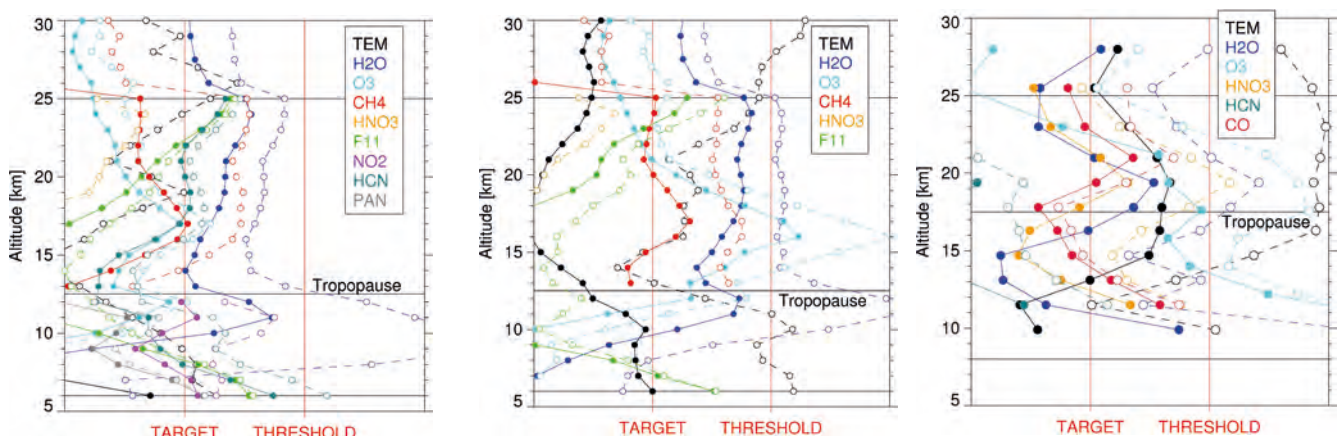
instrument errors in Table 7.11) and true values (as represented by the Global Environmental Multiscale model of Air Quality, GEM-AQ), divided by threshold accuracy requirements (Table 4.1), for IRLS in CM. Compliance is achieved with the exception of the small white areas (surrounded by black and red contours in the plot), down to the lower limit of the retrieval range, which is determined by cloud limb opacity.

Figure 7.22(b) shows similar results as for Fig. 7.22(a), for STEAMR. Requirements are generally met down to mm-wave opacity limit, ~5–7 km below the tropopause, and also in the presence of cirrus which would obscure the IRLS in this orbit segment.

7.3.3 Summary of Overall Compliance with Geophysical Data Requirements

As shown in Table 7.13, linear error analyses performed on the basis of the Level-1b specifications for the IRLS CM and DM, and STEAMR demonstrate

Figure 7.21. Ratios of estimated retrieval random errors (full lines and solid circles) and RSS totals (dashed lines and open circles) to threshold accuracy requirements for individual profiles of temperature and constituents for IRLS CM (left), IRLS DM (centre) and STEAMR (right). The scale is logarithmic and values have been normalised to overlay the target to threshold ranges for all variables. Values largely exceeding the target requirements are off scale to the left. The tropopause heights, the lower limits for PREMIER UTLS profiling and the 25 km upper limit are indicated by horizontal grey lines. (A. Dudhia).



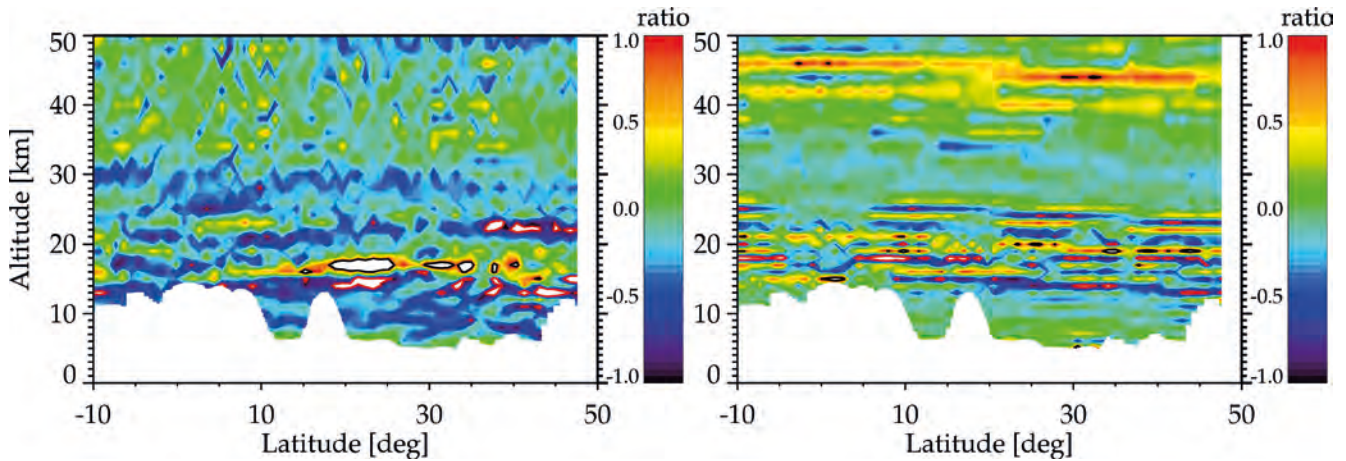


Figure 7.22(a). Difference between retrieved values and true values divided by the threshold accuracy requirements for water vapour (left) and ozone (right) for the IRLS CM for a contiguous set of profiles comprising an orbit segment (10°S–50°N) in the periphery of the Southeast Asian monsoon circulation (Subsection 7.4.3). (N. Glatthor)

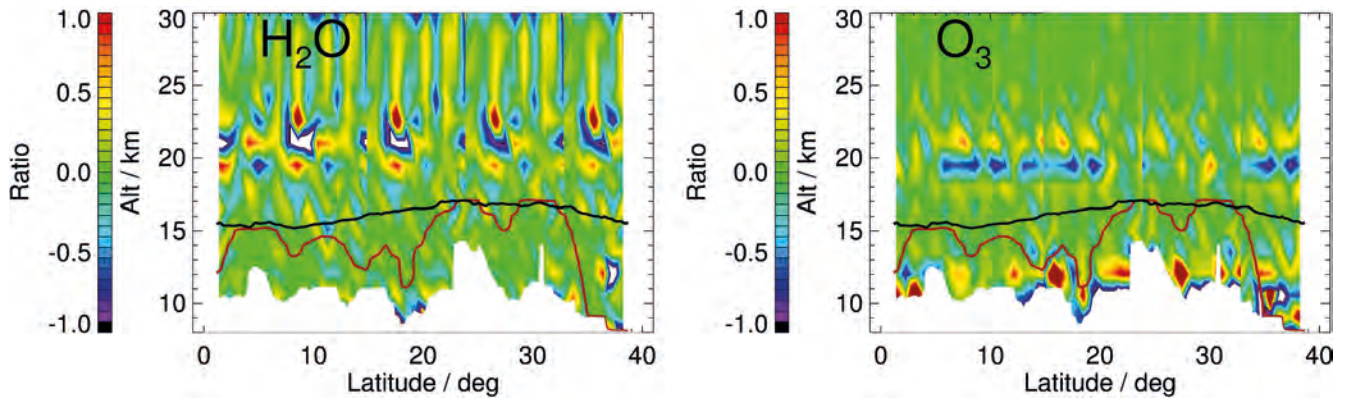


Figure 7.22(b). Comparison of water vapour (left) and ozone (right) random errors for a 2D STEAMR retrieval with accuracy requirements in an orbit segment through the core of the Asian monsoon circulation (Subsection 7.4.3). The black line represents the tropopause and red line the IR opacity limit. (A. Waterfall)

that the PREMIER Level-2 requirements can generally be met at the threshold levels specified in Table 4.1 and in a number of cases the target levels can be reached. The target vertical resolution of 500 m is particularly ambitious and is not achievable by the system as specified; however, the system configuration will provide a vertical resolution of 1 km or better for many species, which is unprecedented for a limb-emission sounder. Errors will be assessed more extensively in the retrieval study extension, taking into account refinements to instrument specifications and identified mitigation procedures for prominent errors. Once implemented, threshold requirements will be met with greater margin and target requirements will be achieved in additional cases.

7.4 Scientific Impact

PREMIER will be the first mission to generate atmospheric trace-gas fields at a resolution high enough to study stratosphere–troposphere exchange, tropical convection, the Indian monsoon, pyroconvection, long-range transport of air pollution (and associated chemical conversions) and signatures of mesoscale dynamics including gravity waves. The following sections demonstrate the potential scientific impact in case studies of relevance to the mission objectives.

Parameter	Driving Objectives	Altitude Range ⁽¹⁾ (km)	Targets		Thresholds	
			Along-track: 50 km		Along-track: 100 km	
			Across-track: 25 km		Across-track: 100 km	
			Vertical Resolution [km]	Accuracy ⁽³⁾ [ppbv unless stated otherwise]	Vertical Resolution [km]	Accuracy ⁽³⁾ [ppbv unless stated otherwise]
T	A	50–25	1	0.5K	1.5	1K
	A,B,C,D	25–6	0.5	0.5K	1.5	1K
	D	6–sfc ^(2,4)	<6	1K	6	2K
H ₂ O	A	50–25	1	5%	3	15%
	A,B,C,D	25–6	0.5	5%	1.5	10%
	D	6–sfc ⁽⁴⁾	<6	5%	6	10%
O ₃	A	50–25	1	3%	3	8%
	A,B,C,D	25–TP ⁽²⁾	0.5	25 ppb/3%	1.5	50 ppb/8%
	A,B,C,D	TP–6	0.5	15	1.5	30
	D	6–sfc ⁽⁴⁾	<6	15	6	30
CH ₄	A	50–25	1	10%	3	20%
	A,C,D	25–TP	1	5%	1.5	10%
	A,C,D	TP–6	1	25	6	50
	D	6–sfc ⁽⁴⁾	<6	25	6	50
CO	B,C,D	25–TP	0.5	10	3	20
	B,C,D	TP–6	0.5	20	3	40
	D	6–sfc ⁽⁴⁾	<6	45	6	90
HNO ₃	B,C,D	25–6	0.5	0.5	1.5	1
CFC-11	B	25–6	0.5	0.015	1.5	0.03
HCN	C	25–6	0.5	0.1	3	0.2
NO ₂	C,D	TP ⁽⁵⁾ –6	0.5	0.2	1.5	0.4
	D	6–sfc ⁽⁵⁾	<6	0.2	6	0.4
PAN	D	TP ⁽⁵⁾ –6	1	0.045	1.5	0.09
Extinction coefficient	A,C,D	25–6	0.5	10 ⁻⁴ km ⁻¹	1.5	2.10 ⁻⁴ km ⁻¹

Colour coding: **dark red** = non-compliant, **green** = compliant, **blue** = compliant with margin.

(1) As covered by PREMIER limb observations down to ~6 km altitude at mid-latitude (i.e. down to 8 km at equator; down to 4 km at high latitude) and in combination with MetOp/MetOp-SG down to the surface (Subsection 7.4.4.1).

(2) TP = tropopause level; sfc = Earth's surface.

(3) Precision instead of accuracy is given for temperature.

(4) Refers to lower-tropospheric column mean mixing ratio; i.e. 0–6 km at mid-latitude and 0–8 km in Tropics.

(5) NO₂ and PAN apply only if above background.

Table 7.13. Overall assessment of PREMIER's capabilities to address the geophysical (Level-2) data requirements specified in Table 4.1, based on the error analyses for IRLS and STEAMR summarised in Subsection 7.3.2 and taking into consideration identified mitigation strategies for prominent instrumental errors.

7.4.1 Impact of UTLS Variability and General Circulation on Surface Climate (Objective A)

Recent research has described the importance of a well-resolved upper troposphere and stratosphere for the prediction of future regional, seasonal, and inter-annual changes of surface climate. This implies that changes and variability in UTLS composition and the underlying processes need to be understood in a quantitative manner and accurately represented in models.

PREMIER’s impact on the validation of trace-gas variability obtained in this altitude region in CCMs is discussed in Subsection 7.4.1.1, followed by selected examples of improvements to the representation of processes in models.

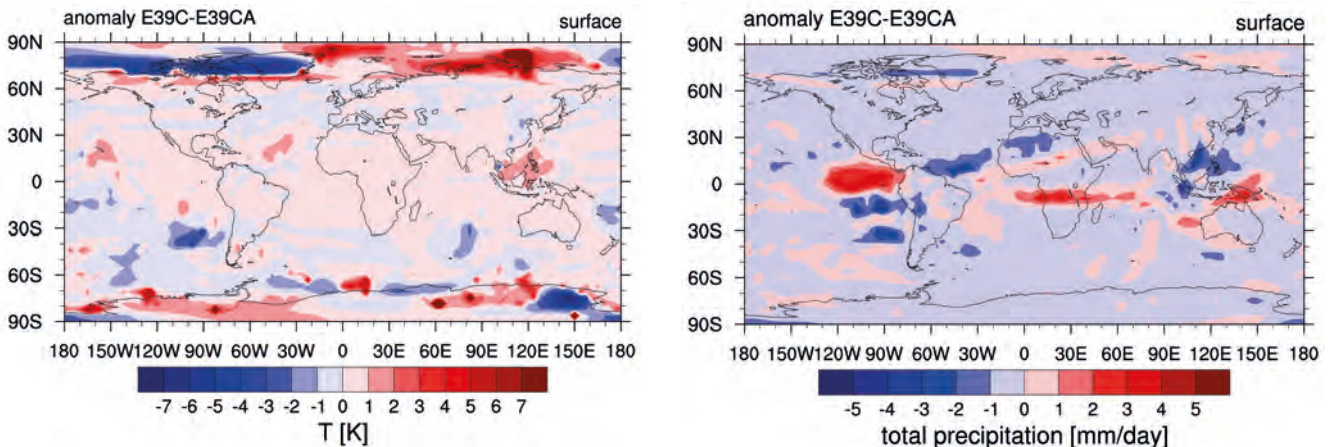
Stenke et al. (2008) analysed the results of two long-term CCM simulations (E39C and E39C-A). The simulations only differed in the transport schemes used. The authors found that an unrealistic distribution of UTLS water vapour, resulting from a too diffusive transport scheme in E39C, was largely responsible for significant cold biases in the simulated UTLS temperatures at polar latitudes. As illustrated in Fig. 7.23, the differences in the transport schemes also result in large differences in surface climate variables such as temperature and total precipitation. In Subsection 7.4.2, we demonstrate PREMIER’s capability to narrow down current uncertainties in model representations of transport.

There is also growing evidence that dynamic coupling effects in the stratosphere–troposphere system have a significant impact on regional weather patterns and climate (Chapter 2). Predicted changes of the strength of the stratospheric Brewer–Dobson circulation may modify tropospheric weather patterns as demonstrated by Scaife et al. (2011). Parameterised gravity-wave drag accounts for much of the potential future trend of the Brewer–Dobson circulation models (Li et al., 2008; McLandress & Shepherd, 2009). PREMIER’s capability to provide constraints on atmospheric gravity waves through 3D observations with the necessary resolution is demonstrated in Subsection 7.4.1.2.

7.4.1.1 PREMIER’s impact on CCM validation

CCMs are used to make projections of future climate, and also to understand past climate variability and feedback processes between chemical constituents and the physical climate. As is summarised in further detail in Chapter 8, there are major international efforts that concentrate on the validation of the dynamic, chemical, and radiative processes in CCMs to gain confidence in their projections. However, as pointed out by the SPARC CCMVal report (2010), the information gained from such evaluations depends critically on the quality of the observational data that are used. Without accurate observations, it is not possible to tell whether a model is realistic. Errors in observed mean values can arise from measurement biases or from sampling errors, which may be random or systematic. These errors can be especially large in the UTLS, where measurements are sparse and natural variability is high (e.g., Hegglin et al., 2008).

Figure 7.23. Annual mean differences in surface temperature and precipitation resulting from long-term CCM simulations (E39C and E39C-A) employing different transport schemes that result in large differences in UTLS water vapour and ozone. (M. Dameris)



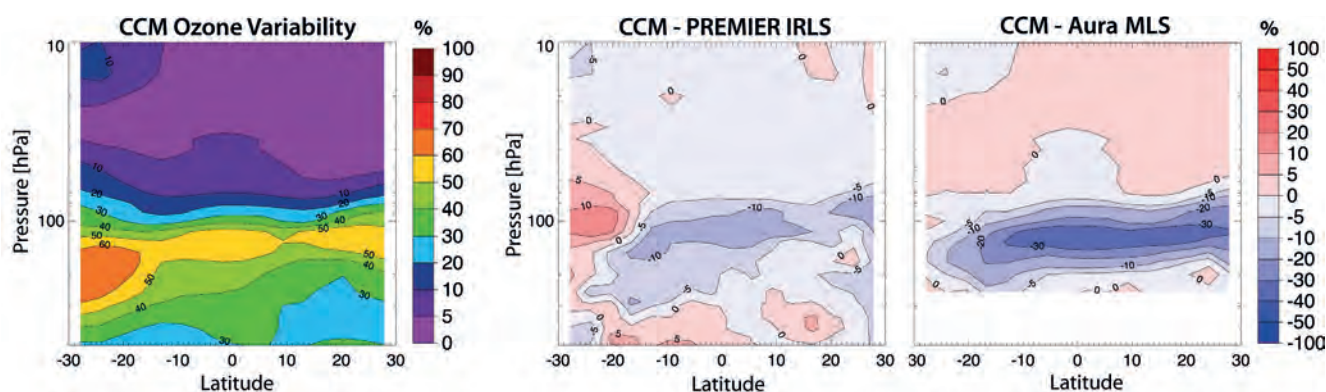
PREMIER's potential to improving the explanatory power of CCM validation diagnostics has been assessed (Riese et al., 2011). The observations of PREMIER and current limb sounders were synthesised from constituent fields of a state-of-the-art CCM according to their spatio-temporal sampling patterns. These synthetic observations were then used to produce climatologies commonly used as CCM validation diagnostics such as zonal mean cross sections, seasonal cycles, and vertical profiles, and compared to the corresponding climatologies derived from the fully-sampled CCM fields. The differences in the climatologies of the sub-sampled and fully-sampled CCM fields are then solely attributable to sensor sampling biases. Imposition of randomised and systematic errors on each synthetic profile in a second step yields insight into how the climatologies are influenced additionally by those instrument characteristics.

An example is provided in Fig. 7.24, featuring the evaluation of how sampling, vertical resolution and measurement errors and biases influence the intramonthly variability of ozone in the Tropics and subtropics. The results indicate that the geographical and temporal sampling of Aura MLS captures well the predicted ozone variability (not shown). The same is true for PREMIER IRLS. However, when adding the effect of vertical averaging kernels (i.e. vertical resolution) and measurement errors to the synthetic observations, the zonal mean structure in the ozone variability especially around the tropopause height (around 100 hPa) cannot be captured in the case of the Aura MLS-like instrument. PREMIER IRLS's estimate of the truth, however, remains almost unchanged owing to its higher vertical resolution. This example for ozone illustrates how PREMIER will help to improve CCM validation, especially in the UTLS where observations with adequate vertical resolution are sparse, by defining climatological means and variability without introducing major sampling errors. Furthermore, PREMIER will yield insight into natural variability on shorter time and length scales than hitherto accessible by limb-sounding. These high-spatial resolution observations on a sub-monthly timescale will allow the development of more particular process-oriented diagnostics, which are currently lacking but are needed for a deeper understanding of CCM performance and representation of physical, radiative and chemical processes governing trace-gas distributions in the UTLS.

7.4.1.2 Gravity wave momentum flux and gravity wave sources

The vertical flux of horizontal momentum deposited by gravity waves, or Gravity Wave Momentum Flux (GWMF) accelerates (or decelerates) the background winds and is thus a major driver of the QBO and Brewer–Dobson

Figure 7.24. Tropical zonal mean cross section of ozone variability for August 2004 derived from a full CCM field (left). The impact of sampling the full CCM field according to the patterns of PREMIER IRLS and Aura MLS is shown in the centre and right panels, respectively, in terms of differences from the fully-sampled field. While the 'true' variability is seen to be underestimated by MLS in the UTLS range, it is seen to be well-captured by PREMIER IRLS, which is primarily due to the much higher vertical resolution in this height range. (M. Hegglin)



circulation (Subsection 2.3.1). Zonal-mean balances are required to quantify the impact of GWMF on the QBO and Brewer–Dobson circulation. In particular, the zonal mean acceleration can be calculated from the vertical gradient of the zonal component of the zonal mean GWMF. Estimates of the zonal mean and total hemispheric GWMF are limited by the number of observations and require global coverage. They are therefore difficult to gain from *in situ* or ground-based observations. For a single gravity wave the horizontal direction of GWMF is in the direction of the horizontal wave vector. Accordingly, a gravity wave propagating to the east carries positive zonal GWMF while a gravity wave propagating to the west carries negative zonal GWMF. As gravity waves are excited for a wide variety of horizontal directions, GWMF of the individual waves partly cancels when calculating the average. Therefore, it is essential to determine accurately both direction and magnitude of GWMF for the individual events.

The ability of PREMIER to measure GWMF has been assessed in a dedicated study (Preusse et al., 2012). Based on high resolution ECMWF global temperature fields, resolving a large part of the wave spectrum explicitly, PREMIER ‘observational’ data were synthesised and the GWMF derived through an end-to-end simulation. The derivation of GWMF involves several steps including tomographic temperature retrieval, isolation of mesoscale temperature fluctuations from larger scale (planetary) waves and 3D gravity wave analysis, providing both direction and amplitude. These processing steps involve retrieval errors and approximations (e.g. relations for calculating GWMF from temperature amplitudes). Using synthesised ‘observations’, these approximations have been validated by comparison with the true values determined from the model winds. The end-to-end simulation allows a quantitative assessment of the individual steps as well as the whole processing chain. An example of a comparison for sampled ECMWF data from 29 January 2008 is shown in Fig. 7.25. The general structure and individual events are well reproduced. Note, the high variability spanning several orders of magnitude.

For a systematic assessment, comparisons were statistically evaluated for five one-week periods representative of different seasons. The results are summarised in Table 7.14. Compared to current satellite measurements, the accuracy of absolute values of GWMF for individual waves is improved by almost an order of magnitude. Zonal mean and total hemispheric GWMF require directional information for individual events, which becomes feasible for the first time with PREMIER observations. The achievable accuracy for GWMF will enable a major advance to constrain atmospheric dynamics (Preusse et al., 2012).

To characterise the role of gravity waves in climate change fully will require a physical representation and a better understanding of their sources (Subsection 2.3.1). Various gravity wave sources have been investigated using satellite data for over a decade. This, however, has been based on spatially collocating observed waves and their potential sources followed by an iterative ad hoc process of forward modelling, data comparison and model tuning. For PREMIER, the 3D temperature measurements will, for the first time, permit backward ray-tracing as a powerful tool for interpretation of global measurements. An example of backward ray-tracing from simulated observations at 25 km altitude down to the surface topography of Greenland is illustrated in Fig. 2.5. The end-points of rays launched from simulated gravity wave observations at 25 km altitude are shown in Fig. 7.26. The colour indicates the minimum altitude to which the rays can be followed before they cease to be propagating waves. In each case, the wave source has to be located at this minimum altitude or somewhere along the ray.

Two interesting features identified in the global distribution of end-points are marked by red ellipses. Firstly, west of Norway a particularly large number of end-points marks a low pressure system with wind velocities of more than

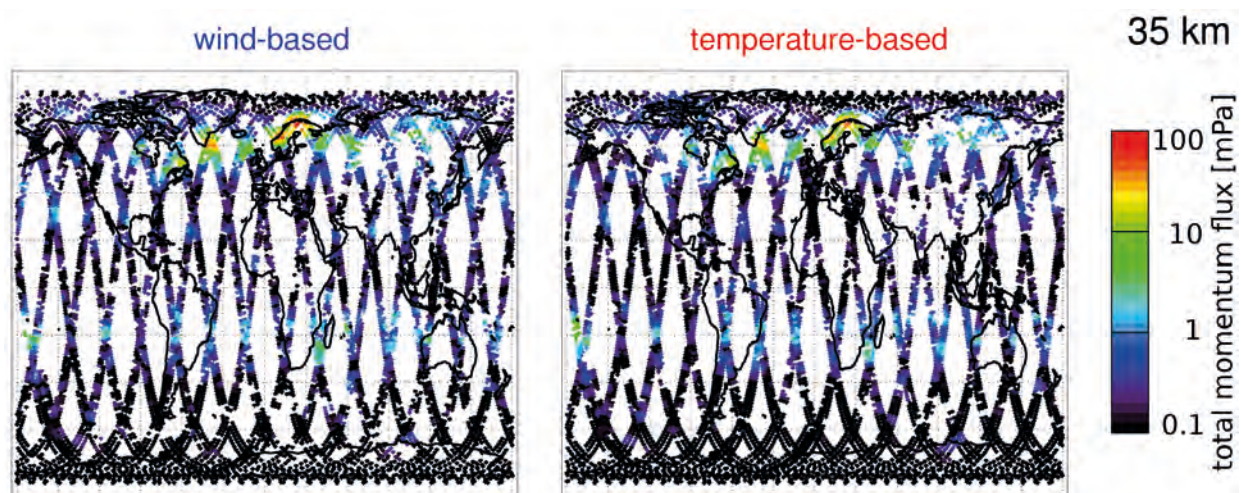


Figure 7.25. Magnitudes of momentum fluxes determined for gravity waves resolved by the ECMWF model. Data are for 29 January 2008 and 35 km altitude. There is a point-by-point correspondence between (left) the reference data calculated from the model winds and (right) the values calculated via a relation inferred by Ern et al. (2004) from temperature observations synthesised for PREMIER IRLS. (P. Preusse)

30 m/s at the 500 hPa level. The high GWMF values in Fig. 7.25 observed over northern Norway and also the enhanced GWMF values further east originate from this storm. By simple spatial collocation, these GWs would have been misinterpreted as mountain waves. Secondly, a large number of end-points around tropopause level in the southern Tropics and subtropics indicate gravity waves which were excited around that level two days before the observations. Many of these end-points match strong precipitation at this time, as shown in the right panel of Fig. 7.26. Ray-tracing thus identifies that convection in the ECMWF model can trigger gravity waves at cloud top height, and that these propagate quite slowly. It should be emphasised, however, that these are features of the gravity wave-field as resolved and represented in the current ECMWF model, which uses a parameterisation for convection. The convective parameterisation causes the generation of gravity waves in the ECMWF model frequently at cloud top, but rarely in the mid troposphere where GWs are expected to be excited by the latent heat release and strong updrafts and downdrafts associated with convection, if these were resolved by the model. It therefore appears that the parameterisation does not couple these fully into the dynamic variables of the model. PREMIER observations will reveal the properties of real sources similar to the way simulated PREMIER observations have revealed the origins of gravity waves as represented in the current ECMWF model.

7.4.2 Stratosphere–Troposphere Trace-gas Exchange (Objective B)

Important greenhouse gases such as water vapour and ozone, with steep gradients between their tropospheric and stratospheric mixing ratios, exhibit large spatial and temporal variability in the UTLS as a result of stratosphere–troposphere exchange (STE). Prominent underlying processes are the

Quantity	Current satellite observations	PREMIER
Single event accuracy	250%	<30%
Single event precision	unknown	<25%
Zonal mean GWMF	not possible	~30%
Total hemispheric GWMF	not possible	~30%

Table 7.14. Systematic assessment of GWMF accuracy for the full processing chain including temperature retrievals.

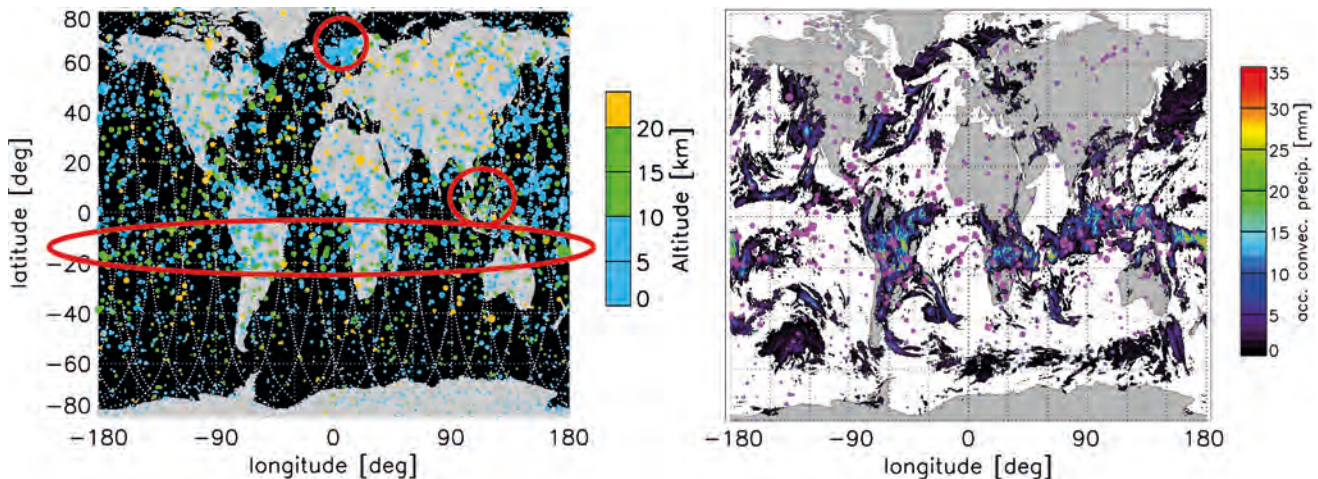


Figure 7.26. Global application of ray-tracing. The left panel indicates in colour the altitude of end points of backward rays launched from PREMIER observations at 25 km. End-points with altitudes of 12–20 km repeated in the right panel match patterns of precipitation (six-hour accumulation) two days previously. Selected features highlighted in red are discussed in the text. Backward ray-tracing requires full characterisation of the waves and can be performed using PREMIER data but not with current satellite measurements. (P. Preusse)

Brewer-Dobson circulation, quasi-horizontal isentropic transport between the tropical upper troposphere and the extra-tropical lowermost stratosphere, and vertical transport from below by convection (Subsection 2.3.2). It is a challenging task to model all the complex transport processes and their spatial and temporal variability. The impact of the advection scheme on the simulated surface climate has been demonstrated in Subsection 7.4.1 based on results obtained from two CCM simulations (E39C–E39C-A). In addition to uncertainties arising from inadequate advection schemes, all transport schemes used by models are subject to uncertainties concerning the influence of mixing, the irreversible part of transport.

The influence of uncertainties in the atmospheric mixing strength on the global UTLS distributions of greenhouse gases (water vapour, ozone, methane, and nitrous oxide) and associated radiative effects have been assessed (Riese et al, 2011). The study is based on multi-annual simulations with the Chemical Lagrangian Model of the Stratosphere (CLaMS) driven by ERA-Interim meteorological data and a state of the art radiance code (Forster et al, 2011). CLaMS is particularly suited for this study, because it employs a physically based sophisticated mixing scheme. Mixing, the irreversible part of transport is controlled in this scheme by the local horizontal strain and vertical shear of the atmospheric flow with an adjustable mixing parameter (critical Lyapunov exponent λ).

The radiative effects of uncertainties in the strength of atmospheric mixing are calculated by a two-step approach. First, the sensitivity of simulated UTLS trace-gas distribution to uncertainties in the atmospheric mixing strength (value of critical Lyapunov coefficient λ) is determined. Afterwards, the resulting differences of trace-gas concentrations are converted into radiative effects to assess the potential impact of uncertainties in the atmospheric mixing strength on climate projections. To determine the sensitivity of the trace-gas fields to the mixing strength, two simulations were made that only differ in the value of the mixing parameter λ , a ‘reference case’ with a value of $\lambda=1.5$ and an ‘enhanced mixing case’ with a value of $\lambda=1.2$. These particular values of the mixing parameter are well inside the current uncertainty range (compare e. g., Khosrawi et al., 2005; Konopka et al., 2005).

For ozone and water vapour, Fig. 7.27 shows the mixing ratio difference between the reference and enhanced mixing cases. For ozone, the altitudes of the largest increases are found in the lower stratosphere, a region where ozone

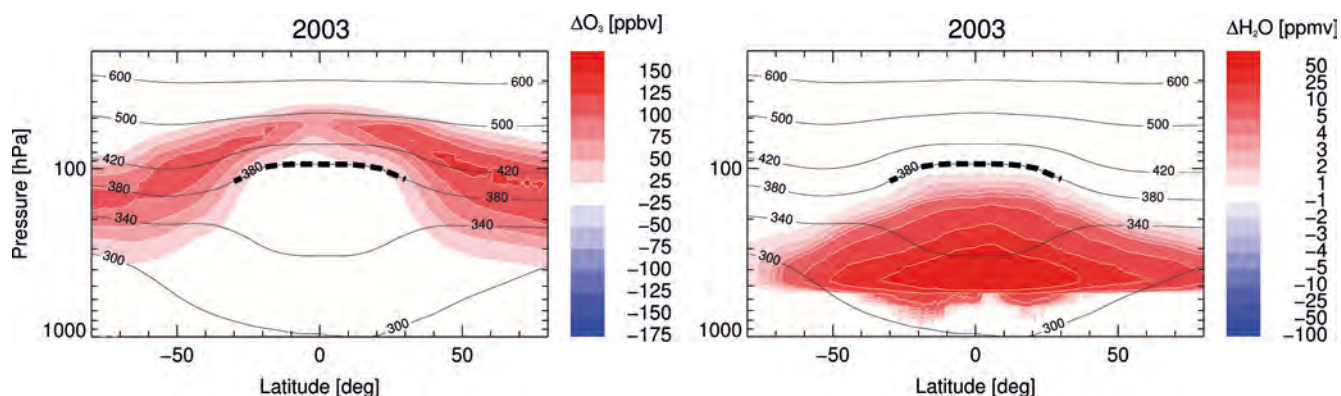


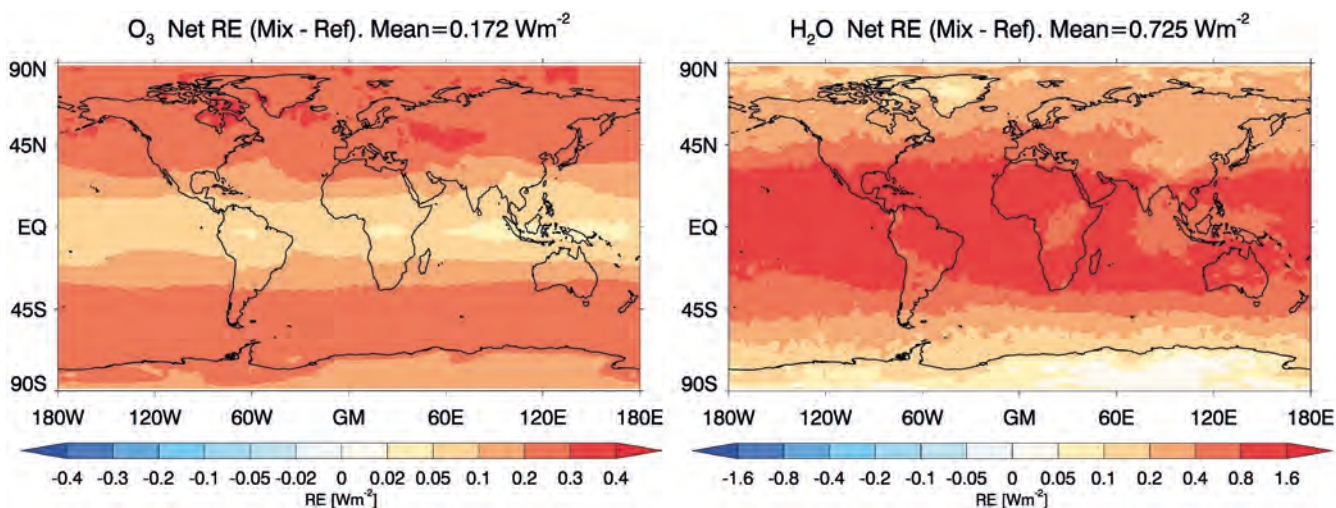
Figure 7.27. Difference in ozone (left) and water vapour mixing ratios (right) between a ClAMS simulation with enhanced mixing ($\lambda=1.2$, see text) and a reference simulation ($\lambda=1.5$). Zonally-averaged annual mean percentage differences are shown for 2003. Potential temperature levels are indicated by solid lines. The tropical tropopause is denoted by the thick dashed black line. (F. Plöger)

changes have the largest impact on surface temperature (Fig. 2.2). Maximum values correspond to a percentage change of about 30%. For water vapour, the largest changes occur in the tropical upper troposphere. Water vapour percentage changes in the TTL and lower stratosphere also amount to 5–10%, however, they are well below 1ppm as a result of the low background values in this region.

The latitudinal distribution of the ozone and water vapour changes shown in Fig. 7.27 are well reflected in their associated radiative effects shown in Fig. 7.28. Radiation fluxes of both water vapour and ozone are very sensitive to uncertainties in the mixing. In contrast, simulated radiative effects of N_2O , and CH_4 , both relatively well-mixed, turn out to be rather insensitive (Riese et al., 2011).

Globally-averaged effects are 0.72 W/m^2 for water vapour and 0.17 W/m^2 for ozone, respectively. The combined radiative effect is therefore about 0.9 W/m^2 . This number is about as large as changes of the radiative forcing since 1980 due to well-mixed greenhouse gases, aerosols, and stratospheric water vapour (Solomon et al., 2010). Solomon et al. (2010) derived the impact of this radiative forcing change on surface temperature by employing a model with a climate sensitivity of 3°C for a doubling of CO_2 . They found a surface temperature increase of 0.4K , demonstrating the significance of globally-averaged radiative

Figure 7.28. Radiative effect measured as radiative forcing (RF) of enhanced mixing compared to the reference run for ozone (left) and water vapour (right). Zonally-averaged annual mean values are shown for 2003. (A. Rap)

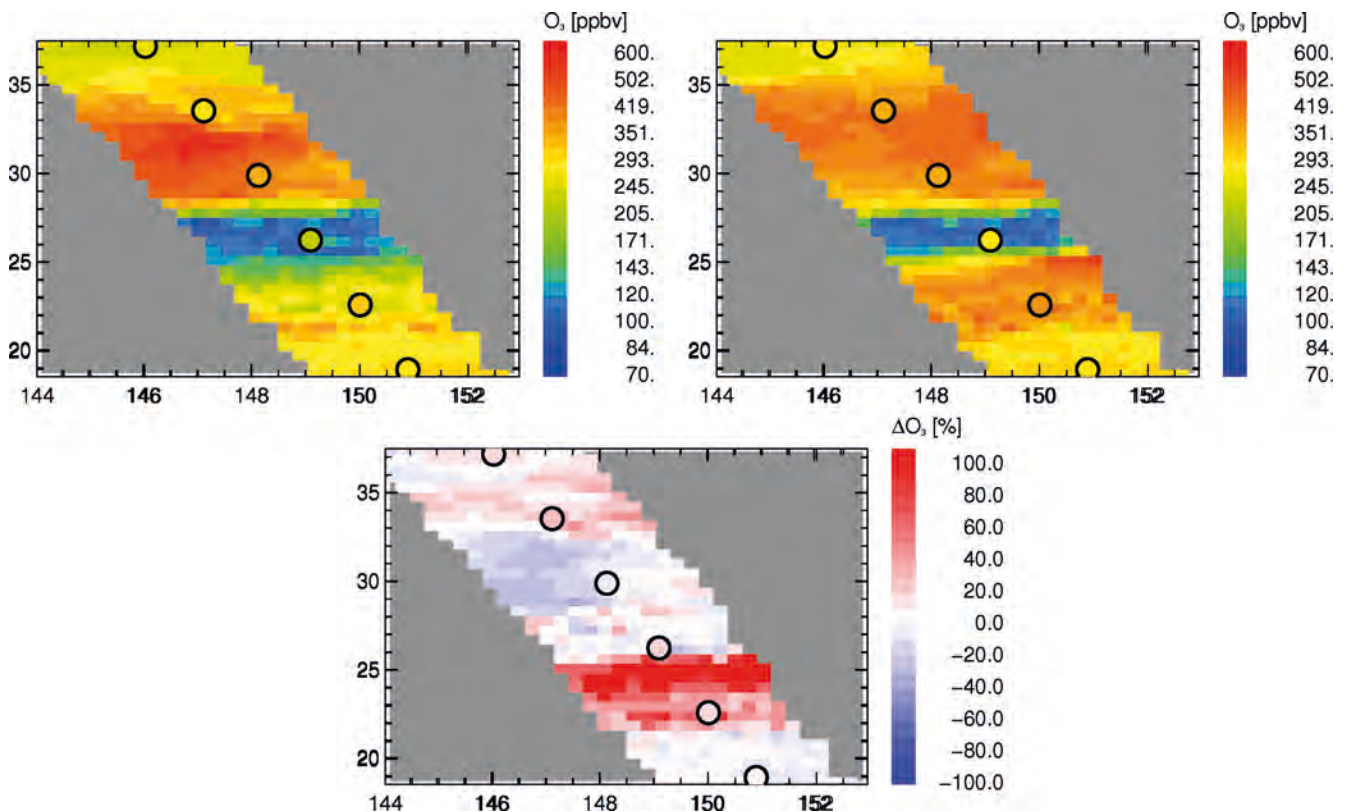


effects in the order of 0.9 W/m^2 . Thus, representation of mixing in the model is important, not only to the UTLS distributions of water vapour and ozone, but also to the representation of radiative forcing and feedback in climate models.

The capability of PREMIER to narrow down these uncertainties was investigated based on highly-resolved snapshots of the region of the Asian monsoon (see also Fig. 2.6), generated by CLaMS for 8 August 2003. For this purpose, the horizontal and vertical resolution of the simulation was increased to 25 km and 200 m, respectively. The top row of Fig. 7.29 shows simulated ozone mixing ratios, for the reference case (left) and for the enhanced mixing case (right), as sampled by PREMIER (IRLS DM) along an orbit track and including effects of the vertical and horizontal averaging kernels (which are rather small, since the simulation and observation have comparable resolution). For both cases, a pronounced filament of ozone-poor air can be seen. Filled circles show corresponding simulated MIPAS observations for comparison, which are strongly influenced by the broad vertical averaging kernel. The bottom plot shows the ozone differences between both cases, which are of the order of 50% in the range of the ozone-poor filament, i.e. well above the detection limits of both instruments. While the PREMIER IRLS horizontal sampling and vertical resolution allow the difference between the reference and enhanced mixing cases to be retrieved, MIPAS horizontal sampling is too sparse and vertical resolution too coarse to pick them up.

The capability of high-resolution limb-sounding to provide constraints on the representation of atmospheric transport processes in models is further illustrated by CRISTA-NF observations from the high-flying Russian aircraft Geophysica in early March 2010 (Ungermaun et al., 2011). CRISTA-NF is a limb-scanning infrared instrument with a spectral resolution comparable to the PREMIER IRLS DM. Figure 7.30 shows CFC-11 mixing ratios observed between

Figure 7.29. Ozone along a selected PREMIER orbit (IRLS DM) in the Asian monsoon region at 18 km on 8 August 2003 from the high-resolution (25 km) simulation for the reference case (top left) and enhanced mixing case (top right). Differences are shown in the bottom panel. Filled circles show the corresponding MIPAS observations (upper panel) and differences (lower panel) for comparison. (F. Plöger)



Svalbard and Kiruna in northern Sweden during a flight on 2 March 2010, where CRISTA-NF encountered a situation of strong mixing between polar air (low CFC-11 values) and mid-latitude air (high CFC-11 values).

Structure in the CFC-11 cross-section retrieved along the flight track (left panel) is resolved in sufficient detail to compare with CLaMS and to differentiate between the reference case and the enhanced mixing case discussed above. The reference case ($\lambda=1.5$) provides somewhat better results for the situation encountered by CRISTA-NF, e.g. the feature with higher CFC-11 mixing ratios around 12 km altitude and 11:15 (UTC). The observation demonstrates the capability of high-resolution limb-sounding to provide constraints for atmospheric transport and mixing schemes.

From this example observation and the comparison of simulations shown in Fig. 7.29, it can be anticipated that PREMIER global observations will provide the dataset and statistics needed to study quantitatively the spatial and seasonal variation of the atmospheric mixing strength as well as the implications for simulated climatological trace-gas fields and associated radiative effects.

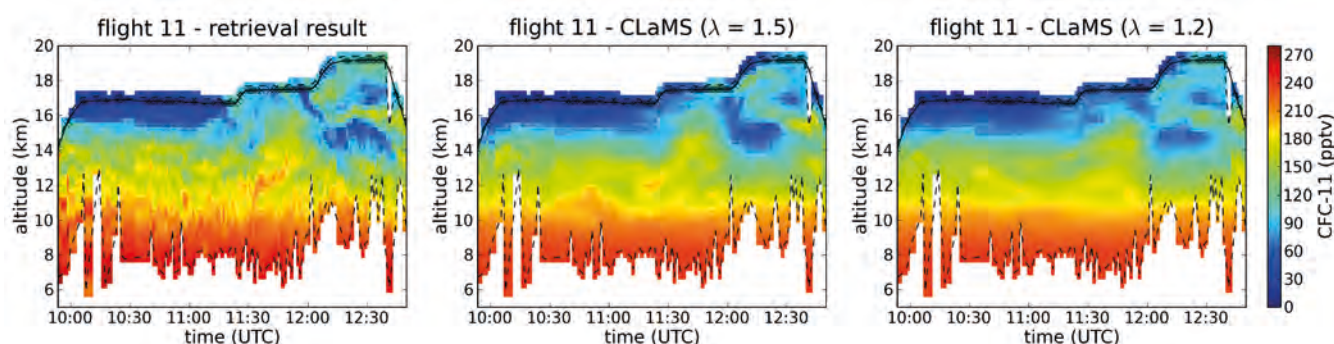
One of the complementary attributes of mm-wave and IR for limb-sounding of the upper troposphere was demonstrated by MARSCHALS and MIPAS-STR flying on Geophysica at around 18 km in the PREMIER_Ex campaign on 10 March 2010. In the presence of a cirrus layer at 10 km during the last half hour of the flight (9.45–10.15 UT), ozone retrieval from the mm-wave sounder is unaffected. The retrieval from the IR sounder is restricted to altitudes above cirrus (Fig. 7.31). In addition, combining information from both sensors (fusion) improves on the precision of either one sensor over the full range.

The airborne limb-imaging FTIR (GLORIA_AB) made its first observations in December 2011 alongside MARSCHALS and MIPAS-STR. Analysis of data from this ESSENCE campaign is in progress.

7.4.3 Impacts of Convection, Pyroconvection and Outflow on the UTLS (Objective C)

Understanding convection processes and their impact on the UTLS is vital, as noted in Chapter 2, since they provide a means to transport constituents including greenhouse gases, ozone precursors and aerosols rapidly into the UT and sometimes the lowermost stratosphere. Pyroconvection is associated with particularly rapid upward transport of gaseous and particulate products of burning. The transport of CH_4 can have a direct radiative effect, while the ozone generated from precursors not only has a radiative effect but also increases OH which depletes CH_4 . In the PREMIER Impact study (Riese et al., 2011) it was shown that biomass burning gaseous products caused an annual

Figure 7.30. Comparison of CRISTA-NF observations and CLaMS simulation results. The left panel displays CRISTA-NF CFC-11 observations that were obtained during the PremierEX campaign. The Geophysica flight altitude is indicated by the black solid line. The middle and right panels show corresponding CFC-11 values obtained from CLaMS simulations using critical Lyapunov coefficients λ of 1.5 and 1.2, respectively. (C. Kalicinsky)



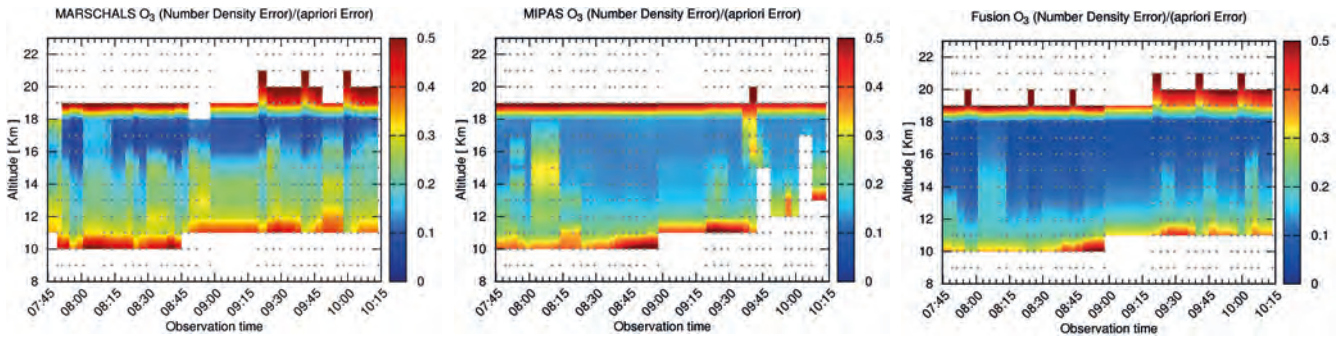


Figure 7.31. Time-height cross-sections showing the regions of information content for ozone retrievals from the mm-wave limb sounder (MARSCHALS) and ir limb-sounder (MIPAS-STR) from a Geophysica aircraft flight on 10 March 2010. The ratio of retrieved to *a priori* error is plotted for the two sensors individually and for their combination. The presence of upper-level cirrus at ~10 km (9–10 UT) limits the retrieval range for the IR but not the mm-wave. (U. Cortesi)

radiative effect at the top of the troposphere of $\sim 50 \text{ mW/m}^2$, mostly owing to the generation of ozone in the upper troposphere, where sensitivity is highest (Fig. 2.2). The spatial distribution of the biomass burning radiative effect in Fig. 7.32 shows the importance of representing pyroconvective processes in a changing climate regime.

This rapid injection of material into the UTLS often results in plumes containing HCN and CH₃CN, which are produced only by biomass burning and therefore provide a signature of this source. Other species associated with high temperature combustion, such as CO, are also lofted in these plumes, elevating their UT concentrations well above the background levels from other sources. As shown below, PREMIER will observe the composition of plumes from convection and pyroconvection, thereby quantifying their contributions to ozone production and its radiative effects and also biomass burning emission sources.

An example of a pyroconvective event which appears to have been solely driven by the intense heat from the fire rather than an unstable meteorological situation is the Kilmore East (Victoria, Australia) event of 7 February 2009. This pyroconvective event rapidly transferred large quantities of gases and smoke into the UTLS, where plumes were transported over hemispheric distances. Smoke was observed in the lower stratosphere by the Calipso lidar (e.g. de Laat et al., 2012) and OSIRIS shortwave limb-sounder (Siddaway & Petelina, 2011) and trace gases were observed by the Aura MLS (Pumphrey et al., 2011) and Envisat MIPAS limb sounders (Glatthor et al., 2012). A mesoscale model simulation of this fire and a careful assessment of emissions were made to assess PREMIER's capability to capture important biomass burning signature species and also the spatial characteristics of the plumes. For the time period chosen and with the input characteristics the model produced a 'double' plume and retrieval simulations were performed for a N–S transect $\sim 191.5^\circ\text{E}$ on 11 February 2009 through this double plume; one of which is just above the tropopause and one just below. The subsequent trajectories of the two plumes, and their respective influences on ozone production, were therefore markedly different. As Fig. 7.33 shows, the IRLS CM retrieval is seen to resolve the two distinct plumes of HCN, whereas MIPAS is unable to distinguish the two plumes and barely able to detect them, due to vertical smearing. This simulation illustrates the improvement PREMIER will provide in discriminating pyroconvective sources from anthropogenic and biogenic sources and quantifying ozone production.

The Southeast Asian monsoon is of major importance to the composition of the UTLS (Chapter 2). Large-scale convective systems associated with the monsoon circulation loft trace gases and aerosols in large quantities from surface sources, including blackbody, into the TTL, from where they can be

transported around the globe and upwards into the stratosphere via the BD circulation.

The convectively-uplifted species initially circulate in an anticyclone (Fig. 2.6) in the UT before being dispersed. In addition, sub-tropical lower stratospheric air is entrained into the anticyclone and mixed into the tropical UT, and can intrude downwards into the mid-troposphere on the low-latitude side of the system. In order to show how the evolving structure associated with the monsoon would be revealed by PREMIER, a high resolution ($15 \times 15 \text{ km}^2$) model simulation was performed for August 2008. As an example, the 750 pptv 3-D isosurface of the HCN distribution in the monsoon region for 23 August is shown in Fig. 7.34.

The figure also shows latitude cross sections for several longitudes revealing the mesoscale structures which develop. For retrieval simulation purposes, a transect crossing Bangladesh in the core of the monsoon circulation and a transect crossing the southern tip of India at $\sim 75^\circ\text{E}$ at the westerly periphery of the monsoon circulation on 23 August 2008 were chosen.

Figure 7.35 shows STEAMR CO and HCN retrieval simulations for the transect through the core of the monsoon circulation. Distributions of CO and HCN are shown to be well-captured through the lower stratosphere and upper troposphere, i.e. down to $\sim 12 \text{ km}$, even in the presence of ubiquitous cirrus which obscures IRLS observations in this region below $\sim 18 \text{ km}$. Elevated

Figure 7.32. Spatial distributions of the radiative effects of methane and ozone changes owing to biomass burning. Global distributions of the differences between annual average radiative effects with and without inclusion of biomass burning sources are shown. The annual global average for methane is -1.4 W/m^2 while that for ozone is 47 mW/m^2 . (A. Lupu)

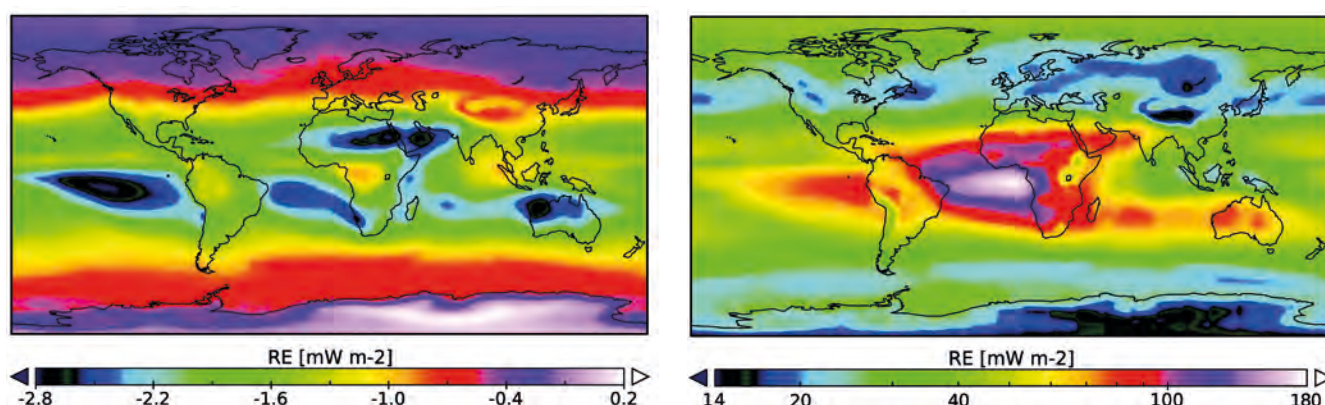


Figure 7.33. Comparison of height-latitude cross-sections of HCN as observed by PREMIER IRLS in chemistry mode and Envisat MIPAS for a transect through a double plume east of New Zealand from the Kilmore East pyroconvective event. The left panel is the HCN distribution from the GEM-AQ model. The centre and right panels show the simulated retrieved distributions of HCN for PREMIER IRLS in chemistry mode and Envisat MIPAS, respectively, performed on a common basis. PREMIER IRLS captures well the double plume and separates them above and below the tropopause, indicated by the white line. The retrieval range limit is due to cloud limb opacity. (N. Glatthor)

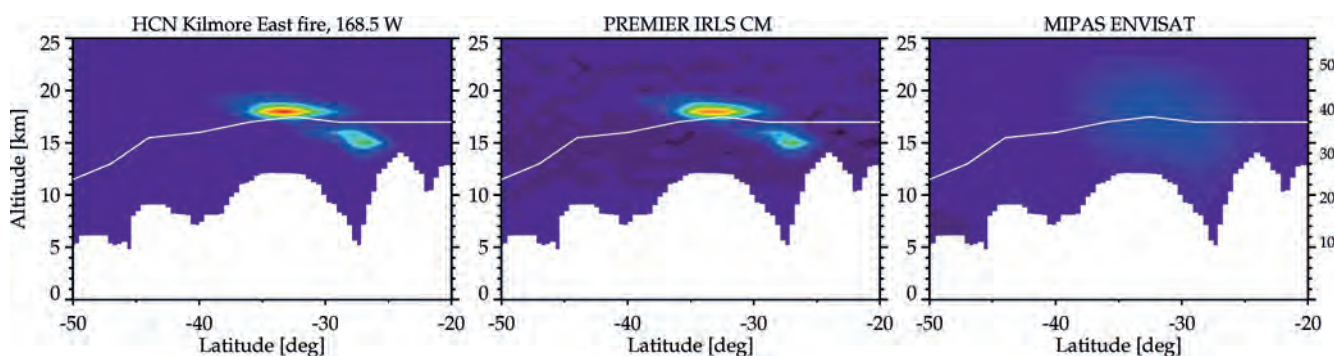
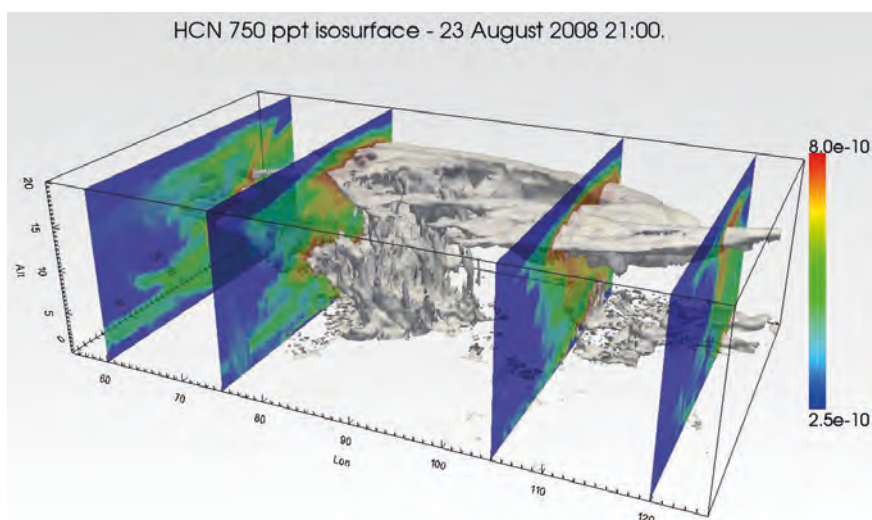


Figure 7.34. The 750 pptv HCN isosurface produced from a $15 \times 15 \text{ km}^2$ simulation using GEM-AQ also showing vertical slices at several longitudes through the monsoon. (A. Lupu)



concentrations of HCN are especially prominent, due to uplift of surface emissions from biomass-burning via the monsoon circulation. From the point of view of understanding processes, it is important to note that the STEAMR retrieved signature of HCN shown in Fig. 7.35 is given by a single orbit pass as compared to that shown for ACE in Fig. 2.8 which required zonal averaging over several months of data.

While Fig. 2.6 shows the instantaneous structure of the Monsoon anticyclone over the whole region, Fig. 7.36 shows an across-track swath observed by PREMIER at 12 km altitude for water vapour and ozone mixing ratios. Ozone and water vapour distributions from 2D retrieval simulations for the IRLS DM are compared with the high-resolution model distributions. Detailed mesoscale structure associated with the monsoon circulation is seen to be retrieved along-track and across the IRLS swath ($\sim 360 \text{ km}$), illustrating that high-fidelity 3D information retrieved from PREMIER will enable critical testing of the dynamics and transport associated with the Southeast Asian monsoon.

Cross-sections of O_3 , CO and HNO_3 are shown in Fig. 7.37 for the same transect as the H_2O and O_3 distributions at 12 km altitude shown in Fig. 7.36. The upper panels of Fig. 7.37 show structure from the $15 \text{ km} \times 15 \text{ km}$ resolution model while the lower panels show simulated retrievals which combine PREMIER and MetOp-SG nadir sensors. PREMIER provides detail in the middle and upper troposphere, while MetOp-SG extends coverage down into the lower troposphere. The simulated retrievals show detailed spatial structure to be captured, extending to near-surface CO enhancement from emissions over northern India in a cloud-free section northward of 20°N . This illustrates how uplift of surface emissions and transport through the monsoon circulation will be probed by PREMIER in the UTLS and how combination with MetOp-SG will extend the range downwards. The complementary value added by PREMIER to MetOp-SG for retrieval of tropospheric composition and quantification of surface emissions and air quality is described in Subsection 7.4.4.

PREMIER's capabilities to investigate convective and pyroconvective processes have been illustrated through examples of retrieval simulations for the required trace gases. However, the potential of the mission will extend to gases which are also observable within the specified spectral bands. Simulations have therefore been performed also for these additional gases for scenarios including the Kilmore East pyroconvective event and the Southeast Asian monsoon (Kerridge et al, 2012). Elevated plume concentrations of ethane (C_2H_6), ethyne (C_2H_2), methanol (CH_3OH) and sulphur dioxide (SO_2) are retrievable by IRLS (chemistry mode) and methyl cyanide (CH_3CN) and sulphur dioxide (SO_2) by STEAMR. Furthermore, elevated concentrations of

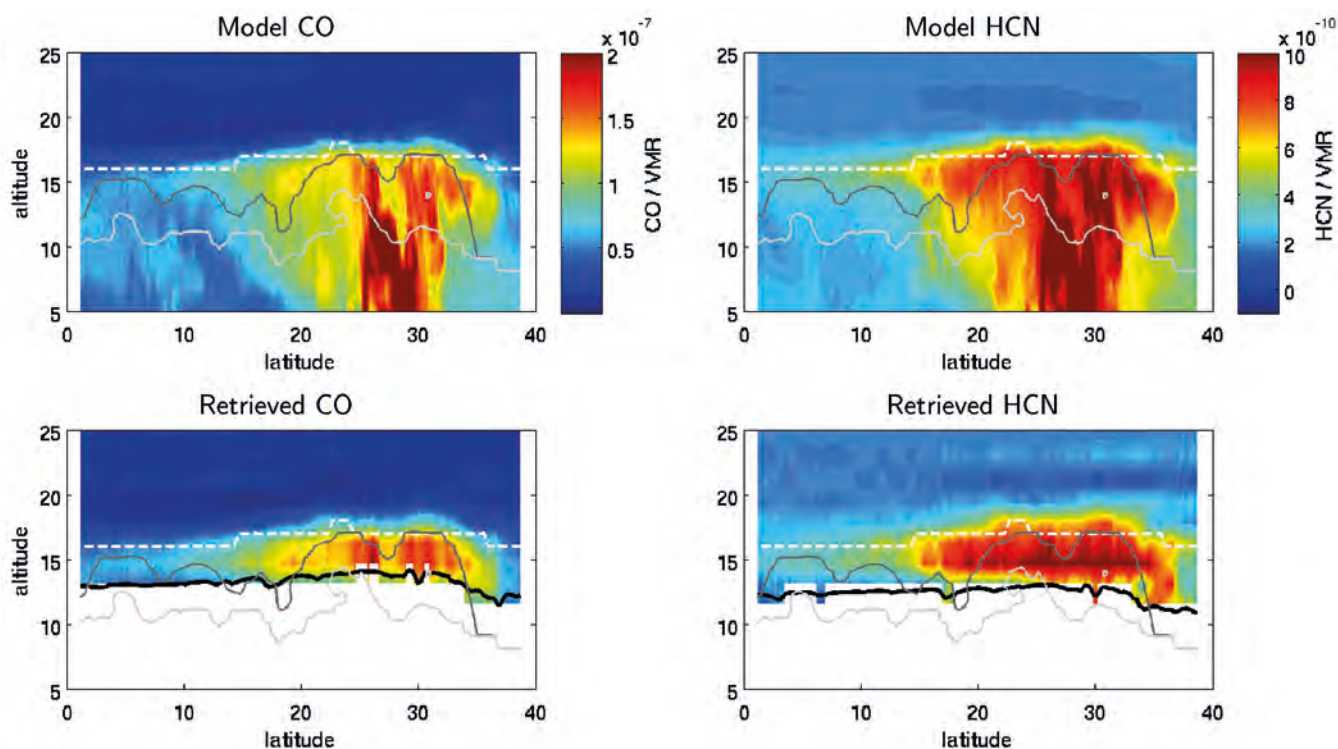


Fig. 7.35. Comparison of height-latitude cross-sections of CO and HCN from the GEM-AQ model (upper panels) and simulated STEAMR retrievals (lower panels) for a transect through the core of the Southeast Asian monsoon circulation on 23 August 2008 over Bangladesh. The dashed white line shows the location of the tropopause. The dark grey line indicates the IRLS lower limit, which is determined by the opacity of upper level cirrus. The light grey line shows the STEAMR opacity limit, driven by water vapour attenuation; the black line represents the altitude where the minimum useful information content of STEAMR retrievals is reached. (J. Urban)

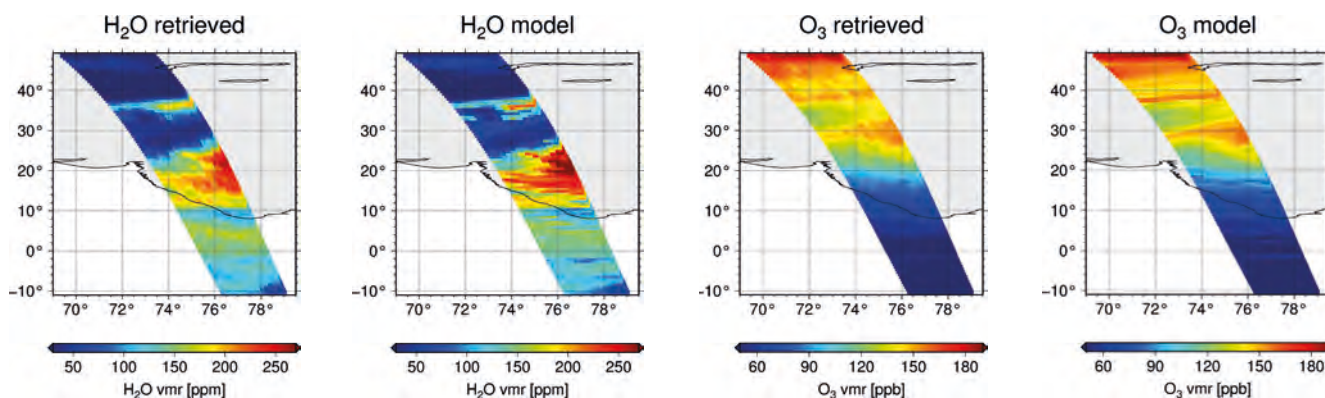
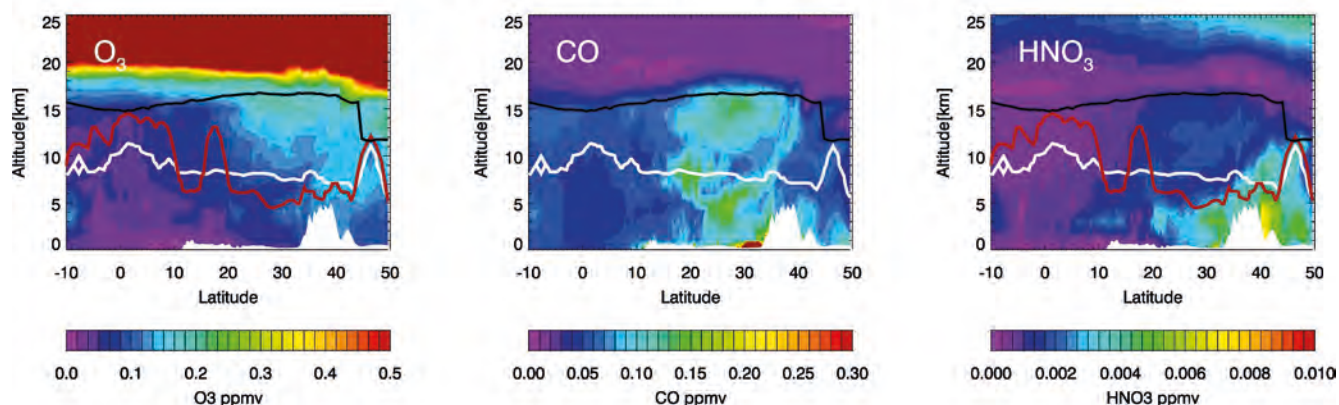


Figure 7.36. Comparison of GEM-AQ ($15 \text{ km} \times 15 \text{ km}$ resolution) model distributions of H_2O and O_3 near 12 km altitude with 2D retrieval simulations for the DM across the IRLS swath, showing horizontal structure along- and across-track. (L. Hoffmann)

isoprene (C_5H_8) in plumes uplifted rapidly through tropical convective events are retrievable for IRLS (CM).

7.4.4 Processes Linking the Composition of UTLS and Lower Troposphere (Objective D)

Meeting this objective relies on using PREMIER in conjunction with MetOp or MetOp-SG data. The two following subsections briefly assess two complementary approaches to achieve this combination. The first approach is to combine retrievals from different instrument sensors. The second approach,

Modelled O₃, CO & HNO₃ cross-sections

Simulated limb/nadir combined retrievals

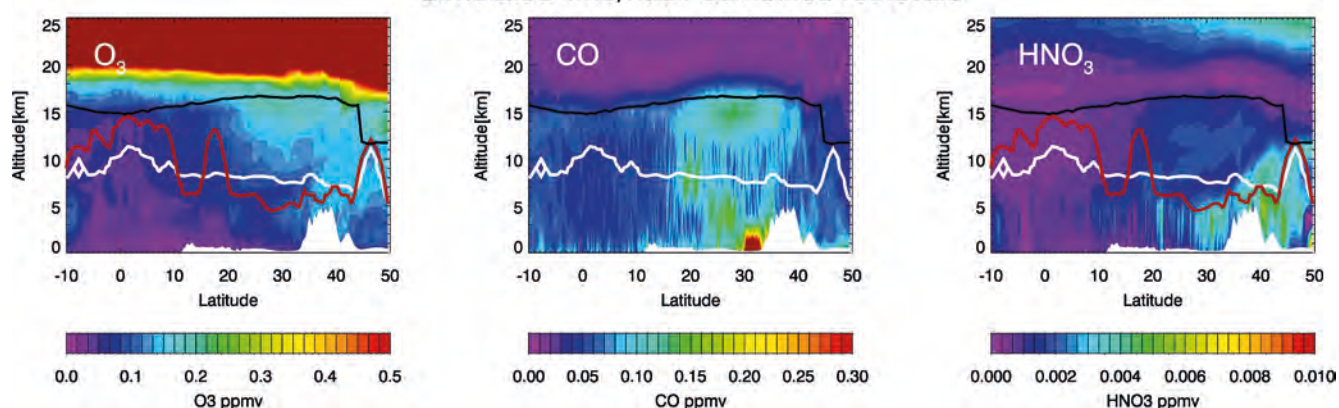


Figure 7.37. Cross-sections of O₃, CO and HNO₃ in the monsoon periphery extending to the surface. The GEM-AQ model (upper panels) is compared with simulated retrievals for PREMIER combined with MetOp-SG (lower panels). For O₃, the IRLS CM and STEAMR are combined with IASI-NG and S5 UVNS, for CO, STEAMR is combined with IASI-NG and S5 UVNS and, for HNO₃, IRLS CM is combined with IASI-NG. The tropopause is indicated by the black line and the limb opacity limits for IRLS and STEAMR are indicated by the red and white lines, respectively. (A. Waterfall)

illustrated here in the case of methane surface fluxes inversions, uses modelling and data assimilation as transfer tools.

7.4.4.1 Assessment of combined sensor performances in the lower troposphere

To explore links to surface emissions and air quality, PREMIER's Level-2 requirements extend below the limb-sounding range into the lower troposphere (Table 4.1). The benefit to lower troposphere sounding of combining information from the PREMIER limb-sounders with that from the nadir sounders on MetOp or MetOp-SG can be quantified through an optimal estimation retrieval simulation. For PREMIER, errors are representative of an individual profile retrieval, taking into consideration contributions other than noise (Section 7.3). The simulation for MetOp-SG sensors is based on the retrieval scheme and fit precision achieved with real flight data from MetOp IASI and GOME-2 (Kerridge et al, 2012). Fitting precision for IASI-NG and S5 UVNS is in line with their predicted performances. Estimated precision for O₃, CH₄, CO and NO₂ retrievals from MetOp-SG sensors and their combination with PREMIER are compared with Level-2 requirements for the 0–6 km layer average in Table 7.15 for two radically different *a priori* assumptions; one extremely loose and the other with reduced variances and vertical correlations

from an atmospheric model. For O₃, CH₄ and NO₂, the estimated uncertainty for MetOp-SG is reduced substantially through combination with PREMIER IRLS, which accurately determines their profiles down to 6 km. For CO, estimated uncertainty is also improved significantly through combination with STEAMR, which accurately determines the profile down to ~10 km. It is important to note that sensitivity of estimated retrieval precision for the 0–6 km layer to *a priori* assumptions is markedly reduced in the case of the PREMIER combination in comparison to the MetOp-SG sensors alone. Although uncertainties on IASI-NG and S5 UVNS retrievals associated with knowledge of surface and atmospheric properties are not considered, so MetOp-SG-only estimates are best case, the combination with PREMIER is seen to meet threshold requirements with factor 2 margin in all four cases. A more extensive error analysis is in progress.

A priori and retrieval uncertainties on 0–6 km layer average mixing ratios (ppbv) are shown for two cases. Values not in brackets are for a very loose *a priori* uncertainty: 1000% on retrieval levels spaced at 1 km. Retrieved values in this case indicate information on the 0–6 km layer coming from the sensors alone. Values in brackets adopt an *a priori* uncertainty of 300% for O₃, CO & NO₂ and 20% for CH₄ on retrieval levels spaced at 1 km, and vertical correlations are from the covariance matrix for MACC profiles about their global monthly mean for August 2008. These somewhat tighter *a priori* constraints are nonetheless still sufficient to capture atmospheric variability encountered under most circumstances. The additional value in blue for MetOp-SG (S5) retrieval of NO₂ employs an *a priori* uncertainty of 1% at every stratospheric level. This represents schemes which subtract a stratospheric column estimate from a total column to derive a tropospheric NO₂ column.

7.4.4.2 Improving CH₄ surface emission inversions using CH₄ vertical profile observations

The CH₄ vertical profile in the mid-upper troposphere and stratosphere will be observed by PREMIER. In combination with IASI/IASI-NG, these vertical profile observations will provide important constraints on UTLS atmospheric processes that affect the total column average mixing ratio of CH₄ (X_{total}). Observations of X_{total} from the Sciamachy and GOSAT short-wave-IR (SWIR) nadir sounders are currently used for CH₄ surface emission inversions, adding important information to the regional and global surface networks (e.g. Bergamaschi et al., 2009). Observations of X_{total} with improved spatial sampling and accuracy will be made by advanced SWIR sensors on Sentinel-5 precursor (launch in 2015) and Sentinel-5 onboard MetOp-SG. However, SWIR nadir-sounders provide only total column information.

Important processes that affect X_{total} include tropopause height variations, stratosphere–troposphere exchange, deep convection and mid-upper tropospheric long-range transport. These processes cause horizontal variability in X_{total} which is not directly related to surface emission variability. Currently, these indirect relationships have to be represented by the transport model that is used in the emission inversion. Any misrepresentation, for example in the timing of convection, or in the grid-area averaged tropopause

	O ₃ (ppbv)	CH ₄ (ppbv)	CO (ppbv)	NO ₂ (ppbv)
Target requirement	15	25	45	0.2
Threshold requirement	30	50	90	0.4
<i>A priori</i> uncertainty	230 (100)	10 000 (300)	790 (290)	13 (4)
MetOp-SG (IASI-NG + S5)	26 (13)	244 (9)	49(14)	2.2 (1.6, 0.4)
MetOp-SG + PREMIER	6 (5)	6 (4)	37 (11)	0.18 (0.11, 0.11)

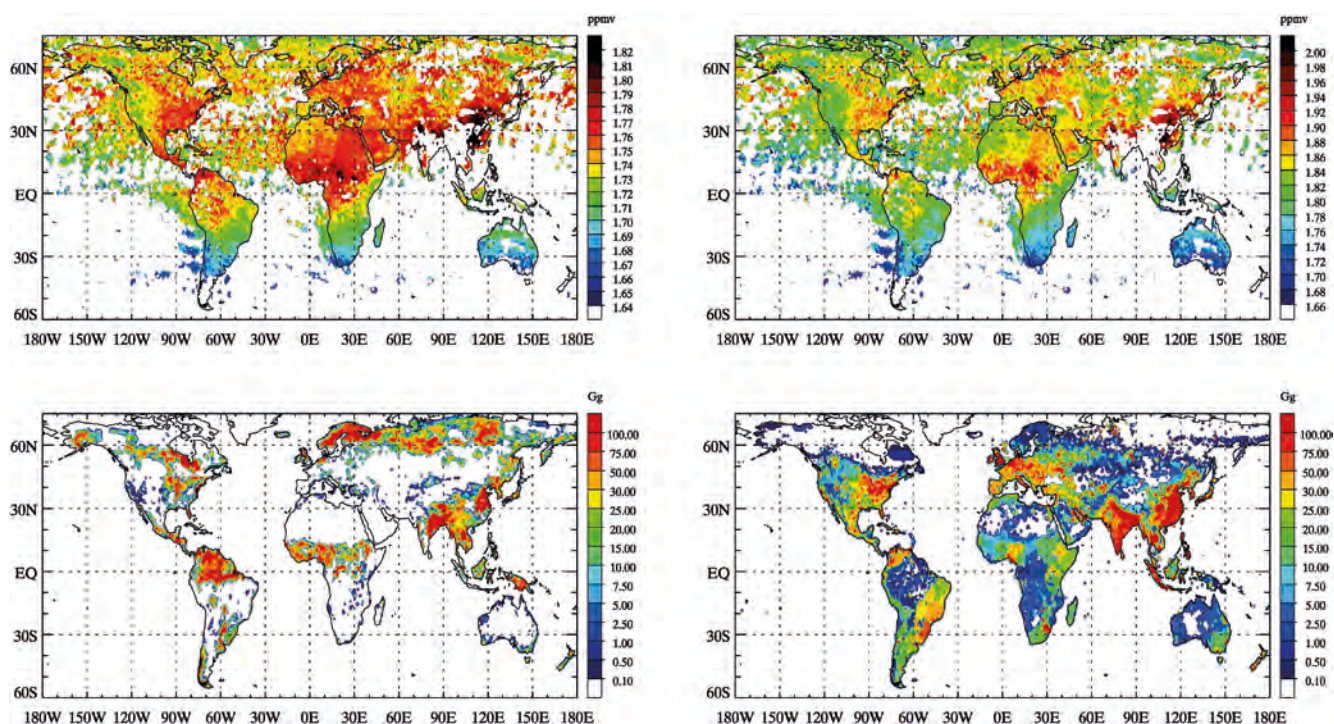
Table 7.15. Comparison of estimated errors on mid-latitude 0–6 km columns of O₃, CH₄, CO and NO₂ retrieved from MetOp-SG nadir sounders and in combination with PREMIER.

height, will cause spurious structure in the simulated X_{total} which are wrongly assigned to surface emissions. PREMIER in combination with IASI/IASI-NG will constrain the CH_4 profile.

In order to illustrate the importance of the UTLS variability for the interpretation of X_{total} , the difference in the global spatial distribution between X_{total} and a lower tropospheric column mixing ratio (X_{trop}) is shown in Fig. 7.38. The distribution of X_{total} is from the Sciamachy observations for August 2004, as presently used in emission inversions. The distribution of X_{trop} shows the same Sciamachy observations after subtracting the contribution above the 500 hPa level as simulated by the TM5 chemical transport model (Huijnen et al, 2010). To calculate X_{trop} for each Sciamachy total column observation the simulated column above the 500 hPa level was subtracted taking into account the Sciamachy averaging kernel, and then converted back to mixing ratio for the air pressure column from the surface to the 500 hPa level.

The X_{trop} distribution reflects the surface emission distributions (Fig 7.38: bottom panels) more directly than the X_{total} distribution. For example, westward long-range transport in the upper troposphere from the important South-Asian emission region causes enhanced values of X_{total} over the Middle East, which are much less evident in X_{trop} . Although variability in CH_4 mixing ratio increases with altitude in the stratosphere, variability at higher levels in the stratosphere contributes less than that in the mid-upper troposphere to the variability in X_{total} , due to the lower air density in the stratosphere. Improvement to the precision of the CH_4 0–6 km layer average retrieval from MetOp-SG Sentinel-5 UVNS and IASI-NG through the addition of PREMIER is shown in Table 7.15.

Figure 7.38. Sciamachy observations for August 2004 of column average methane mixing ratios (ppmv). The total column average (X_{total}) and derived lower tropospheric column average (X_{trop}) are shown in the top-left and top-right panels, respectively. UTLS transport patterns (e.g. over the Middle-East) and tropopause height variations affect the total column, whereas the lower tropospheric column is more closely related to CH_4 surface emission regions. Note that the range and colour scale used for X_{total} and X_{trop} differ. Bottom left: Climatological June-July-August natural surface fluxes (Spahni et al., 2011). Bottom right: Anthropogenic CH_4 emissions (EC-JRC/PBL, 2009). Both in Gg per $1 \times 1^\circ$ cell. (M. van Weele)



7.5 Value-Added Operational Applications

7.5.1 Introduction

Limb-emission sounders have been providing a distinct contribution to the Global Observing System (GOS) for over three decades. As a result, they have long been used and assimilated in operational meteorological applications as well as for monitoring stratospheric ozone. Emerging operational environmental forecasting applications, in particular in the context of GMES in Europe (see Chapter 8), require information on several constituents in the UTLS that PREMIER will observe, both for monitoring changes in the context of an evolving climate and to support assimilation and forecasting of tropospheric composition and air quality. The results from four studies that have assessed the performances of PREMIER for operational applications, using a range of tools and different perspectives are presented in this section.

7.5.2 Impact of MIPAS and IASI Data on the Analysis and Forecast of Tropospheric Ozone

As described in Subsection 7.4.4.2 in regard to methane surface flux estimation and also in Subsection 2.3.4 for ozone, current chemical data assimilation systems are able to combine information from a range of different observational data streams and, in particular, to combine observations from limb-sounders with those from nadir-sounders. The *Impact Study* (Riese et al., 2011) has demonstrated that synergistic use of MIPAS profile and IASI tropospheric column ozone data was indeed beneficial in the MOCAGE system of Météo-France. Figure 2.10 shows how data from the two individual instruments combine in the joint analyses and provide, as a result, a better agreement with independent ozone sonde profiles. In that study, MIPAS, MLS and IASI data were used as proxies or precursors for future PREMIER and IASI-NG data (Barré et al., 2012). The performance obtained with the current instruments provides in fact a bottom line estimate for what the advanced instruments will provide in the future, as described in the next sub-sections.

Already, the ozone profile information provided by the current limb sounders MIPAS or MLS in the stratosphere and UTLS is useful for tropospheric applications. This is primarily because more realistic distributions in the UTLS (through assimilation) allow better analyses and forecasts of intrusions of stratospheric ozone into the troposphere and, thus, a better description of the regional tropospheric budget of ozone as well as of the variability of ozone in the free troposphere (Barré et al., 2011). Although they do not significantly influence seasonal statistical skill scores of ozone forecasts against surface networks, on occasions of intrusions reaching down to the planetary boundary layer in the mid-latitudes (e.g. Elbern, 1997, Akritidis et al., 2010), assimilation based forecasts will demonstrate a much better skill at predicting the extent of the phenomenon. As a result, European air quality forecasts and assessments will be improved. This is also of importance in the context of air quality policy monitoring and modelling, as measures that can be taken on anthropogenic emissions of ozone precursors are not able to mitigate levels of ozone which originates from the transport of air masses of stratospheric origin.

7.5.3 Impact of PREMIER Data on Background Error Covariances

The background error covariance B matrix employed by a data assimilation system reflects estimated errors and covariances in the forecast model, and determines the extent to which observations can influence the analysis. The value which PREMIER could potentially add to MetOp or MetOp-SG through data assimilation into an operational system can therefore be estimated in terms of the reduction in diagonals of the B matrices. This has been done for

mid-latitude using the ECMWF matrix for H₂O and those for O₃, CH₄ and CO used by MACC-II, the pre-operational system for GMES Atmosphere Service. Figure 7.39 shows an estimate for the ECMWF/MACC-II vertical grid using IRLS and STEAMR single-profile measurement errors and corresponding random errors for IASI-NG and Sentinel-5 UVNS on MetOp-SG. It can be seen that STEAMR substantially reduces background variance down to ~10 km for O₃ and ~5 km for H₂O and that IRLS does so down to ~5 km and ~4 km for O₃ and H₂O, respectively. It can also be seen that STEAMR substantially reduces background variance down to ~10 km for CO and that IRLS does so down to ~4 km for CH₄. The figure also shows that information from IRLS and STEAMR is highly complementary to that from the MetOp-SG sensors. It is noteworthy that value is added for O₃, H₂O and CH₄ even below the height-range of the limb observations. This is indicated by the combined estimate improving on the IASI-NG plus S5 UVNS estimate at altitudes where the IRLS and STEAMR estimates do not improve on B, as is evident below 5 km for O₃ and CH₄.

7.5.4 The Impact of PREMIER in Numerical Weather Prediction

Limb-emission sounders observing in the mm-wave and IR have been long used in operational NWP for the initialisation of temperature, humidity and ozone in the UTLS. In the context of the *Impact Study* (Riese et al., 2011), a dedicated Observing System Simulation Experiment (OSSE) has been conducted in order to assess the value of PREMIER’s IRLS and STEAMR compared to current operational capabilities provided by Aura MLS. The set-up of an OSSE is to synthesise observations by sampling a realistic reference model run (nature run), to assimilate these observations in a state-of-the-art NWP suite and to verify the analyses (and the forecasts based upon them) against the nature run. This allows the performance of future instruments to be assessed against (or in addition to) current instruments in the GOS through an approach in common to that used over the last decade for NWP applications.

Global assimilation and 10-day forecasting experiments were conducted with the GEM forecast model with the addition of a linearised stratospheric ozone chemistry parameterisation. The assessment of the relative impact of IRLS, STEAMR, and MLS-type data on assimilation analyses, six-hour forecasts, and medium-range forecasts relied mainly on examining monthly

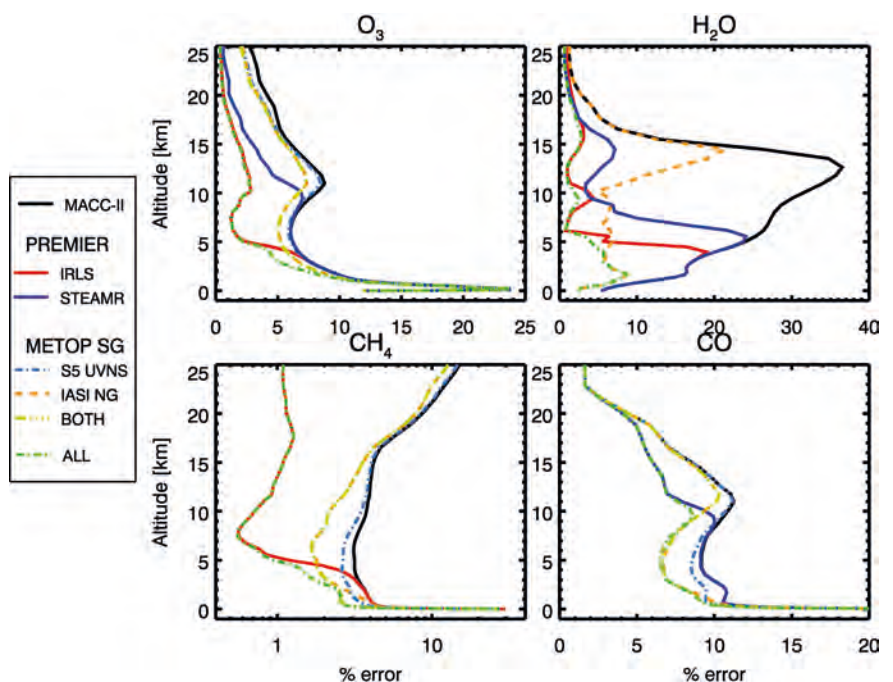


Figure 7.39. Mid-latitude profiles of background errors used by MACC-II (ECMWF for H₂O), together with improvements achieved by adding information from the MetOp-SG and PREMIER sensors; individually and in combination. (A. Waterfall)

mean RMS errors, differences and ratios of RMS errors, time mean errors and differences, and anomaly correlation coefficients.

The largest beneficial impact on analyses and forecasts from the addition of IRLS as compared to MLS-type data were found for ozone and water vapour in the troposphere and UTLS. The initial analysis benefits for water vapour and ozone can partially persist over the entire 10-day forecasts depending on the vertical level, this being most notable for the UTLS.

Overall, the results from the OSSE indicate that the assimilation of PREMIER's instruments on top of all the other instruments in the GOS will improve operational NWP forecasts. While this OSSE was capable of showing improved skill on the short range, additional improvements are expected on theoretical grounds for medium and long-range NWP because of the relatively long radiative and dynamic timescales in the UTLS. The expected benefits from the IRLS and STEAMR instruments are superior, or at least equivalent to, those from Aura MLS, which currently contributes significantly to the skill of meteorological analyses and forecasts in the UTLS (as shown for instance for water vapour in Fig. 2.11).

7.5.5 The Impact of PREMIER in Detection of Volcanic Ash Plumes

The importance to air traffic control of detecting and avoiding volcanic ash plumes was emphatically demonstrated by the widespread disruption caused by eruptions of Iceland's Eyjafjallajökull volcano in spring 2010. Satellite data provide an important input to the Volcanic Ash Advisory Centres (VAACs) for monitoring and forecasting the evolution of volcanic plumes. Imagery from geostationary satellites can be used to detect and differentiate ash from thin cirrus. However, conventional visible/IR imagery is limited in regard to both the optical thickness and height registration of ash layers which can be detected. Plume injection height is a key parameter for modelling and, depending on particle number density and size distribution, a thin layer of ash which is either not detectable or cannot be located precisely in altitude could potentially constitute an important aviation hazard. The Calipso satellite lidar was able to determine the vertical structure of ash layers from Eyjafjallajökull along its orbit tracks and this capability could potentially be available from future satellite lidars such as ADM-Aeolus and EarthCARE. Trials have recently been initiated on commercial aircraft of onboard forward-looking IR cameras. PREMIER's IRLS will routinely supply IR limb-images on a global basis of the height-range of specific importance to aviation. These will enable thin ash layers to be detected and their altitudes to be precisely determined, as illustrated in the following example, thereby augmenting the ash observing capabilities of the operational satellite system.

IR limb images have been simulated with a 3D multiple-scattering model based on properties of the ash plume from the Eyjafjallajökull (Iceland) volcano on 7 May 2010 retrieved in an orbit cross-section by Calipso and collocated SEVIRI image. The effective radius was 2 μm and visible optical thickness was 0.2, which was scaled down to 0.02. A layer this thin is difficult for Calipso to detect, but is semi-transparent in the limb. The ability of IRLS to discriminate this ash layer is indicated in Fig. 7.40 which compares images of the brightness temperature difference between 10.41 μm and 12.02 μm for structure in the scaled Calipso cross-section calculated for ice cloud and ash properties. The signature of ash is different in sign to ice. The simulation shows that PREMIER will add a unique perspective by detecting and differentiating ash and cirrus layers which are too thin to be detected by nadir imagers, and precisely determining their altitudes, providing valuable information for aviation as well as processes controlling UTLS composition.

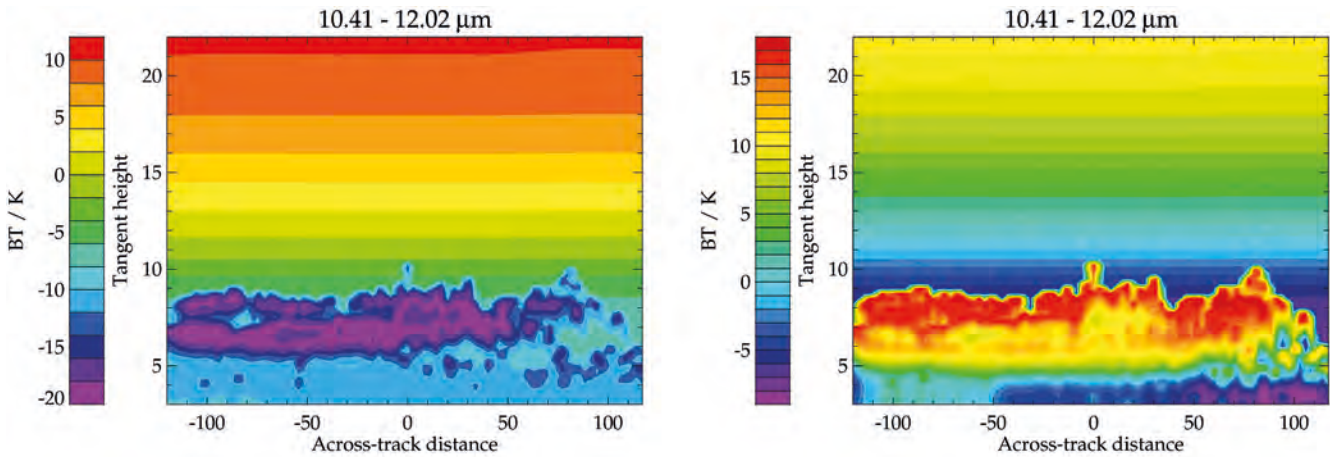


Figure 7.40. Simulated image of limb brightness temperature difference 10.41–12.02 μm calculated for the ash layer from Eyjafjallajökull observed by Calipso on 7 May 2010 (right), scaled down in optical thickness. IR optical properties for cirrus have been substituted and the 10.41–12.02 μm difference signature is of opposite sign(left). (R. Siddans)

7.6 Summary

This chapter has assessed the capability of the PREMIER mission to address its four scientific objectives which centre on the domain of the mid/upper troposphere and lower stratosphere, for which major advances in scientific understanding were defined in Chapters 2 and 3 and for which requirements were quantified in Chapter 4, namely:

- Impact of UTLS variability and the general circulation on surface climate.
- Trace-gas exchange between the troposphere and stratosphere.
- Impact of convection, pyroconvection and their outflow on UTLS composition.
- Processes linking the composition of the UTLS and the lower troposphere.

The performances of IRLS and STEAMR have been assessed at Level-1b by means of simulation and analysis. Their performances at Level-2 have been assessed by state-of-the-art retrieval simulation schemes, drawing on scientific experience from thirty-years of satellite limb-emission sounding and close interaction with the Agency’s technical and engineering experts, and thereby also the Phase-A industry teams. The scientific value of the mission has been demonstrated through retrieval simulations for selected phenomena of importance to PREMIER’s scientific objectives and by quantifying the impact which these retrieved distributions would have on the four scientific objectives. Retrievals combining PREMIER limb-emission observations with collocated MetOp-SG nadir sensors have also been simulated. The simulations have demonstrated that by meeting the specified Level-1b and Level-2 requirements, PREMIER will observe atmospheric structure down to finer scales in the mid-upper troposphere and lower stratosphere than previously accessible from space. This, in turn, will allow processes controlling composition in this height region of particular importance to climate and links to surface emissions and pollution to be quantified globally and PREMIER’s scientific objectives thereby to be met. The value to be added to the GMES Atmosphere Service and other operational applications from limb emission data is unique in this timeframe and has also been demonstrated.

A consolidation of this performance assessment is in progress, based on information from extensions to the Phase A studies and related ESA and national activities. Error analyses will elaborate identified mitigation procedures and the scientific impact assessment will be extended. The first airborne observations from a limb-imaging FTIR (GLORIA_AB) were made in

the December 2011 (ESSENCE) campaign and will be presented together with those from the mm-wave limb sounder (MARSCHALS).

→ MISSION CONTEXT

8 Mission Context

8.1 Introduction

This chapter identifies the scientific user community for PREMIER (Section 8.2), describes the global context for the mission, in terms of planned operational satellites and research missions (Section 8.3), and outlines the operational applications for PREMIER data (Section 8.4).

8.2 PREMIER Scientific User Community and its Readiness

The user community for PREMIER data is large and well-organised, spanning climate and Earth-system science research, global and regional atmospheric chemistry and air-quality research, as well as operational centres (Section 8.4), environmental agencies and national and international bodies with the responsibility for environmental policy and international conventions.

Fundamental research into atmospheric processes is a well-established field in which a large international community is engaged. To explore the mid/upper troposphere and lower stratosphere, this community has depended heavily upon observations from campaigns using aircraft and balloons. The PREMIER data will bridge the gap in scales observable from airborne platforms, including future unmanned airborne vehicles, as well as from other satellite missions. The international community will exploit these data for process-oriented research that would not otherwise be possible.

An increasing number of climate models now resolve the stratosphere and adopt high vertical-resolution in the UTLS. In recent years, the Stratospheric Processes And their Role in Climate (SPARC) community has provided a lead for process-oriented validation of chemistry-climate models (CCMVal) and extensive experience has been gained using current satellite datasets for this purpose. For the UTLS, the need for improved vertically-resolved satellite datasets has been clearly stated. The latest model evaluation exercise (SPARC/CCMVal, 2010) specifically includes the following recommendations:

- Long-term vertically-resolved datasets of constituent observations in the stratosphere are required to assess model behaviour and test model predictions. This includes ozone, but also other species that can be used to diagnose transport and chemistry. The current set of GCOS essential climate variables is not sufficient for process-oriented validation of CCMs.
- More global vertically-resolved observations are required, particularly in the UTLS. As CCMs evolve towards including tropospheric chemistry, lack of observations in this region will become a major limitation on model validation.

CCMs, which in the past have been developed by different communities focusing either on the troposphere or the stratosphere, are evolving rapidly towards full ESMS, incorporating fully-coupled tropospheric and stratospheric chemistry modules, representing two-way couplings between the physical climate and atmospheric composition and including more interactions with the biosphere and climate-sensitive emissions. The Climate Model Inter-comparison Project (CMIP-5) for the IPCC 5th assessment report in 2014 will include many more simulations with interactive chemistry and a well-resolved stratosphere than the CMIP-3 exercise for the IPCC 4th assessment report. Preparations for the IPCC 5th assessment report include the Atmospheric CCM

Intercomparison Project (ACC-MIP, www.giss.nasa.gov/projects/accmip) to specifically assess climate-chemistry interactions, including the role of UTLS changes and links with surface climate (Solomon et al., 2010).

A key development in the global atmospheric chemistry and regional air-quality research community is the integration with NWP on the short-term ‘chemical weather’ and the general tendency towards on-line chemistry modelling as opposed to off-line chemistry-transport modelling to improve the accuracy of short-term interactions between composition and the physical and chemical processes. In the PREMIER timeframe, the community will be ready to address, and in more detail than today, the use of UTLS observations and the role of UTLS composition variability for regional air-quality forecasting, e.g., in relation to the long-range transport of pollutants.

With coming advances in computing power, model resolution will continue to increase and, together with parallel advances in data archiving and visualisation systems, the community will be ready in the EE-7 timeframe to take full advantage of PREMIER observational data. Utilisation of PREMIER data is assured through international activities such as the IPCC, WCRP, IGAC and SPARC, through European projects in the context of Horizon 2020 and also through national activities such as those of the UK’s National Centre for Earth Observation, the German Helmholtz association’s climate initiative REKLIM or the French programme on atmospheric composition LEFE/CHAT.

8.3 PREMIER in Global Context

The capability to sound atmospheric composition from space will advance during the coming decade as the current operational system and research satellites are superseded by planned new missions. In regard to the operational system, Eumetsat’s first polar satellite, MetOp-A, which occupies a morning orbit (09:30), is scheduled to be followed in the same orbit by MetOp-B in 2012 and MetOp-C in 2017, and subsequently by the second generation series, MetOp-SG, which will include Sentinel-5 UVNS in addition to IASI-NG, MHS, MetImage and 3MI, the first of which is planned for 2020. Sentinel-5 UVNS and IASI-NG are nadir-viewing spectrometers to observe backscattered solar shortwave radiation and thermal IR radiation, respectively. Through technical advances, their capabilities will improve significantly on MetOp’s GOME-2 and IASI, respectively. Sentinel-5 will also build upon the experience that will be gained with Sentinel-5 Precursor, to be launched in 2015 to complement MetOp w.r.t. lower tropospheric composition for climate monitoring and air quality. Similar to S-5P, Sentinel-5 UVNS will exploit 2D array technology to achieve a broader swath and smaller ground pixel than GOME-2, for improved geographical (cloud-free) sampling of trace gases and will add SWIR channels to observe CO and CH₄ columns. IASI-NG will increase both spectral resolution and sensitivity for trace retrievals of higher accuracy. The 3MI instrument will be a novel multiwavelength, multi-angle, multipolarisation imager with a broad swath to observe aerosol properties. Together with the MetImage advanced multiwavelength imager, MetOp-SG will provide aerosol, cloud and surface properties which improve significantly on MetOp’s AVHRR/3. The first two Sentinel-3 satellites are planned for launch into a morning polar orbit (10:00) in 2013 and 2015, respectively. Although they are dedicated to ocean and land monitoring, their multiwavelength, dual-view imaging capabilities should also provide height-integrated aerosol data of high quality.

Europe’s third and fourth Meteosat Second Generation (MSG) satellites are due to be launched in 2012 and 2015, respectively, to be followed by Meteosat Third Generation Imager (MTG-I) and Sounder (MTG-S) satellites in six launches from 2019, with the Flexible Combined Imager (FCI) and Lightning Imager (LI) on MTG-I and the IRS and Sentinel-4 UVN on MTG-S. In combination, MTG-S and -I will provide a substantial advance from MSG

for atmospheric composition sounding from geostationary orbit over Europe and surrounding region, most notably through the addition of trace-gas sounding capabilities by IRS and Sentinel-4 UVN. The USA launched NPP into an afternoon (13:30– A-Train) polar orbit in October 2011, which is due to be followed in the same orbit by JPSS-1 in 2016 and JPSS-2 in 2021. The OMPS and CrIS instruments on JPSS-1 and -2 are nadir-viewing spectrometers to measure backscattered solar shortwave and thermal IR emission, respectively, and therefore analogues of GOME-2 and IASI, respectively. NOAA is scheduled to launch further GOES satellites into geostationary orbit in 2015 and 2017. In the coming decade China and Russia are planning to launch polar orbiting satellites and China, India, Japan, Korea and Russia are planning to launch satellites into geostationary orbit, several of which will have solar shortwave and thermal IR nadir-sounding as well as imaging capabilities.

In parallel to this evolution of the operational system, several research missions are also planned to sound atmospheric constituents. The Canadian Polar Communications and Weather (PCW) mission will observe northern high latitudes with a 20 channel imager every 15–30 minutes from two satellites in highly elliptical orbits. In addition to this operational payload, PCW is intended to also support air quality, CH₄ and CO₂ applications by deploying an imaging FTS with mid-IR to near-IR channels and an imaging grating spectrometer with UV to near-IR channels. NASA's GEOCAPE, an imaging spectrometer with both solar shortwave and thermal IR coverage to target air quality from geostationary orbit over America, and ASCENDS, a multiwavelength lidar to measure CO₂, are tier 2 missions in the Decadal Survey, for which launches are currently anticipated towards the end of this decade. NASA's OCO-2, a grating spectrometer with shortwave-IR and near-IR channels, is anticipated to be launched in 2014–15 into afternoon polar orbit (A-Train) to target CO₂. Follow-on missions are being considered with shortwave-IR coverage extended to CH₄ and CO: OCO-3/TCM in low-Earth orbit and GEOCARB in geostationary orbit. The candidate ESA Earth Explorer 8 (EE-8) mission CarbonSat would also target CO₂ and CH₄, through nadir-viewing shortwave-IR and near-IR spectrometry, possibly flying in formation with Sentinel-3. Other missions, such as MERLIN (lidar for measuring CH₄) will also complement the observing system for atmospheric composition.

During the coming decade, the satellite observing system will evolve towards a more extensive and sophisticated nadir-viewing capability to sound atmospheric composition. However, none of these planned missions include a limb-emission sounder.

The OMPS instrument recently launched on NPP has a capability to observe solar radiation backscattered in limb- as well as nadir-geometry. Limb- as well as nadir-capability is planned for OMPS on JPSS-2 and is an objective for JPSS-1 as well. The ALTIUS mission proposed by Belgium would image limb-scattered solar UVN radiation with an acousto-optical tunable filter. If flying in parallel, either OMPS (1:30pm) or ALTIUS could potentially complement PREMIER (09:30 and 21:30) with respect to profiling of stratospheric ozone in daytime, although their coverage would not extend into the troposphere or to other trace gases targeted by PREMIER.

Several sensors proposed for deployment on the International Space Station (ISS) would use limb-geometry. NASA's SAGE III-ISS, a shortwave solar occultation sensor, is in preparation for launch targeted for 2014. Other proposals are for MACE, an FTIR limb-emission sounder to observe the mesosphere and lower thermosphere, and SMR-ISS, a sub-mm limb-emission sounder to observe the stratosphere and lower mesosphere, to provide continuity with Odin SMR. SAGEIII-ISS, if deployed in the PREMIER time-frame, could provide vertical profile data of high accuracy for trace gases measured in common which, although sparse, could nonetheless serve as a valuable additional contribution to validation. The ISS is in a low inclination (51.5°) orbit, which correspondingly limits geographical coverage to middle

and low latitudes, and which precesses, so that the local time of emission observations vary from day to day, thereby also restricting applicability of MACE or SMR-ISS data for validation of PREMIER. NASA's GACM is a tier 3 mission in the Decadal Survey, which would seek to combine advanced limb-emission and nadir-sounding in an analogous way to PREMIER, but for which launch is not envisaged until the latter half of the next decade.

It is important to note that none of these proposed limb-sounders could meet the mission requirements of PREMIER and that only OMPS and SAGE III-ISS are approved.

By the time of its flight, the PREMIER mission will bring a distinct contribution to the Global Observing System of atmospheric composition described here, with observing capabilities dedicated to high-resolution profiling of the mid/upper troposphere and lower stratosphere by limb-emission sounding. The data from PREMIER will be highly complementary to that from nadir-sounders flying concurrently on operational or research satellites, particularly the collocated data from MetOp/MetOp-SG, and thereby contribute significantly to the GCOS essential climate variables for water vapour, methane and ozone (Subsection 8.4.1).

8.4 Application Potential of PREMIER

The global height-resolved data on mid/upper tropospheric and lower stratospheric composition to be delivered by PREMIER will not only serve the research objectives of the mission, as outlined in Chapters 2 and 3, but will contribute also to operational applications and thereby serve as the demonstrator for a new element of the GMES space component, in support of the evolving GMES Atmosphere Monitoring Service. Three operational applications to which PREMIER will contribute are outlined below.

8.4.1 Global Height-resolved Monitoring of Atmospheric Composition and Links with Climate

The requirement for global height-resolved monitoring of atmospheric composition from space has been consistently identified by a number of international bodies:

- Report of the IGOS Integrated Global Atmospheric Chemistry Observation Theme Team (IGACO, 2004).
- Eumetsat Position Paper on Operational Atmospheric Chemistry Monitoring in the Post-MetOp Time Frame beyond 2020 (Kelder et al., 2006).
- Gap Analysis of the Committee on Earth Observation Satellites (CEOS) Atmospheric Composition Constellation (Reburn et al., 2008).
- Final Report of the Implementation Group for the GMES Atmosphere Core Service (GACS, 2009).

This is reflected in the specification of limb-sounders in the post-MetOp Mission Requirements Document (Schluessel et al., 2010). Most recently, there have been clear recommendations from GCOS. To monitor atmospheric composition and critical links to climate (Chapter 2), the GCOS Implementation Plan (GCOS, 2010) calls specifically for the development of a strategy for systematic global acquisition of height-resolved data on the three trace gases: ozone, water vapour and methane. In particular, this plan calls for the following actions:

- Establish long-term limb scanning satellite measurements of profiles of water vapour, ozone and other important species from the UTLS up to 50 km (*IP-10 Action A26*).
- Continue production of satellite ozone data records (column, tropospheric ozone and ozone profiles) suitable for studies of inter-annual variability and trend analysis; reconcile residual differences between ozone datasets produced by different satellite systems (*IP-10 Action A32*).

Planned missions will ensure the continuity of the total ozone climate data record, but the continuity of height-resolved (limb viewing and occultation) missions is not guaranteed, while space agencies have on-going projects to create homogenous records of existing data of total ozone, low-resolution ozone profiles and high-resolution ozone profiles, by combining several instruments. GCOS (2010) calls for urgent continuation of the limb-viewing measurements of high-resolution ozone, as presently only one limb-viewing instrument (NPP/JSS-J2) is planned to measure ozone profiles in the stratosphere, and it is expected that there will be serious gaps in the high-resolution ozone profile datasets in the future. For monitoring ozone at high latitudes, it is also important to measure ozone in the dark (during the polar night) and no instruments are planned for continuing the ozone profile records in the mesosphere after the present instruments stop operating. The supplement to GCOS (2010) on *Systematic observation requirements for satellite-based products for climate*, GCOS (2011) specifies target requirements as provided in Table 8.1.

PREMIER will provide unique contributions to these required datasets during its period of flight and will support future climate assessments by IPCC and, in the case of ozone, monitoring of the impact of the Montreal Protocol and its amendments.

8.4.2 Operational GMES Atmosphere Services

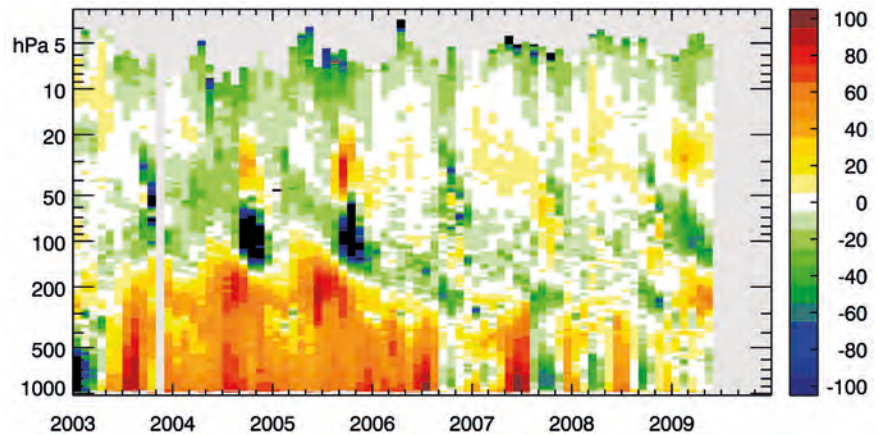
GMES is the European programme for the provision of reliable and sustained information for the global environment and security. It will support environmental legislation and policies with a particular focus on climate change, monitor their implementation and assess their effects. GMES also supports the critical decisions that need to be made quickly during emergencies, such as when natural or manmade catastrophes and humanitarian crises occur. Users will be provided with information through services dedicated to a systematic monitoring and forecasting in six thematic areas: marine, land, atmosphere, emergency, security and climate change.

The atmospheric range of services focuses on atmospheric composition (greenhouse gases, aerosol and reactive gases) at the global scale and over Europe (air quality), as well as UV and solar radiation. The FP7 EU-funded project MACC-II is bridging the gap to the full operations phase (GMES Atmospheric Monitoring Service, GAMS), which will commence in mid-2014.

Variable/Parameter	Horizontal resolution (km)	Vertical resolution (km)	Temporal resolution	Accuracy
O ₃ profile in the UTLS	100–200	1–2	4 h	10%
O ₃ profile in upper stratosphere and mesosphere	100–200	3	Daily	5–20%
CH ₄ in the stratosphere	100–200	2	Daily	5%
Water vapour profile in the UTLS	25 (UT) 100–200 (LS)	2	4 h (UT) Daily (LS)	5%

Table 8.1: Extract of GCOS Requirements on satellite-based atmospheric composition products.

Fig. 8.1. Time series of monthly mean differences (%) between ozonesondes and ozone from the GEMS reanalysis at the Antarctic Neumayer station. MIPAS data were assimilated in the GEMS reanalysis up to 26 March 2004, MLS data were assimilated from 16 January 2006 to the end of 2008. Between these two periods, the profiles in the GEMS reanalysis deteriorate markedly, illustrating the major importance of limb data within the range observed (<200 hPa), and also in the troposphere below. (A. Inness)



Applications cover monitoring, reanalyses and forecasting. There is a wide range of actors involved: meteorological services, research institutes, environment institutes, space agencies, SMEs and ‘downstream’ activities. Several services are run today in pre-operational mode using existing capacities. These capacities include the ‘chemistry’ payload on Envisat (Sciamachy, MIPAS, GOMOS), IASI and GOME-2 on MetOp and MSG/SEVIRI, MetOp/AVHRR/3, Envisat/MERIS (for fires, aerosols, clouds). Also worth mentioning is the European OMI instrument on NASA’s Aura. Beyond the dedicated Sentinel-5P, -4 and -5 missions, the highest priority is to guarantee the continuity of space observations of atmospheric composition with stable performances and quality.

In regard to monitoring of stratospheric ozone and its relations with surface UV (e.g. Hegglin and Shepherd, 2009a), the quality of lower stratospheric ozone profile analysis depends critically on availability of limb-sounding data. In the multi-annual reanalysis which was conducted in the GEMS (Hollingsworth et al., 2008) and MACC projects, that preceded MACC-II, there is a striking loss of performance in the periods when limb data were missing. This is illustrated on Fig. 8.1, which compares analyses with the sondes at the Neumayer station in the Antarctic. The figure indicates that the other types of information assimilated (columns or partial columns from nadir-sounders) are not sufficient to constrain state-of-the-art systems.

PREMIER data will not only allow improvement of chemical models in the UTLS by providing more insight into the vertical structures of ozone worldwide, but will also be critical to the quality of the operational GEMS Atmosphere Monitoring Service products related to stratospheric ozone.

Developments in the perspective of the GAMS also relate to the monitoring of greenhouse gases, as well as to the monitoring and forecasting of the long-range transport of atmospheric pollutants in support of European policy. In particular, the capabilities of PREMIER for capturing the variability of methane in the lower stratosphere will help improve source inversion activities. The suite of reactive species measured by PREMIER in the UT will be assimilated in the global system operated at ECMWF and will also be used to evaluate both the representation of vertical transport processes and the quantification of fire emissions in particular (Kaiser et al., 2012). The synergy of PREMIER with the GOME-2 and IASI instruments on MetOp-SG will also be useful for volcanic eruptions, as the GAMS provides analysis and forecast information to the Volcanic Ash Advisory Centres (e.g. www.gmes-atmosphere.eu/news/grimsvotn).

A cornerstone activity for MACC-II and the GAMS is the monitoring and forecasting of air quality in Europe, up to a few days ahead. Tropospheric ozone is a particular focus and long-range transport and local/regional contributions combine to build up high levels downwind of precursor emissions. This activity

relies on a combination of modelling and assimilation of remote-sensing or *in situ* (at the surface and at altitude) instruments in the Global Observing System. As described in Chapter 2, PREMIER will bring a very distinct contribution to help constrain the ozone profiles with adequate resolution in the UTLS region, allowing exchange fluxes at the tropopause to be represented realistically. The combination of PREMIER data with nadir observations from MetOp/MetOp-SG with sensitivity to the lower troposphere and with surface observations is expected to provide a breakthrough in skill and performance.

PREMIER high-resolution limb-sounding measurements will contribute to the Global Observing System of atmospheric composition that is used by the GMES Atmospheric Monitoring Service to provide its range of high-quality and time-critical products, as discussed in GACS, 2009. The pre-operational global and regional assimilation and forecasting systems currently run in the context of MACC-II are ready for the full operations phase and are taking into account PREMIER data streams.

8.4.3 Operational Numerical Weather Prediction

The NWP community plays a pivotal role in today's society, helping better preparedness for high-impact weather. This community is composed of national weather services, international actors such as ECMWF, and a large number of research groups worldwide who investigate the underpinning science to improve the skill of forecasts at all temporal ranges.

The UTLS and stratosphere is a region of specific interest for NWP, especially for medium- to long-range forecasting (see Chapter 2). The usefulness of a limb-emission sounding mission with the capabilities of PREMIER is two-fold:

- The need for vertically-resolved temperature, ozone and humidity data in the UT and above for assimilation into models to improve forecasts through their direct radiative effects.
- The need to account accurately for UTLS distribution and variability of key species absorbing in the IR in the assimilation of radiances from nadir-sounders.

For these reasons, ozone has been a variable in leading NWP models for more than a decade. Today, there is significant literature on the use of UTLS and stratospheric ozone for NWP operations. The link between ozone and potential vorticity (Danielsen, 1968) also makes the UTLS ozone information useful for forecasters to assess the validity of initial steps in the forecast trajectories in the case of fast-developing and high-impact weather system. Recent developments have also shown the direct potential of ozone limb data to improve stratospheric winds analyses and forecasts (Semane et al., 2008).

The trend towards including an increasing number of atmospheric constituents in NWP models makes it likely that they will evolve from 'meteorological' to 'environmental' models. International groups working on NWP (WCRP/WGNE, THORPEX) recognise this and are already giving attention to ozone, stratospheric water vapour, greenhouse gases and aerosol. In the timeframe of PREMIER, there is no doubt that the currently developing capabilities in integrating composition into NWP models, as exemplified by (Flemming et al., 2009) for ECMWF or the activities within the COST action 1004 (<http://eumetchem.info>), will have been implemented in operations.

→ PROGRAMMATICS

9. Programmatic

9.1 Introduction

This chapter presents the technical maturity, heritage and risks associated with both the mission-level scientific concepts and the system-level technical concepts as developed in the frame of the scientific and industrial Phase-A studies and the Swedish nationally-funded STEAMR Programme, and described in Sections 9.2 and 9.3. The corresponding development approach and schedule is presented and discussed in Section 9.4 with respect to the compatibility of a target launch for the seventh Earth Explorer mission in 2019.

9.2 Scientific Maturity, Critical Areas and Risks

After completion of Phase-0 activities, the Earth Science Advisory Committee (ESAC) recommended the selection of PREMIER for Phase-A without any serious concerns that would require particular attention. A minor caveat on the capability of the mission with respect to analysis of gravity wave momentum flux has been addressed within an end-to-end simulation study dedicated to gravity waves, where the accuracy of momentum flux retrievals has been demonstrated and validation methods outlined.

The fundamental scientific issues to be addressed by PREMIER have been identified in various international assessments. They are well recognised and will not be resolved by any other existing or planned mission and, therefore, remain valid.

Scientific objectives have been detailed and related geophysical mission requirements quantified in interaction between the Mission Advisory Group and scientific study teams, taking due account of the current state-of-the-art and expected developments in atmospheric research. Observation requirements at Level-1b have been systematically derived from the geophysical requirements, using sophisticated retrieval tools. The requirements can be considered as well consolidated.

In the analysis of PREMIER data, the scientific community can build on retrieval techniques developed for previous limb emission sounders on missions such as Envisat, Aura, and Odin. Two-dimensional tomographic retrieval algorithms have been demonstrated operationally. Their optimisation for the most efficient exploitation of the full information content of PREMIER limb spectra is a matter of technical work rather than a scientific challenge. The feasibility of processing the complete PREMIER dataset at least at the speed of data acquisition has been shown.

Mission performance at the level of geophysical data products is demonstrated through simulations and measurements taken by airborne precursor instruments. Simulations achieved compliance with the geophysical data requirements for most data products. Airborne spectrometers operating in both IR and mm-wave spectral regions demonstrated the feasibility of upper-troposphere limb sounding. Residual effects of uncertainties in radiometric, spectral and spatial calibration upon the retrieval, as well as analysis of data from a recent additional airborne measurement campaign, are being addressed in extended study activities.

The large scientific impact of the mission has been demonstrated in dedicated studies for each of the four mission objectives. A high data uptake by a wide international community can be expected.

Data assimilation systems for atmospheric composition measurements, ingested either in the form of radiance spectra or retrieved profiles, are far progressed. These schemes have been applied successfully to MIPAS and

MLS stratospheric limb-sounding data in scientific and operational contexts. Further refinements will be needed to assimilate PREMIER observations of fine-scale filament structures, especially in the tropopause region. Further work is also needed to improve the synergistic combination of limb and nadir observations in the data assimilation framework.

Spaceborne data of stratospheric and tropospheric composition have been used extensively to improve and validate atmospheric models. To take full benefit of PREMIER data, further development of these models will be needed, primarily the full representation of troposphere and stratosphere; high spatial resolution, in particular in the tropopause region; and full coupling between composition, chemistry, radiation and dynamics.

It should be noted that the required improvements of data assimilation schemes and models are indeed part of already ongoing developments in the scientific community, progressively integrating previously separated components, towards the development of Earth system models. There is confidence in the availability of suitable models and assimilation tools at the time of a possible PREMIER launch.

A large body of experience exists on validation of spaceborne atmospheric composition data. High-resolution spatial structures observed by PREMIER will be validated using newly developed airborne systems in combination with specific flight patterns.

Part of the science objectives depends on the availability of MetOp/MetOp-SG data. The associated risk is considered low, due to the continuity and high reliability of the operational weather satellite system. A launch delay of either PREMIER or MetOp-SG would not have a serious impact on the fulfillment of PREMIER's synergistic science objectives.

9.3 Technical Maturity, Critical Areas and Risks

9.3.1 Summary

PREMIER is considered technically feasible, but some risks about the compatibility of the development with the target date of 2019 have been identified owing to the length of time needed for the development and manufacturing of the IRLS detectors.

The system design is well consolidated. However, at this stage of development, the small clearance within the Vega fairing is considered a risk for the mission. An optimisation of the payload size leading to an increased margin is in progress.

The platform subsystems are largely based on flight-proven designs and are considered technologically mature with no major associated risks. Careful consideration however needs to be given to the detailed design of the solar array and to the minimisation of microvibrations.

The IRLS is considered a challenging, but feasible, instrument with few risk items identified (see Section 9.3.3). The large existing heritage (e.g. IASI, MIPAS, GOSAT), the ongoing predevelopments and the large amount of similarities both in common equipment and risk areas with the MTG-IRS (see Section 9.3.3) increase the confidence on the instrument feasibility.

The STEAMR is a complex instrument with heritage from the sub-mm wave radiometer on the Swedish Odin mission. The development plan proposed within the Swedish national programme is based on early prototyping and testing. The instrument is considered feasible, but a potential risk for the development may exist depending on the space qualification approach of critical components, which is still to be clearly defined in the development programme (e.g. HIFAS correlator chips, IQ mixers, LNAs, mixer diodes and multipliers, that currently do not exceed TRL 4). The ground segment is not considered critical.

9.3.2 Satellite and Platform

The two platform concepts are similar and based on flight-proven designs with extensive reuse of off-the-shelf components. At this stage, the TRL of all the individual components and platform subsystems is higher than 7. As a result, the platform is considered technologically mature with no major associated risks although the following areas need to be carefully considered in following phases:

- Solar array design, with respect to the deployment mechanism and interface with the platform both in the stowed and deployed configurations.
- Microvibration minimisation and propagation through the structure.
- STEAMR Sun avoidance requirements (Chapter 5) in safe mode and during launch and LEOP.

For both design concepts, the satellite clearance with respect to the dynamic envelope of Vega is about 2 cm, which represents a risk for the mission. The clearance is driven by the non-deployable sunshield on top of the IRLS for Concept A and by the size of the IRLS/STEAMR in Concept B. An alternative design option aimed at improving the volume margin in Concept A involves modifying the front part of the sunshield so as to fold it in the stowed configuration and deploy it after separation from the launcher. The deployment can be based on flight-proven solutions. For Concept B, a size optimisation exercise for both STEAMR and the IRLS is being performed within the Phase-A extension.

9.3.3 IRLS

9.3.3.1 Summary

The IRLS is a complex high-performance instrument. It benefits from the heritage of similar instruments such as IASI, GOSAT or MIPAS, and from IRS on MTG, which is currently under development. Some of the critical components/subsystems such as the cryocooler and the detectors share many common requirements with the IRS on MTG and hence will benefit from the MTG pre-developments and implementations. Also, relevant issues such as pseudo-noise generated from LOS instability or an enhanced metrology system to measure lateral corner cube jitter, will benefit from the MTG experience.

The IRLS integration is considered challenging owing to the high performance required and to the inherent complexity of an imaging FTS. Two representative breadboards are under development with the objective of verifying critical performance such as the spectral response and demonstrating that both IASI and GOSAT interferometers can be adapted to fulfil the PREMIER requirements.

Critical subsystems/equipment such as the detectors (Concept A and B) and cryostat (Concept A) are at present at a TRL of 4, however pre-development activities are underway and, subject to a successful outcome of the activities, will reach TRL 5 by the end of Phase-B1.

All remaining components/subsystems either have a TRL of 5 or higher at this stage, or a corresponding pre-development is ongoing to achieve such TRL by the end of Phase-B1. As a result, an instrument meeting the PREMIER performance requirements is considered feasible in the timeframe of 2019–20.

The following sections define the technology readiness status and the criticality of each instrument subsystem; wherever a criticality is identified the proposed pre-development and the impact is assessed.

9.3.3.2 Mechanical and thermal

The mechanical and thermal configuration of Concept B benefits from heritage of IASI. Its operational temperature at 293K is not critical, although the implementation of a cold entrance compartment embedding the blackbody in an environment of 240K increases the complexity of the thermo-mechanical configuration. Furthermore, because thermal stability is of key importance to achieve the required performance, particular attention is needed during the development phases.

Concept A operates at 240K and benefits from the heritage of MIPAS. Operation at such low temperatures will require that some of the integration, testing and performance verification is carried out at this temperature. An athermal aluminium design will minimise deformation during cool-down from room temperature to ~240K. The thermal control based on an MLI tent with foil radiators benefits from heritage from several other missions and is well mastered.

9.3.3.3 Scan mechanism/pointing mirror

The scan mechanism in Concept B implements a two-axis gimbal mechanism with high pointing performance accuracy. The stepper motor technology and kinematic concept benefits from heritage from the MECALIB mechanism developed for the Helios-2 mission; however, a specific pre-development activity has started to verify that the required pointing performance can be achieved. The pointing mechanism could be on the critical path if the performance cannot be achieved with the current design, since the accommodation of a single-axis mechanism is not compatible with the current baseline concept. The estimated TRL is 3–4.

The scan mechanism in Concept A is a single-axis device and does not present any criticality. The estimated TRL is 5.

9.3.3.4 Blackbody

Not considered as critical. The estimated TRL is above 5.

9.3.3.5 Front optics

Both concepts baseline an anastigmatic front telescope. Concept B does not require any critical technology or materials, and the TRL level is estimated to be above 5 at this stage.

The front optics of Concept A requires however a specific pre-development, which is on-going. The objective is to assess the compliance of the surface quality and to prove the compatibility of the manufacturing process with the specific front optics modular design. Current estimated TRL is 3, and it is expected to achieve TRL 5 by the end of Phase-B1.

9.3.3.6 Interferometer

The interferometer baselined in Concept B largely benefits from the IASI heritage. The spectral range of PREMIER is reduced compared to IASI and MTG, so the beam splitter and the compensating plate should not require pre-development. Currently, the TRL level is considered 5. The corner cube is based on a technology developed in the framework of IASI and will also be implemented on MTG-IRS. The TRL is higher than 5. The interferometer mechanism is based on the recurring IRS-MTG linear mechanism with heritage from IASI. However, the maximum stroke required by the IRLS is not validated, neither for IASI nor for MTG-IRS. Therefore, the verification of performance and the adaptation of the IASI interferometer to the PREMIER stroke characteristic

need to be performed. This is the subject of ongoing pre-developments. The TRL level is estimated to be 4 at this stage and expected to reach 5 at the end of Phase-B1.

Concept A largely benefits from heritage of the GOSAT interferometer and is based on the ABB-GFI interferometer; however, as for Concept B, the compliance with the specific PREMIER requirements (stroke and velocity) has to be verified and is subject of ongoing pre-development activities. The TRL level is estimated to be 4 at this stage and is expected to reach 5 at the end of Phase-B1.

9.3.3.7 Laser metrology

The single-point laser metrology system for PREMIER is based on a heritage solution, but would require slight modifications to implement the measurement of sine and cosine signals. For this reason, the estimated TRL is 4 to 5. The performance of the single-point laser metrology will be verified within the breadboard pre-development. If a more accurate 3D metrology system, similar to the one foreseen in MTG-IRS, were needed to monitor the trajectory and velocity of the corner cubes, a new development would be required. The laser source of this 3D metrology is not critical but the Transmission and Reception Unit and the entire correction and processing method are new. A related development is being carried out for the MTG programme and is expected to reach TRL 5 by the end of Phase-B1.

9.3.3.8 Back optics

Same assessment as per front optics (Subsection 9.3.3.5) with respect to the modular design of Concept A.

9.3.3.9 Cryostat

The cryostat includes critical elements such as the cold optics with characterised glass index at low temperature and anti-reflecting coating, the dichroic with optimised coating and the detectors. Concept B benefits from heritage of IASI and will largely follow the pre-development and requalification programme from MTG-IRS, reaching a TRL above 5 by the end of Phase-B1.

For the Concept A design, the technology of the low conductive spacers is considered critical and an early breadboard of the cryostat is being developed. The Current TRL is considered to be 4 and expected to reach 5 by the end of the current pre-development.

The dichroic beam splitter will need to be custom designed to match the band gap of PREMIER for both concepts.

9.3.3.10 Cryocooler

The cooling power required is compatible with the MTG IRS cryocoolers, which are the baseline for both concepts. The Sentinel-3 cryocoolers could also be used. Therefore, the current TRL is considered higher than 5. A cryocooler with a non-redundant mechanical part and redundant control electronics has been selected since its reliability is considered adequate. Nevertheless, a fully redundant cryocooler could be accommodated without fundamentally changing the baseline concept.

9.3.3.11 Detector

The baseline detector configurations benefit from MTG heritage and will use the same building blocks, although the macro-pixel configuration (detector format) and the charge handling capacity are different. Given the commonality

with the MTG programme, pre-development is not required during Phase-A, but, owing to the duration of the detector development and the manufacturing, which are expected to be of the order of 44 months, this will start during Phase-B1. The TRL level is considered 3–4 at this stage.

For Concept A, detector skimming has been proposed. This technology is considered relatively new and therefore a specific pre-development activity within the Phase-A has been implemented.

9.3.3.12 Front-end electronics

The IRLS performance relies on a 16-bit ADC with low noise characteristics, operated at a sampling frequency of 2–4 MHz. This can be achieved using a high-performance ADC such as the VASP. A verification of the suitability of the VASP ADC performance for PREMIER is being carried out within the Phase-A pre-development activities and within the MTG programme.

9.3.3.13 Control electronics

No criticalities have been detected with respect to the instrument control electronics except that of the interferometer, which has heritage from IASI and GOSAT but requires specific adaptation. Adaptation of the electronics will be performed within the breadboard activities.

9.3.3.14 Processing chain

The IRLS onboard processing presents no criticalities in terms of hardware and at this stage the TRL level is considered to be 5. With regard to the processing algorithm and compression, heritage from previous missions (e.g. IASI and MIPAS) is applicable with minor modifications.

9.3.3.15 Calibration

No criticalities have been identified on the radiometric calibration. Spectral calibration will be performed using the atmospheric features. The instrument requires a good spectral stability so that the calibration performed in CM can be transferred to DM. Current results from Phase-A confirm this assumption. LOS calibration using stars or the Moon is not considered critical and benefits from experience in other instruments (e.g. MIPAS).

9.3.4 STEAMR

9.3.4.1 Summary

The STEAMR instrument concept has a strong heritage from the sub-mm radiometer flown on the Swedish-led international Odin mission, in operation for more than 11 years. A development of a breadboard-level radiometer core was completed in 2011, incorporating the front-end, the IF unit and the back-end of the radiometer chain. Excellent performance of the front-end was demonstrated and also a margin with respect to the required bandwidth of the autocorrelator ASIC's was verified. The complete receiver with back-end was stable, even without active temperature stabilisation, for 40 s, as showed by the Allan variance measurements. The required sensitivity could be met even at room temperature. All key components and the subsystem showed compliance to the performance requirements. No major issues regarding the use in space was identified within the Swedish national programme. The only customised ASIC in the system was tested for radiation during development, and found to meet the requirements. In early 2012, high-altitude field measurements were carried out using the breadboard receiver, confirming proper operation.

General schedule risk mitigation measures include early testing, keeping backup solutions and suppliers available where possible and increasing flexibility through extra models on several levels. To further increase confidence in the design, it is also planned to test the integrated instrument for longer periods in flight-similar configurations. The design will be further verified at circuit board, unit and system levels, according to previously used methods. The front-end, IF, and back-end subsystems will be tested for compliance with the STEAMR environment at unit level already in the ongoing demonstration model phase, a pre-qualification of the intended design.

Identified system critical components, in the sense of being important to meet expected instrument performance, are: HIFAS correlator integrated circuits (ICs); IQ mixers; LNAs; mixer diodes; and multipliers. They were all measured and environmentally tested to various degrees on receiver prototype level. The only sole-source component is the HIFAS IC. There are alternative suppliers for all other critical components.

Development is being carried out with special emphasis on early prototyping and testing, in order to verify design choices and performance, and in particular to reveal unforeseen problems. For the STEAMR baseline design, no technology development and testing at component level is being carried out as available and mature technology is introduced to minimise risk and reduce cost and keep to schedule.

9.3.4.2 Instrument

The STEAMR instrument is complex with many aspects being interrelated. Using a staged prototype testing approach is assumed to considerably reduce risks associated with hardware implementation, e.g. by revealing late unforeseen problems, practical integration and test difficulties, insufficient resource planning, long delivery times. It also helps in the selection of the final supplier and build working relations.

In parallel with core prototyping of the radiometer, the complete quasi-optics of STEAMR was designed and optimised using physical optics simulation tools, e.g. GRASP. Tolerance analyses with modelled thermal deformations were also simulated. Following these activities, a demonstration model phase is being carried out to verify subsystem and system level performance, using densely packaged subsystems and units similar to flight models. This is expected to reduce risks and cost in the next phases. The demonstration model will also include some optical breadboarding, for the same reasons.

9.3.4.3 Mechanical and thermal design

The mechanical design is based on highly accurate and stable inner CFRP structure that holds the optics and the focal plane unit with mixers and the high-frequency section of the local oscillators. An outer structure protects the reflectors from direct sunlight. It also provides thermal isolation and helps to keep the correlation spectrometers and IF-amplifiers at stable temperatures. Modelling shows orbital variations of less than 1K, achieved by passive means only. Active local temperature regulation can be implemented to provide further margins, should the need arise.

9.3.4.4 Moving parts

The only moving parts in the instrument are the chopper and beam selector mechanisms used in the calibration scheme. Their design is directly based on heritage from Odin. Even if the chopper motor were slightly larger, it would be of the same model series from the same supplier and qualified in the same manner. The risk is considered low for moving parts.

9.3.4.5 Antenna (telescope) and quasi-optics

Telescope design and manufacturing processes based on the Odin CFRP primary reflector with 8 μm RMS surface accuracy are available. In addition, STEAMR telescope prototyping, exploiting advances in CFRP materials since Odin, shows that it is possible to improve further on the accuracy, using space-proven manufacturing. Two critical considerations for the antenna and the quasi-optics are structural integrity and optical performance verification. Structures compatible with the requirements have been realised for several space projects, including Odin. The optical design was simulated in GRASP, showing compliance with the STEAMR requirements. The focal plane assembly is based on heritage from CHARM and SMART focal plane arrays for the KOSMA 340 GHz receiver ground telescope. The STEAMR horn and focal plane assembly was breadboarded and tested with results agreeing well with simulations. The complete system including the antenna, optics and receivers will be tested by near-field scanning, as used for the MLS instrument at higher frequency. The performance of the scanner system is compliant with the STEAMR requirements. Other concepts and components in the optics, such as mirrors manufactured to custom shapes, polarising grids, and low-pass filter have all been used in space. The risk is considered low for the antenna and optics.

9.3.4.6 Calibration

The calibration concept is similar to that of Odin, using cold sky and warm loads and, for pointing calibration, astronomical objects such as the Moon. Apart from the moving parts, described above, warm loads will be based on flight-proven or ESA-developed designs.

9.3.4.7 Front-end electronics

The front-end electronics is based on double-sideband 340 GHz sub-harmonically pumped Schottky mixers, with embedded LNAs, connected to Schottky-based LO frequency multipliers and active multipliers. The critical components are thus the mixer diodes, the LNA, and the multipliers. The components are radiation tolerant. Schottky technology has been used in many types of mm- and sub-mm receivers, also in space. Prototypes of the STEAMR mixers with LNA's and multipliers show excellent performance and have passed the first thermal cycling test. Experience shows that thermal cycling is a good early design discriminator for this type of equipment. The design uses commercial components, with multiple suppliers for all components.

Sideband ratio will be determined on the ground and verified in-orbit, utilising a tuneable line source with a high-frequency power detector. The source will be the existing LO design, with an additional passive Schottky doubler. A demonstrator, namely the mentioned demonstration model with four full receiver chains is under development and will be tested for performance and environment (radiation, thermal cycling, vibration) in 2012. This is the next stage in the development approach described above. One main reason for this model relates to the packaging of the receivers according to the STEAMR subsystem design. The risk for the front-end electronics is considered low.

9.3.4.8 IF and back-end electronics

The IF subsystem and the microwave part of the back-end spectrometer is based on standard, commercial microwave components and technology. There are two parts of the back-end system that can be considered critical, an IQ mixer and the HIFAS correlator ASIC, developed under an ESA activity. For the IQ mixer, the datasheet does not cover the performance range for the intended use of the device. The IQ mixer was therefore tested and showed

compliance with the performance requirements. Alternative suppliers exist and, in addition, the IQ function could also be implemented by combining standard mixers, which use slightly more space, but have numerous alternative suppliers. This sideband separation concept was used in earlier spectrometers.

The HIFAS ASIC was tested for performance, showing compliance with requirements. The ASIC was produced using a 0.18 μm BiCMOS line that will be available for the next five years. Devices from that line were used for both industrial and military applications. As the ASIC is used as a naked die, no packaging aspects apply to the device and the ASIC is fully passivated. The technology is vacuum compatible and radiation tolerant up to 25 krad integrated dose, thus compliant with STEAMR requirements.

Back-end systems will also be part of the demonstration model, again being subjected to performance testing and environmental pre-qualification, focussing on packaging aspects and on any spurious leakage between compartments and similar. The risk for the back-end is considered low.

9.3.4.9 Power system

The power system will be optimised for efficiency, especially for low voltage rails such as 1.8 V used for the HIFAS ASIC. The power electronics for the Odin satellite with very similar requirements has now been in orbit and operational for over 11 years.

9.3.4.10 Control system

Many similar systems have been built for space projects, including the instrument subsystem controllers for the Odin satellite, based on commercial ICs and FPGAs.

9.4 Development Approach and Schedule

9.4.1 Overall Design and Development Approach

The IRLS and the satellite platform will follow the traditional phased development process (Phases B/C/D/E) with system reviews (System Requirements Review (SRR), Preliminary Design Review (PDR), Critical Design Review (CDR) etc.) to assess the status of system design, development, procurement and integration of the flight models. STEAMR will be developed within a Swedish national programme in parallel with the IRLS and the platform. In order to establish a robust development schedule, the instrument and platform developments are widely decoupled, i.e. parallel development activities on the instruments, platform and spacecraft are foreseen, with integration performed during the AIT phase.

9.4.1.1 IRLS

The Concept A model philosophy for the IRLS follows a thorough development approach based on a Structural Model (SM), a Structural and Thermal Model (STM), an Electrical Functional Model (EFM) and a Proto Flight Model (PFM) approach. The SM comprises the IRLS structure and mass dummies of representative instrument components. It is delivered to the prime contractor to be part of the structural model of the satellite. The STM comprises a near-flight standard structural hardware and mass dummies for other items, near-flight standard thermal hardware (no active coolers) and thermal dissipators. It is used for mechanical interface check, harness routing, structural/thermal qualification and mechanical model correlation, check of the passive cooling concept of the instrument and test of the satellite thermal system. The EFM

is used for electrical/functional tests of the platform-to-instrument interface and is built on EM standards. The PFM comprises all instrument items built at PFM standard and submitted to proto-qualification tests. The PFM is used for structural acceptance level tests, Thermal Balance and Thermal Vacuum tests, EMC tests, functional qualification and integrated optical performance. The ST, EFM and PFM will be delivered to the PREMIER prime contractor for integration in the respective spacecraft model. The flight spares are assumed to be refurbished component QMs.

For Concept B, considering the heritage acquired with previous similar concepts and the reuse of many of the design practices and elements, a lighter model approach based on no SM and no STM has been proposed. It consists of a test bench, an avionic model and a PFM. The IRLS Test Bench (ITB), is used for functional and command control early validation. The ITB is representative of complete electrical and functional aspects. The ITB will also be used in parallel to the PFM integration and test to verify the AIT procedures and support the Electrical Ground Support Equipment (EGSE) verification. To this end, a platform simulator provided by the prime contractor will be required. The Avionic Model (AVM) consists of a IRLS simulator to test the electrical, and data interfaces with the system. The PFM has the same objectives as for the previous development approach. Both the AVM and the PFM are delivered to the prime contractor.

9.4.1.2 STEAMR

The overall development and verification approach follows the same philosophy as for the development of the Odin 487–582/119 GHz radiometer. It consists of early prototyping and testing, emphasising incremental development until reaching a working system with the goal to minimise risks and cost. Depending on the instrument subsystem, different model philosophy will be used: demonstration models, STMs, EMs, QMs and FMs. Table 9.1 shows a summary of the STEAMR schedule.

On the ground, performance verification and functional testing will be carried out in various environments, ambient, vacuum and thermal vacuum. In orbit, operations will be optimised through, for example, refinement of pointing knowledge and calibration.

Parallel testing on structure, mass properties and thermal aspects is foreseen at system and instrument level. STEAMR will be integrated electrically and mechanically (including LOS alignment) onto the platform, followed by integration of the sunshield above the IRLS.

9.4.1.3 Satellite

The baseline model follows a classical approach based on the SM, AVM, and PFM. The SM comprises models of the structure, the two instruments, the propulsion module and the solar array, and includes mass dummies for all other units. It is used for the qualification of the structure, the validation of the interface loads and the verification of the structural models. The avionics

Activities/milestones	Start	End
Demonstration model	Q4 2011	Q3 2013
Engineering qualification model	Q4 2013	Q3 2015
Structural/thermal model production and test	Q4 2013	Q4 2014
Flight model	Q3 2015	Q2 2017
Delivery of flight model for system integration; alignment and system testing	Q2 2017	

Table 9.1. Summary of STEAMR nominal schedule.

model is used for command, control and electrical interface verification, software validation, functional interfaces verification and AOCS performance evaluation. The PFM is used for full (i.e. mechanical, thermal, EMC, functional/operational requirements) satellite qualification and acceptance testing.

In addition to these satellite models, satellite simulators will be delivered to the instrument contractors (both IRLS and STEAMR) for early validation of instrument interfaces.

9.4.2 Schedule

The following assumptions have been used when building schedule for the satellite development:

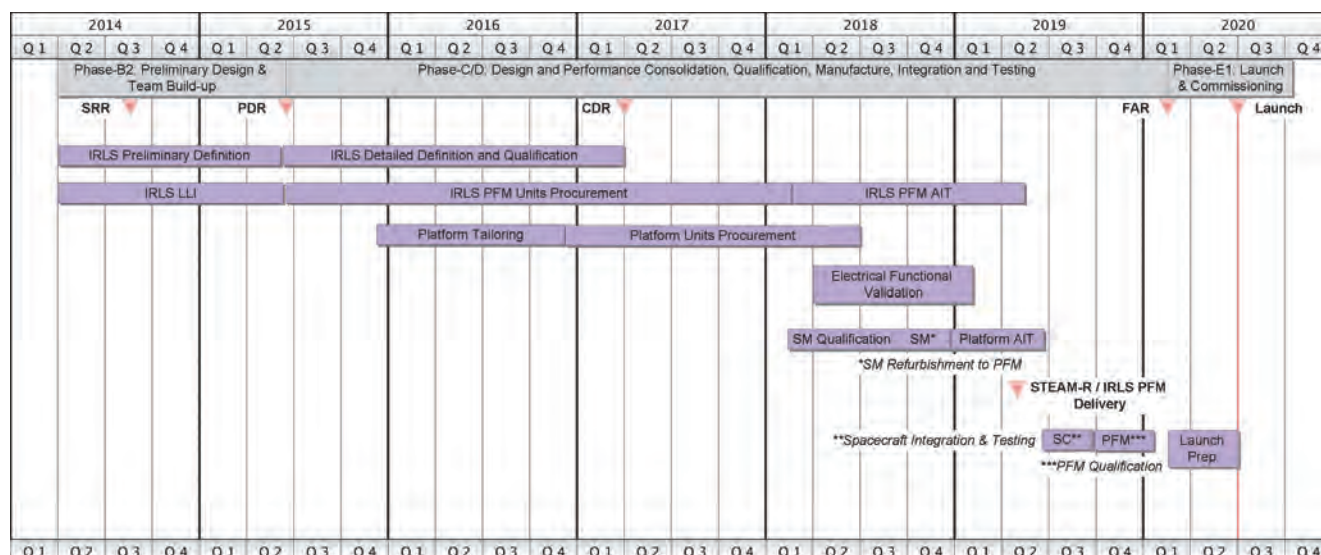
- Phase-B1 kick-off: Q2 2013
- Phase-B2 kick-off: Q2 2014, following competitive ITT
- STEAMR models delivered as per satellite need dates (i.e. same dates as the IRLS instrument)
- Three-month margin between satellite delivery and start of launch campaign
- Three-month launch campaign

The detailed schedule is presented in Figure 9.1. The critical path is represented by the IRLS and is driven by the earliest kick-off for the manufacturing of the FM detectors, currently assumed to take place three month after the start of Phase-B2. The development time is 3.5 to 4 years, assuming a detector pre-development during Phase-B1, making a launch feasible in Q1 of 2020.

9.5 Conclusion

Assuming the expected successful outcome of ongoing and planned pre-developments, the maturity of critical technologies will reach the required level prior to the start of the implementation phase. Nevertheless, the two instruments are on the critical path. For the IRLS, the schedule is driven by the development of the detectors. For STEAMR, the space qualification of critical components is considered as a potential development risk. Based on these elements and assuming that a technology maturity elongation in Phase-B1 is not required, the launch would be feasible in early-2020.

Figure 9.1. PREMIER outline schedule.



→ REFERENCES

References

- ACP (2006). Atmospheric Chemistry and Physics, Special Issue on “MIPAS (Michelson Interferometer for Passive Atmosphere Sounding): Potential of the Experiment, Data Processing and Validation of Results” (eds. Hartogh, P. & Espy, P.J.), http://www.atmos-chem-phys.net/special_issue70.html.
- Akritidis, D., Zanis, P., Pytharoulis, I., Mavraklis, A. & Karacostas, Th. (2010). A Deep Stratospheric Intrusion Event Down to the Earth’s Surface of the Megacity of Athens. *Meteorol. Atmos. Phys.*, **109**:9–18, doi:10.1007/s00703-010-0096-6.
- Alexander, M.J., et al. (2010). Recent Developments in Gravity Wave Effects in Climate Models, and the Global Distribution of Gravity Wave Momentum Flux from Observations and Models. *Q. J. Roy. Meteorol. Soc.*, **136**, pp1103–1124, doi:10/1002/qj.637.
- Austin, J. (1992). Towards the Four-Dimensional Variational Assimilation of Stratospheric Chemical Constituents. *J. Geophys. Res.*, **97**, pp2569–2588.
- Baker, A.K., Schuck, T.J., Slemr, F., van Velthoven, P., Zahn, A. & Brenninkmeijer, C.A.M. (2011). Characterization of Non-Methane Hydrocarbons in Asian Summer Monsoon Outflow Observed by the CARIBIC Aircraft. *Atmos. Chem. Phys.*, **11**, pp503–518, doi:10.5194/acp-11-503-2011.
- Baldwin, M.P. & Dunkerton, T. (1999). Downward Propagation of the Arctic Oscillation from the Stratosphere to the Troposphere, *J. Geophys. Res.*, **104**, pp30 937–30 946.
- Baldwin, M.P. & Dunkerton, T.J. (2001). Stratospheric Harbingers of Anomalous Weather Regimes. *Science*, **244**, pp581–584.
- Barath, F.T., et al. (1993). The Upper Atmosphere Research Satellite Microwave Limb Sounder Instrument. *J. Geophys. Res.*, AGU, **98**, pp10751–10762.
- Barré, J., Peuch, V.-H., Attié, J.-L., El Amraoui, L., Lahoz, W.A., Josse, B., Claeysman, M. & Nédélec P. (2011). Stratosphere-Troposphere Ozone Exchange from High Resolution MLS Ozone Analyses. *Atmos. Chem. Phys. Disc.*, **11**, pp33419–33463.
- Barré J., Peuch, V.-H., Attié, J.-L., El Amraoui, L., Lahoz, W.A., Josse, B. & Nédélec, P. (2012). Joint Assimilation of IASI Tropospheric Ozone Columns and MLS Ozone Profiles. Personal communication.
- Bergamaschi, P., et al. (2009). Inverse Modeling of Global and Regional CH₄ Emissions using SCIAMACHY Satellite Retrievals. *J. Geophys. Res.*, **114**, D22301, doi:10.1029/2009JD012287.
- Birner, T., Sankey, D. & Shepherd, T.G. (2006). The Tropopause Inversion Layer in models and analyses, *Geophys. Res. Lett.*, **33**, L14804, doi:10.1029/2006GL026549.
- Boers, R., de Laat, A.T., Stein Zweers, D.C. & Dirksen R.J. (2010). Lifting Potential of Solar Heated Aerosol Layers, *Geophys. Res. Lett.*, **37**, L24802, doi:10.1029/2010GL045171.
- Bormann, N. & Thepaut, J.N. (2007). Assimilation of MIPAS Limb Radiances in the ECMWF Ssystem. I: Experiments Observation with a 1-Dimensional Operator. *Q. J. Roy. Meteorol. Soc.*, **133** (623): 309-327.
- Brenninkmeijer, C.A.M., et al. (1999). CARIBIC – Civil Aircraft for Global Measurement of Trace Gases and Aerosols in the Tropopause Region. *J. Atmos. Oceanic Technology*, **16**, pp1373–1383.
- Brito, J. & Zahn, A. (2011). An Unheated Permeation Device for Calibrating Atmospheric VOC Measurements. *Atmos. Meas. Tech.*, **4**, pp2143–2152, doi:10.5194/amt-4-2143-2011.
- Butchart, N., et al. (2010). Chemistry-Climate Model Simulations of Twenty-First Century Stratospheric Climate and Circulation Changes. *J. Climate*, **23**, pp5349–5374, doi:10.1175/2010JCLI3404.1.
- Carlotti, M., Brizzi, G., Papandrea, E., Prevedelli, M., Ridolfi, M., Dinelli, B.M. & Magnani, L. (2006). GMTR: Two-Dimensional Geofit Multitarget Retrieval Model for Michelson Interferometer for Passive Atmospheric Sounding/Environmental Satellite Observations. *Appl. Opt.*, **45**, pp716–727.
- Ceccherini, S., Cortesi, U., Del Bianco, S., Raspollini, P. & Carli, B. (2010). IASI-MetOp and MIPAS-Envisat Data Fusion. *Atmos. Chem. Phys.*, **10**, pp4689–4698, doi:10.5194/acp-10-4689-2010.
- Charlton, A.J., O’Neill, A., Lahoz, W.A. & Massacand, A.C. (2004). Sensitivity of Tropospheric Forecasts to Stratospheric Initial Conditions. *Q. J. Roy. Meteorol. Soc.*, **130** (600), pp1771–1792. doi:10.1256/qj.03.167.
- Clement, A.C. & Soden, B. (2005). The Sensitivity of the Tropical-mean Radiation Budget. *J. Climate*, **18**, pp3189–3203.
- Clerbaux, C., et al. (2009). Monitoring of Atmospheric Composition Using the Thermal Infrared IASI/MetOp Sounder. *Atmos. Chem. Phys.*, **9**, pp6041–6054, doi:.
- Cortesi, U., del Bianco, S., Gai, M., Dinelli, B.M., Castelli, E., Gerber, D., Oelhaf, H. & Woiwode, W. (2011). PREMIER – Analysis of Campaign Data, Final Report of ESA study contract 4000101374/NL/10/CT.
- Cressman, G. (1959). An Operational Objective Analysis System. *Mon. Wea. Rev.*, **87**(10), pp367–374.
- Danielsen, E. F. (1968). Stratospheric-Tropospheric Exchange Bases Based upon Radioactivity, Ozone and Potential Vorticity. *J. Atmos. Sci.*, **25**, pp502–518.
- de Laat, A.T.J., Stein Zweers, D.C., Boers R. & Tuinder O.N.E. (2012). A Solar Escalator: Observational Evidence of the Self-Lifting of Smoke and Aerosols by Absorption of Solar Radiation in the February 2009 Australian Black Saturday Plume. *J. Geophys. Res.*, in press.
- Denman, K.L., et al. (2007). Couplings Between Changes in the Climate System and Biogeochemistry. In: *Climate Change 2007: The Physical Science Basis. Contribution of Working Group I to the Fourth Assessment Report of the Intergovernmental Panel on Climate Change* (eds. Solomon, S., Qin, D., Manning, M., Chen, Z., Marquis, M., Averyt, K.B., Tignor, M. & Miller, H.L.). Cambridge University Press, Cambridge, United Kingdom and New York, NY, USA.

- Drummond, J.R., Houghton, J.T., Peskett, G.D., Rodgers, C.D., Wale, M.J., Whitney, J.G. & Williamson, E.J. (1980). The Stratospheric and Mesospheric Sounder on Nimbus 7. *Phil. Trans. R. Soc.*, **296**, pp219–241.
- Drummond, J.R. & Mand, G.S. (1996). Evaluation of Operational Radiances for the Measurement of Pollution in the Troposphere (MOPITT) Instrument CO Thermal-Band Channels. *J. Geophys. Res.*, **109**, doi:10.1029/2003JD003970.
- Dunkerton, T.J. (1997). The Role of Gravity Waves in the Quasi-Biennial Oscillation. *J. Geophys. Res.*, **102**, pp26 053–26 076.
- Dyroff, C., Fütterer, D. & Zahn, A. (2010). Compact Diode-Laser Spectrometer ISOWAT for Highly Sensitive Airborne Measurements of Water-Isotope Ratios. *Appl. Phys. B* **98**, pp537–548.
- EC-JRC/PBL: European Commission-Joint Research Centre (JRC)/Netherlands Environmental Assessment Agency (PBL) (2009). Emission Database for Global Atmospheric Research (EDGAR), release version 3.2, available at: <http://edgar.jrc.ec.europa.eu>, last access: 1 August 2009.
- El Amraoui, L., Semane, N., Peuch, V.-H. & Santee M.L. (2008). Investigation of Dynamical and Chemical Processes in the Polar Stratospheric Vortex during the Unusually Cold Winter 2004/2005. *Geophys. Res. Lett.*, **35**, L03803, doi:10.1029/2007GL031251.
- Elbern, H., Kowol, J., Sladkovic, R. & Ebel, A. (1997). Deep Stratospheric Intrusions: A Statistical Assessment with Model Guided Analyses. *Atmos. Environ.*, **31**, pp3207–3226.
- Eriksson, P., Ekström, M., Rydberg, B. & Murtagh, D. (2007). First Odin Sub-Mm Retrievals in the Tropical Upper Troposphere: Ice Cloud Properties. *Atmospheric Chemistry and Physics*, **7** (2), pp471–483.
- Erler, A.R. & Wirth, V. (2011). The Static Stability of the Tropopause Region in Adiabatic Baroclinic Life Cycle Experiments. *J. Atmos. Sci.*, **68**, pp1178–1193, doi:10.1175/2010JAS3694.1.
- Ern, M., Preusse, P., Alexander, M.J. & Warner, C.D. (2004). Absolute Values of Gravity Wave Momentum Flux Derived from Satellite Data. *J. Geophys. Res.*, **109**, D20103, doi:10.1029/2004JD004752.
- ESA (2006). The Changing Earth – New Scientific Challenges for ESA’s Living Planet Programme, ESA-SP-1304. <http://esamultimedia.esa.int/docs/SP-1304.pdf>.
- Fischer, H., et al. (2008). MIPAS: An Instrument For Atmospheric and Climate Research. *Atmos. Chem. Phys.*, **8**, pp2151–2188.
- Flath, H.P., Wilcox, L.C., Akçelik, V., Hill, J., van Bloemen Waanders, B. & Ghattas, O. (2011). Fast Algorithms for Bayesian Uncertainty Quantification in Large-Scale Linear Inverse Problems Based on Low-Rank Partial Hessian Approximations. *SIAM J. Sci. Comput.*, **33**, pp407–432.
- Flemming, J., Innes, A., Flentje, H., Huijnen, V., Moinat, P., Schultz M.G. & Stein, O. (2009). Coupling Global Chemistry Transport Models to ECMWF’s Integrated Forecast System. *Geosci. Model Dev.*, **2**, pp253–265.
- Forster, P.M. de F. & Shine, K.P (1997). Radiative Forcing and Temperature Trends from Stratospheric Ozone Changes. *J. Geophys. Res.* **102**, pp10 841–10 855.
- Forster, P.M., et al. (2011). Evaluation of Radiation Scheme Performance Within Chemistry Climate Models. *J. Geophys. Res.*, **116**(D10302), doi:10.1029/2010JD015361.
- Francis, G.L., Edwards, D.P., Lambert, A., Halvorson, C.M., Lee-Taylor, J.M. & Gille, J.C. (2006). Forward Modeling and Radiative Transfer for the NASA EOS-Aura High Resolution Dynamics Limb Sounder (HIRDLS) Instrument. *J. Geophys. Res.*, **111**, D13301.
- Frankenberg, C., et al. (2011). Global Column-Averaged Methane Mixing Ratios from 2003 to 2009 as Derived from SCIAMACHY: Trends and Variability. *J. Geophys. Res.*, **116**, D04302, doi:10.1029/2010JD014849.
- Friedl-Vallon, F., Maucher, G., Kleinert, A., Lengel, A., Keim, C., Oelhaf, H., Fischer, H., Seefeldner, M. & Trieschmann, O. (2004). Design and Characterization of the Balloon-borne Michelson Interferometer for Passive Atmospheric Sounding (MIPAS-B2). *Appl. Opt.*, **43**, pp3335–3355.
- Frisk, U., et al. (2003). The Odin satellite - I. Radiometer Design and Test. *Astronomy & Astrophysics*, **402**, L27–L34.
- Fritts, D.C., & Alexander M.J. (2003). Gravity Wave Dynamics and Effects in the Middle Atmosphere. *Rev. Geophys.*, **41** (1), 1003, doi: 10.1029/2001-RG000106.
- Fromm, M., Lindsey, D.L., Sevranckx, R., Yue, G., Trickl, T., Sica, R., Doucet P. & S. Godin-Beemann (2010). The Untold Story of Pyrocumulonimbus. *Bull. Amer. Meteor. Soc.* pp1193–1209.
- Fueglistaler, S., Dessler, A.E., Dunkerton, T.J., Folkins, I., Fu, Q. & Mote, P.W. (2009). Tropical Tropopause Layer. *Rev. Geophys.*, **47**, RG1004, doi:10.1029/2008RG000267.
- GACS (2009): Final Report of the GMES Atmosphere Core Service Implementation Group, Waldteufel, P., et al., GMES Bureau, <http://www.gmes.info/pages-principales/library/implementation-groups/gmes-atmosphere-core-service/>.
- GCOS (2010). Implementation Plan for the Global Observing System for Climate in Support of the UNFCCC (2010 Update), WMO, UNESCO, IOC, UNEP, ICSU. GCOS-138, <http://www.wmo.int/pages/prog/gcos/Publications/gcos-138.pdf>.
- GCOS (2011). Systematic Observation Requirements for Satellite-Based Products for Climate, 2011 update. Supplemental details to the satellite-based component of the “Implementation Plan for the Global Observing System for Climate in Support of the UNFCCC (2010 Update)”, WMO, UNESCO, IOC, UNEP, ICSU. GCOS-154, <http://www.wmo.int/pages/prog/gcos/Publications/gcos-154.pdf>.
- Geer, A.J., et al. (2006). The ASSET Intercomparison of Ozone Analyses: Method and First Results. *Atmos.Chem.Phys.*, **6**, pp5445–5474.
- Generoso, S., Bey, I., Attié, J.-L., and Bréon, F.-M. (2007). A Satellite- and Model-Based Assessment of the 2003 Russian Fires: Impact on the Arctic Region, *J. Geophys. Res.*, **112**, D15302, doi:10.1029/2006JD008344.
- Gottelman, A., Hoor, P., Pan, L.L., Randel, W., Hegglin, M.I., Birner, T. (2011). The Extratropical Upper Troposphere and Lower Stratosphere. *Reviews of Geophysics*, **49**, RG3003, 10.1029/2011RG000355.
- Gille, J.C. & Russell III, J.M. (1975). The NIMBUS 6 User’s Guide: LRIR, Section 7, pp141–161.

- Gille, J.C. & Russell III, J.M. (1984). The Limb Infrared Monitor of the Stratosphere: Experiment Description, Performance, and Results. *J. Geophys. Res.*, **89**, No. D4, pp5125–5140.
- Gille, J., et al. (2008). High Resolution Dynamics Limb Sounder (HIRDLS): Experiment Overview, Recovery and Validation of Initial Temperature Data. *J. Geophys. Res.*, **113**, D16S43; doi:10.1029/2007JD008824.
- Glatthor, N. (2012). The Australian Bush Fires of February 2009: MIPAS Observations and GEM-AQ Model Results. To be submitted to ACPD
- Gonzi, S. & Palmer, P.I. (2010). Vertical Transport of Surface Fire Emissions Observed from Space. *J. Geophys. Res.*, **115**, D02306, doi:10.1029/2009JD012053.
- Granier, C., et al. (2011). Evolution of Anthropogenic and Biomass Burning Emissions of Air Pollutants at Global and Regional Scales During the 1980–2010 Period. *Climatic Change*, **109**, pp163–190, doi:10.1007/s10584-011-0154-1.
- Grossmann, K.U., Offermann, D., Gusev, O., Oberheide, J., Riese, M. & Spang, R. (2002). The CRISTA-2 Mission. *J. Geophys. Res.*, **107** (D23), pp8173–8185, doi:10.1029/2001JD000667.
- Guan, H., et al. (2010). A Multi-Decadal History of Biomass Burning Heights Identified Using Aerosol Index Measurements. *A. C. P. Diss.*, **10**, pp1–25.
- Hartmann, G.K., et al. (1996). Measurements of O₃, H₂O and ClO in the Middle Atmosphere Using the Millimeter Wave Atmospheric Sounder (MAS). *Geophys. Res. Lett.*, **23**, pp2313–2316.
- Haynes, P.H. & Shuckburgh, E.F. (2000). Effective Diffusivity as a Diagnostic of Atmospheric Transport, 1. Stratosphere. *J. Geophys. Res.*, **105**, pp22 777–22 794.
- Hegglin, M. I., et al. (2004). Tracing Troposphere-to-Stratosphere Transport Within a Mid-Latitude Deep Convective System. *Atmos. Chem. Phys.*, **4**, pp741–756.
- Hegglin, M.I., et al. (2006). Measurements of NO, NO_y, N₂O, and O₃ During SPURT: Implications for Transport and Chemistry in the Lowermost Stratosphere. *Atmos. Chem. Phys.*, **6**, pp1331–1350.
- Hegglin, M.I., Boone, C.D., Manney, G.L., Shepherd, T.G., Walker, K.A., Bernath, P.F., Daffer, W.H., Hoor, P. & Schiller, C. (2008). Validation of ACE-FTS Satellite Data in the Upper Troposphere/Lower Stratosphere (UTLS) Using Non-Coincident Measurements. *Atmos. Chem. Phys.*, **8**, pp1483–1499.
- Hegglin, M.I. & Shepherd, T.G. (2009a). Large Climate-Induced Changes in UV Index and Stratosphere-to-Troposphere Ozone Flux. *Nature Geoscience*, **2**, pp687–691.
- Hegglin, M.I., Boone, C.D., Manney, G.L. & Walker, K.A. (2009b). A Global View of the Extratropical Tropopause Transition Layer from Atmospheric Chemistry Experiment Fourier Transform Spectrometer O₃, H₂O, and CO. *J. Geophys. Res.*, **114**, D00B11, doi:10.1029/2008JD009984.
- Hollingsworth, A., et al. (2008). The Global Earth-system Monitoring using Satellite and *In-situ* Data (GEMS) Project: Towards a Monitoring and Forecasting System for Atmospheric Composition. *Bull. Amer. Meteor. Soc.*, **89**(8), pp1147–1164, doi:10.1175/2008BAMS2355.1.
- Holton J, & Gettelman, A. (2001). Horizontal Transport and the Dehydration of the Stratosphere. *Geophys. Res. Lett.*, **28**, pp2799–2802.
- Höpfner, M., Luo, B.P., Massoli, P., Cairo, F., Spang, R., Snels, M., Di Donfrancesco, G., Stiller, G., von Clarmann, T., Fischer, H. & Biermann, U. (2006). Spectroscopic Evidence for NAT, STS, and Ice in MIPAS Infrared Limb Emission Measurements of Polar Stratospheric Clouds. *Atmos. Chem. Phys.*, **6**, pp1201–1219.
- Huijnen, V., et al. (2010). The Global Chemistry Transport Model TM5: Description and Evaluation of the Tropospheric Chemistry Version 3.0. *Geosci. Model Dev.*, **3**, pp445–473, doi:10.5194/gmd-3-445-2010.
- Hurst, D.F., et al. (2011). Stratospheric Water Vapour Trends Over Boulder, Colorado: Analysis of the 30-year Boulder Record. *J. Geophys. Res.*, **116**, D02306, doi:10.1029/2010JD015065.
- IGACO (2004). Report of the Integrated Global Atmospheric Chemistry Observation Theme Team, Barrie, Langen (co-chairs), ESA SP-1282, GAW Report No. 159, WMO TD No. 1235.
- Inatani, J., et al. (2000). Submillimeter Limb-Emission Sounder JEM/SMILES Aboard the Space Station. *Proc. SPIE 4152* pp243–254, <http://dx.doi.org/10.1117/12.41604>.
- Ineson, S. & Scaife, A.A. (2009). The Role of the Stratosphere in the European Climate Response to El Niño. *Nature Geoscience*, **2**, pp32–36, doi:10.1038/ngeo381.
- Jung, T., Miller M.J. & Palmer T.N. (2010). Diagnosing the Origin of Extended-Range Forecast Errors. *Month. Wea. Rev.*, **138** (6), pp2434–2446, doi: 10.1175/2010MWR3255.1.
- Kaiser, J. W., et al. (2012). Biomass Burning Emissions Estimated with a Global Fire Assimilation System Based on Observed Fire Radiative Power. *Biogeosciences*, **9**, pp527–554, doi:10.5194/bg-9-527-2012.
- Kelder, H., Kerridge, B., Isaksen, I., Carli, B., Harris N. & Hilsenrath, E. (2006). Requirements for Operational Atmospheric Chemistry Monitoring in the Post-EPS Time Frame beyond 2020. http://www.eumetsat.int/groups/pps/documents/document/pdf_peps_pp_atmos_chem.pdf.
- Kerridge, B.J., et al. (2012). PREMIER Consolidation of Requirements and Synergistic Algorithms (CORSA) Study Final Report of ESA contract 4200022848/09/NL/CT.
- Khosrawi, F., Grooss, J.-U., Mueller, R., Konopka, P., Kouker, W., Ruhnke, R., Reddmann, T. & Riese, M. (2005). Intercomparison between Lagrangian and Eulerian Simulation of the Development of Mid-Latitude Streamers as Observed by CRISTA. *Atmos. Chem. Phys.*, **5**, pp85–95.
- Khosravi, R., et al. (2009a). Overview and Characterization of Retrievals of Temperature, Pressure, and Atmospheric Constituents from the High Resolution Dynamics Limb Sounder (HIRDLS) Measurements. *J. Geophys. Res.*, **114**, D20304, doi:10.1029/2009JD011937.
- Kiefer, M. et al. (2010). Impact of Temperature Field Inhomogeneities on the Retrieval of Atmospheric Species from MIPAS IR Limb Emission Spectra. *Atmos. Meas. Tech.*, Vol. **3**(5), pp1487–1507, doi: 10.5194/amf-3-1487-2010.

- Konopka, P., Grooss, J.-U., Guenther, G., Ploeger, F., Pommrich, R., Mueller, R. & Livesey, N. (2010). Annual Cycle of Ozone At and Above the Tropical Tropopause: Observations Versus Simulations with the Chemical Model of the Stratosphere (CLaMS). *Atmos. Chem. Phys.*, **10**, pp121–132.
- Konopka, P., Guenther, G., McKenna, D.S., Mueller, R., Offermann, D., Spang, R. & Riese, M. (2005). How Homogeneous and Isotropic is Stratospheric Mixing? Comparison of CRISTA-1 Observations with Transport Studies Based on the Chemical Lagrangian Model of the Stratosphere (CLaMS). *Q. J. R. Meteorol. Soc.*, **131**(606), pp565–579, doi:10.1256/qj.04.47.
- Kort, E.A., et al. (2011). Tropospheric Distribution and Variability of N₂O: Evidence for Strong Tropical Emissions. *Geophys. Res. Lett.*, **38**, L15806, doi:10.1029/2011GL047612.
- Kueller, V., et al. (2005). Tropopause Region Temperatures and CFC-11 Mixing Ratios from CRISTA 2. *J. Geophys. Res.*, **110**, D16104, doi:10.1029/2004JD005592.
- Lacis, A.A., Wuebbles, D.J. & Logan, J.A. (1990). Radiative Forcing of Climate by Changes in the Vertical Distribution of Ozone. *J. Geophys. Res.*, **95**, pp9971–9981.
- Lahoz, W.L., Errera, Q., Swinbank, R. & Fonteyn, D. (2007). Data Assimilation of Stratospheric Constituents: A Review. *Atmos. Chem. Phys.*, **7**, pp5745–5773.
- Laj, P., et al. (2009). Measuring Atmospheric Composition Change. *Atmos. Env.*, **43**, pp5351–5414, <http://dx.doi.org/10.1016/j.atmosenv.2009.08.020>.
- Lavoué, D., Gong, S. & Stocks, B.J. (2007). Modelling Emissions from Canadian Wildfires: A Case Study of the 2002 Quebec Fires. *Int. J. Wildland Fire*, **16**, pp649–663, doi:10.1071/WF06091.
- Li, F., Austin, J. & Wilson, J. (2008). The Strength of the Brewer Dobson Circulation in a Changing Climate: Coupled Chemistry Climate Model Simulations. *J. Clim.*, **21**, pp40–57, doi:10.1175/2007JCLI1663.1.
- Livesey, N.J. & Read, W.G. (2000). Direct Retrieval of Line-of-Sight Atmospheric Structure from Limb Sounding Observations. *Geophys. Res. Lett.*, **27**, pp891–894.
- Livesey, N.J., Snyder, W.V., Read, W.G. & Wagner, P.A. (2006). Retrieval algorithms for the EOS Microwave Limb Sounder (MLS) instrument. *IEEE Trans. Geosci. Remote Sensing*, **44**, no. 5, pp1144–1155.
- Lupu, A., et al. (2009). Hydrogen Cyanide in the Upper Troposphere: GEM-AQ Simulation and Comparison with ACE-FTS Observations. *Atmos. Chem. Phys.*, **9**, pp4301–4313.
- Marenco, A., et al. (1998). Measurement of Ozone and Water Vapour by Airbus In-Service Aircraft: The MOZAIK Airborne Program, An Overview. *J. Geophys. Res.*, **103**, pp25 631–25 642.
- Marshall, A.G. & Scaife, A.A. (2010). Improved Predictability of Stratospheric Sudden Warming Events in an Atmospheric General Circulation Model with Enhanced Stratospheric Resolution. *J. Geophys. Res.*, **115**, doi: 10.1029/2009JD012643.
- Massie, S., et al. (2007). High Resolution Dynamics Limb Sounder Observations of Polar Stratospheric Clouds and Subvisible Cirrus. *J. Geophys. Res.*, **112**, D24S31, doi:10.1029/2007JD008788.
- Maycock, A.C., Shine, K.P. & Joshi, M.M. (2011). The Temperature Response to Stratospheric Water Vapour Changes. *Q. J. Roy. Meteorol. Soc.*, **137** (657), pp1070–1082, doi:10.1002/qj.822.
- McLandress, C. & Shepherd T.G. (2009). Simulated Anthropogenic Changes in the Brewer Dobson Circulation, Including its Extension to High Latitudes. *J. Clim.*, **22**, pp1516–1540, doi:10.1175/2008JCLI2679.1.
- Mendrok, J., Schreier, F. & Höpfner, M. (2007). Estimating Cirrus Cloud Properties from MIPAS Data. *Geophys. Res. Lett.*, Vol. **34**, No. 8, L08807, doi:10.1029/2006GL028246.
- Moore, D.P. & Remedios, J.J. (2010). Seasonality of Peroxyacetyl Nitrate (PAN) in the Upper Troposphere and lower Stratosphere Using the MIPAS-E Instrument. *Atmos. Chem. Phys.*, **10**, pp6117–6128, doi:10.5194/acp-10-6117-2010.
- Murk, A., Duric, A. & Patt, F. (2008). Characterization of ALMA Calibration Targets. Proc. *19th International Symposium on Space Terahertz Technology, Groningen, 28–30 April 2008*.
- Murtagh, D., et al. (2002). An Overview of the Odin Atmospheric Mission. *Can. J. Phys.*, **80**, pp309–319.
- Offermann, D., Grossmann, K.U., Barthol, P., Knieling, P., Riese, M. & Trant, R. (1999). Cryogenic Infrared Spectrometers and Telescopes for the Atmosphere (CRISTA) Experiment and Middle Atmosphere Variability. *J. Geophys. Res.*, **104**, pp16 311–16 325.
- Ordóñez, C., et al. (2007). Strong Influence of Lowermost Stratospheric Ozone on Lower Tropospheric Background Ozone Changes Over Europe. *Geophys. Res. Lett.*, **34**, L07805, doi:10.1029/2006GL029113.
- Orsolini, Y.J., Kindem I.T. & Kvamsto, N.G. (2011). On the Potential Impact of the Stratosphere Upon Seasonal Dynamical Hindcasts of the North Atlantic Oscillation: A Pilot Study. *Clim. Dyn.*, **36**, pp579–588, doi:10.1007/s00382-009-0705-6.
- Pan, L.L., et al. (2009). Tropospheric Intrusions Associated with the Secondary Tropopause. *J. Geophys. Res.*, **114**, D10302, doi:10.1029/2008JD011374.
- Park, M., Randel, W.J., Emmons, L.K. & Livesey, N.J. (2009). Transport Pathways of Carbon Monoxide in the Asian Summer Monsoon Diagnosed from Model of Ozone and Related Tracers (MOZART). *J. Geophys. Res.*, **114**, D08303, doi:10.1029/2008JD010621.
- Parrington, M., et al. (2008). Estimating the Summertime Tropospheric Ozone Distribution Over Northamerica Through Assimilation of Observations from the Tropospheric Emission Spectrometer. *J. Geophys. Res.*, **113**, D18307, doi:10.1029/2007JD009341.
- Parrish, D.D., Millet, D.B. & Goldstein, A.H. (2009). Increasing Ozone in Marine Boundary Layer Inflow at the West Coasts of North America and Europe. *Atmos. Chem. Phys.*, **9**, pp1303–1323, doi:10.5194/acp-9-1303-2009.
- Peuch, A., Thépaut, J.-N. & Pailleux, J. (2000). Dynamical Impact of Total-Ozone Observations in a Four-Dimensional Variational Assimilation. *Q. J. Roy. Meteorol. Soc.*, **126**(566), pp1641–1659.
- Preusse et al. (2012). Observation of Gravity Waves from Space. Final Report of ESA study contract 22561/09/NL/AF.

- Pumphrey, H.C., Santee, M.L., Livesey, N.J., Schwartz, M.J. & Read W.G. (2011). Microwave Limb Sounder Observations of Biomass-Burning Products from the Australian Bush Fires of February 2009. *Atmos. Chem. Phys. Discuss.*, **11**, pp6531–6554.
- Randall, D.A., et al. (2007). Climate Models and Their Evaluation. In: Climate Change 2007: The Physical Science Basis. Contribution of Working Group I to the Fourth Assessment Report of the Intergovernmental Panel on Climate Change (eds. Solomon, S., Qin, D., Manning, M., Chen, Z., Marquis, M., Averyt, K.B., Tignor, M. & Miller, H.L.). Cambridge University Press, Cambridge, United Kingdom and New York, NY, USA.
- Randel, W.J. & Park, M. (2006). Deep Convective Influence on the Asian Summer Monsoon Anticyclone and Associated Tracer Variability Observed with Atmospheric Infrared Sounder (AIRS). *J. Geophys. Res.*, **111**, D12314, doi:10.1029/2005JD006490.
- Randel, W.J., et al. (2009). An Update of Observed Stratospheric Temperature Trends. *J. Geophys. Res.*, **114**, D02107, doi:10.1029/2008JD010421.
- Randel, W.J., et al. (2010). Asian Monsoon Transport of Pollution to the Stratosphere. *Science*, **328**, 611, doi:10.1126/science.1182274§.
- Raspollini P., et al. (2006). MIPAS Level-2 Operational Analysis. *Atmos. Chem. Phys.*, Vol. **6**, pp5605–5630.
- Reburn, J., Hilsenrath, E., Killough, B. (2008). CEOS Atmospheric Composition Constellation Gap Analysis Study. http://www.ceos.org/images/PDFs/ACC/CEOS_ACC_Final_Report_v2.pdf
- Richter, J.H., Sassi, F. & Garcia, R.R. (2010). Toward a Physically Based Gravity Wave Source Parameterization in a General Circulation Model. *J. Atmos. Sci.*, **67**, pp136–156, doi:10.1175/2009JAS3112.1.
- Ridolfi, M., et al. (2010). Optimized Forward Model and Retrieval Scheme for MIPAS Near-Real-Time Data Processing. *Applied Optics*, **39**, 8, pp1323–1340, doi: 10.1364/AO.39.001323
- Riese, M., et al. (2011). PREMIER – Quantification of Atmospheric Pollution and Climate Aspects. Final Report of ESA study contract 4000101294/10/NL/CBi.
- Riishojgaard, L.P. (1996). On Four-Dimensional Variational Assimilation of Ozone Data in Weather-Prediction Models. *Q. J. Roy. Meteorol. Soc.*, **122** (535), pp1545–1571.
- Roche, A.E., Kumer, J.B., Mergenthaler, J.L., Ely, G.A., Uplinger, W.G., Potter, J.F., James, T.C. & Sterritt, L.W. (1993). The Cryogenic Limb Array Etalon Spectrometer (CLAES) on UARS: Experiment Description and Performance. *J. Geophys. Res.*, **98**, pp10 763–10 775.
- Rodgers, C.D. (2000). Inverse Methods for Atmospheric Sounding: Theory and Practice. World Scientific Publishing Co., Singapore, 238 pp.
- Roff, G., Thompson, D.W.J. & Hendon, H. (2011). Does Increasing Model Stratospheric Resolution Improve Extended-Range Forecast Skill? *Geophys. Res. Lett.*, **38**, L05809, doi: 10.1029/2010GL046515.
- Russell III, J.M., Mlynczak, M.G., Gordley, L.L., Tansock, J.J. & Esplin, R.W. (1999). An Overview of the SABER Experiment and Preliminary Calibration Results. *SPIE*, **3756**, pp277–288.
- Schlüssel, P., Phillips, P., Accadia, C. & Munro, R. (2010). Post-EPS Mission Requirement Document, EUM/PEPS/REQ/06/0043, version v3C, http://www.eumetsat.int/groups/pps/documents/document/pdf_peps_mrd.pdf.
- Scaife, A.A., et al. (2011). Climate Change Projections and Stratosphere-Troposphere Interaction. *Clim. Dynam.*, doi:10.1007/s00382-011-1080-7, in print.
- Schuck, T.J., Brenninkmeijer, C.A.M., Baker, A.K., Slemr., F., von Velthoven, P.F.J. & Zahn, A. (2010). Greenhouse Gas Relationships in the Indian Summer Monsoon Plume Measured by the CARIBIC Passenger Aircraft. *Atmos. Chem. Phys.*, **10**, pp3965–3984, doi:10.5194/acp-10-3965-2010.
- Semane, N., Peuch, V.-H., Pradier, S., Desroziers, G., El Amraoui, L., Brousseau, P., Massart, S., Chapnik, B. & Peuch, A. (2008). On the Extraction of Wind Information from the Assimilation of Ozone profiles in Météo-France 4D-Var Operational NWP Suite. *Atmos. Chem. Phys.*, **9**, pp4855–4867.
- Sherwood, S.C., Roca, R., Weckwerth, T.M. & Andronova, N.G. (2010). Tropospheric Water Vapor, Convection and Climate. *Rev. Geophys.*, **48**, RG2001, doi:10.1029/2009RG000301.
- Shindell, D.T., Faluvegi, G., Koch, D.M., Schmidt, G.A., Unger, N. & Bauer, S.E. (2011). Improved Attribution of Climate Forcing to Emissions. *Science*, **326** (5953), pp716–718, doi:10.1126/science.1174760.
- Shiotani, M., Masuko, H. & the SMILES Science Team (2002). JEM/SMILES Mission Plan, Version 2.1, *National Space Development Agency (NASDA) and Communications Research Laboratory (CRL)*.
- Siddaway, J.M. & Petelina, S.V. (2011). Transport and Evolution of the 2009 Australian Black Saturday Bushfire Smoke in the Lower Stratosphere Observed by OSIRIS on Odin. *J. Geophys. Res.*, **116**, D06203, doi:10.1029/2010JD015162.
- Simmons, A.J. & Hollingsworth, A. (2002). Some aspects of the improvement in skill of numerical weather prediction. *Q. J. Roy. Meteorol. Soc.*, **128**(580), pp647–677.
- Solomon, S., Rosenlof, K.H., Portmann, R.W., Daniel, J.S., Davis, S.M., Sanford, T.J. & Plattner, G.-K. (2010). Contributions of Stratospheric Water Vapor to Decadal Changes in the Rate of Global Warming. *Science*, **327**, pp1219–1223, doi: 10.1126/science.1182488.
- Son, et al. (2008). The Impact of Stratospheric Ozone Recovery on the Southern Hemisphere Westerly Jet. *Science*, **320** (5882), pp1486–1489, doi:10.1126/science.1155939.
- Søvde, O.A., Gauss, M., Isaksen, I.S.A., Pitari, G. & Marizy, C. (2007). Aircraft Pollution – A Futuristic View. *Atmos. Chem. Phys.*, **7**, pp3621–3632.
- Spahni, R., et al. (2011). Constraining Global Methane Emissions and Uptake by Ecosystems. *Biogeosciences*, **8**, pp1643–1665, doi:10.5194/bg-8-1643-2011.
- Spang, R., Remedios, J.J. & Barkley, M.P. (2004). Colour Indices for the Detection and Differentiation of Cloud Types in infrared Limb Emission Spectra. *Advances in Space Research*, **33**, pp1041–1047.
- Spang, R. et al. (2010). Cloud Information Retrieval from MIPAS Measurements, Final Report of ESA Contract No. 20601/07/I-OL.

- Spang., R., et al. (2011). Technical Assistance for the Deployment of Airborne Infra-Red and Millimetre-Wave Limb-Sounders during the PREMIER-EX Experiment. Final Report of ESA study contract 22670/09/NL/CT.
- SPARC CCMVal (2010). SPARC Report on the Evaluation of Chemistry-Climate Models. (eds. Eyring, V., Shepherd, T.G. & Waugh, D.W.) SPARC Report No. 5, WCRP-132, WMO/TD-No. 1526, <http://www.atmosp.physics.utoronto.ca/SPARC>.
- SPARC Report on the Evaluation of Chemistry-Climate Models (eds. Eyring, V., Shepherd, T.G. & Waugh, D.W.), SPARC Report No. 5, WCRP-132, WMO/TDNo. 1526, 2010. (available at <http://www.atmosp.physics.utoronto.ca/SPARC>)
- Sprenger, M., Maspoli, M.C. & Wernli, H. (2003). Tropopause Folds and cross-tropopause exchange: A Global Investigation Based upon ECMWF Analyses for the Time Period March 2000 to February 2001. *J. Geophys. Res.*, **108**, 8518, doi:10.1029/2002JD002587.
- Stenchikov, G., Robock, A., Ramaswamy, V., Schwartzkopf, M.D., Hamilton, K. & Ramachandran, S. (2002). Arctic Oscillation response to the 1991 Mount Pinatubo Eruption: Effects of Volcanic Aerosols and Ozone Depletion. *J. Geophys. Res.*, **107**, 4803, doi:10.1029/2002JD002090.
- Stenke, A., Grewe, V. & Ponater M. (2008). Lagrangian Transport of Water Vapor and Cloud Water in the ECHAM4 GCM and its Impact on the Cold Bias. *Clim. Dyn.*, **31**(5), pp491–500, doi:10.1007/s00382-007-0347-5.
- Stevenson, D.S., et al. (2006). Multimodel Ensemble Simulations of Present-Day and Near-Future Tropospheric Ozone. *J. Geophys. Res.*, **111**, D08301, doi:10.1029/2005JD006338.
- Stiller, G.P., et al. (2008). Global Distribution of Mean Age of Stratospheric Air from MIPAS SF6 Measurements. *Atmos. Chem. Phys.*, **8**, pp677–695, doi:10.5194/acp-8-677-2008.
- Sturges, W.T., Oram, D.E., Carpenter, L.J., Penkett, S.A. & Engel A. (2000). Bromoform as a Source of Stratospheric Bromine. *Geophys. Res. Lett.*, **27**, pp2081–2084.
- Takahashi, C., Ochiai, S. & Suzuki, M. (2010). Operational Retrieval Algorithms for JEM/SMILES Level-2 Data Processing System. *J. Quantitative Spectroscopy and Radiative Transfer*, **111**, pp160–173.
- Taylor, et al. (1993), The Improved Stratospheric and Mesospheric Sounder (ISAM) on UARS: Experiment Description and Performance. *J. Geophys. Res.*, pp10 799–10 814.
- Thompson, D.W.J., Baldwin, M.P. & Wallace, J.M. (2002). Stratospheric Connection to Northern Hemisphere Wintertime Weather: Implications for Prediction. *J. Climate*, **15**, pp1421–1428.
- Thuburn, J. & Craig, G.C. (2000). Stratospheric Influence on Tropopause Height: The Radiative Constraint. *J. Atmos. Sci.*, **57**, pp17–28, doi:10.1175/1520-0469(2000)057<0017:SIOHT>2.0.CO;2.
- Trenberth, K.E., et al. (2007). Observations: Surface and Atmospheric Climate Change. In: *Climate Change 2007: The Physical Science Basis. Contribution of Working Group I to the Fourth Assessment Report of the Intergovernmental Panel on Climate Change* (eds. Solomon, S., Qin, D., Manning, M., Chen, Z., Marquis, M., Averyt, K.B., Tignor M. & Miller, H.L.). Cambridge University Press, Cambridge, United Kingdom and New York, NY, USA.
- Ungermann, J., Blank, J., Lotz, J., Leppkes, K., Hoffmann, L., Guggenmoser, T., Kaufmann, M., Preusse, P., Naumann, U. & Riese, M. (2011). A 3-D Tomographic Retrieval Approach with Advection Compensation for the Air-Borne Limb-Imager GLORIA. *Atmos. Meas. Tech.*, **4**, pp2509–2529.
- Ungermann, J., Hoffmann, L., Preusse, P., Kaufmann M. & Riese, M. (2010). Tomographic Retrieval Approach for Mesoscale Gravity Wave Observations by the PREMIER Infrared Limb-Sounder. *Atmos. Meas. Tech.*, **3**, pp339–354.
- Ungermann, J., et al. (2011). CRISTA-NF Measurements with Unprecedented Vertical Resolution during the RECONCILE Aircraft Campaign. *Atmos. Meas. Tech. Discuss.*, **4**, pp6915–6967. doi:10.5194/amtd-4-6915-2011.
- Urban, J., et al. (2005). Odin/SMR Limb Observations of Stratospheric Trace Gases: Level 2 Processing of ClO, N₂O, HNO₃, and O₃. *J. Geophys. Res. Atmos.* **110**, D14307. doi: 10.1029/2004.JD005741.
- Velders, G.J.M., Anderson, S.O., Daniel, J.S., Fahey, D.W. & McFarland, M. (2007). The importance of the Montreal Protocol in Protecting Climate. *Proc. Natl. Acad. Sci.*, **104**, no.12, pp4814–4819.
- Voigt, C., et al. (2010). In-situ Observations of Young Contrails – Overview And Selected Results from the CONCERT Campaign. *Atmos. Chem. Phys.*, **10**, pp9039–9056, doi:10.5194/acp-10-9039-2010.
- von Clarmann, T. (2006). Validation of Remotely Sensed Profiles of Atmospheric State Variables: Strategies and Terminology. *Atmos. Chem. Phys.*, **6**, pp4311–4320.
- von Clarmann, T., et al. (2003). Retrieval of Temperature and Tangent Altitude Pointing from Limb Emission Spectra Recorded from Space by the Michelson Interferometer for Passive Atmospheric Sounding (MIPAS). *J. Geophys. Res.*, **108**, No. D23, 4736, doi:10.1029/2003JD003602.
- Waters, J.W., et al. (2006). The Earth Observing System Microwave Limb Sounder (EOS MLS) on the Aura Satellite. *IEEE Trans. Geosci. Remote Sensing*, **44**, no. 5, pp1075–1092.
- Wild, O. & Akimoto, H. (2001). Intercontinental Transport of Ozone and its Precursors in a Three-Dimensional Global CTM. *J. Geophys. Res.*, **106**, pp27 729–27 744.
- WMO (World Meteorological Organization) (2007). Scientific Assessment of Ozone Depletion: 2006, Global Ozone Research and Monitoring Project – Report No. 50, 572 pp., Geneva, Switzerland.
- WMO (World Meteorological Organization) (2011). Scientific Assessment of Ozone Depletion: 2010, Global Ozone Research and Monitoring Project–Report No. 52, 516 pp., Geneva, Switzerland.

- Woiwode, W., et al. (2011). MIPAS-STR Measurements in the Arctic UTLS in Winter/Spring 2010: Instrument Characterization, Retrieval and Validation. *Atmos. Meas. Tech. Discuss.*, **4**, pp7035–7108. doi:10.5194/amtd-4-7035-2011.
- Ziemke, J.R., Chandra, S., Labow, G.J., Bhartia, P.K., Froidevaux, L. & Witte, J.C. (2011). A Global Climatology of Tropospheric and Stratospheric Ozone Derived from Aura OMI and MLS Measurements. *Atmos. Chem. Phys.*, **11**, pp9237–9251, doi:10.5194/acp-11-9237-2011.

→ **ACRONYMS**

Acronyms

ACAP	Azimuthally Collapsed Antenna Pattern	CORSA	Consolidation of Requirements and Synergistic Algorithms
ACCMIP	Atmospheric Chemistry and Climate Model Intercomparison Project	COST	European Cooperation in Science and Technology
ACE-FTS	Atmospheric Chemistry Experiment–Fourier Transform Spectrometer	CPU	Central Processing Unit
ACS	AutoCorrelator Spectrometer	CrIS	Cross-track Infrared Sounder
AD	Analogue-to-Digital	CRISTA (-NF)	CRyogenic Infrared Spectrometers and Telescopes for the Atmosphere (-New Frontiers)
ADC	Analogue-to-Digital Converter	CTM	Chemical Transport Model
ADM-Aeolus	Atmospheric Dynamics Mission-Aeolus	DA	Data Assimilation
AIT	Assembly, Integration and Testing	DC	Direct Current
AKE	Absolute Knowledge Error	DET	Direct Energy Transfer
ALMA	Atacama Large Millimetre/submillimetre Array	DM	Dynamics Mode
ALTIUS	Atmospheric Limb Tracker for the Investigation of the Upcoming Stratosphere	DOAS	Differential Optical Absorption Spectrometer
AMSU	Advanced Microwave Sounding Unit	DPU	Data Processing Unit
AOCS	Attitude and Orbit Control Subsystem	DSB	Double Side-Band
APE	Absolute Performance/Pointing Error	EarthCARE	Earth Clouds Aerosols and Radiation Explorer
AQ	Air Quality	ECMWF	European Centre for Medium-range Weather Forecasts
ARW	Angle Random Walk	EEMCS	Earth Explorer Mission Control System
ASCENDS	Active Sensing of CO ₂ Emissions over Nights, Days and Seasons	EFM	Electrical Functional Model
ASIC	Application-Specific Integrated Circuit	EGSE	Electrical Ground Support Equipment
AVHRR	Advanced Very High Resolution Radiometer	EMS	Estrack Management and Scheduling System
AVM	Avionic Model	ENSO	El Niño Southern Oscillation
BiMOS	Bipolar Complementary Metal Oxide Semiconductor	Envisat	Environmental Satellite
BOL	Beginning Of Life	EOL	End of Life
CAD	Computer Aided Design	EPS	Electrical Power Subsystem
Cal/Val	Calibration and Validation	EPS(SG)	Eumetsat Polar System (Second Generation)
CarbonSat	Carbon monitoring Satellite	EQM	Engineering Qualification Model
CARIBIC	Civil Aircraft for Remote sensing and In-situ measurements in troposphere and lower stratosphere Based on the Instrumentation Container concept	ERS	European Remote Sensing satellite (-1/-2)
CCM	Chemistry-Climate Model	ESA	European Space Agency
CDHS	Command and Data Handling Subsystem	ESAC	Earth Science Advisory Committee
CDR	Critical Design Review	ESM	Earth-System Model
CEOS	Committee on Earth Observation Satellites	ESOC	ESA's European Space Operations Centre
CFC	Chlorofluorocarbon	ESSENCE	ESA Sounder Campaign
CFRP	Carbon Fibre Reinforced Plastic	ExTL	Extratropical Transition Layer
CHARM	Compact Heterodyne Array Receiver Module	FCI	Flexible Combined Imager
CLAES	Cryogenic Limb Array Etalon Spectrometer	FDIR	Failure Detection, Isolation and Recovery
CM	Chemistry Mode	FEE	Front End Electronics
CMIP	Climate Model Inter-comparison Project	FEM	Finite Element Models
CMOS	Complementary Metal Oxide Semiconductor	FP7	Framework Programme 7
		FPE	Focal Plane Electronics
		FOS	Flight Operation Segment
		FOV	Field of View
		FPA	Focal Plane Assembly
		FTIR	Fourier-Transform Infra-Red spectrometer
		FTS	Fourier-Transform Spectrometer

FWHM	Full Width at Half Maximum	ISS	International Space Station
GACM	Global Atmospheric Composition Mission	ITB	IRLS Test Bench
GACS	GMES Atmospheric Core Service	JPSS	Joint Polar Satellite System
GAMS	GMES Atmospheric Monitoring Service	KOPRA	Karlsruhe Optimized and Precise Radiative transfer Algorithm
GCOS	Global Climate Observing System	KOSMA	Kölner Observatorium für SubMillimeter Astronomie
GEM(-AQ)	Global Environmental Multiscale model (-Air Quality)	LCL	Latching Current Limiter
GEMS	Global and regional Earth-system (Atmosphere) Monitoring using Satellite and <i>in situ</i> data	LEFE/CHAT	Les Enveloppes Fluides et l'Environnement/CHimie ATmosphérique
GEOCAPE	Geostationary Coastal and Air Pollution Events	LEOP	Launch and Early Operation Phase
GEOCARB	Geosynchronous Carbon Mission	LI	Lightning Imager
GLORIA-AB	GLObal Limb Radiance Imager of the Atmosphere - AirBorne	LIR	Launcher Interface Ring
GMES	Global Monitoring for Environment and Security	LMS	Lowermost Stratosphere
GNSS	global navigation satellite system	LNA	Low Noise Amplifier
GOCE	Gravity field and steady-state Ocean Circulation Explorer	LOS	Line Of Sight
GOES	Geostationary Operational Environmental Satellite	LRIR	Limb Radiance Inversion Radiometer
GOME	Global Ozone Monitoring Experiment	LS	Lower Stratosphere
GOMOS	Global Ozone Monitoring by Occultation of Stars	LSB	Lower Side-Band
GOS	Global Observing System	LTDN	Local Time of Descending Node
GPS	Global Positioning System	LVA	Launch Vehicle Adapter
GWMF	Gravity Wave Momentum Flux	MACC	Monitoring Atmospheric Composition and Climate
HALO	High Altitude and Long Range Research Aircraft	MACE	Mesosphere and Climate Experiment
HALOE	Halogen Occultation Experiment	MAG	Mission Advisory Group
HCFC	Hydro-Chloro-Fluoro-Carbon	MARSCHALS	Millimetre-Wave Airborne Receivers for Spectroscopic CHaracterisation in Atmospheric Limb Sounding
HIFAS	Highly Integrated Full Custom Autocorrelation Spectrometer	MAS	Millimetre-wave Atmospheric Sounder
HIRDLS	High Resolution Dynamics Limb Sounder	MCS	Mission Control System
HKTM	House Keeping and Telemetry	MCT	Mercury Cadmium Telluride
IAGOS	In-service Aircraft for a Global Observing System	MECALIB	Calibration Mechanism
IAP	Institute of Applied Physics	MERIS	Medium Resolution Imaging Spectrometer
IASI(NG)	Infrared Atmospheric Sounding Interferometer (Next Generation)	MERLIN	MEthane Remote Lidar missioN
ICU	Instrument Control Unit	MetImage	Meteorological Imager (on EPS-SG)
IFOV	Instantaneous Field Of View	MetOp (SG)	Meteorological Operational Satellite (Second Generation)
IFS	Integrated Forecast System	MHS	Microwave Humidity Sounder
IGAC	International Global Atmospheric Chemistry	MIPAS	Michelson Interferometer for Passive Atmospheric Sounder
IGACO	Integrated Global Atmospheric Chemistry Observations	MIPAS(B/STR)	Michelson Interferometer for Passive Atmospheric Sounding (Balloon/Stratospheric aircraft)
IGOS	Integrated Global Observing Strategy	MLI	Multi-Layer Insolation
ILS	Instrument Line Shape	MLS	Microwave Limb Sounder
IPCC	Intergovernmental Panel on Climate Change	MMIC	Monolithic Microwave Integrated Circuit
IR	Infra-Red	MMU	Mass Memory Unit
IRLS	Infra-Red Limb-Sounder	MOCAGE	MOdèle de Chimie Atmosphérique à Grande Echelle
IRS	Infra-Red Sounder	MOPD	Maximum Optical Path Difference
ISAMS	Improved Stratospheric and Mesospheric Sounder	MPL	Mission Positioning Line System
		MPS	Mission Planning System
		MSG	Meteosat Second Generation
		MTG (-S/I)	Meteosat Third Generation (-Sounder/Imager platform)
		MTL	Mission Time Line

MW	Millimetre-Wave or Micro-Wave	RIU	Remote Interface Unit
MWS	Micro-Wave Sounder	RMS	Root Mean Squared
NASA	National Aeronautics and Space Administration	ROIC	Read-Out Integrated Circuits
NDACC	Network for the Detection of Atmospheric Composition Change	RPE	Relative Pointing Error
NEBT	Noise Equivalent Brightness Temperature	RPE	Relative Performance Error
NEdL	Noise Equivalent delta Radiance	RSS	Root of Sum of Squares
NEdT	Noise Equivalent delta Temperature	S4/5	Sentinel-4/-5
NESR	Noise Equivalent Spectral Radiance	SABER	Sounding of the Atmosphere using Broadband Emission Radiometry
NOAA	National Oceanic and Atmospheric Administration	SADM	Solar Array Drive Mechanism
NPP	NPOESS Preparatory Project	SAGE	Stratospheric Aerosol and Gas Experiment
NRT	Near-realtime	SAMS	Stratospheric and Mesospheric Sounder
NWP	Numerical Weather Prediction	SAR	Synthetic Aperture Radar
OBC	On-Board Computer	Sciamachy	Scanning Imaging Absorption Spectrometer for Atmospheric Cartography
OBCP	On-Board Control Procedures	SCOC3	Space Controller On a Chip with LEON 3
OCO	Orbiting Carbon Observatory	SDRAM	Synchronous Dynamic Random Access Memory
ODS	Ozone Depleting Substances	SEVIRI	Scanning Enhanced Visible and Infrared Imager
OGAD	On-Ground Satellite Attitude Determination	SIMSAT	Simulation Infrastructure for the Modelling of Satellites
OGOD	On-Ground Satellite Orbit Determination	SM	Structural Model
OI	Optimal Interpolation	SMART	Small Missions for Advanced Research in Technology
OMPS	Ozone Monitoring and Profiling Suite	SME	Small/Medium Enterprise
OPD	Optical Path Difference	SMILES	Sub-Millimetre Wave Limb-Emission Sounder
ORATOS	Orbit and Attitude Operations System	SMOS	Soil Moisture and Ocean Salinity mission
OSIRIS	Optical Spectrograph and InfraRed Imaging System	SMR	Sub-Millimetre Radiometer
OSSE	Observation System Simulation Experiment	SNR	Signal-to-Noise Ratio
PAN	Peroxyacetylnitrate	SPARC	Stratospheric Processes And their Role in Climate
PCDU	Power Conditioning and Distribution Unit	SPU	Signal Processing Unit
PCM	Pulse-Code Modulation	SRR	Systems Requirements Review
PCW	Polar Communication and Weather satellite system	SSD	Spatial Sampling Distance
PDGS	Payload Data Ground Segment	SSP	Sub-Satellite Point
PDHT	Payload Data Handling and Transmission	STE	Stratosphere-Troposphere Exchange
PDR	Preliminary Design Review	STEAMR	Stratosphere-Troposphere Exchange And climate Monitor Radiometer
PFM	Proto Flight Model	STM	Structural Thermal Model
PIP	Payload Interface Panel	STR	Startracker
PPBV	part per billion by volume	SWIR	Short-Wave Infra-Red
PPMV	part per million by volume	TC4	Tropical Composition Cloud and Climate Coupling
PPTV	part per trillion by volume	TCM	Tropical Carbon Mission
PREMIER	PRocess Exploration through Measurements of Infrared and millimetre-wave Emitted Radiation	THORPEX	THE Observing system Research and Predictability EXperiment
PSC	Polar Stratospheric Cloud	TIL	Tropopause Inversion Layer
PSF	Point-Spread Function	TIMED	Thermosphere, Ionosphere, Mesosphere, Energetics and Dynamics
PSLV	Polar Satellite Launch Vehicle	TRL	Technology Readiness Level
QBO	Quasi-Biennial Oscillation	TT&C	Telemetry, Tracking and Command
QPSK	Quadrature Phase Shift Keying	TTL	Tropical Tropopause Layer
RAAN	Right Angle of Ascending Node	TWTA	Travelling Wave Tube Amplifiers
REKLIM	Regionale Klimaänderungen		
RF	Radio Frequency		
RF	Radiative Forcing		
RFM	Reference Forward Model		

UARS	Upper Atmosphere Research Satellite
UAV	Unmanned Aerial Vehicle
USB	Upper Side-Band
UT	Upper Troposphere
UTLS	Upper Troposphere/Lower Stratosphere
VAAC	Volcanic Ash Advisory Centre
VASP	Video Acquisition Signal Processor
VII	Visible and Infrared Imager
VIS	Visible
VMR	Volume Mixing Ratio
VOC	Volatile Organic Compound
WCRP	World Climate Research Programme
WGNE	Working Group on Numerical Experimentation
WMO	World Meteorological Organization
ZPD	Zero Path Difference
3MI	Multi-viewing, Multi-channel, Multi-polarisation Imager

Chemical Species

BrO_x	Reactive bromine oxides
BrO	Bromine monoxide
BrONO₂	Bromine nitrate
CCl₂F₂	Difluorodichloromethane (CFC-12)
CCl₃F	Trichlorofluoromethane (CFC-11)
CFC	Chlorofluorocarbon
C₂H₂	Ethyne
C₂H₆	Ethane
C₅H₈	Isoprene
CH₃Br	Methyl bromide or Bromomethane
CH₃Cl	Methylchloride or Chloromethane
CH₃CN	Acetonitrile or Methyl cyanide
CH₃OH	Methanol
CH₄	Methane
CHClF₂	Chlorodifluoromethane (HCFC-22)
ClO_x	Reactive chlorine oxides
ClO	Chlorine monoxide
ClONO₂	Chlorine nitrate
CO	Carbon monoxide
CO₂	Carbon dioxide
D	Deuterium (hydrogen isotope)
H₂CO or HCHO	Formaldehyde
HO_x	Reactive hydrogen oxides
H₂O	Water vapour
HCN	Hydrogen cyanide
HDO	Semi-heavy water
HNO₃	Nitric acid
HO₂NO₂	Peroxynitrous acid
NO_x	Reactive nitrogen oxides
NO	Nitric oxide
NO₂	Nitrogen dioxide
N₂O	Nitrous oxide
N₂O₅	Dinitrogen pentoxide

¹⁸O	Oxygen isotope
O₂	Oxygen
O₃	Ozone
OCS	Carbonylsulphide
OH	Hydroxyl
PAN	Peroxyacetylnitrate
SF₆	Sulphur hexafluoride
SO₂	Sulphur dioxide



ESA Member States

Austria
Belgium
Czech Republic
Denmark
Finland
France
Germany
Greece
Ireland
Italy
Luxembourg
Netherlands
Norway
Portugal
Romania
Spain
Sweden
Switzerland
United Kingdom